

**Dissertation**  
submitted to the  
**Combined Faculties for the Natural Sciences and for Mathematics**  
**of the Ruperto-Carola University of Heidelberg, Germany**  
for the degree of  
**Doctor of Natural Sciences**

Put forward by  
Robert Grajcarek  
Born in Krasnik (Poland)

Oral examination: May 22, 2013



**Anisotropic flow of the charmed  $D^{*+}$  meson in non-central  
Pb–Pb collisions at  $\sqrt{s_{\text{NN}}} = 2.76$  TeV**

Referees:

Dr. Kai Schweda  
Prof. Dr. Ulrich Uwer



## **Anisotropischer Fluss des $D^{*+}$ Mesons in nicht-zentralen Blei-Blei-Kollisionen bei einer Schwerpunktsenergie von $\sqrt{s_{NN}} = 2.76$ TeV**

Der Fokus dieser Arbeit liegt auf der Messung der azimuthalen Anisotropieparameter  $v_2$  und  $v_3$  des  $D^{*+}$  Mesons und seines negativ geladenen Partners  $D^{*-}$  in den vollständig rekonstruierten Zerfallskanälen  $D^{*+} \rightarrow D^0\pi^+$  und  $D^{*-} \rightarrow \bar{D}^0\pi^-$  unter Anwendung der Eventplane-Methode. Für diese Messung wurden Daten verwendet, die mit dem ALICE-Detektor (A Large Ion Collider Experiment) während des Blei-Blei-Runs ende des Jahres 2011 am LHC (Large Hadron Collider) aufgezeichnet wurden. Die  $v_2$ - und  $v_3$ -Parameter wurden als Funktion des Transversalimpulses  $p_T$  des  $D^{*+}$  Mesons in einem Bereich von  $2 \text{ GeV}/c < p_T < 20 \text{ GeV}/c$  bestimmt. Der gemessene  $v_2$ -Parameter ist vergleichbar mit den  $v_2$ -Werten von nicht identifizierten, geladenen Teilchen. Die Signifikanz für ein von null verschiedenes  $D^{*+}$   $v_2$  im  $p_T$ -Bereich von  $2 \text{ GeV}/c < p_T < 6 \text{ GeV}/c$  beträgt drei Standardabweichungen, wenn man nur statistische Messunsicherheiten betrachtet, beziehungsweise zwei Standardabweichungen, wenn statistische und systematische Messunsicherheiten kombiniert werden. Die gemessenen  $v_3$ -Werte sind in der Größenordnung  $v_3 \approx 0.2$  im  $p_T$ -Bereich  $2 \text{ GeV}/c < p_T < 8 \text{ GeV}/c$  und in der Größenordnung  $v_3 \approx 0$  im  $p_T$ -Bereich  $12 \text{ GeV}/c < p_T < 20 \text{ GeV}/c$ . In beiden  $p_T$ -Bereichen sind die statistischen und systematischen Messunsicherheiten des  $v_3$ -Parameters in einem Bereich von  $\sigma \pm (0.2 - 0.4)$  angesiedelt.

## **Anisotropic flow of the charmed $D^{*+}$ meson in non-central Pb–Pb collisions at $\sqrt{s_{NN}} = 2.76$ TeV**

The focus of this thesis is the measurement of the azimuthal anisotropy parameters  $v_2$  and  $v_3$  of the charmed meson  $D^{*+}$  and its charge conjugate  $D^{*-}$  in the fully reconstructed decay channels  $D^{*+} \rightarrow D^0\pi^+$ , respectively  $D^{*-} \rightarrow \bar{D}^0\pi^-$  by applying the event plane method. For this measurement, lead-lead collision data from the heavy-ion run end of 2011 at the LHC (Large Hadron Collider) taken by ALICE (A Large Ion Collider Experiment) was exploited. The  $v_2$ - and  $v_3$ -parameters were determined as a function of the transverse momentum  $p_T$  of the  $D^{*+}$  in a range of  $2 \text{ GeV}/c < p_T < 20 \text{ GeV}/c$ . The measured  $v_2$  is comparable to the  $v_2$  of unidentified charged particles, with a significance of three standard deviations for a non-zero  $D^{*+}$   $v_2$  in the  $p_T$  range of  $2 \text{ GeV}/c < p_T < 6 \text{ GeV}/c$  if considering the statistical uncertainty only, respectively with a significance of two standard deviations if considering the combination of statistical and systematic uncertainties. The measured  $v_3$ -values are of the order of  $v_3 \approx 0.2$  in the  $p_T$  range of  $2 \text{ GeV}/c < p_T < 8 \text{ GeV}/c$ , respectively of the order of  $v_3 \approx 0$  in the  $p_T$  range of  $8 \text{ GeV}/c < p_T < 20 \text{ GeV}/c$ . In both  $p_T$ -ranges the statistical and systematic uncertainties of the  $v_3$  are in the range of  $\sigma = \pm(0.2 - 0.4)$ .



# Contents

<b>1. Introduction</b>	<b>1</b>
<b>2. Theoretical background</b>	<b>5</b>
2.1. Phenomenology of the Quark-Gluon Plasma . . . . .	5
2.2. High-energy nuclear collisions . . . . .	10
2.3. Flow . . . . .	18
2.4. Charm physics . . . . .	26
<b>3. LHC and ALICE</b>	<b>41</b>
3.1. LHC . . . . .	41
3.2. ALICE . . . . .	43
3.2.1. Inner Tracking System (ITS) . . . . .	44
3.2.2. Time Projection Chamber (TPC) . . . . .	47
3.2.3. Time Of Flight (TOF) . . . . .	49
3.2.4. Other non-central barrel detectors . . . . .	50
3.2.5. Trigger and event selection . . . . .	52
3.2.6. Event Reconstruction . . . . .	54
<b>4. <math>D^{*+}</math> reconstruction strategy</b>	<b>57</b>
4.1. Analysis Cuts . . . . .	59
4.2. Particle Identification . . . . .	75
4.3. Yield extraction . . . . .	77
<b>5. Road to the final results for the <math>D^{*+} v_2</math>- and <math>D^{*+} v_3</math>-anisotropy parameters</b>	<b>84</b>
5.1. Event plane determination and flattening . . . . .	84
5.2. $v_n$ -extraction with different approaches . . . . .	94
5.3. Consistency checks and systematic . . . . .	101
<b>6. Final <math>D^{*+} v_n</math>-results</b>	<b>118</b>
6.1. $D^{*+} v_2$ - and $D^{*+} v_3$ -results . . . . .	118
6.2. $D^{*+} v_2$ comparison to other $v_2$ -measurements . . . . .	119
6.3. $D^{*+} v_2$ comparison to $v_2$ -predictions from models . . . . .	121
6.4. $D^{*+} v_3$ comparison to other $v_3$ -measurements . . . . .	123
<b>7. Summary and Outlook</b>	<b>125</b>
<b>A. Appendix</b>	<b>128</b>
A.1. $D^{*+}$ yield extraction figures for the $3-\Delta\phi$ -bin case . . . . .	128
A.2. $D^{*+}$ yield extraction figures for the $2-\Delta\phi$ -bin case . . . . .	130



# 1. Introduction

In high-energy nuclear collisions, a strongly interacting, color-deconfined and high energy-density matter is formed, the Quark-Gluon Plasma (QGP) [1, 2]. It is expected that this kind of matter existed shortly after the Big Bang. Due to the small size of a few femtometers and short life time of a few fm/c the experimental access to the properties of the QGP such as energy density, entropy density or temperature is only possible through detection of the final decay products of its initial constituents. Today, after many years of successful operation of the two heavy-ion and hadron colliders, the Relativistic Heavy Ion Collider (RHIC) and the Large Hadron Collider (LHC), a powerful tool to study the QGP is now accessible, namely the heavy charm quarks. This tool has become available because of continuous increase of the center-of-mass energies of heavy-ion colliders over the last decades. The LHC delivers high-energy nuclear collisions at an unprecedented center-of-mass energy of currently  $\sqrt{s_{\text{NN}}} = 2.76$  TeV. At that high energy, charm quarks are abundantly produced and are used to study the properties of the QGP. In QGP research charm quarks have an outstanding role because of their following properties:

- Charm quarks are produced in initial hard scattering processes on a short time scale of the order of  $\tau \approx 1/2m_q$ , with  $m_q$  being the quark mass, so well before the QGP is formed. Therefore they are sensitive to the full evolution of the high-energy nuclear collision. They lose energy within the formed QGP by energy loss mechanisms that are addressed in detail in the theory chapter of this thesis. Moreover, charm quarks may thermalize in the expanding QGP. The collective expansion of the QGP is nowadays modeled with frameworks inspired by hydrodynamic calculations. An overview of existing hydrodynamic models with an embedded charm quark parameterization is given in the theory chapter.
- Charm quarks acquire most of their mass from the symmetry breaking in the electroweak sector. This is visualized in fig. 1.1. In contrast, the main constituents of the QGP, the light-flavored quarks up, down and strange acquire their mass via strong interactions and the chiral symmetry breaking in Quantum Chromodynamics. In a QGP, the chiral symmetry is expected to be partially restored and thus the light quarks become almost massless. The other main constituents of the QGP are massless gluons. As a result, charm quarks serve as unique probes providing a tomography of the QGP when propagating in the medium.

The ALICE detector, whereas ALICE stands for A Large Ion Collider Experiment, at the LHC is the dedicated tool to study high-energy nuclear collisions. The particles, which are detected in the active volumes of this detector, are not the charm quarks but decay products of mesons and baryons containing charm quarks. Due to their short decay lengths of typical  $100 \mu\text{m}$  these hadrons do not reach the first layers of the ALICE detector. In case of charmed mesons, which are hadrons containing one charm quark and one light

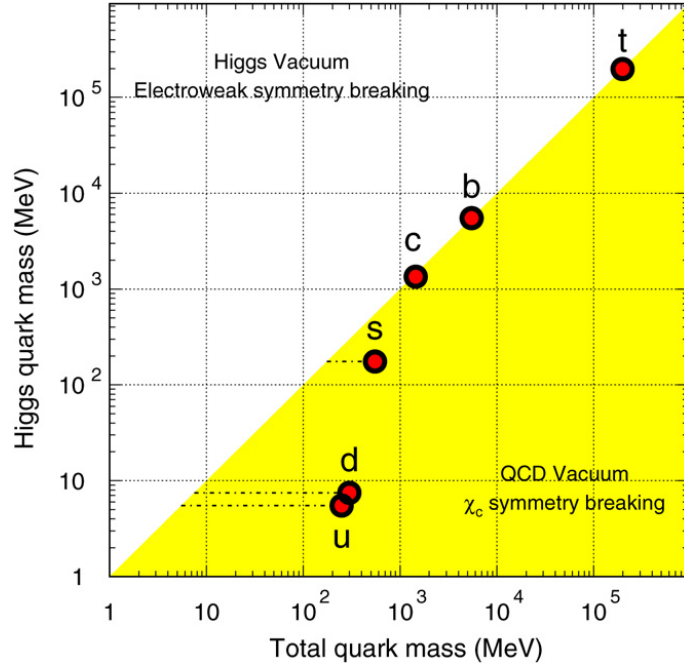


**Figure 1.1.:** Masses of heavy flavored (charm, beauty, top) and light flavored (up, down, strange) quarks in the Higgs-vacuum (white) and in condensed QCD matter (yellow). A large fraction of the light quark mass is generated by the QCD chiral symmetry breaking. In contrast to that, most of the heavy-quark mass originates from the symmetry breaking in the electroweak sector. This figure has been taken from [3].

flavored quark, the decay position can be separated from the colliding vertex of the nuclei if the provided detector resolution is sufficiently accurate in space. Such highest detector resolutions are achieved by ALICE among other detectors at the LHC.

In order to quantify the strength of interactions of charm quarks with the QGP, also called in-medium effects, there are several physical observables, which are accessible using kinematically fully reconstructed charmed hadrons. Within this thesis the analysis of the full reconstruction of the charged charmed meson  $D^{*+}$  is described. The  $D^{*+}$  meson consists of one charm quark and one anti-down quark. The exploited decay channels are the strong interaction decay channel  $D^{*+} \rightarrow D^0 \pi^+$  and the subsequent weak-interaction decay channel  $D^0 \rightarrow K^- \pi^+$  of the neutral charmed meson  $D^0$ . The neutral charmed meson  $D^0$  consists of one charm quark and one anti-up quark. One of those physical observables is the nuclear modification factor  $R_{AA}$ . This factor is the ratio of the charmed hadron production yields in proton-proton and nucleus-nucleus collisions. However, in order to account for the fact that a nucleus consists of a multitude of protons and neutrons, the production yield measured in proton-proton collisions is scaled with a proper number of nucleon-nucleon collisions occurring in the nucleus-nucleus collisions. The number used for this scaling procedure is extracted from dedicated models [4]. Thus for measuring the nuclear modification factor both measurements in nucleus-nucleus and proton-proton collisions are necessary. As the LHC provides not only high-energy nuclear collisions but also high-energy proton-proton collisions at a current center-of-mass energy of up to  $\sqrt{s} = 8$  TeV, ALICE measures charmed hadrons both in nucleus-nucleus and proton-

proton collisions. In case of no nuclear effects the  $R_{AA}$  equals unity.

In combination with the measured  $R_{AA}$  the charmed hadron production is studied as a function of the azimuthal angle around the collision vertex of the two colliding nuclei. If the overlap of the two colliding nuclei is not symmetric but has a shape of a convex lens as depicted in fig. 1.2 (left), the azimuthal distribution of the produced particles is asymmetric as well. It turned out that in high-energy nuclear collisions at RHIC and LHC

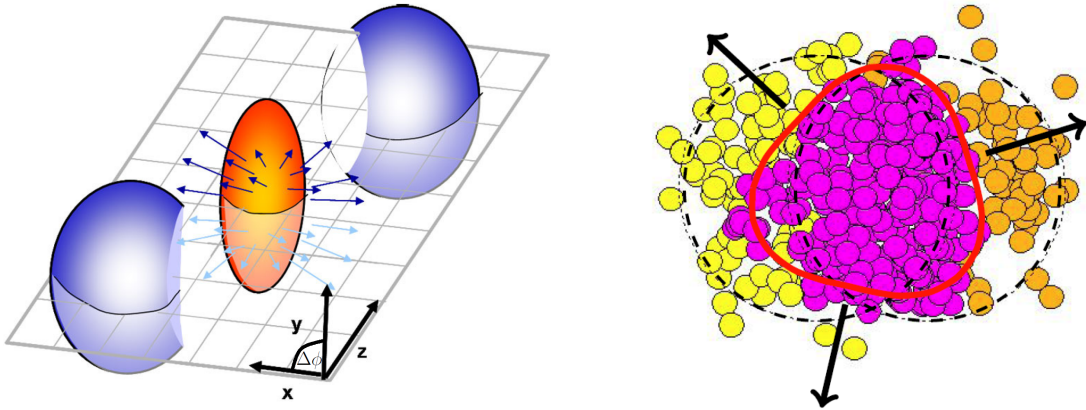


**Figure 1.2.:** (left) Sketch of a non-central heavy-ion collision. The orange lenticularly shaped volume represents the volume of overlapping nucleons (participants) and the blue spheres represent the remnants of the colliding nuclei (spectators). This figure has been taken from [5]. (right) A heavy-ion collision with triangularly shaped participant zone in the transverse plane. This figure has been taken from [6].

energies more light flavored particles stemming from up, down and strange quarks as well as from gluons are produced in the x-z plane depicted in fig. 1.2 (left) than perpendicular to it. This x-z plane is called the reaction plane and is spanned by the vector connecting the two centers of the nuclei and the z-axis, which is parallel respectively anti-parallel to the flight direction of the colliding nuclei. There are two explanations for this collective behavior depending on the transverse momentum of the produced particles. At low transverse momentum for  $p_T \lesssim 5$  GeV/c this behavior is explained by the fact that in the reaction plane the pressure gradient within the produced QGP is larger than in the perpendicular direction to this plane. This is due to the initial spatial anisotropy. At higher transverse momenta this anisotropy is generated through the path length difference of fast partons propagating the QGP in the reaction plane (shorter path length) and in the perpendicular direction (longer path length) to the plane. For studying the distribution of produced particles as a function of the azimuthal angle  $\Delta\phi$  depicted in fig. 1.2 (left), a special technique based on a Fourier expansion of this distribution has been developed. The phenomenon that this distribution is not homogeneous but shows a modulation is known as anisotropic flow. The magnitude of the anisotropy is quantified by anisotropy parameters called *harmonics*. The second order anisotropy parameter  $v_2$  quantifies the aforementioned anisotropy of the particle production in the two planes (in-reaction- and out-of-reaction-plane). These harmonics are studied in general as a function of the transverse momentum  $p_T$  of the particles of interest. The third order anisotropy parameter  $v_3$  quantifies the magnitude of anisotropy which arises in particle production

in some events, where the zone of participating nucleons from the colliding nuclei does not have a lenticular shape as depicted in fig. 1.2 (left) but a triangular shape [7, 8]. The zone of participating nucleons can have this kind of shape in some events because of fluctuations in the individual nucleon-nucleon collision points from heavy-ion collision to heavy-ion collision. Such an event is depicted in fig. 1.2 (right). The measurement of the  $v_2$ - and  $v_3$ -parameters imposes limits on physical quantities used within hydrodynamic model calculations such as e.g. the shear viscosity to entropy density ratio  $\eta/s$ , which provide predictions for the anisotropy parameters, see e.g. [9]. The measurement of the  $v_2$  and  $v_3$  is particularly interesting for particles stemming from heavy charm quarks due to their properties describes above: sensitiveness to the full to the full evolution of the QGP and their large mass with respect to the main constituents of the QGP.

The technique based on the Fourier expansion of the particle production as a function of the azimuthal angle has been successfully applied for particles stemming from gluons and light flavored quarks up, down and strange over many years at RHIC and LHC. For kinematically fully reconstructed charmed hadrons stemming from heavy charm quarks, this technique has become available for the first time in QGP research only since the first data taken by ALICE. The presentation and explanation of the results of this technique applied for the charged charmed meson and its charge conjugate  $D^{*-}$  in the fully reconstructed decay channels  $D^{*+} \rightarrow D^0\pi^+$ , respectively  $D^{*-} \rightarrow \bar{D}^0\pi^-$  as well as a comparison to theoretical models is the main focus of this thesis.

This thesis is organized as follows. The next chapter gives an overview of the physics of matter created in high-energy nuclear collisions. A substantial part of this chapter is dedicated to charm physics of those collisions. Chapter 3 describes the tools to study charm quarks in high-energy nuclear and proton-proton collisions: the LHC and ALICE. The subsequent chapter explains the strategy of the reconstruction and identification of the charged charmed meson  $D^{*+}$  with the ALICE detector. Chapter 5 presents the road to the final results of the anisotropic flow analysis of the charmed meson  $D^{*+}$ . Finally in chap. 6, results are compared to the flow analysis of light flavored particles and of other charmed mesons as well as comparisons to predictions provided by theoretical models are discussed.

## 2. Theoretical background

In this chapter a theoretical background about the physics of high-energy nuclear collisions is given. After a general description of fundamental properties of the matter created in high-energy nuclear collisions, the remaining part of this chapter focuses on the description of the special role of charm quarks in these collisions.

### 2.1. Phenomenology of the Quark-Gluon Plasma

#### Quarks and fundamental forces

Common baryonic matter present in our cooled down universe is built up of nuclei which consist of protons and neutrons. Looking deeper inside the protons and neutrons, which make up 99% of the mass of baryonic matter, one finds quarks. Today, the experimental limit on the size of quarks is of the order of  $\approx 10^{-18}$  m =  $10^{-3}$  fm, i.e. to this limit quarks are point-like and fundamental constituents of baryonic matter. An overview of the existing quark types is given in tab. 2.1. The first two flavors up and down and to some extent the flavor strange in neutron stars build up the cooled down baryonic matter

quark flavor	bare mass [MeV/c <sup>2</sup> ]	constituent mass [MeV/c <sup>2</sup> ]	charge [e]	spin [ $\hbar$ ]
up	$2_{-0.5}^{+0.7}$	220-360	2/3	1/2
down	$4.8_{-0.3}^{+0.7}$	220-360	-1/3	1/2
strange	$95 \pm 5$	419-540	-1/3	1/2
charm	$1275 \pm 25$	1550-1710	2/3	1/2
bottom	$4180 \pm 30$	$\approx 4000$	-1/3	1/2
top	$173500 \pm 1000$	-	2/3	1/2

**Table 2.1.:** Overview of quarks and some of their properties. The bare quark masses are taken from [10]. The constituent quark masses are taken from [11] and the references therein. The constituent quark mass of the b-quark is taken from [3].

in the universe. The remaining three flavors charm, bottom and top are produced in particle colliders such as the LHC. After the production they hadronize and then decay via weak interaction into the stable flavors up and down. In tab. 2.1 one can find two values for the masses of the quarks: bare mass and constituent mass. The constituent mass is the effective mass of a quark, which is only defined if the quark is confined and bound in a hadron. Thus this mass depends on the used particular hadron model. For existing models providing constituent quark masses see [11] and the references therein. As the top quark decays before hadronizing, a constituent top quark mass is not defined. The bare quark mass, often called the current or the running quark mass, is dependent on the used

renormalization scheme and the renormalization scale  $\mu$  in Quantum Chromodynamics. The values reported in tab. 2.1 are extracted from the QCD-Lagrangian at the  $\overline{\text{MS}}$ -scheme at a renormalization scale of 2 GeV. For details see [10]. In general, the interaction among the quarks is mediated via the strong and weak as well as electromagnetic and gravitational forces. The gravitational force is negligible in sub-atomic physics at the current maximum collider energies with respect to the three other forces and thus it does not exist in the standard model of particle physics. An overview of the four fundamental forces is given in tab. 2.2. The electroweak theory combines the electromagnetic and weak forces.

Force	mediator vector boson	boson mass	relative strength	range
Gravitation	Graviton? (postulated)	0	$10^{-41}$	$\infty$
Weak	$W^\pm$	80 GeV/ $c^2$	$10^{-12}$	$\ll 1$ fm
	$Z^0$	91 GeV/ $c^2$		
Electromagnetic	Photon	0	$10^{-2}$	$\infty$
Strong	Gluon	0	1	1 fm

**Table 2.2.:** Overview of the four fundamental forces.

### Phenomenology of QCD

The experimental observation is that there are no free quarks but that they only exist bound in hadrons. This phenomenon is known as *confinement*. The potential of a quark-antiquark pair in vacuum as a function of their relative distance  $r$  is approximated as:

$$V_{\text{QCD}}(r) = -\frac{4}{3} \frac{\alpha_s(r)}{r} + k \cdot r \quad (2.1)$$

with  $\alpha_s(r)$  being the strong coupling constant and  $k$  the "string tension". The factor  $\frac{4}{3}$ , called color factor, is not arbitrary and has to be determined from QCD couplings prescriptions for quark-antiquark, quark-quark, gluon-quark and gluon-gluon couplings. The different color factors are an important feature of the QCD and will be addressed later in this chapter because in high-energy nuclear collisions there is an experimental access to test this feature. Looking at eq. 2.1 one can see that while pulling two quarks away from each other the potential becomes larger and larger. At some point it is energetically favorable that a pair of two new quarks is created. Separating two quarks to an infinite distance would require an infinite amount of energy. Therefore there is no possibility to observe free quarks. On the other hand, the closer quarks approach each other, the weaker the interaction between them becomes, which is known as *asymptotic freedom* [12, 13]. The strong coupling constant, which is strictly speaking not a constant at all, is parameterized by the following formula:

$$\alpha_s(Q^2) = \frac{12\pi}{(33 - 2n_f)(\ln(Q^2/\Lambda_{\text{QCD}}^2))} \quad (2.2)$$

with  $Q$  being the four-momentum transfer from one quark to the other during scattering,  $n_f$  the number of participating quark flavors and  $\Lambda_{\text{QCD}}$  the scaling factor of the QCD. The value of  $\Lambda_{\text{QCD}}$  can only be determined experimentally and is of the order of

$\Lambda_{\text{QCD}} \approx 200$  MeV [10]. The larger the momentum transfer  $Q$ , the smaller the distance of the two quarks becomes and vice versa. The dependence of  $\alpha_s$  on the momentum transfer  $Q$  is shown in fig. 2.1. Although there is no possibility to observe free quarks, matter with

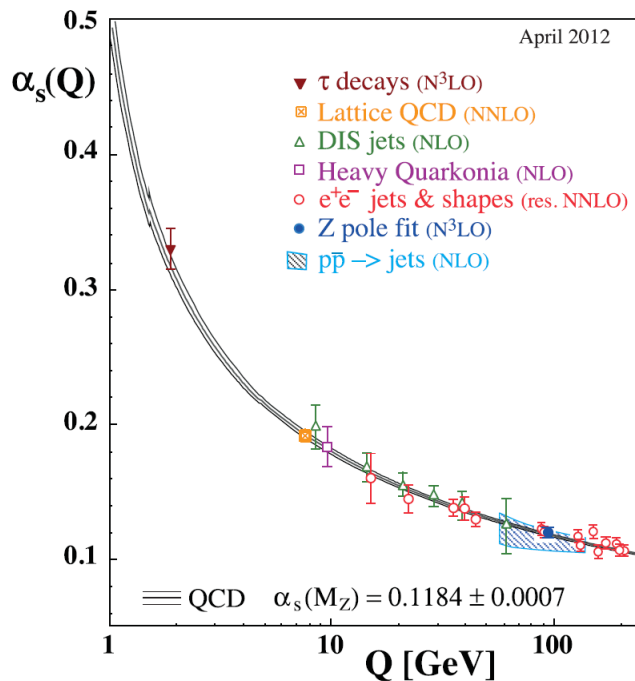


**Figure 2.1.:** Strong coupling constant  $\alpha_s$  as a function of the four-momentum transfer  $Q$ . This figure has been taken from [10].

quarks and gluons not assigned to one single hadron can be created. This can be achieved via two methods:

1. One heats up the system of hadrons to extreme temperatures, so that the scatterings among them become so hard that they start to break up. A sketch of this procedure is shown in Fig. 2.2 (upper panel). Above a critical Temperature  $T_c$  quarks from individual hadrons start to interact with each other. Because of the high energy density a large number of quark-antiquark pairs is produced. This medium of quark-antiquark pairs screens the color charge of individual quarks. This phenomenon is known from classical electrostatic physics and is known as *Debye screening* [14]. Then the formula in eq. 2.1 must be replaced by the following one:

$$V_{\text{QCD}}(r) = -\frac{4}{3} \frac{\alpha_s(r)}{r} e^{-\frac{r}{\lambda_D}} \quad (2.3)$$

with  $\lambda_D$  being the *Debye length* [14]. A hot and dense form of matter with quasi-free quarks and gluons is created, the Quark-Gluon Plasma (QGP). This kind of matter existed some  $\mu\text{s}$  after the Big Bang. It is created in high-energy nuclear collisions at the Relativistic Hadron Collider (RHIC) and the Large Hadron Collider (LHC) and its properties are studied with large particle detectors such as ALICE, ATLAS and CMS at the LHC, respectively STAR and PHENIX at RHIC.

2. One compresses the system to large densities so that the hadrons start to overlap. A sketch of this procedure is shown in Fig. 2.2 (lower panel). A hadron needs a volume of the order of  $V_h \approx (4\pi/3)r_h^3$  with  $r_h \approx 1$  fm. So the critical hadron density should be of the order of  $\rho_c \approx 1/V_h = 0.24 \text{ fm}^{-3}$ .

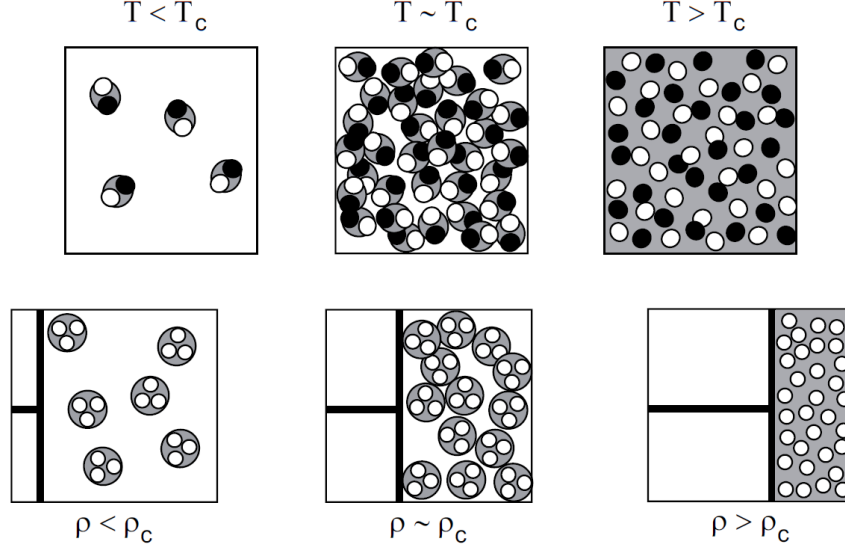


**Figure 2.2.:** Schematic sketch of creation of a QGP by heating (upper panel) and compressing (lower panel) a system with hadrons. This figure has been taken from [15].

### The QCD phase diagram

The QCD phase diagram is shown in fig. 2.3. The temperature is on the ordinate and the net baryon density on the abscissa. The net baryon density is the number of baryons minus anti-baryons per volume unit in the system. It was close to 0 in the early universe and a small deviation from 0 of the order of  $10^{-9}$  makes up today's baryonic matter in the universe. The origin of this deviation is unknown and under theoretical and experimental investigation. At the LHC the nucleons are collided at ultra-relativistic energies at the TeV-scale. At that high energy the nucleons are fully transparent and the net baryon density at mid-rapidity, i.e. in a small angular window perpendicular to the beam direction, is close to zero [17]. More details about the LHC and the involved detectors are given in chap. 3. In fig. 2.3 the direction of the evolution of hadronic matter at the LHC in a heavy-ion collision is depicted by a red arrow on the QCD-phase diagram. The cold nuclear matter with a net baryon density of 1 and  $T \approx 0$ , which is made up of lead ions, is heated up by accelerating and colliding two beams of ions. In the collision zone the hadronic matter changes its state to a deconfined QGP. After cooling down, quarks and gluons get confined again into hadrons.

### Critical temperature $T_c$ of QCD phase transition

Already in 1965, even before QCD was established, Rolf Hagedorn knowing that there was

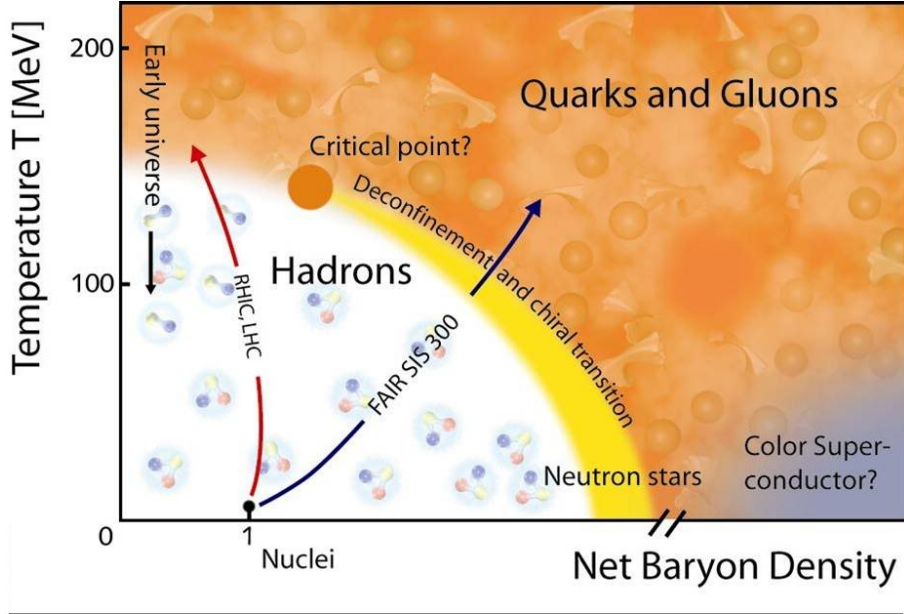


Figure 2.3.: The QCD phase diagram. This figure has been taken from [16]

a minimum temperature  $T = 0$  for matter argued that there must be also a maximum temperature for matter, see [18]. The reason for this limiting temperature is the following: in Hagedorn's bootstrap model [18] the number density of hadron species in a hadron gas as a function of resonance mass  $\rho(m)$  increases exponentially

$$\rho(m) \propto \exp(m/T_c). \quad (2.4)$$

with  $T_c$  being the "boiling point temperature of hadronic matter" as named by Hagedorn in his original paper [18]. For large resonance masses with respect to the gas temperature  $m \gg T$  the probability  $f(m)$  of occupying these hadron species states follows Boltzmann's law:

$$f(m) \propto \exp(-m/T). \quad (2.5)$$

Therefore the total energy  $\epsilon(T)$  stored in a finite volume of the hadron gas when neglecting the hadron momentum  $p_i$  of hadrons with a large mass  $m$  as a function of the temperature  $T$  is given by:

$$\epsilon(T) \approx \sum_{m_\pi}^M \epsilon(m_i, T) + \int_M^\infty m \underbrace{\frac{f(m)\rho(m)}{\exp(m(1/T_c - 1/T))}}_{\text{}} dm \quad (2.6)$$

The integral in eq 2.6 diverges for  $T > T_c$ , which is non physical because the total energy of a system has to be always finite. The limiting Temperature  $T_c$  is of the order of  $\approx 160$  MeV [18] and is known as the *Hagedorn limiting temperature*. The remarkable fact about the obtained value for this temperature is that today theorists using the framework of lattice QCD with huge computer resources obtain a number in the same range, namely in the range  $T_c \approx 150$  MeV – 190 MeV [19]. Lattice QCD is a technique to compute

the partition sum  $Z$  out of the QCD-Lagrangian arranging the four dimensional space-time continuum on a lattice. The sites of this lattice are represented by quarks and the links between these sites by gluon-fields, see [19, 20] and the references therein. From the partition sum thermodynamic quantities such as the energy density

$$\epsilon = \frac{T^2}{V} \left( \frac{\partial \ln Z}{\partial V} \right)_V \quad (2.7)$$

are derived. Lattice QCD is a non-perturbative approach and is the only way to obtain meaningful results out of the QCD Lagrangian at finite temperatures. Perturbative QCD (pQCD) cannot be applied because at finite temperatures the strong coupling constant is comparable to 1. The divergences which appear in the calculations when calculating integrals which require  $p \rightarrow \infty$ , with  $p$  being the momentum of the quarks, are naturally avoided by the finite lattice spacing  $a$ . This spacing corresponds to a momentum cutoff  $1/a$ . Therefore the lattice approach not only turns the infinite-body problem, which would correspond to calculations with a lattice spacing  $a = 0$ , to a many-body problem but also provides a solution to the UV-divergence problem. The problem here is that nobody knows how seriously one can take the lattice results given the fact that the lattice spacing is finite. Collaborations performing lattice calculations try to face this issue by doing calculations of thermodynamic quantities for different values of lattice spacing  $a$  and then extrapolating to  $a = 0$ . Fig. 2.4 shows the ratio of the thermodynamic quantities  $\epsilon$  and  $T^4$ , given by  $\epsilon/T^4$ , as a function of the dimensionless ratio  $T/T_c$  calculated with the framework of lattice QCD. The ratio  $\epsilon/T^4$  is flat for  $T \gtrsim 1.5 T_c$ . An ideal gas with massless constituents shows the same behavior known as Stefan-Boltzmann law but in case of the QCD matter the proportionality factor between  $\epsilon$  and  $T$  is decreased by 20-30% with respect to the factor of the ideal gas case. This is indicated with colored arrows in fig. 2.4 labeled with  $\epsilon_{SB}/T^4$  for the three lattice QCD calculations with different numbers of quark-flavors. This deviation can be interpreted as an effect of remaining interactions between the quarks in the QGP, which is a deviation from the ideal gas limit. The energy density of an ideal gas of massless particles as a function of temperature is given by (Stefan-Boltzmann law):

$$\epsilon = n_{\text{dof}} \frac{\pi^2}{30} T^4 \quad \text{for Bosons,} \quad (2.8)$$

$$\epsilon = n_{\text{dof}} \frac{7\pi^2}{240} T^4 \quad \text{for Fermions.} \quad (2.9)$$

with  $n_{\text{dof}}$  being the number of degrees of freedom of the particles within the gas. For a bosonic pion gas below  $T_c$ , the number of degrees of freedom is 3 ( $\pi^0, \pi^\pm$ ) and for a quark-gluon gas consisting of bosons (gluons) and fermions (quarks) with 2 quark flavors  $n_{\text{dof,quarks}} = N_{\text{charge}}(2) \times N_{\text{spin}}(2) \times N_{\text{color}}(3) \times N_{\text{flavor}}(2) = 24$ , respectively  $n_{\text{dof,gluons}} = N_{\text{spin}}(2) \times N_{\text{color}}(8) = 16$ . The large jump of the ratio  $\epsilon/T^4$  around  $T_c$  in fig. 2.4 can be interpreted as phase transition from a pion gas to a deconfined Quark-Gluon Plasma.

## 2.2. High-energy nuclear collisions

### Kinematic variables

Kinematic variables describing the properties of emitted particles produced in a high-energy nuclear collision are:

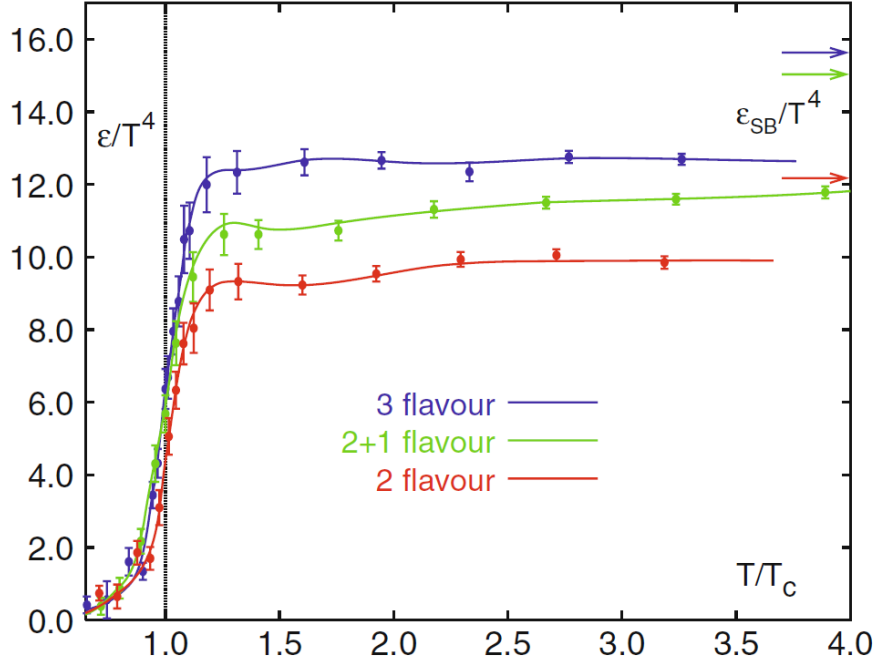


**Figure 2.4.:**  $\epsilon/T^4$  as a function of temperature for different types of lattice QCD calculations. This figure has been taken from [20]

- the transverse momentum  $p_T = \sqrt{p_x^2 + p_y^2}$ ,
- the rapidity  $y = \frac{1}{2} \ln \frac{E+p_z}{E-p_z}$ ,
- the pseudorapidity  $\eta = \frac{1}{2} \ln \frac{p+p_z}{p-p_z} = \frac{1}{2} \ln \frac{p(1+\cos\theta)}{p(1-\cos\theta)} = -\frac{1}{2} \ln \tan \frac{\theta}{2}$ .

The Cartesian coordinate  $z$  defines the beam direction and the  $xy$ -plane the plane perpendicular to the beam direction. A sketch visualizing the coordinate system and the ALICE detector is given in fig. 2.5. The ALICE detector including its sub-detectors is described in detail in chap. 3. Physical observables as for example cross sections are often expressed as function of pseudorapidity and/or transverse momentum in high-energy nuclear and proton-proton collision research:  $\frac{d\sigma}{dp_T dy}(y, p_T)$ . The practical reason, why these kinds of variables are chosen, is that they have a convenient behavior under Lorentz transformations along the beam-axis. The rapidity  $y$  is namely additive:  $y(1) - y(2) = y_2(1)$ . This equation means that the particle rapidity difference measured in frame 1 and frame 2 given by  $\Delta y = y(1) - y(2)$  is the same as the rapidity of frame 2 measured in frame 1. The transverse momentum is even Lorentz-invariant under Lorentz-transformation along the beam-axis. This convenient behavior is important for the theoretical (model) calculations of different observables as for example the cross sections of different particle species. The center-of-mass system of the colliding heavy ions and protons at colliders such as RHIC or LHC coincides with the non-moving laboratory frame. This is due the same but oppositely oriented momenta of the two colliding beams at symmetric colliders. However, due to the

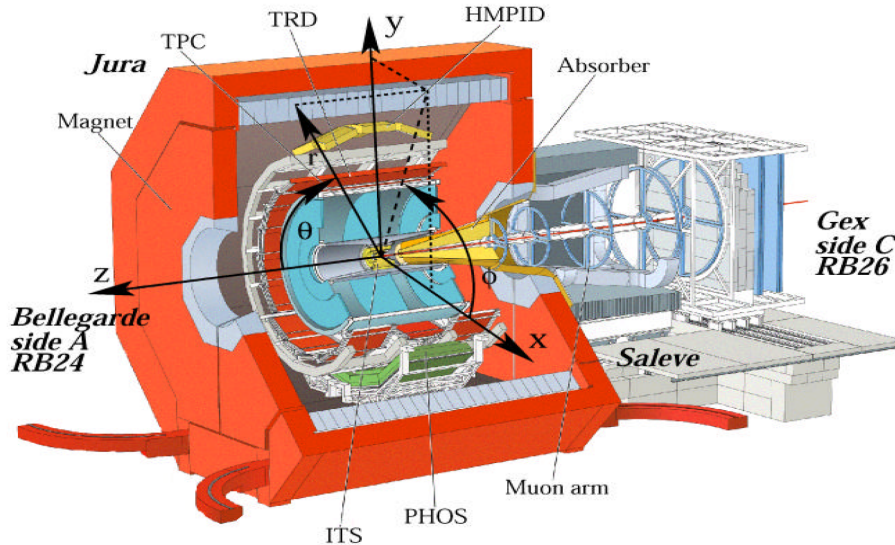


**Figure 2.5.:** Definition of the ALICE coordinate system. The ALICE-detector including its sub-detectors is described in detail in chap. 3.

ultra-relativistic energies of the nuclei, the interactions during the collision occur on a gluon-gluon, quark-gluon and quark-quark scattering level. The partons of the nuclei always carry a certain but not the full fraction of the total nucleon momentum. Therefore the scatterings of the nucleon constituents always occur in different center-of-mass reference frames having different velocities with respect to the beam-axis. Choosing as phase space variables the transverse momentum  $p_T$  and the rapidity  $y$ , theoretical calculations become simpler due to the convenient behavior of these variables under Lorentz-transformations along the beam-axis.

### Geometry of high-energy nuclear collisions

There are two important variables describing the geometry and the violence of a high energy-nuclear collision:

- the center-of-mass energy per nucleon  $\sqrt{s_{NN}} = \sqrt{(P_{\text{beam}_1} + P_{\text{beam}_2})^2}$  with  $P_{\text{beam}_{1,2}}$  being the four momentum-vectors of the colliding ions,
- the centrality percentile of a heavy-ion collision.

In a symmetric collider such as RHIC or LHC the momenta of the ions are equal but opposite and aligned with the z-axis and therefore

$$\sqrt{s_{NN}} = \sqrt{((E_{\text{beam}_1}, -\vec{p}_{\text{beam}_1}) + (E_{\text{beam}_2}, \vec{p}_{\text{beam}_2}))^2} = E_{\text{beam}_1} + E_{\text{beam}_2} = 2E_{\text{beam}} \quad (2.10)$$

Thus the center-of-mass energy per nucleon is twice the energy per nucleon of the beam ions. The center-of-mass energy per nucleon is the total energy available per nucleon in the center-of-mass frame. At the LHC, which is described in more detail in chap. 3, the

current center-of-mass energy per nucleon is  $\sqrt{s_{NN}} = 2.76$  TeV.

The variable, which describes the geometry of a heavy-ion collision, is the centrality percentile. There are different types of collisions which are depicted in fig. 2.6. The nuclei appear as pancakes due to the Lorentz-contraction in the  $z$ -direction. *Head-on* or *central collisions* (fig. 2.6c) correspond to collisions with an impact parameter of the two nuclei  $b$  close to 0. The impact parameter is the distance between the centers of the two colliding nuclei. The following expressions are used for classifying the collisions with increasing impact parameter: *semi-central* (fig. 2.6b), *semi-peripheral* (fig. 2.6b) and finally for  $b$  getting close to  $2R$  with  $R$  being the radius of the colliding identical nuclei, the collisions become *peripheral* (fig. 2.6b). Collisions with  $b \gtrsim 2R$  are called *ultra-peripheral* (fig. 2.6a). In order to quantify the centrality, one groups heavy-ion events in bins of percentage of

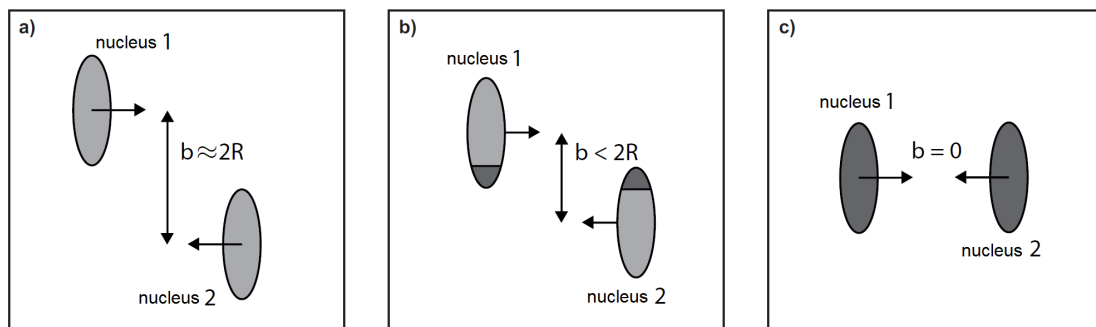


**Figure 2.6.:** Different types of heavy-ion collisions. (a) ultra-peripheral collision, (b) peripheral heavy-ion collision and (c) head-on or central heavy-ion collision. This figure has been taken from [21].

the inelastic hadronic cross section  $\sigma_{\text{inel}}^{\text{AA}}$ . For example, the fraction  $F = 5\%$  of most central collision corresponds to heavy-ion collisions with a maximum impact parameter  $b_{\text{max}}$  defined by the following requirement:

$$F = \frac{\int_0^{b_{\text{max}}} \frac{d\sigma_{\text{inel}}^{\text{AA}}}{db} db}{\int_0^{\infty} \frac{d\sigma_{\text{inel}}^{\text{AA}}}{db} db} \stackrel{!}{=} 5\% \quad (2.11)$$

In order to have an access to the centrality percentile from the experimental side, an assumption that needs to be made is that the number of produced charged particles  $n_{\text{ch}}$  increases with decreasing impact parameter. This is a fair and intuitive assumption because the more central the collision becomes, the higher the number of participating nucleons (participants) within the collision and accordingly the lower the number of not participating nucleons (spectators). With this assumption one can integrate the distribution of  $n_{\text{ch}}$  in intervals with the same binning as the fraction of the inelastic hadronic cross section  $\sigma_{\text{inel}}^{\text{AA}}$ . This way one can assign to different *centrality classes* a mean number of the impact parameter  $\langle b \rangle$  and a mean number of participating nucleons  $\langle N_{\text{part}} \rangle$ . Figure 2.7 shows a sketch of a typical distribution for  $n_{\text{ch}}$ . The figure does not contain real measured values

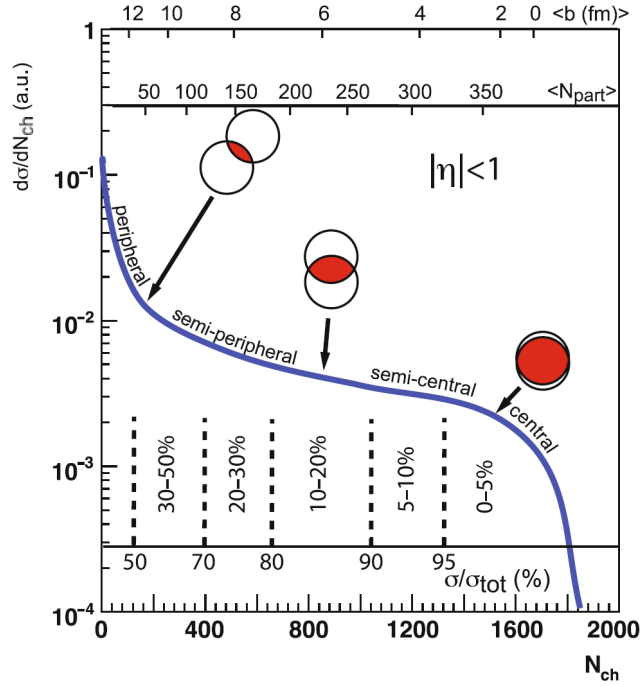


**Figure 2.7.:** A cartoon demonstrating the experimental determination of centrality classes on the basis of the measurement of the number of produced charged particles  $n_{ch}$  in heavy-ion collisions. This figure has been taken from [22].

for  $n_{ch}$  but is only a cartoon to demonstrate how bins of centrality are defined in heavy-ion collisions and how they are connected to values for  $\langle N_{part} \rangle$  and  $\langle b \rangle$ . Generally, there is no possibility to directly measure the impact parameter  $b$  nor  $N_{part}$ . The  $b$ -differential cross section  $\frac{d\sigma_{inel}^{AA}}{db}$  in eq. 2.11 and the dependence of  $N_{part}$  on the impact parameter  $b$  are obtained with the framework of Glauber Monte Carlo [4]. The inputs to this framework are:

- the Woods-Saxon nucleon density within a nucleus  $\rho(r) = \frac{\rho_0}{1 + \exp[(r - R_A)/a]}$ , with  $R_A$  being the radius of the nucleus where the density drops to 50% and  $a$  controls the skin depth  $t$  given by  $t = 2a \ln 9$ . The skin depth  $t$  is defined as the range over which the nucleon density drops from 90% to 10% of  $\rho_0$ ,
- the nucleon-nucleon inelastic cross section  $\sigma_{NN}^{inel}$ .

In the Glauber Monte Carlo simulations, the nucleons within the nucleus are distributed according to the Woods-Saxon density distribution and "collided" in small ranges of the centrality percentile. The output are mean values for  $N_{part}$  and  $b$  in the chosen centrality percentile intervals. For more details, see [4].

### Space-time evolution of a high-energy nuclear collision

The space-time evolution of a high-energy nuclear collision at center-of-mass energies of

$\sqrt{s_{NN}} \gtrsim 100$  GeV are described by the Bjorken reaction picture [23]. At that high energy, the colliding ions are fully transparent. This behavior is depicted in fig. 2.8. The ions approach each other Lorentz-contracted in  $z$ -direction (fig. 2.8 (a,left)) and them pene-

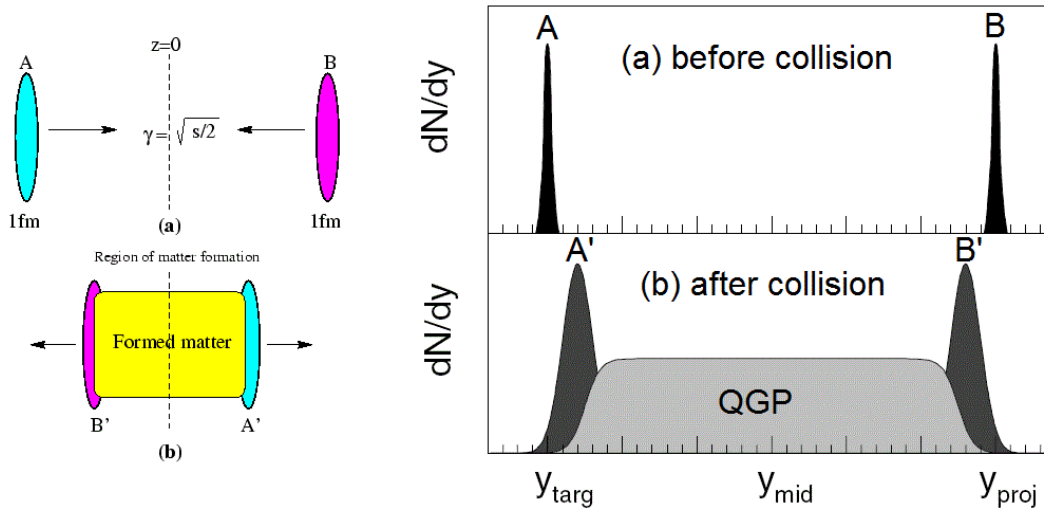


**Figure 2.8.:** Cartoon of a high-energy nuclear collision of two nuclei A and B before (a, figure taken from [24]) and after the collision (b, figure taken from [25]).

trate each other (fig. 2.8 (b,left)). During the penetration the nucleons lose energy and leave a highly excited and high energy density matter in between (fig. 2.8 (b,left), yellow area). Because of their very high energy the nucleons within the nuclei are not stopped but appear after the collision at high rapidities  $y$  (fig. 2.8 (b,right)). Here the net baryon density  $n_b = n_{\text{baryon}} - n_{\text{anti-baryon}}$  is significantly larger than zero. The particle production at midrapidity, around  $|y| < 2$ , is mainly energy driven and not due to pile-up of the neutrons and protons within the nuclei. The net baryon density  $n_b$  is close to zero here. The processes, which take place during the interpenetration time of the two nuclei, fix the initial conditions before a QGP in thermal equilibrium appears at  $t = \tau_0$ .

The time before equilibrium for  $0 < t < \tau_0$  is called the pre-equilibrium and during that time the thermalization happens. The initial conditions are given for example by the energy density profile  $\epsilon(x, y, z)$  at the time  $t = \tau_0$ . Other quantities such as the entropy density profile  $s(x, y, z)$  or the pressure density profile  $P(x, y, z)$  are obtained using an equation of state (EOS). The EOS of choice can be the EOS obtained by lattice QCD calculations. In order to fix the initial conditions for further calculations, one relies on models. There is no analytic method to calculate initial conditions. Two different type of models are used in modern initial condition calculations. One of them relies on Monte Carlo Glauber simulations [4] and is often simply referred as *Glauber initial conditions*. For details about calculation of full three dimensional initial conditions, see [26–28]. Another approach for obtaining initial conditions is the *Color Glass Condensate* (CGC) model. This model describes the properties of the high density gluon-fields within heavy ions at ultra-relativistic energies. For more details about this model see [29]. Within the CGC

framework one can calculate the energy density  $\epsilon(x, y, z)$  of produced gluons after the heavy-ion collision.

The evolution after  $\tau_0$  of the bulk of the fireball is nowadays described by relativistic hydrodynamics. According to the measurements of QGP properties at RHIC, see [30], the strongly coupled QGP behaves like a perfect fluid with very low viscosity. In case of zero viscosity the equations of motion in covariant notation are:

$$\partial_\mu T^{\mu\nu} = 0 \text{ with } T^{\mu\nu} = \begin{pmatrix} \epsilon(x) & 0 & 0 & 0 \\ 0 & P(x) & 0 & 0 \\ 0 & 0 & P(x) & 0 \\ 0 & 0 & 0 & P(x) \end{pmatrix} \text{ (Energy-momentum conservation)} \quad (2.12)$$

$$\partial_\mu j_B^\mu(x) = 0, \text{ with } j_B^\mu = n_B u^\mu \text{ (Baryon number current conservation)} \quad (2.13)$$

with  $x$  being the four space-time vector. These two conservation laws and the EOS of choice provide six independent differential equations. For a given initial condition, for example obtained with the CGC- or the Glauber-model, one can solve these equations. This provides full knowledge of six properties of the expanding fluid in the space-time:

- The thermodynamical quantities:
  - energy density  $\epsilon(x)$ ,
  - pressure  $P(x)$ ,
  - baryon number density  $n_B(x)$ .
- The motion profile in three dimensions of the fluid, i.e. the flow vector  $\vec{v} = \begin{pmatrix} v_x(x) \\ v_y(x) \\ v_z(x) \end{pmatrix}$ .

In case of a non perfect fluid, i.e. with viscosity being significantly greater than zero, the procedure for calculation of the thermodynamic quantities and the flow vector are the same. Also here the conservation laws presented in eqs. 2.12, 2.13 are valid but the terms for the baryon number current  $j_B^\mu(x)$  and the energy-momentum tensor  $T^{\mu\nu}$  need to be complemented with additional dissipative expressions. For more details see [15].

Before the QGP can reach the freeze-out time  $\tau_f$  it undergoes a phase transition to hadrons. The hadron phase is still thermalized but the temperature has dropped below  $T_c$  and the partons are confined in hadrons. There are two stages of freeze-outs:

1. *Chemical freeze-out*: no more inelastic collisions occur among the constituents and the abundances of particle species become fixed.
2. *Kinetic freeze-out*: particles do not scatter anymore and the momentum-distributions become fixed. Free streaming to the detectors sets in.

Fig. 2.9 shows a sketch of a heavy-ion collision in the space-time picture. The abscissa represents the z-axis, which points in the beam direction and the ordinate is the time

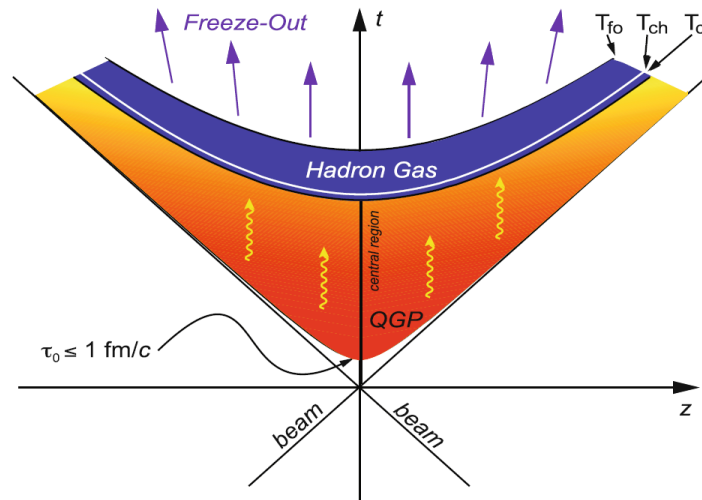


**Figure 2.9.:** Space-time evolution of a heavy-ion collision. The space-time curves, when the critical temperature  $T_c$ , the *chemical freeze-out* temperature  $T_{ch}$  and the *kinetic freeze-out* temperature  $T_{fo}$  are reached, are drawn in. This figure has been taken from [22].

direction. The space-time curves, when the three characteristic temperatures are reached, are drawn in.  $T_c$  is the critical temperature when the strongly interacting system undergoes a phase-transition and turns into a hadron gas.  $T_{ch}$  is the temperature, when the *chemical freeze-out* takes place. Finally,  $T_{fo}$  is the temperature when the hadron gas has cooled down and *kinetic freeze-out* sets in.

To summarize, in order to get an appropriate model of the evolution of a high-energy nuclear collision, the following ingredients are necessary:

- Initial conditions for hydrodynamic calculations.
- Hydrodynamic calculations with a decoupling prescription, i.e. with a transition prescription to free streaming of particles.
- Equation of state which describes the dependencies among the various thermodynamic quantities such as energy density, pressure etc. over a wide range of temperature, i.e. from the temperature at  $\tau_0$  to the temperature at the kinetic freeze-out.

In order to put constraints on parameters of the model of choice, which describes the evolution of heavy-ion collisions, e.g. constraints on the magnitude of the viscosity, comparisons of measured physical observables to predicted observables provided by the corresponding model of choice have to be performed. At the end of the following section this procedure will be demonstrated on the basis of comparisons of measured and predicted so-called flow harmonics using several hydrodynamic calculations. The definition of flow harmonics and experimental access to them in heavy-ion collisions will be given.

## 2.3. Flow

### Types of flow

In general, flow describes the collective behavior of matter produced in heavy-ion collisions. As performed in [15], one can derive from the conservation laws presented eqs. 2.12 and 2.13 the following relativistic generalization of the Euler equation:

$$\frac{\partial \vec{v}}{\partial t} + (\vec{v} \cdot \nabla) \vec{v} = -\frac{1 - v^2}{\epsilon + P} \left[ \nabla P + \vec{v} \frac{\partial P}{\partial t} \right] \quad (2.14)$$

The left side of eq. 2.14 is the total derivative of the fluid motion field, i.e. the acceleration of the fluid cells, parameterized by  $\vec{v}$ . It is driven by the pressure gradient ( $\nabla P$ ) which is on the right side. This means that the collective motion of partons within the thermalized QGP is driven by initial pressure gradients which are due to initial spatial density profiles. Generally, flow in the transverse x-y plane (see fig. 2.5 for definition of this plane) in heavy-ion collisions is categorized in two main types:

- isotropic or radial flow,
- anisotropic flow.

Radial flow is driven by the radial expansion of the produced fireball. The pressure is the highest at the center of the expanding fireball and drops to zero at the edge and this gradient drives the collective motion of the partons. One method to access this phenomenon experimentally is to investigate  $p_T$ -spectra of produced particles at different centralities of a heavy-ion collision. In central collisions the temperature and system size are larger than in peripheral collisions. The same holds for the magnitude of the pressure gradient and

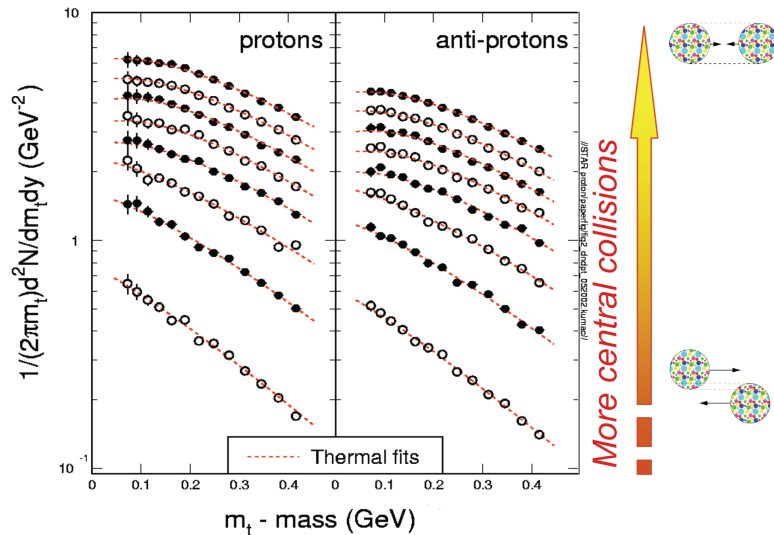


**Figure 2.10.:** Transverse mass-spectra ( $m_T = \sqrt{p_T^2 + m_0^2}$ ) for protons and anti-protons for different centralities in heavy-ion collisions at RHIC at  $\sqrt{s_{NN}} = 130$  GeV. This figure has been taken from [31].

as a consequence for the flow velocity. Therefore the  $p_T$ -spectra of particles are expected to be harder in central collisions than in peripheral collisions, i.e. with relatively more entries at higher  $p_T$  than at lower  $p_T$ . This is demonstrated in fig. 2.10. In this figure the distributions of the quantity  $m_T - m_0$  with  $m_T = \sqrt{p_T^2 + m_0^2}$  for protons and anti-protons for different centralities in heavy-ion collisions at RHIC at  $\sqrt{s_{NN}} = 130$  GeV are depicted. The quantity  $m_0$  is the rest mass of the proton. With increasing centrality indicated with the yellow arrow, i.e. with rising system size and temperature, the spectra become harder.

In case of anisotropic flow the anisotropy refers here to the different flow velocities due to different pressure gradients projected on the x-y plane perpendicular to the beam direction in z direction. For definition of the coordinate system see fig. 2.11. The reason for the different pressure gradients are asymmetric density profiles of the QGP after the collision. These density profiles can have different shapes depending on the centrality of the collision. If the collision is of non-central type, i.e. with significant impact parameter, the collision zone will have the shape of a convex lens. This kind of anisotropic flow is called *elliptic flow*. A sketch is given in fig. 2.11 (right). The red area represents the thermalized

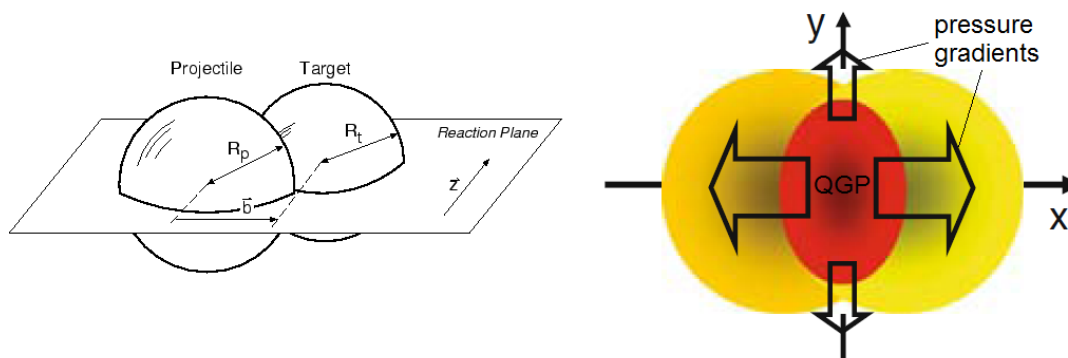


**Figure 2.11.:** (left) Definition of the reaction plane in a heavy-ion collision. (Right) Elliptic fireball created after a non-central heavy ion collision. The different magnitudes of the pressure gradients in x- and y-direction due to the spatial anisotropy are depicted. This figure has been taken from [22].

QGP and the arrows the magnitude of the pressure gradients. In this configuration the flow velocity will be larger in x direction than in y direction. The plane, which is spanned by the impact parameter vector  $\vec{b}$  coinciding with the x-axis depicted in fig. 2.11 (right) and the beam-direction coinciding with the z-axis is called the *reaction plane*, see fig. 2.11 (left). Note that the x-axis and the y-axis depicted in fig. 2.11 (right) only coincide with the  $x'$ - respectively  $y'$ -axis of the laboratory frame depicted in fig. 2.5 if the vector  $\vec{b}$  is parallel to the  $x'$ -axis of the laboratory frame. The particles emitted in x-direction (in-plane) will be pushed more severely to higher  $p_T$  than the ones in y-direction (out-of-plane). Starting from some  $p_T$  on and looking at the difference in particle production in x- versus y-direction, one expects an excess in the counting rate in x-direction with respect to the counting rate in y-direction.

In general, the collision zone will not have the shape of a perfect convex lens because of fluctuations in the individual nucleon-nucleon collision points from collision to collision, see e.g. [7]. The collision zone, often referred as *participant zone* due to the participating nucleons in the heavy ion collision, can have for example a triangular or quadrupole shape, see fig. 2.12. The type of the shape is referred as *participant eccentricity*, see [32], and the

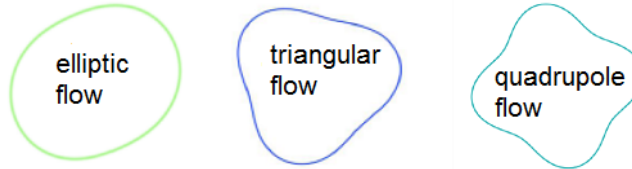


**Figure 2.12.:** Different shapes of the participant zone in heavy ion collisions.

corresponding plane of symmetry as the *participant plane*. Without fluctuations in the individual nucleon-nucleon collision points from collision to collision, the participant plane of the elliptic flow and the reaction plane defined in fig. 2.11 (left) above would coincide for each collision. Moreover, without fluctuations the arrangement of the participating nucleons would be smooth and the only possible plane of symmetry would be the reaction plane. A triangularly shaped participant zone with the reaction plane as plane of symmetry would not be possible [8]. But due to these fluctuations

1. the participant plane of the elliptic flow jitters around the reaction plane event-by-event, see fig. 2.13 (left),
2. in some events the participant eccentricity has a triangular shape, see 2.13 (right). In other words, event-by-event participant fluctuations generate in some events planes of symmetry of triangular shaped participant zones [8].

### Quantifying flow

In order to quantify the magnitude and type of anisotropic flow, several methods have been developed in the past years. The well-established *event plane method* proposed in [34] is presented in the following. It is not possible to measure directly pressure gradients nor density profiles in the QGP but one has to measure the  $\phi$ - and  $p_T$ -distributions of the emitted particles in the final state and then compare to models where one has control of the initial shapes of the geometry. The expression  $\phi$  denotes the azimuthal angle in the transverse x-y-plane in the laboratory frame depicted in fig. 2.5. The differential  $\phi$ -distribution of the emitted particles of interest  $\frac{dN}{d\phi}$ , e.g. protons, pions or charmed mesons, is a periodic function with a phase  $2\pi$ . Every continuous or piecewise continuous periodic function can be expressed as a Fourier sum:

$$\frac{dN}{d\phi} = \frac{N_0}{2\pi} \left[ 1 + 2 \sum_{n=0}^{\infty} v_n \cos [n(\phi - \Psi_n)] \right] \quad (2.15)$$

Due to the introduced symmetry plane angles  $\Psi_n$  for each index  $n$  the sine-terms, which are usually present in a standard Fourier expansion, vanish due to reflection symmetry [34].

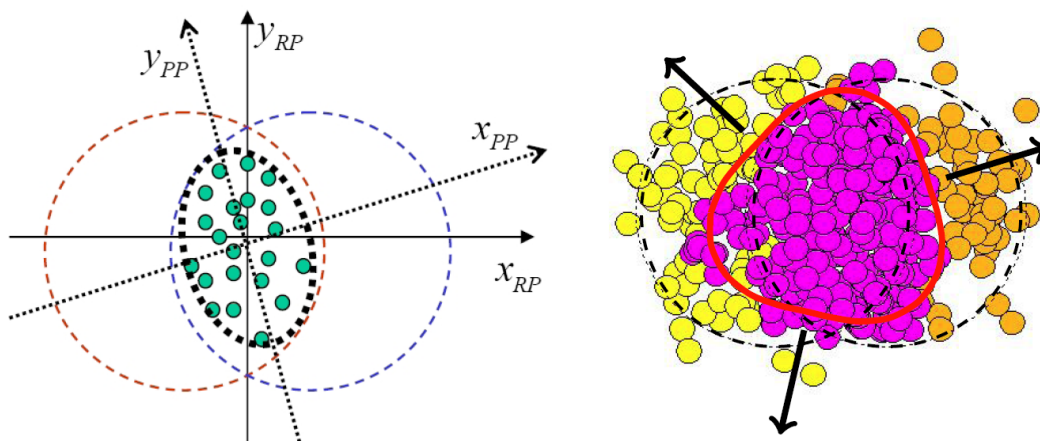


**Figure 2.13.:** (left) Definition of the true reaction plane (RP) and the participant plane (PP). This figure has been taken from [33]. (right) Heavy-ion collision with a triangular shape of the area of participating nucleons. This figure has been taken from [6].

These symmetry plane angles are estimated even-by-event using the particle distribution  $\frac{dN}{d\phi}$  itself. Their values are determined in the laboratory frame depicted in 2.5 with respect to the x-axis, similar to the  $\phi$ -angle. Details about the estimation procedure of these symmetry plane angles are given further below. The planes are referred to as *event planes* and their corresponding angle *event plane angle*  $\Psi_n$  in the following. The index  $n$  specifies the order. They are strongly correlated with the aforementioned participant planes of the colliding nucleons, see e.g. [32]. The second order event plane angle  $\Psi_2$  is strongly correlated with the elliptic flow participant plane introduced above and the third order event plane angle  $\Psi_3$  is strongly correlated with the triangular flow participant plane [32] shown in fig 2.13 (right). The expressions  $\cos[n(\phi - \Psi_n)]$  of the Fourier sum are a complete system of orthonormal base unit vectors and the coefficients  $v_n$  are the lengths of the vectors building up the  $\phi$ -distribution  $\frac{dN}{d\phi}$ . These coefficients are called *harmonics*. To get the  $n$ -th harmonic, one has to project the  $\phi$ -distribution  $\frac{dN}{d\phi}$  on the  $n$ -th unit vector:

$$v_n = \int_0^{2\pi} \frac{dN}{d\phi} \cos[n(\phi - \Psi_n)] d\phi = \langle \cos[n(\phi - \Psi_n)] \rangle \quad (2.16)$$

In order to extract the  $n$ -th harmonic, one has to calculate the average  $\langle \cos[n(\phi - \Psi_n)] \rangle$  over all particles of interest in a single event and over many events to keep the statistical error small. In case of individual particles, the variable  $\phi$  is not a running value any more but corresponds to discrete values of the individual particles of interest. An alternative approach to obtain the harmonics is to fit the  $\frac{dN}{d\Delta\phi}$ -distribution for each harmonic with the Fourier coefficient  $v_n$  being a free parameter:

$$\frac{dN}{d\Delta\phi_n} = \frac{N_0}{2\pi} [1 + 2v_n \cos(n\Delta\phi_n)] \quad \text{with } \Delta\phi_n = \phi - \Psi_n \quad (2.17)$$

Note the substitution  $\phi \rightarrow \Delta\phi$  in eq. 2.17 with respect to eq. 2.15. At first glance the reader might get the impression that eq. 2.17 is wrong because the sum over all  $n$ , which

## 2. Theoretical background

---

is present in eq. 2.15, disappeared. However, equation 2.17 is valid for each harmonic  $v_n$  independently if the distribution  $\frac{dN}{d\Delta\phi}$  is determined out of an ensemble of many events and the event plane angles  $\Psi_n$  are uncorrelated among each other event-by-event. If this requirements are fulfilled, the contributions from all other harmonics to e.g. the second order distribution  $\frac{dN}{d\Delta\phi_2}$  cancels on average.

If the statistics in the considered  $v_n$ -analysis is small, sometimes only two  $\Delta\phi$ -bins are available. One can show by integrating eq. 2.17 that the  $v_n$ -parameter can be calculated out of the entries in the first bin (in-plane) and second one (out-of-plane):

$$\begin{aligned}
 N_{\text{in-plane}} &= \frac{N_0}{2\pi} \cdot 2n \cdot \int_0^{\pi/2n} [1 + 2v_n \cos(n\Delta\phi)] d\Delta\phi = \frac{N_0}{2} + \frac{2N_0v_n}{\pi} \\
 N_{\text{out-of-plane}} &= \frac{N_0}{2\pi} \cdot 2n \cdot \int_{\pi/2n}^{\pi/n} [1 + 2v_n \cos(n\Delta\phi)] d\Delta\phi = \frac{N_0}{2} - \frac{2N_0v_n}{\pi} \\
 \rightarrow \frac{N_{\text{in-plane}} - N_{\text{out-of-plane}}}{N_{\text{in-plane}} + N_{\text{out-of-plane}}} &= \frac{4v_n}{\pi} \rightarrow v_n = \frac{\pi}{4} \frac{N_{\text{in-plane}} - N_{\text{out-of-plane}}}{N_{\text{in-plane}} + N_{\text{out-of-plane}}}
 \end{aligned} \tag{2.18}$$

The crucial ingredient for the event plane method is the determination of the azimuthal angle of the event plane  $\Psi_n$  on a event-by-event basis. This is done by using the  $\phi$ -angles of the reconstructed charged particles of one event. The event plane angle  $\Psi_n$  is measured through the  $Q$ -vector, which is a weighted sum of the cosine, respectively the sine of the azimuthal angle  $\phi$  of all charged particles from one event. The weights  $w_i$  are a product of the  $p_T$  of the  $i$ -th particle and the inverse value of the measured normalized particle  $\phi$ -distribution at the considered  $\phi$ -angle. The  $p_T$ -weighting is performed because the  $v_n$  increases as a function of  $p_T$  linearly up to a certain  $p_T$ , see e.g. [8] and examples of  $v_n$ -measurements further below. Applying a  $p_T$ -weighting improves the performance of the determination of the azimuthal angle of the event plane  $\Psi_n$  [33]. The  $\phi$ -weighting is done to remove a possible detector acceptance bias of the  $Q$ -vector. In other words, the deviation from a homogeneous distribution for the  $\phi$  of the charged particles should origin from anisotropic flow event-by-event and not from detector acceptance inefficiencies as function of  $\phi$ . Another possibility to remove detector acceptance effects is to subtract the mean of the  $Q$ -vector taken over many events from each  $Q$ -vector event-by-event. This procedure is called re-centering. Moreover, for each particle, one wants to measure the azimuthal angle  $\phi_i$  with respect to the event plane angle  $\Psi_n$ , one subtracts the contribution to the  $Q$ -vector. Thus, every particle has its own event plane angle  $\Psi_{n,i}$  and hence its own difference  $\phi_i - \Psi_{n,i}$ . This is done in order to avoid autocorrelations and to correlate each particle with an estimated event plane angle  $\Psi_n$ , whereas for its determination all but the considered particle was used. In formulas the  $Q$ -vector and the event plane angle  $\Psi_n$  are calculated as [34]:

$$Q_n = \left( \begin{array}{c} \sum_{i=0}^N w_i \cos(n\phi_i) \\ \sum_{i=0}^N w_i \sin(n\phi_i) \end{array} \right) \quad \Psi_n = \frac{1}{n} \tan^{-1} \left( \frac{Q_{n,y}}{Q_{n,x}} \right). \tag{2.19}$$

The last missing ingredient to get the real  $v_n$  is the resolution of the event plane. The event plane angle of  $n$ -th order is measured with a finite resolution caused by the finite

multiplicity of the events [34]. This smears out the distribution  $\frac{dN}{d\Delta\phi}$  and the measured  $v_n$  is smaller than the real  $v_n$ . To get the real  $v_n$ , the value obtained with eq. 2.18 or eq. 2.16 has to be multiplied by a factor  $C_n$  accounting for the event plane resolution. This factor is the inverse of the following expression, which is simply referred to as event plane resolution in flow literature [34] and in the following:

$$\langle \cos [n(\Psi_n - \Psi_R)] \rangle = \sqrt{\frac{\pi}{8}} \chi_n \cdot e^{-\chi_n^2/4} \cdot I_0(\chi_n^2/4) + I_1(\chi_n^2/4) \quad (2.20)$$

with  $C_n = \langle \cos [n(\Psi_n - \Psi_R)] \rangle^{-1}$

where  $\chi_n = v_n \sqrt{2N}$  with  $N$  being the multiplicity and  $I_\nu$  the Bessel function of order  $\nu$ .  $\Psi_R$  is the nominal value of the event plane angle of  $n$ -th order or the mean of the probability distribution  $\frac{dP}{d(n(\Psi_n - \Psi_R))}$ . For  $\chi_n \gg 1$  this probability distribution is given by [34]:

$$\frac{dP}{d(n(\Psi_n - \Psi_R))} \approx \frac{\chi_n}{\sqrt{2\pi}} \exp\left(\frac{-\chi_n^2 (\Psi_n - \Psi_R)^2}{2}\right) \quad (2.21)$$

The mean cosine values in eq. 2.20 obtained from a sample of events are less than one, thus the correction always increases the uncorrected Fourier coefficients. The resolution can be measured from data using two sub-events, i.e. two sub-samples of the charged particles used to determine the event plane, provided that they have the same multiplicity and they cover similar rapidity regions in order to expect the flow to be the same in both sub-events. These conditions ensure that the resolution of the two sub-events is the same. The two sub-events are obtained from one full event split in two subsets of particles. If no other correlation is present except for the one due to flow, or if non-flow correlations are negligible, the following relations hold:

$$\langle \cos [n(\Psi_n^A - \Psi_n^B)] \rangle = \langle \cos [n(\Psi_n^A - \Psi_R)] \rangle \times \langle \cos [n(\Psi_n^B - \Psi_R)] \rangle \quad (2.22)$$

$$\langle \cos [n(\Psi_n^A - \Psi_R)] \rangle = \sqrt{\langle \cos [n(\Psi_n^A - \Psi_n^B)] \rangle} \quad (2.23)$$

The angles  $\Psi_n^A$  and  $\Psi_n^B$  are the determined event plane angles of the two sub-events. Thus the sub-event resolution can be measured from data by applying eq. (2.23). Then, by inverting eq. 2.20,  $\chi_n^{\text{sub-event}}$  can be retrieved giving the sub-event resolution as an input. The variable  $\chi_n^{\text{full-event}}$  is then obtained as

$$\chi_n^{\text{full-event}} = \sqrt{2} \chi_n^{\text{sub-event}} \quad (2.24)$$

being  $N^{\text{sub-event}} = \frac{1}{2} N^{\text{full-event}}$  and  $v_n^{\text{sub-event}} = v_n^{\text{full-event}}$ , according to the assumptions made. Finally, the event plane resolution of the full event is obtained by inserting  $\chi_n^{\text{full-event}}$  into the formula given in eq. 2.20.

In case one has to deal with sub-events, which are not "equal", e.g. they have a large rapidity gap and the multiplicity is significantly different, the three-sub-event method as proposed in [34] is used. The three sub-events  $A$ ,  $B$ ,  $C$ , which are used to determine the three event plane angles  $\Psi_n^{A,B,C}$ , can be: the sub-event of a detector at forward rapidity, e.g. at  $2.0 < \eta < 4.0$ , with decreased multiplicity with respect to midrapidity

( $\Psi_n^A$ ), the sub-event of a detector at midrapidity of the negative hemisphere ( $\Psi_n^B$ ), e.g. at  $-0.9 < \eta < 0.0$  and the sub-event of the positive hemisphere ( $\Psi_n^C$ ), e.g. at  $0.0 < \eta < 0.9$ . According to [34], the event plane angle  $\Psi_n^A$  resolution of the detector at forward rapidity in this case is given by:

$$\langle \cos [n (\Psi_n^A - \Psi_R)] \rangle = \sqrt{\frac{\langle \cos [n (\Psi_n^A - \Psi_n^B)] \rangle \langle \cos [n (\Psi_n^A - \Psi_n^C)] \rangle}{\langle \cos [n (\Psi_n^B - \Psi_n^C)] \rangle}} \quad (2.25)$$

In order to determine the  $v_n$ -parameters, also other methods are available. Examples are: Multi-particle correlations, Q-cumulants and the scalar product method. The method of choice for extracting the  $v_n$  of the  $D^{*+}$  meson addressed in chap. 5 is the event plane method. Therefore the other methods are not discussed here. A complete summary of all available  $v_n$ -extraction methods is given in [33].

### Examples of $v_n$ measurements

Figure 2.14 shows a compilation of  $v_n$ -measurements of unidentified charged particles with ALICE at  $\sqrt{s_{NN}} = 2.76$  TeV. Figure 2.14 (left) shows the  $v_2$ ,  $v_3$ ,  $v_4$  and the  $v_5$  as a function

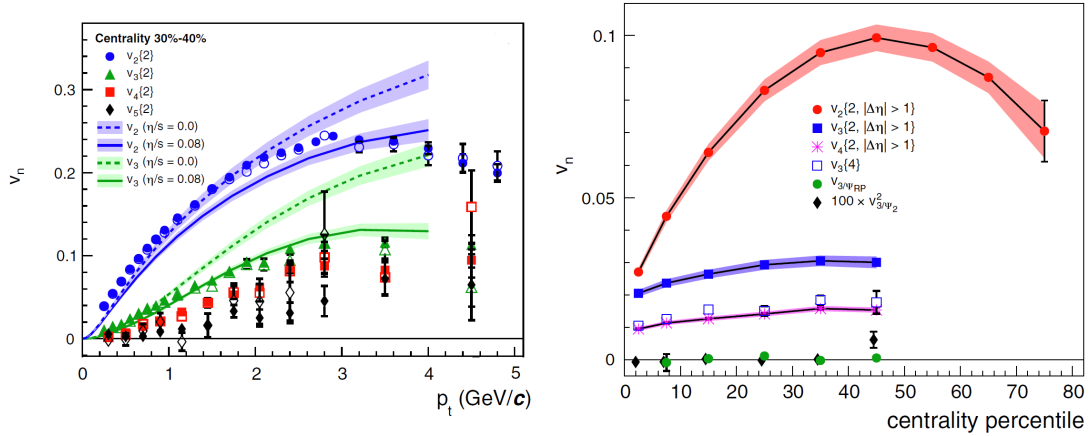


**Figure 2.14.:** (left)  $v_2$ ,  $v_3$ ,  $v_4$  and the  $v_5$  of unidentified charged particles as a function of the transverse momentum  $p_T$  at a centrality percentile of 30-40% measured with ALICE at  $\sqrt{s_{NN}} = 2.76$  TeV. Hydrodynamic model predictions for  $v_2$  (blue solid and dotted lines) and  $v_3$  (green solid and dotted lines) with Glauber initial conditions and different shear viscosity to entropy density ratios  $\eta/s$  are also drawn in. (right)  $p_T$ -integrated  $v_2$ ,  $v_3$  and  $v_4$  of unidentified charged particles as function of collision centrality measured with ALICE with different  $v_n$ -extraction methods at  $\sqrt{s_{NN}} = 2.76$  TeV. This figure has been taken from [8].

of the transverse momentum  $p_T$  at a centrality percentile of 30-40%. Hydrodynamic model predictions for  $v_2$  and  $v_3$  [9] with Glauber initial conditions and different shear viscosity to entropy density ratios  $\eta/s$  (solid and dotted lines) are also drawn in. According to these predictions the  $v_3$  (green lines) is more sensitive to the shear viscosity to entropy density ratio  $\eta/s$  than the  $v_2$  (blue lines) because the  $v_2$ -predictions change only to a small extent in contrast to the  $v_3$ -predictions if the shear viscosity to entropy density ratio is varied. Figure 2.14 (right) shows the  $p_T$ -integrated  $v_2$ ,  $v_3$  and  $v_4$  as function of collision centrality. The  $v_2$  is driven by the collision centrality, i.e. by the size of the impact parameter of

the colliding nuclei, and increases as the collision gets more peripheral up to a centrality percentile of about 50%. The  $v_3$  and  $v_4$  are almost independent of the collision centrality because they are driven by fluctuations in the individual nucleon-nucleon collision points from collision to collision. In fig. 2.14 the  $v_3$  is measured with 2 different methods: the 2-particle cumulants and the 4-particle cumulants, indicated with "4", respectively "2" in the curly brackets in the legend. The expression  $\Delta\eta > 1$  in the brackets indicates that in the 2-particle cumulant method only particles with an  $\eta$ -gap of  $\Delta\eta > 1$  were correlated with each other. For more details see [8]. A detailed compilation of  $v_n$ -measurements at the LHC performed by the CMS and ATLAS collaborations is given in [35–37].

The reason why  $v_n$ -measurements are often done with different methods and then compared is that one tries to quantify the amount of *non-flow* contributions. Non-flow contributions to  $v_n$  are effects that increase the  $v_n$  but this contribution is not due to collective flow but due to other sources. These sources can be:

- Jets that produce a collimated spray of hadrons. These hadrons are correlated in  $\phi$  and  $\eta$ .
- Decays of strange mesons and baryons, e.g.  $\Lambda \rightarrow p\pi^-$ . In this case the decay products, the proton and the pion, are correlated in  $\phi$  and  $\eta$ .
- Momentum conservation. The sum of the  $p_T$  of all particles must be 0 and this constraint imposes some correlation on the particles of one event, especially for low multiplicity events.

The first two non-flow contributions can be suppressed by so-called  $\eta$ -gap methods. In case of the event plane method, the event plane is calculated using particles from a different rapidity window than the particles, which are correlated with the event plane. The price one has to pay when limiting non-flow contributions with  $\eta$ -gap methods is that one has less particles to build the  $Q$ -vector. This deteriorates the event plane resolution and as a result increases the statistical uncertainty of the  $v_n$ -measurement

### $v_n$ at high $p_T$

The reason for a non-zero  $v_n$  at high transverse momenta for  $p_T \gtrsim 5$  GeV/ $c$  is not anisotropic collective flow but different path-lengths in- and out-of-plane a high energetic parton has to travel in the QGP after its production. Quark energy-loss in the QGP will be addressed in the next section with the focus on charm quarks. Figure 2.15 (left) visualizes the effect for the  $v_2$  case. High- $p_T$  partons traveling parallel in the second order event plane have to cross a shorter distance through the QGP and lose less energy than particles propagating in the QGP perpendicular to the second order event plane. Figure 2.15 (right) shows the  $v_2$ ,  $v_3$ , and the  $v_4$  of unidentified charged particles as a function of the transverse momentum  $p_T$  at a centrality percentile of 20-30% measured with ALICE with different  $v_n$ -extraction methods at  $\sqrt{s_{NN}} = 2.76$  TeV. The  $v_2$  is determined with the event plane method, labeled with "EP,  $\Delta\eta > 2.0$ ", with an  $\eta$ -gap of  $\Delta\eta > 2.0$  between the particles used to determine the second order event plane angle and the particles of interest. The particles of interest are all charged particles from the considered events in the centrality class 20-30% after applying single track selections listed in [40]. Moreover

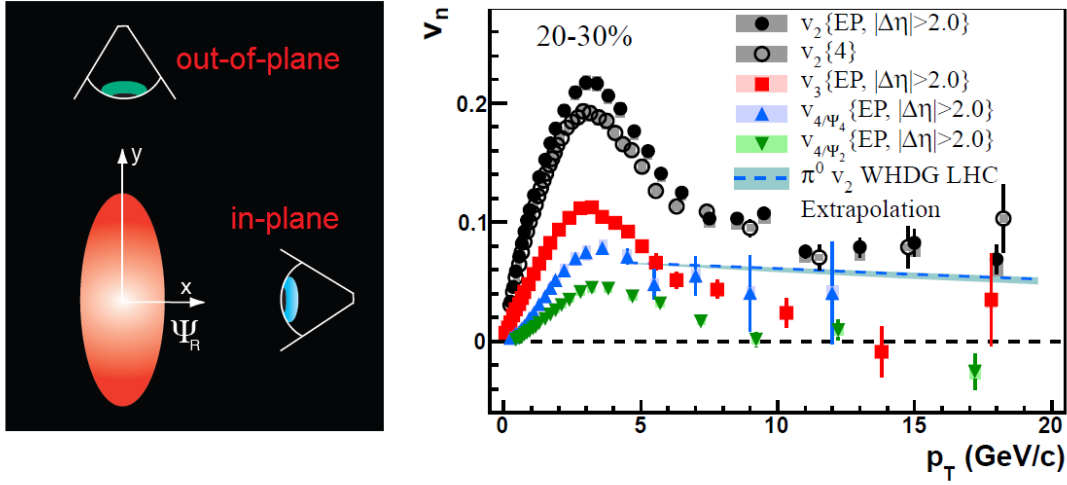


**Figure 2.15.:** (left) Visualization of the effect of path length dependence of parton energy loss. This figure has been taken from [38]. (Right)  $v_2$ ,  $v_3$ , and the  $v_4$  of unidentified charged particles as a function of the transverse momentum  $p_T$  at a centrality percentile of 20-30% measured with ALICE with different  $v_n$ -extraction methods at  $\sqrt{s_{NN}} = 2.76$  TeV over a wide  $p_T$ -range. This figure has been taken from [39].

the 4-particle cumulant method, see [33], labeled as " $v_2(4)$ " was applied to determine the  $v_2$ -parameter. For detailed explanations about the small discrepancy between " $v_2(4)$ " and " $\text{EP}, \Delta\eta > 2.0$ " see [33, 39]. The  $v_3$  was determined with the event plane method but with an  $\eta$ -gap, similar to the first  $v_2$ -case. The  $v_4$  was determined with the event plane method with an  $\eta$ -gap and by correlating the particles of interest with the second order event plane angle (" $v_{4/\Psi_2}$ "), also referred to a mixed harmonics method [33], and with the fourth order event plane angle (" $v_{4/\Psi_4}$ "). For detailed explanations about the discrepancy between " $v_{4/\Psi_2}$ " and " $v_{4/\Psi_4}$ " see [33, 39].

The  $p_T$ -coverage in fig. 2.15 ranges from  $p_T = 0$  GeV/c to  $p_T = 20$  GeV/c. Around  $p_T \approx 5$  GeV/c the  $v_2$  levels off at a constant value of  $\approx 0.1$ . At that  $p_T$  the reason for a non-zero  $v_2$  changes from collective flow to path-length dependence of parton energy loss.

## 2.4. Charm physics

### Discovery of the charm quark and D mesons

In 1970 Sheldon Lee Glashow, John Iliopolus and Luciano Maiani proposed a hypothetical second generation of quarks consisting of the charm-quark and the strange-quark already discovered at that time to explain the very small branching ratio of the decay  $K^0 \rightarrow \mu\mu$ , see [41]. This explanation is known as the *GIM-mechanism*. The  $K^0$  meson, composed of a d- and a s-quark, cannot decay through a neutral current ( $Z^0$ ), because there are no flavor changing neutral currents at tree level. This forbidden decay is shown in fig. 2.16 (left). However, there is a second order flavor changing decay with W-bosons involved, which enables the decay  $K^0 \rightarrow \mu\mu$ , see fig. 2.16 (right, a). In the early 70's it was a puzzle that this second order decay branching ratio was measured to be several orders of

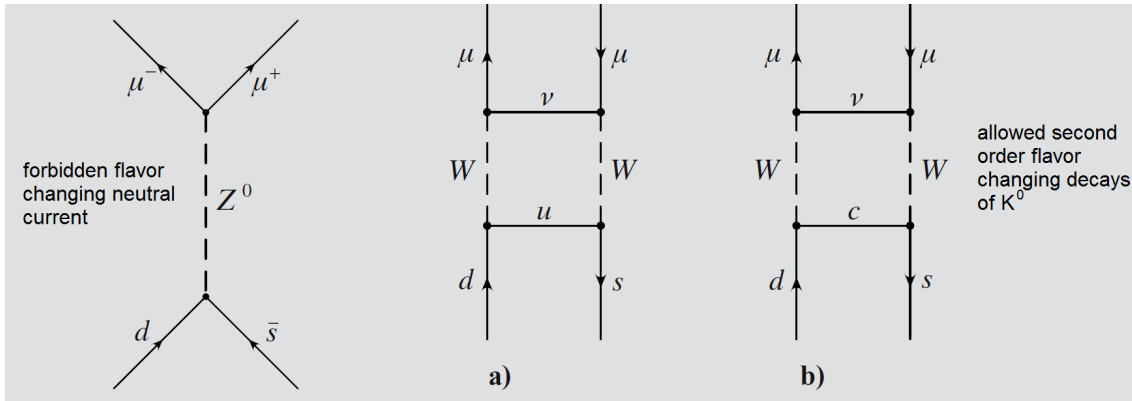


**Figure 2.16.:** (left) Forbidden flavor changing neutral current decay of the  $K^0$  meson. (right, a) and b)) Second order flavor changing decay with  $W$ -bosons of the  $K^0$  meson. This figure has been taken from [42].

magnitude lower, very close to zero ( $\approx 10^{-8}$ ), than the theoretical expectations. The GIM-mechanism provided a solution to this puzzle by introducing a hypothetical charm-quark and enabling a Feynman-graph shown in fig. 2.16 (right, b). Both decay modes a) and b) shown in fig. 2.16 (right) exactly cancel each other if the mass of the  $u$ - and  $c$ -quark are identical. In 1974, Gaillard and Lee even predicted the mass of the (at that time still) hypothetical charm-quark to be of the order of  $m_c < 5 \text{ GeV}/c^2$  using the measured branching ratio of  $K^0 \rightarrow \mu\mu$ , see [43]. In November 1974, a working group lead by Burton Richter at the Stanford Linear Accelerator Center (SLAC) and simultaneously another one lead by Samuel Chao Chung Ting at the proton-synchrotron at Brookhaven discovered the  $J/\psi$  meson, a bound state of a charm- and anti-charm-quark. This discovery is known as the "November-revolution" because it was a door-opener for the acceptance of the standard model. In 1976 Richter and Ting received the Nobel-price for their discovery. The mass of the  $J/\psi$  meson  $m_{J/\psi} = 3097 \text{ MeV}/c^2$  is below twice the mass of the lightest  $D$  meson, the  $D^0$ , composed of a  $c$ -quark and an anti- $u$ -quark. Therefore it cannot decay as analogously the  $\phi$  meson, a bound state of strange-quarks, to  $K$  mesons. The  $D$  mesons were discovered at SLAC in  $e^+e^-$  collisions at a center-of-mass range of  $3.9 \text{ GeV} < \sqrt{s} < 7.8 \text{ GeV}$ :

- The  $D^0$  in 1976 by G. Goldhaber *et al.* using the decay channel  $D^0 \rightarrow K^- \pi^+$ , see [44].
- The  $D^+$  in 1976 by I. Peruzzi *et al.* using the decay channel  $D^+ \rightarrow K^- \pi^+ \pi^+$ , see [45].
- The  $D^{*+}$  in 1976 by G. J. Feldman *et al.* using the decay channel  $D^{*+} \rightarrow D^0 \pi^+$ , see [46].

Figure 2.17 shows the invariant mass spectra of various kaon and pion combinations measured at SLAC. For more details see [44–46]. This technique is used to reconstruct and identify decayed particles, such as  $D$  mesons. This technique will be explained in detail in chap. 4. Using this technique, peaks, i.e. excesses of events, appear at the invariant masses of the decayed particles. In fig. 2.17 (left) this happens at  $m_{D^0} = 1864.86 \text{ MeV}/c^2$  [10], in fig. 2.17 (center) at  $m_{D^+} = 1869.62 \text{ MeV}/c^2$  [10] and in fig. 2.17 (right) at  $m_{D^{*+}} - m_{D^0} = 145.421 \text{ MeV}/c^2$  [10]. In contrast to the  $D^0$  and the  $D^+$ , the  $D^{*+}$  meson is identified via

## 2. Theoretical background

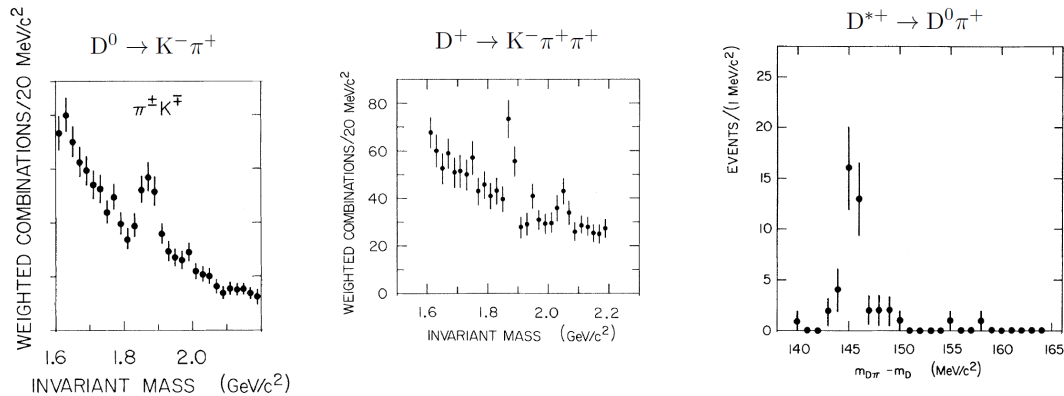


**Figure 2.17.:** Invariant mass spectra as measured at SLAC in  $e^+e^-$  collisions at a center-of-mass range of  $3.9 \text{ GeV} < \sqrt{s} < 7.8 \text{ GeV}$  taken from the D meson discovery papers [44–46]: (left)  $D^0 \rightarrow K^- \pi^+$ , (center)  $D^+ \rightarrow K^- \pi^+ \pi^+$ , (right)  $D^{*+} \rightarrow D^0 \pi^+$ .

the difference between the reconstructed invariant masses of its decay triplet  $K\pi\pi$  and of the decay doublet  $K\pi$  of one of its intermediate decay daughters, namely the  $D^0$ . The details and the advantages of this special procedure will be explained in chap. 4. Tabular 2.3 summarizes the most important physical quantities of the three D mesons.

Particle	quark content	mass [MeV/ $c^2$ ]	mean lifetime [ $\mu\text{m}/c$ ]	charge [e]	spin [ $\hbar$ ]
$D^0$	$c\bar{u}$	$1864.86 \pm 0.13$	$122.9 \pm 0.3$	0	0
$D^+$	$c\bar{d}$	$1869.62 \pm 0.15$	$311.8 \pm 2.1$	1	0
$D^{*+}$	$c\bar{d}$	$2010.28 \pm 0.13$	$(2.1 \pm 0.5) \cdot 10^{-6}$	1	1
			$\leftrightarrow \Gamma = (96 \pm 22) \text{ keV}$		

**Table 2.3.:** Physical quantities of the  $D^0$ ,  $D^+$  and the  $D^{*+}$ . The values have been taken from [10].

### D meson production in high energy proton-proton collisions

Today, modern, state-of-the-art theoretical D meson production cross sections in proton-proton collision, i.e. in the vacuum without any interaction with a QGP, are carried out using the concept of the factorization approach. The three ingredients of this approach are:

- the parton distribution functions (PDF) of the partons within the colliding protons;
- the partonic cross sections of the involved processes, which are calculated using the framework of perturbative QCD (pQCD);
- the fragmentation parameterization, which quantifies the probability of a charm quark to hadronize to a certain D meson species at a given parameter  $z$ . This parameter  $z$  is the ratio of the energy of the D meson and the the energy of the corresponding charm quark.

The gluon, sea-quark and the valence-quark PDFs  $f_i(x)$ , with  $x$  being the momentum fraction carried by the considered parton, cannot be calculated but need to be extracted from measured electron-proton cross-sections in dedicated experiments. Two of the leading experiments in measuring PDFs through deep-inelastic scattering (DIS) of electrons on protons are the H1 and ZEUS experiments at the DESY facility in Hamburg, Germany. There are several theoretical collaborations, which combine many data sets of various experiments to reduce the statistical and systematic errors and provide PDFs by using electron-proton cross-sections and QCD evolution, e.g. the Coordinated Experimental-Theoretical Project on QCD (CTEQ), see [47]. Figure 2.18 (right) shows the PDFs of

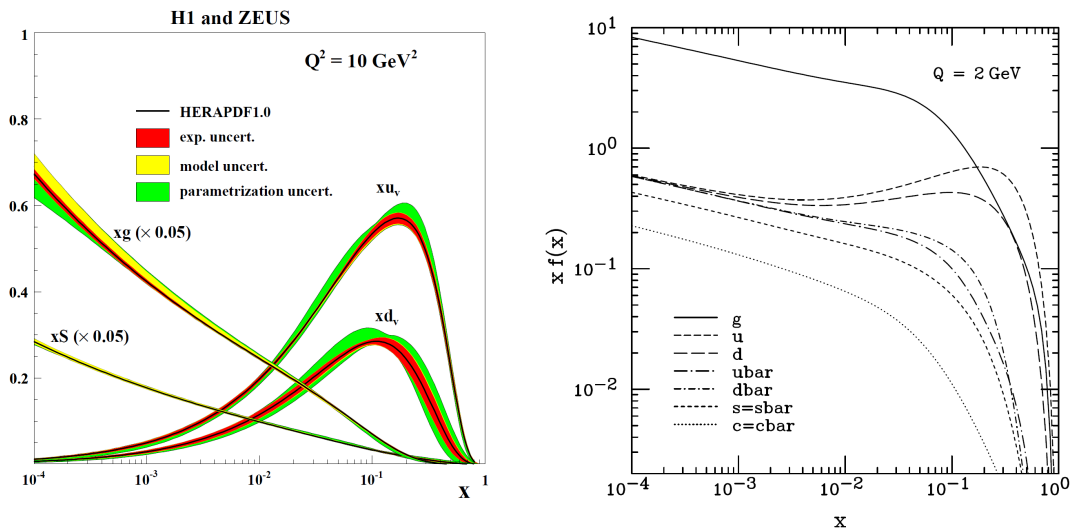


**Figure 2.18.:** Parton distribution functions for valence quarks, sea-quarks and gluons as measured by H1 and ZEUS (combined fit) at the momentum transfer scale  $Q^2 = 10 \text{ GeV}^2$  (left) and obtained by the CTEQ collaboration at  $Q = 2 \text{ GeV}$  from various experimental data sets (right). These figures have been taken from [47, 48].

gluons, sea quarks and valence quarks within protons at the momentum transfer scale  $Q = 2 \text{ GeV}$  obtained by the CTEQ collaboration from various data sets. For details see [47]. Figure 2.18 (left) shows the measured PDFs of gluons, sea quarks and valence quarks within protons at the momentum transfer scale  $Q^2 = 10 \text{ GeV}^2$  measured by the H1 and ZEUS collaborations, see [48]. Both momentum transfer scales are in the relevant range for charm-quark production. It is given by:

$$Q^2 = (2m_c)^2 = 6.8 \text{ GeV}^2 \quad (2.26)$$

For  $m_c$  the value quoted in tab. 2.1 was used. The relevant momentum fraction  $x$  at midrapidity can be estimated with the following formula:

$$Q^2 = (2m_c)^2 = x_1 x_2 \cdot s \quad (2.27)$$

with  $x_i$  being the momentum fractions of the colliding partons in their individual projectile protons and  $s = E_{\text{cms}}^2$ . At midrapidity, i.e. at  $y = 0$ , one can show as in [49] that

## 2. Theoretical background

$x_1 = x_2$ . Therefore the relevant momentum fraction for charm production at the LHC with  $\sqrt{s} = 7$  TeV is given by:

$$x = \frac{2m_c}{\sqrt{s}} = \frac{2.6 \text{ GeV}}{7 \text{ TeV}} = 3.7 \cdot 10^{-4} \quad (2.28)$$

Looking at fig 2.18 (left and right) one can see that the PDFs at  $x = 3.7 \cdot 10^{-4}$  are dominated by gluons. Therefore the dominating charm production processes at the LHC have two gluons in the initial state, each of them from the colliding protons. These processes are:

- **Pair creation:**  $gg \rightarrow Q\bar{Q}$ . The two gluons fuse and a charm quark-antiquark ( $Q\bar{Q}$ ) pair appears in the final state, see fig. 2.19 (left).
- **Flavor excitation:**  $gQ \rightarrow gQ$ . A charm quark stemming from a gluon splitting process from one proton scatters with a gluon from the other proton, see fig. 2.19 (center).
- **Gluon splitting:**  $g \rightarrow Q\bar{Q}$ . A gluon from one proton scatters with a gluon from the other proton and then splits in a charm quark-antiquark pair, see fig. 2.19 (right).

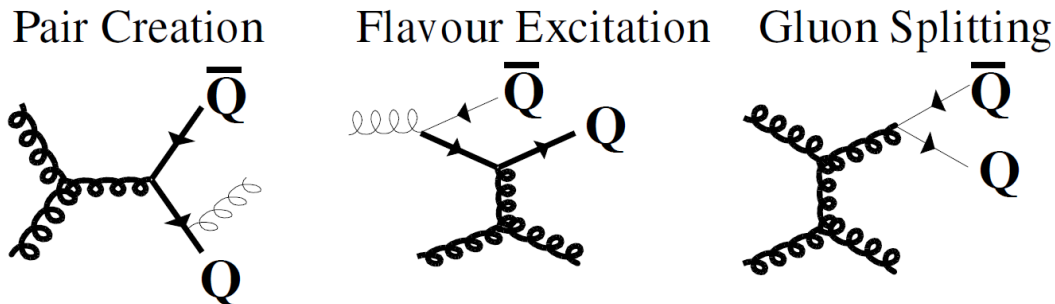


**Figure 2.19.:** Feynman-diagrams of charm production processes at the LHC at leading order (LO): Pair creation (left), flavor excitation (center) and gluon splitting (right). This figure has been taken from [49].

In contrast to the charm-quark production the fragmentation parameterization cannot be calculated in pQCD because it is a soft process and thus the strong coupling constant  $\alpha_s$  becomes too large. A commonly used parameterization describing the probability of a charm quark to fragment into D mesons, is the Peterson-function [50] based on quantum mechanical considerations and given by:

$$D_Q^H(z) = \frac{N}{z [1 - (1/z) - \epsilon_Q / (1 - z)]^2} \quad (2.29)$$

with  $N$  being a normalization constant,  $z = E_H/E_Q$  and  $\epsilon_Q = (m_q/m_Q)^2$ .  $E_H$  is the energy of the D meson, to which the charm quark fragments,  $E_Q$  the energy of the charm quark,  $m_q$  the constituent mass of light flavor quarks (u,d) and  $m_Q$  the constituent mass

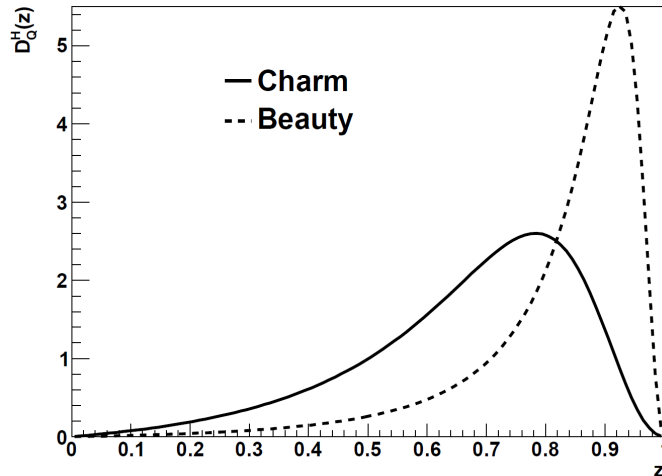


**Figure 2.20.:** The Peterson function for beauty and charm quarks assuming  $\epsilon_Q = 0.06$  for charm quarks and  $\epsilon_Q = 0.006$  for beauty quarks. See eq. 2.29 for explanation of the parameters. This figure has been taken from [51].

of the heavy charm quark, respectively beauty quark. A plot of this function is shown in fig. 2.20 for  $\epsilon_Q = 0.06$  for charm quarks and  $\epsilon_Q = 0.006$  for beauty quarks. The Peterson parameterization is not the result of precise analytic calculations but rather an ansatz as pointed out in [50]. The parameter  $\epsilon_Q$  is technically defined as  $\epsilon_Q = (m_q/m_Q)^2$ , with  $m_q$  being the constituent mass of a light flavored up or down quark and  $m_Q$  the constituent mass of a charm respectively beauty quark. However, it is usually left free and fixed by fits to measured data. This type of fits using  $Z^0$  decays to heavy-quarks data from LEP at CERN can be found in [52]. Alternative fragmentation parameterizations are the Kartvelishvili-Likhoded-Petrov function [53], the Bowler function [54], and the Collins-Spiller function [55]. All of these parameterizations have free parameters, which need to be fixed by fits to experimental data.

Using the PDFs  $f_i(x)$ , the partonic cross sections  $\sigma_{ij \rightarrow QX}$  and the fragmentation function  $D_Q^H(z)$  the cross section for D meson production is given by:

$$d\sigma(pp \rightarrow D + X) = \sum_{i,j} \int \int dx_1 dx_2 f_1(x_1, \mu_F) f_2(x_2, \mu_F) \times \sigma_{ij \rightarrow QX}(\mu_F, \alpha_s(\mu_R), m_c) \times D_Q^H(z) \quad (2.30)$$

where  $i, j$  are the partons (gluons and quarks) in the colliding protons and  $Q$  is the symbol for the charm quark. The quantity  $\mu_R$  is the renormalization scale. In pQCD calculations, this scale is needed to absorb short range (ultraviolet) singularities. On the other hand, the quantity  $\mu_F$  is the factorization scale and is needed to avoid long-range (infrared) singularities in pQCD.

### D meson production in high energy heavy-ion collisions

In general, the production of D mesons is modified in heavy-ion collisions with respect

to proton-proton collisions; this is due to various effects. The first rough classification of these modification effects is to distinguish between *initial-* and *final-state effects*. Initial-state effects are processes that take place in heavy-ion collisions before charm quarks are produced by the processes visualized in the Feynman-diagrams in fig. 2.19. These initial-state effects are not occurring in proton-proton collisions. The two most important initial-state effects are:

- **$k_T$ -broadening:** colliding gluons which yield charm quarks in the final state need to be assigned an intrinsic transversal momentum jittering to reproduce proton-proton data on charm production as explained in [56]. In proton-proton collisions this value is  $\langle k_T^2 \rangle = 1 \text{ GeV}^2$  but needs to be increased to  $\langle k_T^2 \rangle \approx 1.7 \text{ GeV}^2$  in heavy-ion collisions because gluons scatter several times when the two nuclei penetrate each other, see [56]. This effect changes to a small extent the  $p_T$ -distribution of the produced charm quarks but not the total charm cross section.
- **Nuclear shadowing:** as explained in the previous subsection the main contribution to charm-quark production comes from gluon-gluon interaction at Bjorken- $x$  of  $x \approx 10^{-4}$ , see eq. 2.28 and fig. 2.18. This means that one gluon from one nucleon "sees" about  $n=A \times (1/10^{-4})$  gluons from the other nucleon. For lead ions this corresponds to  $n=2 \cdot 10^6$  gluons. Due to this high density, gluons tend to merge together through the process  $g(x_1) + g(x_2) \rightarrow g(x_1 + x_2)$ . Therefore the gluon distribution as shown in fig. 2.18 gets depleted at low Bjorken- $x$  and more populated at higher Bjorken- $x$  which decreases the number of available gluons for charm-quark production. This effect decreases the total charm and subsequently the D meson production cross section. The ratio of modified gluon PDFs within lead ions  $f_g^{Pb}(x, Q^2)$  and unmodified PDFs  $f_g^p(x, Q^2)$  at  $x \approx 10^{-4}$  and  $Q^2 = 5 \text{ GeV}^2$  ranges from 30% to 90%, depending on the theoretical group providing PDFs, see [49]. This uncertainty will be reduced in the future using proton-lead data taken at the LHC beginning of 2013. Fig. 2.21 shows the ratio  $R(x, Q^2) = \frac{f_g^{Pb}(x, Q^2)}{f_g^p(x, Q^2)}$  as a function of the Bjorken- $x$  using different models. For details see [49] and the references therein.

Final state effects are caused by the interaction of charm quarks with the formed QGP and D mesons interacting with other hadrons during the hadronic phase. The special feature of charm quark production is that charm quarks are produced at the very beginning of the heavy ion collisions, before thermalization sets in. The production timescale can be estimated by the Compton wavelength of the exchanged virtual gluon in the Feynman diagram shown in fig. 2.19 (left):

$$\lambda_{\text{gluon}}^{\text{compton}} = \frac{\hbar}{2m_c c} = 0.07 \text{ fm} \quad (2.31)$$

For the charm quark mass  $m_c = 1.5 \text{ GeV}/c^2$  was used. Thus the timescale of charm quark production is of the order of  $\tau_{\text{charm}} \approx \lambda_{\text{gluon}}^{\text{compton}}/c = 0.07 \text{ fm}/c$ . According to theoretical estimations, see e.g. [57], the timescale after a equilibrated QGP is formed is  $\tau_0 \approx 1 \text{ fm}/c$ . The timescale for charm quark production with respect to this timescale is one order of magnitude smaller. Therefore the most state-of-the-art models describing the interaction of charm quarks with a QGP consist of the two following modules:

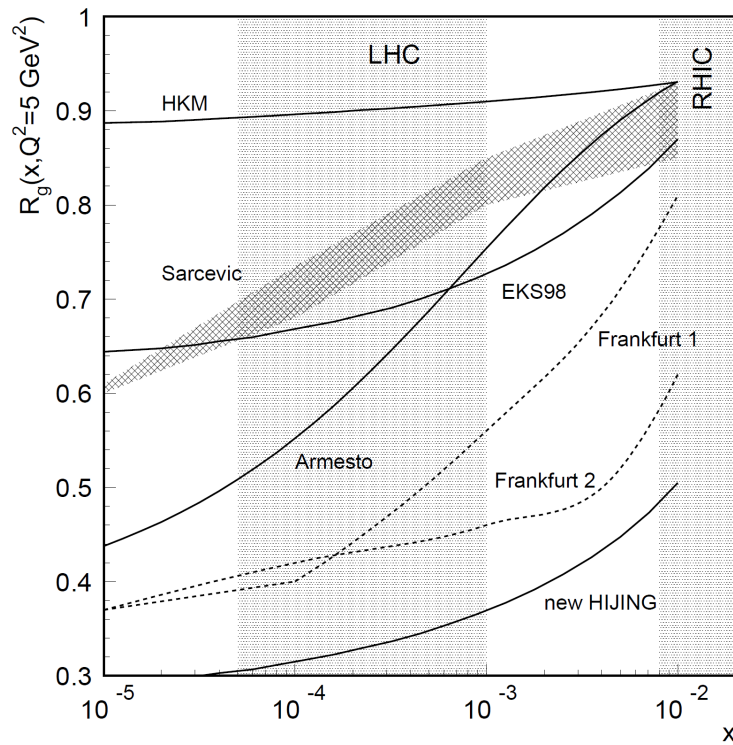


**Figure 2.21.:** Ratio of gluon distribution functions in lead ions to the one in protons using different models. The relevant Bjorken- $x$  regimes for charm quark production at LHC and RHIC energies are depicted (shaded areas). This figure has been taken from [49].

1. an appropriate model for the medium, into which the charm quarks are embedded. The influence of the charm quarks on the evolution of the thermodynamic quantities such as pressure, temperature etc. is neglected. This is a fair assumption because as shown in [58] the number of produced charm quarks is more than two orders of magnitude smaller with respect to the main constituents of the QGP, the gluons and the light flavored up and down quarks.
2. Embedding of the charm quarks into the medium:
  - an initial distribution of charm quarks calculated with pQCD and PDFs with a possible shadowing parameterization and  $k_T$ -broadening described above;
  - modeling the interaction of the produced charm quarks with the medium;
  - a fragmentation parameterization of charm quarks to D mesons.

The charm quark pQCD production and fragmentation parameterizations have already been discussed above, see figs. 2.19, 2.18, 2.20. In most models the aforementioned vacuum fragmentation functions are used to describe the transition of charm quarks to D mesons. In the factorization approach, see eq. 2.30, the energy of the charm quarks  $E_Q$  in the fragmentation parameterization must be reduced by the total energy  $\Delta E$  the charm quark

loses by traversing the QGP. Thus the variable  $z$  changes:

$$D_{Q,\text{vac}}^H(z) \rightarrow P(E_i \rightarrow E_f) \otimes D_{Q,\text{vac}}^H(z) = D_{Q,\text{QGP}}^H(z', E_i \rightarrow E_f) \quad (2.32)$$

with  $E_i$  being the energy of the charm quark after production and  $E_f$  the energy after traversing the QGP. The expression  $P(E_i \rightarrow E_f)$  is called *quenching weight*. The modeling of the interaction of charm quarks with the QGP is the key issue of every model predicting observables, which are compared to measured values. Among other important observables, the proper simultaneous prediction of the elliptic flow parameter  $v_2$  introduced in sec. 2.3 and the nuclear modification factor  $R_{AA}$  of charmed mesons is a fundamental challenge to state-of-the-art charm quark production models in heavy-ion collisions. The  $R_{AA}$  is defined as the ratio of the  $p_T$  spectrum measured in AA collisions to the proton–proton spectrum at the same center-of-mass energy  $\sqrt{s}$  scaled by the number  $N_{\text{coll}}$  of binary nucleon–nucleon collisions in the AA collision:

$$R_{AA}(p_T) = \frac{1}{\langle N_{\text{coll}} \rangle} \cdot \frac{dN_{AA}/dp_T}{dN_{pp}/dp_T} \quad (2.33)$$

$N_{\text{coll}}$  is dependent on the impact parameter  $b$ , see [4], of the colliding nuclei, i.e. on the collision centrality. The ratio  $R_{AA}(p_T)$  equals unity in case of no nuclear effects.

In most charm quark production models in heavy ion collisions one distinguishes between two types of charm quark energy loss:

- Collisional energy loss by elastic scatterings with the QGP constituents, see fig. 2.22 (left).
- Radiative energy loss via induced gluon emission, see fig. 2.22 (center).

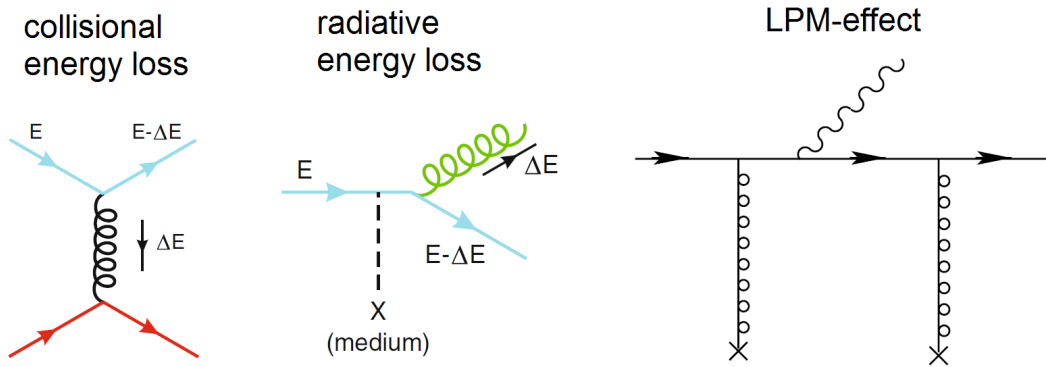


**Figure 2.22.:** Feynman diagrams for collisional (left) and radiative energy loss (center) of charm quarks, represented by the blue lines, propagating in a QGP. This figure has been taken from [22]. Visualization of the Landau-Pomeranchuk-Migdal effect (right). For details see text and [59]. This figure has been taken from [60].

The total energy loss  $\Delta E_{\text{total}}$  is given by  $\Delta E_{\text{total}} = \Delta E_{\text{rad}} + \Delta E_{\text{coll}}$ . In order to formulate a parameterization of the collisional energy loss, the minimal requirement is to consider all

contributing QCD Feynman-diagrams in leading order, which parameterize the coupling of the charm quarks to the medium constituents, i.e. elastic scattering with gluons and quarks. These diagrams are shown in fig. 2.23. As an example, the  $t$ -differential QCD

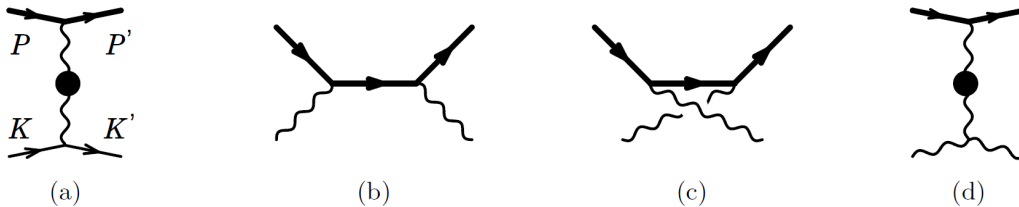


**Figure 2.23.:** QCD Feynman diagrams parametrizing the elastic collisional interaction of charm quarks with quarks (a) and with gluons (b), (c), (d) within the QGP. This figure has been taken from [61].

cross section, with  $t$  being the square of the four-momentum transfer of the charm quark to the medium parton (quark or gluon) is given by:

$$\frac{d\sigma}{dt} = C_i \frac{4\pi\alpha_s^2(t)}{t^2}, \quad \text{with } \alpha_s(t) = \frac{12\pi}{(33 - 2n_f) \ln(t/\Lambda_{\text{QCD}}^2)} \quad (2.34)$$

The constant  $C_i$  is the color factor and is  $C_i = 1$  for quark-gluon, respectively  $C_i = 4/9$  for quark-quark scattering. The contribution of the  $t$ -channel to the total collisional energy loss of a charm quark propagating in a QGP is proportional to the following integral:

$$\Delta E_{\text{coll},t\text{-channel}} \propto \int_{t_{\min}}^{t_{\max}} t \frac{d\sigma}{dt} dt \quad (2.35)$$

The upper integral limit  $t_{\max}$  is given by the center-of-mass energy of the scattering partons. The incident charm quark has the energy  $E$  and the energy of the parton in the plasma is of the order of the temperature  $T$ . The lower integral limit  $t_{\min}$  is fixed by the Debye screening length  $\lambda_D$ , see eq. 2.3, and prevents the integral to diverge. In vacuum the quark-quark potential is approximated by eq. 2.1. In a QGP, however, the color charge of the quarks is screened, which is approximated by a dampening factor, see eq. 2.3. Considering running coupling, proper integral limits and charm quark mass effects, an analytic formula for the collisional energy loss per length unit  $\frac{dE_{\text{coll}}}{dx}$  for heavy quarks propagating in a QGP of massless fermions (quarks) and bosons (gluons) with a defined temperature can be derived, see [61]. Reference [61] reports an energy loss per unit length  $\frac{dE_{\text{coll}}}{dx} = 0.6$  GeV/fm for the following conditions: temperature  $T = 0.2$  GeV, QCD-scale  $\Lambda_{\text{QCD}} = 0.2$  GeV, participating quark flavors in the  $\alpha_s$ -running  $n_f = 3$ , charm mass of  $m_c = 1.3$  GeV and initial energy of the incident charm quark  $E = 20$  GeV.

Radiative energy loss of charm quarks traversing a QGP, see fig. 2.22 (center), is the analogon of QED-Bremsstrahlung. Therefore, in the literature it is often referred to as "gluonstrahlung". One of the contributing Feynman diagrams in leading order is shown in fig. 2.22 (center). If the medium is thick enough, i.e. if the mean free path  $\lambda$  of the

charm quark is short compared to the size of the QGP, the Landau-Migdal-Pomeranchuk (LPM) effect must be taken into account. It was first described and quantified by Migdal when electrons interact with matter, see [59]. This effect describes the fact that it takes a certain time for an electron to emit a photon and the same holds in QCD for quarks emitting gluons. During that time another interaction with the medium quarks and gluons can occur. Several scatterings are then taken as a coherent sum of scatterings, which yields a scattering with one effective scattering center and change the gluon emission spectrum. A Feynman diagram of this process is shown in fig. 2.22 (right). The first who derived an analytic function for radiative energy loss for charm quarks were Mustafa *et al.*, see [62]. They take the LPM-effect and the aforementioned radiative Feynman diagrams into account and derives an analytic formula for the radiative charm quark energy loss:

$$-\frac{dE}{dx} = \frac{3\alpha_s}{\pi} \frac{(\mu_D \cdot q_T^{max})^2}{(q_T^{max})^2 - \mu_D^2} \ln^2 \left( \frac{\mu_D^2}{(q_T^{max})^2} \right), \text{ with } \mu_D^2 = 4\pi\alpha_s T^2, \quad (2.36)$$

and with  $(q_T^{max})^2 = \frac{3ET}{2} - \frac{M^2}{4} + \frac{M^4}{48pT} \ln \left[ \frac{M^2 + 6ET + 6pT}{M^2 + 6ET + 6pT} \right]$

$M, p$  and  $E$  are the mass, momentum and the energy of the incident charm quark and  $T$  is the temperature of the QGP. The dependence on the incident charm quark energy

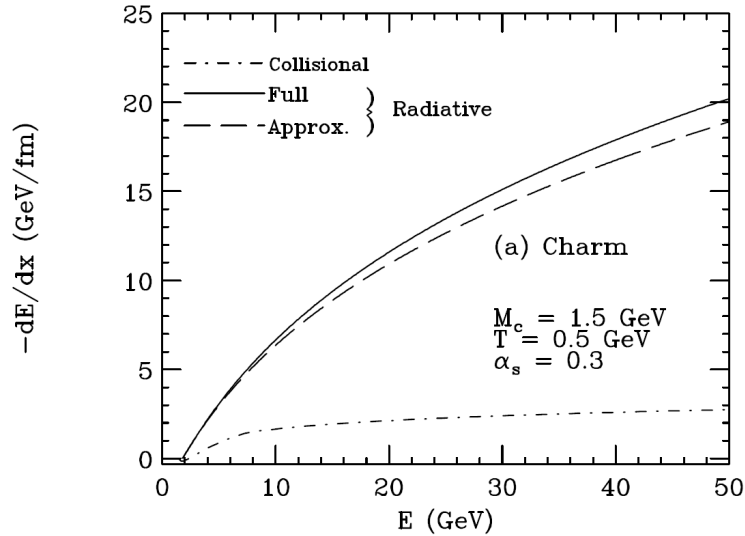


**Figure 2.24.:** Comparison of radiative and collisional energy loss of charm quarks as computed in [62] (radiative loss) and [63] (collisional loss). This figure has been taken from [62].

is shown in fig. 2.24 for QGP and charm quark properties quoted in the figure. This figure also shows a comparison to collisional charm quark energy loss obtained in the reference [63]. According to these results the radiative energy loss dominates for all quark energies and the collisional energy loss contributes significantly to the total energy loss up to  $E_c \approx 10$  GeV. In this energy-region,  $E_c < 10$  GeV, charm quarks may thermalize in the QGP and show a non-zero elliptic flow parameter  $v_2$ . Therefore both energy loss

mechanisms, collisional and radiative, are required in models which aim at a simultaneous description of charm  $R_{AA}$  and  $v_2$ . Moreover, theory predicts another effect which reduces the radiative energy loss of charm quarks, namely the "dead-cone"-effect. Dokshitzer and Kharzeev [64] calculated the double differential gluon emission spectrum as a function of the emission angle  $\theta$  with respect to the flight direction of the charm quark:

$$\omega \frac{dI}{d\omega dk_T^2} = \frac{\frac{4\alpha_s}{3\pi k_T^2}}{\left(1 + \frac{(M/E)^2}{\theta^2}\right)^2} \quad (2.37)$$

with  $I$  being the intensity,  $\omega$  the energy and  $k_T$  the transverse momentum of the emitted gluons.  $M$  and  $E$  are the mass, respectively the energy of the charm quark. At small angles  $\theta$  the spectrum is suppressed by the dead cone suppression factor  $\left(1 + \frac{(M/E)^2}{\theta^2}\right)^2$ . For light quarks and gluons this suppression is small (quarks) or even not present (gluons).

A complete modern state-of-the-art charm-quark energy loss model in a hot QGP incorporates all the aforementioned energy loss effects in a non-static expanding medium. In the following three different modern approaches are presented, which provide simultaneous predictions for the  $R_{AA}$  and the  $v_2$  as a function of transverse momentum for the charmed mesons  $D^{*+}$ ,  $D^+$  and  $D^0$ .

#### **Aichelin *et al.***

One of the modern charm energy loss models in a hot QGP is provided by the framework of P. B. Gossiaux, R. Bierkandt and J. Aichelin. The properties of this model are described in detail in [65–67]. In this approach the initial spatial density distribution of charm quarks is given by a Glauber simulation. Glauber calculations have been addressed in sec. 2.2 and are described in detail in [4]. The momentum-space initial-distribution as well as the charm to bottom quark ratio is given by pQCD results using the framework of Fixed-Order plus Next-to-Leading-Log (FONLL), see [68]. The  $k_T$ -broadening described above is taken into account by convoluting the initial transverse-momentum of the heavy quarks with a Gaussian function. The temperature and the velocity fields of the underlying medium, into which the produced charm quarks are embedded, are parameterized by hydrodynamic calculations using the model of Kolb and Heinz, see [69]. The interaction of the charm quarks with the medium on a microscopic level is formulated using the Boltzmann equation given by

$$\left(\frac{\partial}{\partial t} + \frac{\vec{p}_i}{E_i} \frac{\partial}{\partial \vec{r}}\right) f_i(\vec{r}, \vec{p}_i, t) = C_i^{gQ \rightarrow gQ} + C_i^{gQ \rightarrow gQg} + \dots \quad (2.38)$$

The left side of the equation is the derivative of the phase-space density of the charm quarks  $f_i(\vec{r}, \vec{p}_i, t)$  and the right side is the so-called *collision integral*. The inputs to the collision integral are the microscopic QCD cross sections of elastic collisional and inelastic radiative charm-quark-medium interactions with a running strong coupling constant. The LPM-effect is considered in the radiative energy loss parameterization. Moreover, the thermal density distribution of gluons and light flavored quarks, whose evolution is calculated out of the velocity and temperature fields, is an input to the collision integral. Equation 2.38 is solved applying Monte Carlo techniques described in detail in [70]. The hadronization

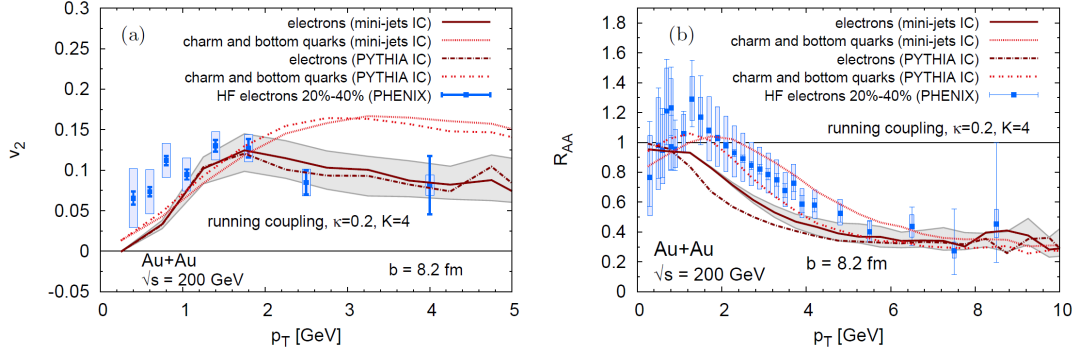


**Figure 2.25.:** Results of calculations for the  $R_{AA}$  and the  $v_2$  as function of transverse momentum for charm-quarks (red lines), for electrons stemming from B meson and D meson semileptonic decays (red lines) and for heavy flavor electrons measured by RHIC [77] (blue datapoints) using the framework BAMPS, see [72–75]. Both figures have been taken from [73].

of the charm quarks to D mesons is described by vacuum fragmentation parameterizations described in detail in [68] at high transverse momenta and by the coalescence model of Dover, see [71], at low transverse momenta.

## BAMPS

Another framework predicting simultaneously the  $R_{AA}$  and  $v_2$  of D mesons is the *Boltzmann Approach of MultiParton Scatterings* (BAMPS), described in detail in [72–75]. This approach has many commonalities with the approach provided by Aichelin *et al.*. The most important differences between the two approaches are:

- No radiative energy loss is considered. Instead of, the elastic cross sections of the charm quarks interacting with the medium constituents are multiplied with an artificial K-factor accounting for the missing radiative energy loss parametrization to describe properly the electron  $R_{AA}$  and  $v_2$ -data from RHIC. These electrons are stemming from B meson and D meson decays. The radiative energy loss is currently being implemented into the calculations [76]. Fig. 2.25 shows results of calculations for the  $R_{AA}$  and the  $v_2$  as function of transverse momentum for charm-quarks (red lines), for electrons stemming from B meson and D meson semileptonic decays (red lines) and for heavy flavor electrons measured by RHIC (blue datapoints), see [77]. The RHIC datapoints have been used to fit the calculations to them and thus to fix the K-factor to  $K=4$  in order to describe the  $v_2$  and  $R_{AA}$  measured by RHIC simultaneously. Using this value for the K-factor, the  $v_2$  and  $R_{AA}$ -predictions for the D meson production at the LHC have been determined. These predictions are shown further below and in chap. 6.
- The evolution of the gluonic QGP is calculated by solving the Boltzmann equation with Monte Carlo techniques. In case of the framework of Aichelin *et al.*, this method is used to calculate the bond of charm quarks to the medium and hence their evolution. BAMPS uses this approach to model both the medium and the bond of charm quarks to the medium.

### WHDG-model

The last model presented here is the WHDG-model, see [78, 79]. The four characters stand for Simon Wicks, William Horowitz, Magdalena Djordjevic and Miklos Gyulassy. In their model they use the same framework as Aichelin *et al.* to calculate the initial charm quark transverse momentum distribution, namely FONLL [68]. However, they neglect  $k_T$ -broadening. They use vacuum fragmentation functions as measured in  $e^+e^-$  collisions claiming that this is a fair assumption because the charm quarks cannot fragment into D mesons until they escape the QGP into the vacuum. A realistic collision geometry based on the Glauber Monte Carlo [4] is used, but without hydrodynamic expansion, so that the predicted  $v_2$  results only from path-length dependent energy loss. The medium density is constrained using the  $\pi^0$ - $R_{AA}$  measurements with RHIC and is extrapolated to LHC center-of-mass energies by using the charged particle multiplicity increase from RHIC to LHC energies. The quenching weights (see eq. 2.32) are calculated using pQCD and both collisional and radiative energy loss. The collisional energy loss calculations are based on the calculations performed by Thoma and Gyulassy referred to as TG, see [80], and Braaten and Thoma [81], referred to as BT. Both approaches give slightly different results on the collisional energy loss. Therefore the spread is treated as a rough estimate of uncertainties from the pQCD leading log approximation, used in both approaches, for collisional energy loss. The radiative energy loss is calculated using the Djordjevic-Gyulassy-Levai-Vitev (DGLV) approach, see [82]. The QGP in this approach consists of a dense arrangement of static scattering centers, which generate a screened Yukawa-potential. The QCD gluonstrahlung spectrum is then calculated using all Feynman diagrams shown in fig. 2.26 (left). Figure 2.26 (right) shows a comparison of the

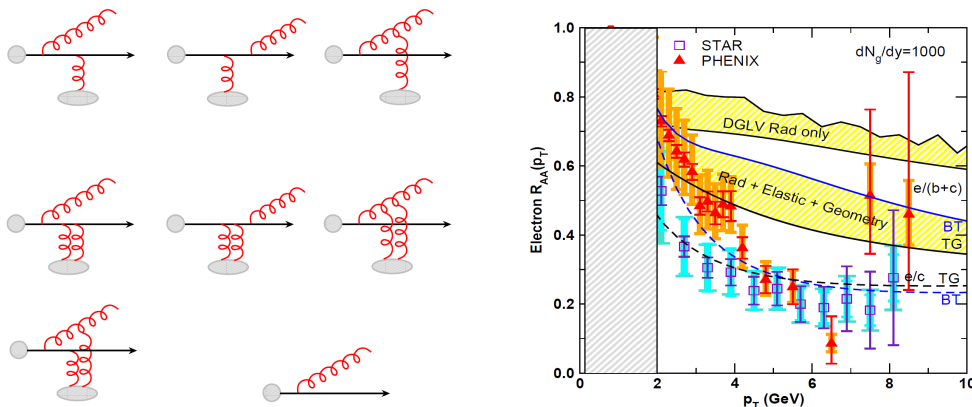


**Figure 2.26.:** (left) Feynman diagrams contributing to the radiative energy loss in the DGLV-approach, see [83]. (right) Comparison of the  $R_{AA}$  of electrons stemming from B meson and D meson decays computed with the DGLV-approach assuming radiative energy loss only (DGLV Rad only, yellow) and on top of the radiative energy loss adding collisional energy loss as well as geometrical path length fluctuations (Rad+Elastic+Geometry, yellow). Heavy-flavor electron  $R_{AA}$  measurements performed by RHIC as well as the extreme case predictions, when b-quarks are removed from the calculations and the electrons come only from D meson semileptonic decays (dotted lines), are also drawn in. The abbreviations BT, see [81] and TG, see [80], refer to different pQCD charm quark collisional energy loss calculations. This figure has been taken from [78].

$R_{AA}$  of electrons stemming from B meson and D meson decays computed with the DGLV-approach assuming radiative energy loss only (DGLV Rad only, yellow) and on top of the radiative energy loss adding collisional energy loss as well as geometrical path length fluctuations (Rad+Elastic+Geometry, yellow). For the second case the aforementioned BT and TG calculations are considered, labeled with the same abbreviations in the figure. Both theoretical predictions are compared to RHIC heavy flavor electron  $R_{AA}$  measurements. Only in the extreme case, when b-quarks are removed from the calculations and the electrons come only from D meson semileptonic decays, the predictions represented by dotted curves are able to reproduce the data.

Figure 2.27 shows the prediction for the elliptic flow parameter  $v_2$  as a function of the transverse momentum  $p_T$  for the three charmed meson species  $D^{*+}$ ,  $D^+$  and  $D^0$  for the

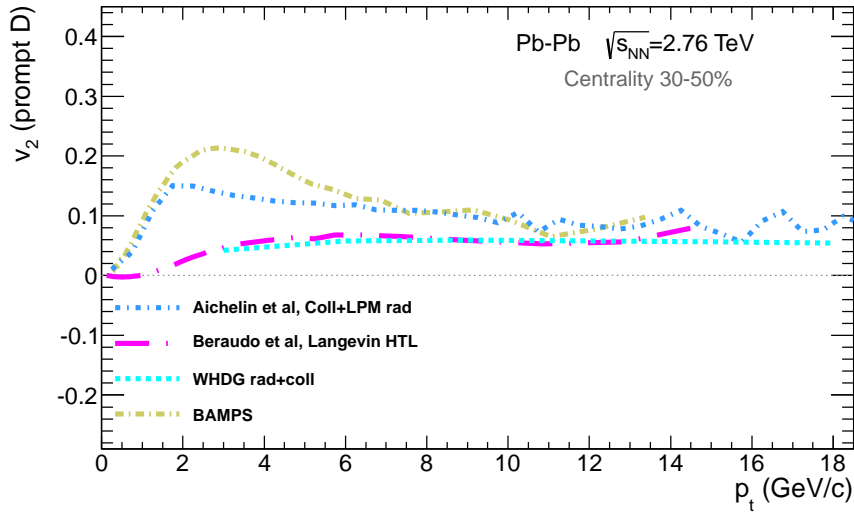


**Figure 2.27.:** Prediction for the elliptic flow parameter  $v_2$  as a function of the transverse momentum  $p_T$  for the three charmed meson species  $D^{*+}$ ,  $D^+$  and  $D^0$  and four different modern state-of-the-art charm quark energy loss models in heavy-ion collisions. Details of BAMPS, Aichelin *et al.* and WHDG are described above in this section, details of Beraudo *et al.* are given in [84].

models described above. The predicted  $v_2$  is equal for the three meson species. One additional model not described above is drawn in labeled as "Beraudo et al., Langevin HTL". Details can be found in [84]. The predictions are calculated in the collision centrality range 30%-50% and a center-of-mass energy of  $\sqrt{s_{NN}} = 2.76$  TeV. The ultimate goal of this thesis is to compare the measured  $D^{*+}$  meson elliptic flow parameter  $v_2$  with these predictions. This comparison will be carried out and discussed in chap. 6, together with a comparison of existing predictions and measurements of the charmed meson nuclear modification factor  $R_{AA}$ .

## 3. LHC and ALICE

In this chapter a brief summary of the most important ingredients needed for the  $D^{*+} v_n$ -measurement is given: the machine, which accelerates and collides the lead ions, the Large Hadron Collider (LHC) and the tool, A Large Ion Collider Experiment (ALICE), which is dedicated to record these collisions and its recorded data are used for the results of this thesis.

### 3.1. LHC

The **L**arge **H**adron **C**ollider (LHC) is placed underground in a depth between 45 and 170 meters at the European organization for nuclear research (CERN) near Geneva. The capabilities of the LHC is to collide two counter rotating beams of protons, lead ions or protons and lead ions at unprecedented high energy and luminosity in a circular tunnel of 26.7 km circumference. The design luminosity of proton-proton collision is  $\mathcal{L} = 10^{34} \text{ cm}^2\text{s}^{-1}$  at a design center-of-mass energy of  $\sqrt{s} = 14 \text{ TeV}$ . Currently the proton-proton collisions are carried out at a decreased center-of-mass energy of  $\sqrt{s} = 8 \text{ TeV}$  due to a severe incident on September 20<sup>th</sup>, 2008 [85], 10 days after the first beam in the LHC. For lead-lead collisions the maximum energy is  $\sqrt{s_{\text{NN}}} = 5.5 \text{ TeV}$  per nucleon pair at a design luminosity of  $\mathcal{L} = 10^{27} \text{ cm}^2\text{s}^{-1}$ . The collisions of lead ions are carried out at a currently decreased center-of-mass energy of  $\sqrt{s_{\text{NN}}} = 2.76 \text{ TeV}$  per nucleon pair. During the lead-lead run in November 2011, whose data is used for this thesis, the luminosity reached a maximum value of  $\mathcal{L} = 0.5 \cdot 10^{27} \text{ cm}^2\text{s}^{-1}$  [86], which is only 50% below the design luminosity.

Before being injected into the LHC and accelerated to their maximum energies, the ions respectively protons are produced in dedicated sources and then pre-accelerated in a sequential procedure in various linear accelerators and synchrotrons. The lead ions are produced by heating up a piece of pure lead to a temperature of 500°C. Then their first electrons are stripped off in an electron cyclotron resonance source and bunched and accelerated by a radio frequency quadrupole. After selecting the charge state  $\text{Pb}^{27+}$  they are further accelerated in the accelerator LINAC3. The first accelerator in the acceleration sequence of the protons, which originate from a hydrogen tank source, is the linear accelerator LINAC2. The acceleration sequence of the two particle types after the LINACs is as follows:

- Lead ions: LEIR  $\rightarrow$  PS  $\rightarrow$  SPS  $\rightarrow$  LHC. On their way through the different accelerators the remaining electrons of the lead ions are stripped off using carbon foils. Their final charge configuration in the LHC is  $\text{Pb}^{82+}$ .
- Protons: PS-Booster  $\rightarrow$  PS  $\rightarrow$  SPS  $\rightarrow$  LHC.

A sketch including the meanings of the abbreviations of the synchrotrons and linear accelerators is shown in fig. 3.1. The figure also shows the positions of the four major

LHC experiments: ALICE, see sec. 3.2, **A Toroidal LHC Apparatus (ATLAS)** [87], **LHC beauty (LHCb)** [88] and the **Compact Muon Solenoid (CMS)** [89]. All four experiments are located at so called interaction points where the two LHC particle tubes intersect and

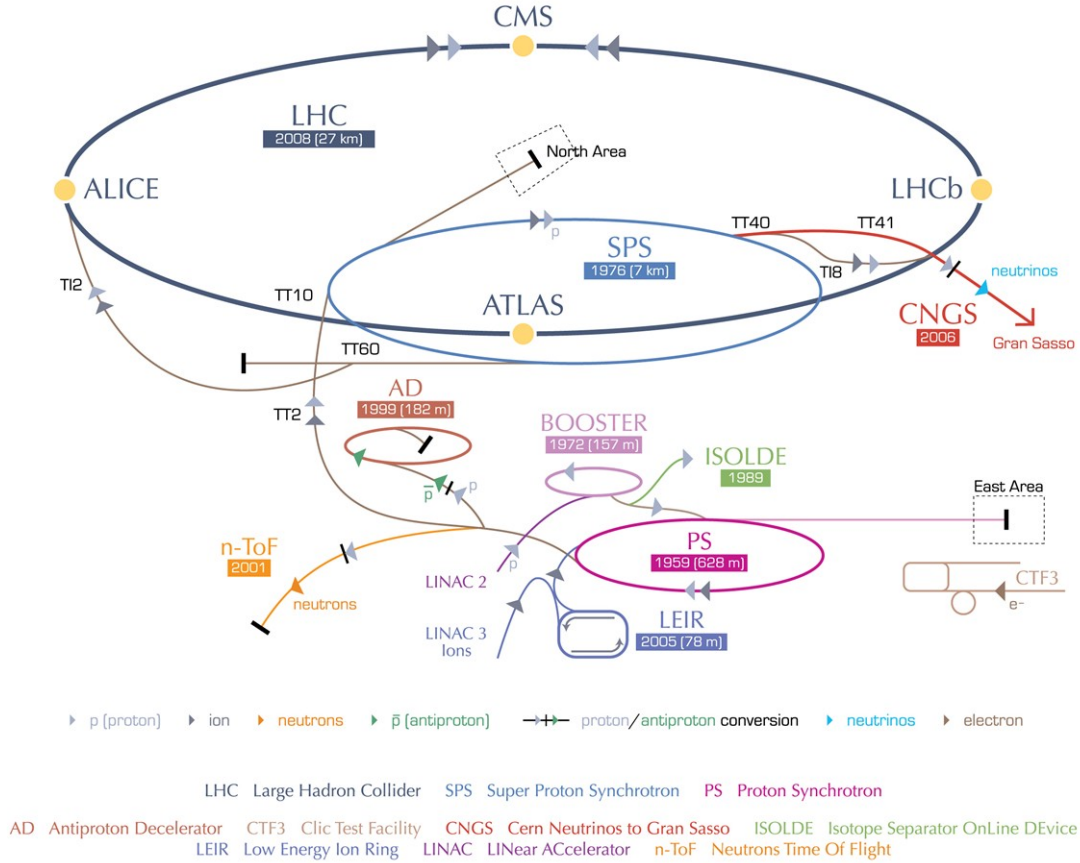


**Figure 3.1.:** Schematic sketch of the LHC with its four main experiments ATLAS, CMS, LHCb, ALICE. The accelerators used to accelerate the ions and protons up to their maximum energies are drawn in. This figure has been taken from [90].

collisions take place. In the following basic facts about the four experiments are given:

- 1. ATLAS:**  
The main goal of the ATLAS experiment is the detection of the Higgs-Boson and the search for physics beyond the standard model, e.g. supersymmetric particles and extra dimensions.
- 2. CMS:**  
The CMS is designed to analyze the nature of matter. In principle the CMS and the ATLAS detectors are built for the same purpose applying different detector technologies.
- 3. LHCb:**  
The LHCb experiment is built to study CP violation in B meson systems. LHCb

helps to understand why the universe appears to be composed almost entirely of matter but not antimatter.

#### 4. ALICE:

ALICE is the dedicated heavy-ion detector at the LHC. Details are given in sec. 3.2.

### 3.2. ALICE

The ALICE detector at the LHC has been designed and built to track charged particles in a wide transverse momentum range of  $0.1 \text{ GeV}/c < p_T < 100 \text{ GeV}/c$  in a high charged particle multiplicity environment provided by lead-lead collisions at a center-of-mass energy per nucleon pair up to  $\sqrt{s_{NN}} = 5.5 \text{ TeV}$ . In order to ensure good spatial tracking resolution, high granularity sub-detectors are used. Moreover, ALICE provides excellent particle identification capabilities over a wide momentum range by combination of the potential of its individual sub-detectors. The Inner Tracking System (ITS), the Time Projection Chamber (TPC) and the Time Of Flight detector (TOF) cover the central rapidity region, the so-called *central barrel*, and detect charged particles with a pseudorapidity of  $|\eta| < 0.9$ . The three detectors are the most important ones for this thesis and details about their performance and mode of operation will be addressed further below in this section. Other detectors, which are part of the central barrel are the Transition Radiation

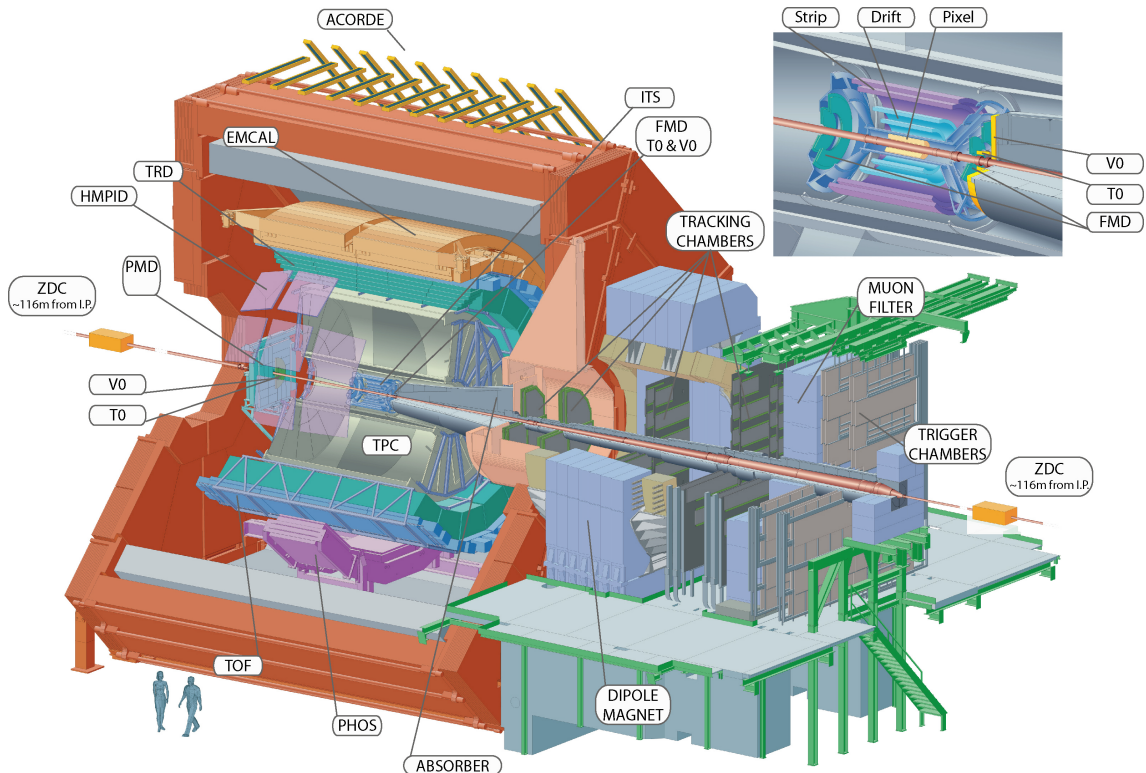


**Figure 3.2.:** The ALICE detector layout.

Detector (TRD), the High Momentum Particle Identification Detector (HMPID), the Pho-

ton Spectrometer and the Electromagnetic Calorimeter (EMCAL). A detailed description of their properties can be found in [91]. All sub-detectors are sketched and labeled in fig. 3.2, where the full ALICE detector is shown. The central barrel detectors are placed a solenoid, which provides a magnetic field of 0.5 T, uniform within  $\pm 2\%$ . The ALICE coordinate system is a right-handed Cartesian coordinate system with the z-axis pointing in the beam-direction away from the so-called *muon arm*. In the xy-plane, which is perpendicular to the z-axis, lie the x-axis and the perpendicular to it the y-axis. The ALICE coordinate system is depicted in fig. 3.3. The Muon Spectrometer placed in the muon arm is used to track and identify muons at forward rapidities. Details are given in [91]. There

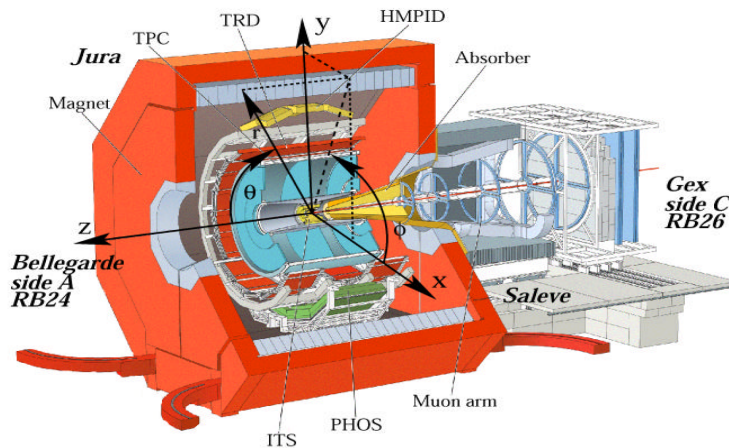


**Figure 3.3.:** Definition of the ALICE coordinate system.

are three more important detectors for this thesis placed not in the central barrel but each of them consisting of modules placed left and right with respect to the interaction point on the z-axis: the VZERO detector, the T0 detector and the Zero Degree Calorimeter (ZDC), see fig. 3.2. Their signals are exploited for triggering and event characterization, e.g. for event plane and centrality percentile determination. More details about them is given further below in this section. Finally, the remaining two detectors not located in the central barrel are the Photon Multiplicity Detector (PMD) and the Forward Multiplicity Detector (FMD), see fig. 3.2. Details are given in [91].

In the following a description of the relevant sub-detectors for this thesis is given. First the central barrel detectors are described starting from the detector closest to the beam pipe, i.e. the ITS, and finishing with the detector placed most distant from the beam pipe, i.e. the TOF detector. Finally, the detectors placed at forward rapidities are described in the following sequence: T0, VZERO, ZDC.

### 3.2.1. Inner Tracking System (ITS)

The ITS surrounds the beam pipe and is placed in the core of the central barrel of ALICE. It consists of 6 layers of high granularity detectors based on silicon detector technology. The first layer, part of the Silicon Pixel Detector (SPD) of the ITS, is installed at a radial distance of 3.9 cm to the interaction point. The layer with the largest radial distance of 43 cm from the interaction point is part of the Silicon Strip Detector (SSD). In between the

two ITS sub-detectors, the Silicon Drift Detector (SDD) is installed. A layout of the full ITS is shown in fig. 3.4. The total radiation length of the ITS is  $7.7\% \cdot X_0$  [92]. This value was minimized to keep multiple scattering of the tracks as low as possible. The alignment of the ITS was carried out with cosmic tracks with the ALICE magnet switched off, survey measurements and proton-proton collision data, see [93]. The excellently accomplished

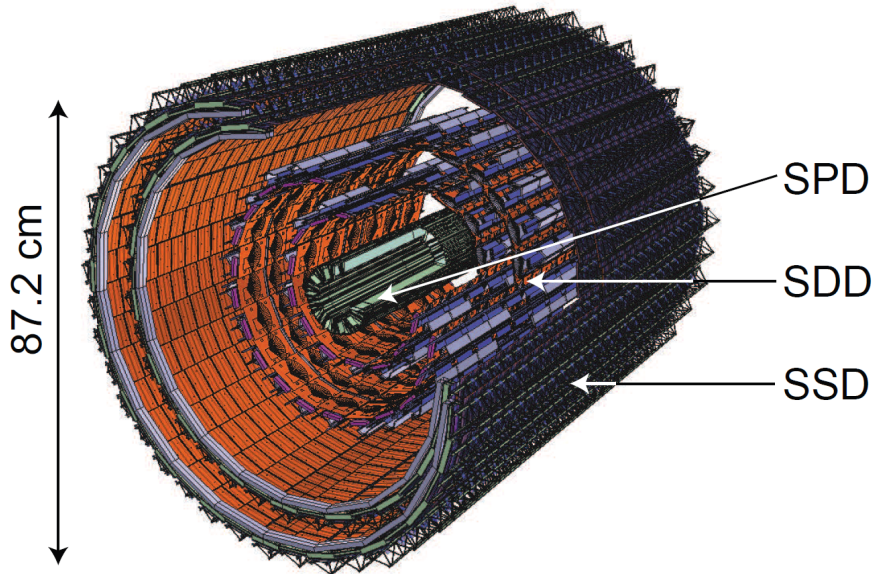


**Figure 3.4.:** Layout of the ITS detector. This figure has been taken from [92].

tasks of the ITS in the past years of proton-proton as well as lead-lead data taking are the following:

- Tracking of charged particles with a spatial resolution better than  $100 \mu\text{m}$  in the  $xy$ -plane down to  $p_T \approx 100 \text{ MeV}/c$  and in a pseudorapidity range of  $\eta < 0.9$  in a high multiplicity environment.
- Combined tracking together with the TPC, whereas the outermost layer of the SSD was optimized in terms of ITS-TPC track matching and cooling performance to ensure the required temperature stability and uniformity within the active volume of the TPC.
- Reconstruction of the primary vertex with a resolution better than  $20 \mu\text{m}$  in central lead-lead collisions.
- Reconstruction of secondary vertices of decayed charmed mesons and hyperons.
- Participation in the triggering scheme both in proton-proton and lead-lead collisions.

In the following, details about the three sub-detectors of the ITS are given.

### SPD

The SPD consists of two layers of silicon pixels with a pixel cell size of  $50 \mu\text{m}$  in the  $xy$ -plane and  $425 \mu\text{m}$  in  $z$ -direction. The first layer has an average radial distance of  $3.9 \text{ cm}$ , the second one of  $7.6 \text{ cm}$  to the interaction point. The pixels are grouped in sensor-matrices of  $256 \times 160$  pixels with an active area of  $12.8 \times 69.6 \text{ mm}^2$  per sensor and a thickness of  $200 \mu\text{m}$ . Each matrix is read out by 5 front end chips, each chip reading out a sub-matrix of  $256 \times 32$  pixels. The total number of pixels is  $9.8 \cdot 10^6$ . The measured spatial resolution during beam tests in the  $xy$ -plane was  $\sigma_{xy} = 12 \mu\text{m}$  and  $\sigma_z = 100 \mu\text{m}$  [92] in the beam direction. The SPD modules consisting of the sensors are arranged in a carbon-fiber space frame and the total radiation length a straight track perpendicular to the active volume has to cross when traversing the full SPD is about  $2\% \cdot X_0$ . The SPD is a fast detector and contributes to the trigger on minimum-bias events both in lead-lead and proton-proton collisions.

### SDD

The first layer of the SSD has an average radial distance of  $15 \text{ cm}$  and the second one of  $23.9 \text{ cm}$  to the interaction point. The SDD is built up of individual modules with an active area of  $7 \times 7.5 \text{ cm}^2$ . In total, 260 modules are placed inside the SDD. Each module is separated in two sub-modules by a central cathode, on which the highest voltage is applied. The drift electric field of the order of  $\approx 500 \text{ V/cm}$  is obtained by applying a gradually decreasing voltage on the 291 drift cathodes for each sub-module in direction to the collection anodes. When a charged particle crosses one of these modules the coordinate in the  $xy$ -plane of the ALICE coordinate system is determined by the drift time of the electrons to the collecting anodes. This situation is depicted in fig. 3.5. The spatial resolution of this coordinate is  $\sigma_{xy} = 35 \mu\text{m}$  [92]. The other coordinate along the beam

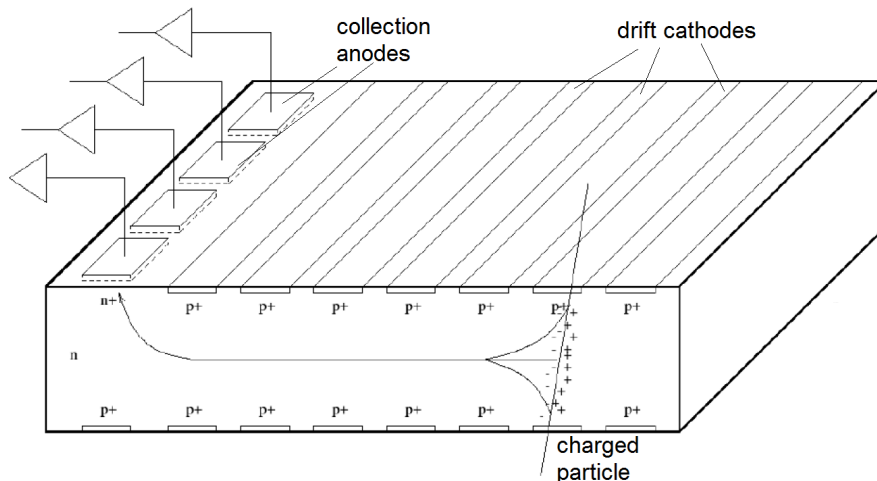


**Figure 3.5.:** The working principle of a SDD module. The traversing charged particle, the drift cathodes and the collection anodes collecting the produced electrons are drawn in. This figure has been taken from [94].

direction is given by the centroid of the collected charge distribution on a fraction of the  $2 \times 256$  anodes per module. The resolution is  $\sigma_z = 25 \mu\text{m}$  [92] in the  $z$ -direction. The total



gas atoms. The created electrons drift in the electric field with a strength of  $0.4 \text{ kV/cm}$  to the endcaps, where the cathode plane is set to a voltage of  $0\text{V}$ . At the TPC endcaps  $2 \times 36$  multi-wire proportional chambers with cathode pad readout are installed. They are grouped in two circles around the beam-axis, whereas the chambers closer to the beam line are called Inner Read Out Chambers (IROCs) and the ones farther away from the beam line Outer Read Out Chambers (OROCs). One of them is labeled as "IROC" and another one as "OROC" in fig. 3.7, where the fully assembled TPC before installation in

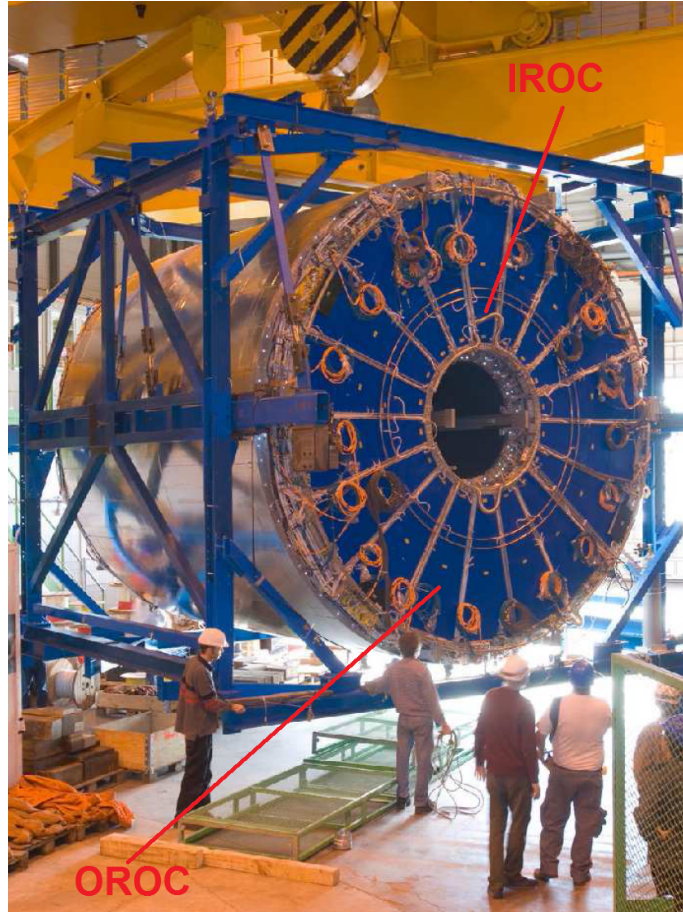


**Figure 3.7.:** The fully assembled TPC before installation in the ALICE cavern. An Inner Read Out Chamber (IROC) and an Outer Read Out Chamber (OROC) placed at one of the TPC endcaps are labeled as OROC respectively IROC. This figure has been taken from [96].

the ALICE cavern is shown. The IROCs and OROCs are filled with the same gas as the active volume of the TPC. When the electrons reach the chambers after a maximum drift time of about  $90 \mu\text{s}$  an avalanche process inside the chambers occurs and the signal is read out on the pad plane of the chambers. The avalanche process is triggered by the voltage of  $1.5 \text{ kV}$  between the anode plane and cathode plane depicted in fig. 3.6. The gating plane wires shown in this figure are set to a negative voltage only if one wants to read out the TPC events. In case the TPC is not delivering data, the applied voltage is positive, the gate is "closed" and the electrons do not reach the cathode plane. This is done to prevent positive ions produced during the avalanche process to drift back to the central

electrode and cause field distortions. The coordinate of the space points of the tracks along the beam axis is given by the time the produced electrons need to drift to the read out chambers. As the drift speed is dependent on the temperature in the TPC, it must be kept constant on a level of  $\pm 0.1$  K. For this purpose a dedicated system of heat shields placed at the inner and outer radii and cooling of the Front End Electronics (FEE) on the endcaps is installed. The other two coordinates in the xy-plane are given by the charge distribution on the mosaic pad plane of the read out chambers, with a total number of read out channels of 557.568. The spatial resolution in the xy-plane is  $\sigma_{xy,in} = 1100 \mu\text{m}$  [96] at the inner radius and  $\sigma_{xy,out} = 800 \mu\text{m}$  [96] at the outer radius. The spatial resolution along the z-axis is  $\sigma_z = 1250 \mu\text{m}$  [96].

### 3.2.3. Time Of Flight (TOF)

The TOF detector is organized in 18 modules placed in a cylindrical shell around the beam line with an inner radius of 3.7 m. It provides a flight time measurement of particles in the pseudorapidity range  $|\eta| < 0.9$  from the primary vertex to its modules. The start time for the measurement is provided by the T0 detector addressed below as the next sub-detector. This way the relativistic velocity  $\beta$  of the detected particles is determined and the particle species are determined. Details of this technique are given in chap. 4, sec. 4.2. The cores of the modules are Multigap Resistive Plate Chambers (MRPC). These chambers, which are filled with gas composed of 90% of  $\text{C}_2\text{H}_2\text{F}_4$ , 5% of  $\text{C}_4\text{H}_{10}$  and 5% of  $\text{SF}_6$ , are equipped with a total of 1638 double gap MRPC strips shown in fig. 3.8 (left). The working principle of the strips is shown in fig. 3.8 (right). A charged particle crosses the strip and ionizes the gas in the gaps between the intermediate plates between the anode and the cathode,

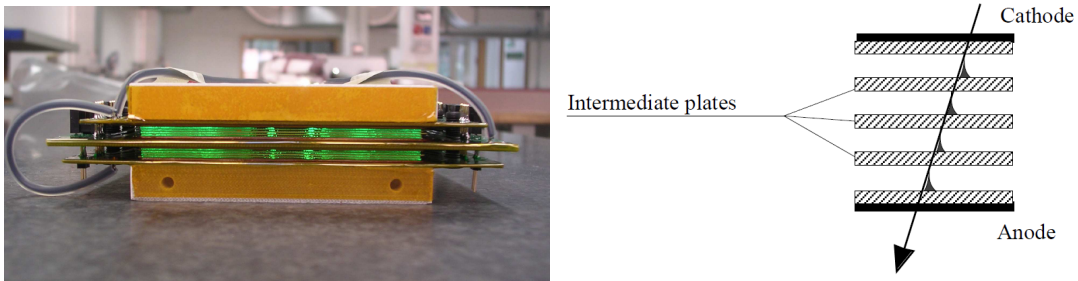


**Figure 3.8.:** (left) Side view of a TOF a double gap MRPC strip. This figure has been taken from [96]. (right) Sketch of the working principle of a a double gap MRPC strip. This figure has been taken from [97].

which are under high voltage. The produced primary electrons trigger an avalanche of secondary electrons and for a short time a current pulse flows between neighboring plates, which is then read out by the electronics. The signal is the analogue sum of the signals of all gaps. The strips are segmented in individual double gap MRPC pads. In the full TOF 157.248 pads are installed. For the TOF detector this kind of detector technique was chosen due to the following properties of the MRPC pads:

- operation at atmospheric pressure and with high gas gain possible;
- simple construction and usage of commercially available materials;

- intrinsic time resolution better than 40 ps [97].

The TOF time resolution including all contributions, e.g. the contribution from the start time measurement performed by the T0 detector, is  $\sigma_{\text{time}} = 85$  ps in lead-lead collisions.

### 3.2.4. Other non-central barrel detectors

#### T0 detector

The T0 detector consists of two sub-detectors placed 72.7 cm away from the interaction point at the C-side (T0-C) and 375 cm away from the interaction point at the A-side (T0-A). T0-C covers a pseudorapidity range of  $-3.28 < \eta < -2.97$  and T0-A a pseudorapidity range of  $4.61 < \eta < 4.92$ . For orientation of the A- and C-side with respect to the interaction point see fig. 3.3. In each sub-detector an array of 12 Cherenkov counters is installed. The time resolution of the T0 detector is  $\sigma_{\text{time}} = 50$  ps and therefore it is used for the start time measurement provided for the time of flight measurement of tracks with the TOF detector.

#### VZERO detector

The VZERO detector consists of two sub-detectors placed 90 cm away from the interaction point at the C-side (VZERO-C) and 340 cm away from the interaction point at the A-side (VZERO-A). VZERO-C covers a pseudorapidity range of  $-3.7 < \eta < -1.7$  and VZERO-A a pseudorapidity range of  $2.8 < \eta < 5.1$ . Both sub-detectors are each built up of 32 scintillators arranged in 4 rings, each ring equipped with 8 scintillators each one covering an azimuthal angle of  $45^\circ$ . Each scintillator is connected to wave-length shifting fibres, which are connected to photomultipliers. Figure 3.9 (left) shows the front view of the VZERO-C

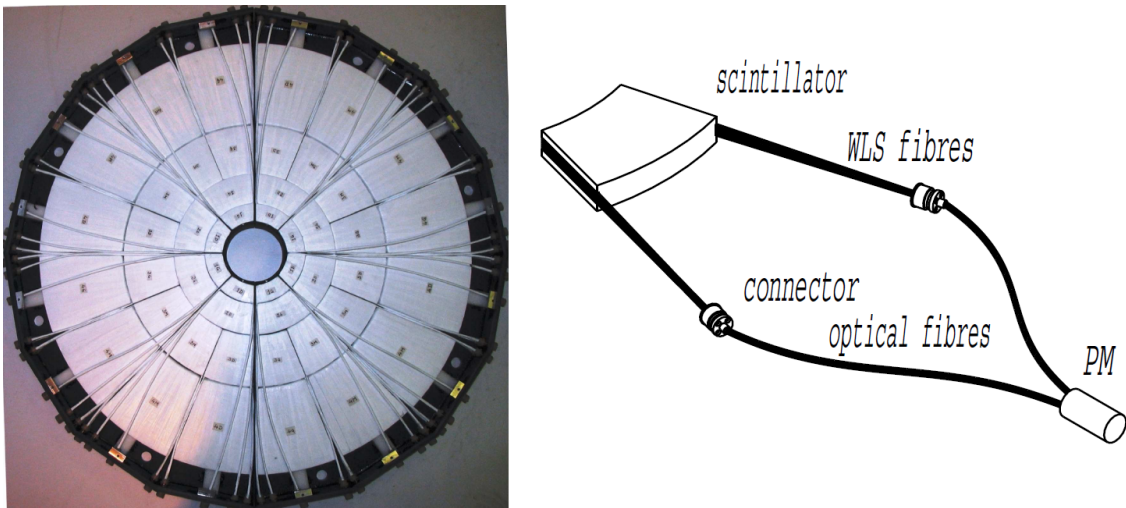


**Figure 3.9.:** (left) Front view of the VZERO-C detector before installation in the ALICE cavern. (right) Schematic design of the VZERO-C detection elements. This figure has been taken from [96].

detector before installation in the ALICE cavern. Figure 3.9 (right) shows the schematic design of the VZERO-C detection elements. The VZERO detector provides signals for the Level 0 minimum bias and centrality trigger decision addressed in sec. 3.2.5. Moreover,



ultra-peripheral collisions.

Moreover, the timing information of the ZDC are used to remove parasitic lead-lead collisions, where the colliding ions are displaced with respect to their nominal position in their bunch. More details are given in the next section.

### 3.2.5. Trigger and event selection

The system, which processes the trigger signals from various ALICE sub-detectors during the data-taking, is the Central Trigger Processor (CTP). There are 3 stages of trigger levels, called Level 0 (L0), Level 1 (L1) and Level 2 (L2). Only the fast ALICE sub-detectors SPD, VZERO, T0 and the muon trigger contribute to the L0-signal, which arrives  $1.2 \mu\text{s}$  after the lead-lead collision. In order to trigger on so-called minimum-bias lead-lead events, i.e. lead-lead events with a totally random collision geometry with minimum-bias from the trigger detector(s) side, the signals in both VZERO detectors (VZERO-A and VZERO-C) were exploited during the lead-lead data-taking in 2011. A signal in both sub-detectors was required and the trigger type is accordingly called "VZERO-AND". The L1 trigger signal arrives  $6.5 \mu\text{s}$  after the L0 signal and collects the information of the slower sub-detectors. After further  $88 \mu\text{s}$  the L2 trigger signal finally arrives. In the time between L0 and L1 and L1 and L2 the sub-detectors contributing to the trigger level decisions have time to process their signals and send their decision to the CTP. This yields a variety of possible trigger classes depending on the physical interest. More details can be found in [91, 96]. In case of the minimum-bias trigger scheme only the decision from the VZERO at L0 was relevant. The L1 and L2 decision was always positive in the data used for the  $D^{*+} v_n$ -analysis. In addition to the requirement of a signal in both VZERO sub-detectors an upper and lower threshold on the sum of the VZERO-amplitudes of both VZERO detectors was applied. This was done to enhance the number of semi-central events in the centrality percentile range 10-53%. This type of trigger was accordingly named as semi-central-trigger. Further event cuts were applied offline, i.e. after the data was written and reconstructed. Event reconstruction is addressed in sec. 3.2.6.

### Offline event quality selections

One of the offline event quality cuts was a selection on the arrival times of the detected particles in the VZERO detectors. Here the distribution of the arrival times of particles stemming from beam-beam and beam-gas collisions is different. Beam-gas collisions are collisions of the ions within the beam and remaining gas in the beam pipe, which are background events and are removed by those cuts. The timing information in the ZDC was used, either, in order to reject events, where the colliding ions were displaced with respect to their nominal position in their bunch. These collisions occurred then displaced from the nominal vertex position. These collisions are normally removed by a vertex position cut of  $\pm 10 \text{ cm}$  on the z-axis, which was applied as another quality cut. However, those collisions could give rise to fake vertices due to the algorithm which reconstructs the vertices assuming that particles are coming from the area around the nominal vertex position. The correlation of the measured sum  $t_A + t_C$  and difference  $t_C - t_A$  of the arrival times of the spectator nucleons at the A-side, respectively the C-side using the ZDC is shown in fig. 3.11. Only events with the timing properties encircled with the black line were selected.

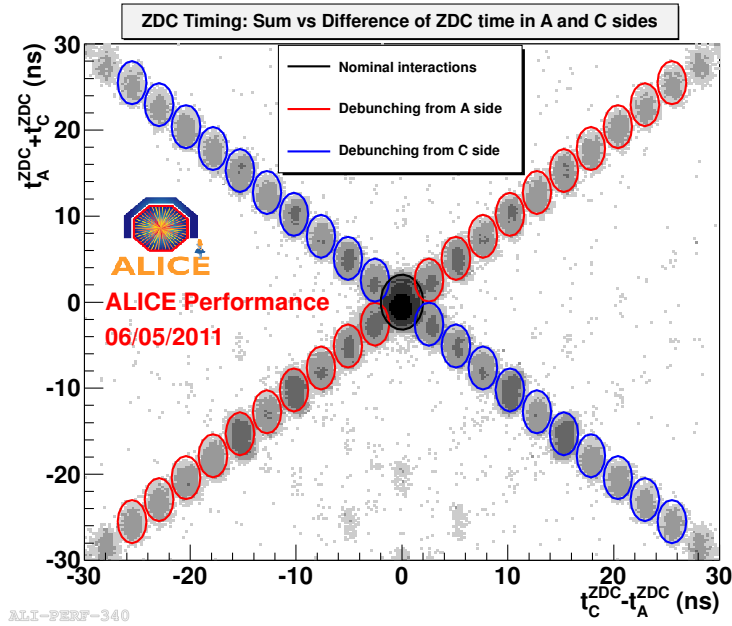


**Figure 3.11.:** Correlation of the measured sum  $t_A + t_C$  and difference  $t_C - t_A$  of the arrival times of the spectator nucleons at the A-side and the C-side using the ZDC.

### Offline collision centrality selection

The selection on the collision centrality in percentiles of the hadronic cross section, see chap. 2, sec. 2.2, for the  $D^{*+} v_n$ -analysis was performed by using distribution of the sum of the amplitudes of both VZERO sub-detectors. The centrality percentile bin 30-50% to measure the  $D^{*+} v_n$  was chosen because of details that are given and explained in chaps. 4, 5. The distribution of the VZERO amplitude, which is proportional to the number of particles hitting the VZERO detectors, was fitted with [98] a function based on:

- the Glauber Monte-Carlo Model [4]. This model provides a connection between the quantities  $N_{\text{part}}$ ,  $N_{\text{coll}}$ ,  $T_{\text{AA}}$  and the fraction of the hadronic cross section, see chap. 2, sec. 2.2 and [4].
- A function, which parameterizes the number of independent sources, the "ancestors", emitting particles as a function of  $N_{\text{part}}$  and  $N_{\text{coll}}$ :

$$N_{\text{ancestors}} = f \cdot N_{\text{part}} + (1 - f) N_{\text{coll}} \quad (3.1)$$

This function is inspired by the fact that particle production in nucleus-nucleus collisions is described by two components, namely by soft and hard interactions. The soft interactions produce particles with an average multiplicity proportional to  $N_{\text{part}}$  and the hard interactions proportional to  $N_{\text{coll}}$ . The parameter  $f$  is kept free in the fit.

- A negative binomial probability density distribution (NBD) to sample the multiplic-

ity of an event:

$$P_{\mu,k}(n) = \frac{\Gamma(n+k)}{\Gamma(n+1)\Gamma(k)} \quad (3.2)$$

with  $n$  being the number of measured hits in the VZERO detector per ancestor,  $\mu$  the mean number of hits and  $k$  controls the width of the NBD distribution. This sampling is done  $N_{\text{ancestors}}$  times for every Glauber Monte-Carlo event for a set of parameters of  $\mu$  and  $k$ .

A fit of the formula presented in eq. 3.1 convoluted with the formula presented in eq. 3.2 to the measured distribution of the VZERO-amplitude is shown in fig. 3.12. The bins for the collision centrality in percentiles of the hadronic cross section are drawn. This

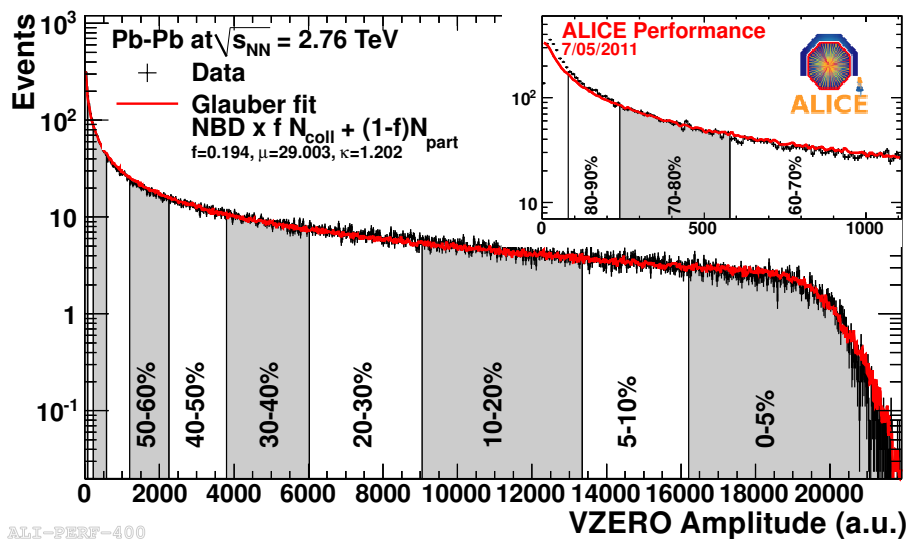


**Figure 3.12.:** Collision centrality determination in percentiles of the hadronic cross section using a fit of a function based on the Glauber Monte-Carlo Model [4] to the measured VZERO amplitude distribution. For more details see text.

procedure provides a direct estimate of the collision centrality percentile for every event. The number of events from the 2011 lead-lead run used for the  $D^{*+} v_n$ -measurement after the event quality cuts and centrality selection is  $9.5 \cdot 10^6$ . Other available methods e.g. based on counting the number of tracks in the SPD or the TPC or studying the deposited energy distribution of spectator nucleons in the ZDC have been checked against the VZERO-method and found to be consistent. Details are given in [98].

### 3.2.6. Event Reconstruction

The event reconstruction on recorded and simulated data starts from a first estimate of the primary collision vertex using the signals of the SPD detector. These signals are stored in *clusters*, which are groups of digitized signals of all ALICE sub-detectors named as *digits*. The digits are the raw data of an event. In case of real collision data those digits are recorded by the ALICE Data AcQuisition System (DAQ), which merges the event information from the individual ALICE sub-detectors triggered by the trigger scheme described in sec. 3.2.5. In case of simulated collision data the digits are the result of simulated

hits in the active volumes of the detectors. These hits are generated by charged-particle trajectories, whereas the momentum and angle distributions of the charged particles are simulated with dedicated lead-lead and proton-proton collision particle generators. In order to calculate efficiencies and study the reconstruction performance of the  $D^{*+}$  in lead-lead collisions, a Hijing [99] minimum-bias lead-lead particle generator with on-top injected charm-signals using the proton-proton particle generator PYTHIA [100–102] was used. The performance of the  $D^{*+}$  reconstruction using these simulations is addressed in chap. 4, sec. 4.1. The flow starting from the data taking respectively from the generation of the particles using Monte-Carlo particle generators to the creation of clusters out of digits is shown in a flow-chart in fig. 3.13. After a first estimate of the primary vertex

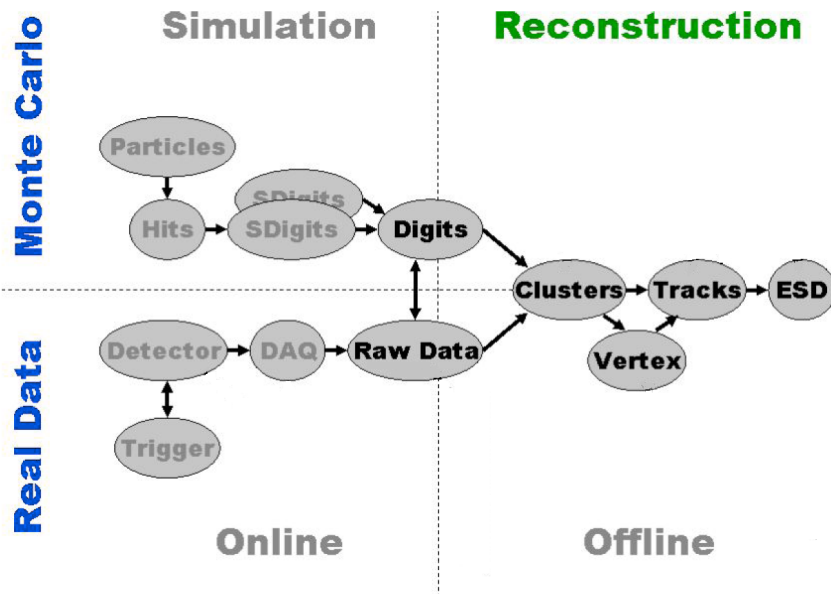


**Figure 3.13.:** A Flow-chart demonstrating the road from data taking, respectively from the generation of the particles using Monte-Carlo particle generators, to the creation of clusters out of digits and then the subsequent reconstruction procedure. This figure has been taken from [103].

using SPD clusters, TPC tracks are constructed out of TPC clusters and fitted towards this first estimated vertex position. The tracking procedure is based on the Kalman filter technique [104], which takes into account multiple scattering and energy loss. When the tracks reach the inner radius of the TPC, the track finding algorithm is called for the ITS. TPC tracks are matched with hits in the SSD and ITS clusters are assigned to the tracks coming from the TPC. Figure 3.14 (right) shows the track prolongation efficiency from the TPC to the ITS as function of  $p_T$  in lead-lead collisions for real data (filled markers) and Hijing [99] Monte-Carlo simulations with a full ALICE detector description (open markers). Two cases are considered: at least 2 ITS hits are required with at least one hit in the SPD (red markers) and at least 2 ITS hits with no further requirements (black markers). The prolongation efficiency is about 95% in the full  $p_T$ -range in the latter case (without the SPD hit requirement) and about 80% in the former case (with the SPD hit requirement). After all the track candidates from the TPC are assigned their clusters in the ITS, a special ITS stand-alone tracking procedure is performed on the remaining ITS clusters.

This procedure tries to recover the tracks that were not found in the TPC because their  $p_T$  was too low to reach the TPC, due to dead zones in the TPC or decays. Then the tracks are refitted backward again, first in the ITS and then in the TPC. As next step, tracks are prolonged and matched to the outer detectors, namely TRD, TOF, HMPID, PHOS and EMCAL and particle identification information are added to the tracks. For this thesis only the PID information from TOF (and TPC) are used. As final step the tracks are propagated to the primary vertex and the vertex position is determined out of the reconstructed tracks. More details can be found in [105]. Figure 3.14 (left) shows the relative  $p_T$ -resolution of TPC-ITS combined tracks as a function of  $p_T$ . It is better than

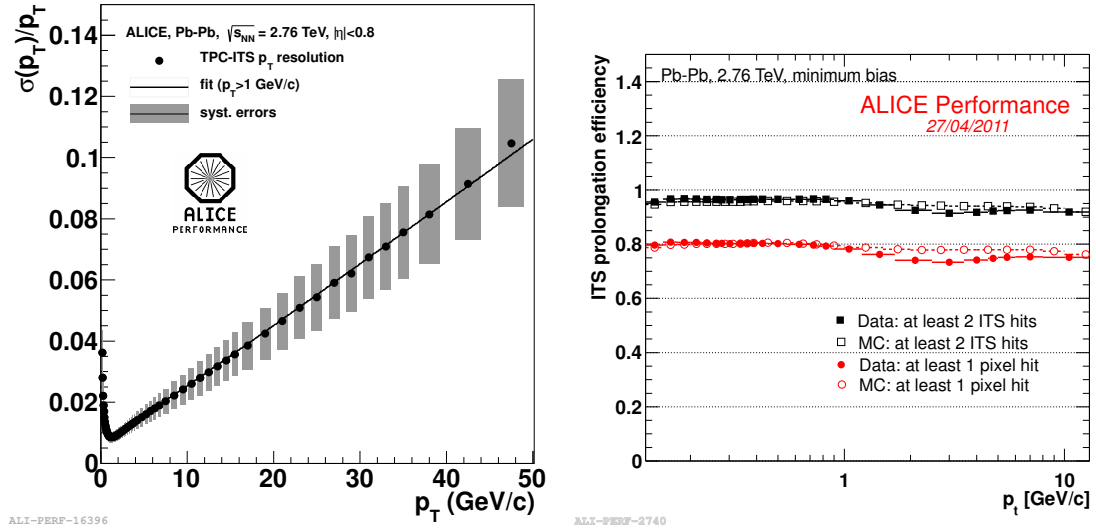


**Figure 3.14.:** (left) Relative  $p_T$ -resolution of TPC-ITS combined tracks as a function of  $p_T$ . (right) Track prolongation efficiency from the TPC to the ITS as function of  $p_T$  in lead-lead collisions for real data (filled markers) and Hijing [99] Monte-Carlo simulations with a full ALICE detector description (open markers). Two cases are considered: at least 2 ITS hits are required with at least one hit in the SPD (red markers), at least 2 ITS hits are required with no further requirements (black markers).

4% for tracks with a transverse momentum of  $p_T < 10$  GeV/c. The relative resolution is best at a transverse momentum of  $p_T \approx 1.5$  GeV/c and deteriorates for larger and smaller transverse momenta. The worsening at low  $p_T$  is due to increasing multiple scattering in the active detector material. On the other hand, the worsening with increasing  $p_T$  is due to the increasing radius of the track helix. At high  $p_T$  the tracks are almost straight and the error of the measurement of the bending becomes large.

The relevant information for the user analysis of the event is stored in so-called Event Summary Data (ESD), see fig. 3.13. Out of the ESDs a more user-friendly and reduced data format, the Analysis Object Data (AOD), is created. The  $D^{*+}$  reconstruction procedure from single tracks is performed on these AODs, which is described in detail in chap. 4.

## 4. $D^{*+}$ reconstruction strategy

The  $D^{*+}$  and the  $D^{*-}$  mesons are reconstructed in the strong interaction decay channel  $D^{*+} \rightarrow D^0\pi^+$ , respectively  $D^{*-} \rightarrow \overline{D^0}\pi^-$  by combination of the charged pion, in the following referred to as *soft pion* due its low momentum as will become clear further below, and the neutral  $D^0$  meson at the reconstructed primary vertex. From now on the symbol  $D^{*+}$  stands for both  $D^{*+}$  and  $D^{*-}$  and the decay channel  $D^{*+} \rightarrow D^0\pi^+$  for both  $D^{*+} \rightarrow D^0\pi^+$  and  $D^{*-} \rightarrow \overline{D^0}\pi^-$ .

The soft pion deposits charge in the ITS and TPC and is thus traceable within the detectors, but the  $D^0$  has no charge and in addition decays before any active detector material. Its displaced secondary vertex is reconstructed from its charged decay daughters. For this purpose the weak-interaction decay channel  $D^0 \rightarrow K^-\pi^+$ , respectively  $\overline{D^0} \rightarrow K^+\pi^-$  is used. In the following the notation  $D^0 \rightarrow K^-\pi^+$  stands for both  $D^0 \rightarrow K^-\pi^+$  and  $\overline{D^0} \rightarrow K^+\pi^-$ . A sketch showing of the topology of the decay channel  $D^{*+} \rightarrow D^0\pi^+$  and the subsequent decay  $D^0 \rightarrow K^-\pi^+$  is shown in fig. 4.1. Important cut variables such as the pointing angle

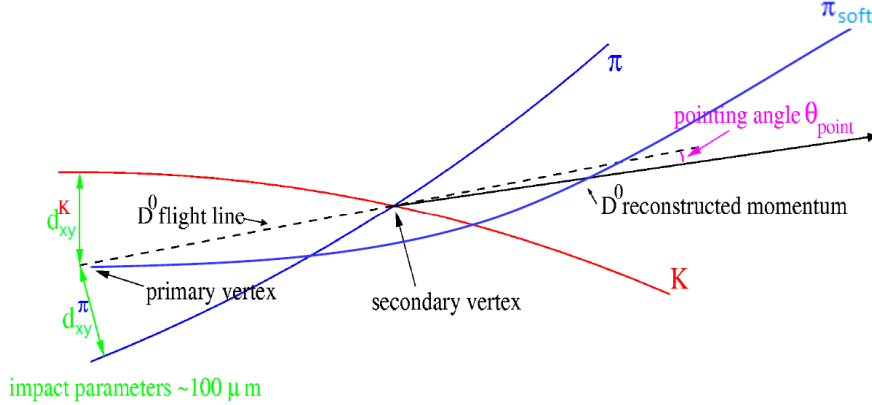


**Figure 4.1.:** Sketch of the topology of the decay channel  $D^{*+} \rightarrow D^0\pi^+$ . The  $D^{*+}$  decays at the primary vertex and the displaced vertex of the  $D^0$  decaying in the channel  $D^0 \rightarrow K^-\pi^+$  is reconstructed. This figure has been taken from [49].

$\theta_{\text{point}}$ , the impact parameters to the primary vertex  $d_{xy}^K$  and  $d_{xy}^\pi$ , which are defined and discussed in detail in sec. 4.1, are depicted. The decay parameters and invariant masses of the involved particles of both channels,  $D^0 \rightarrow K^-\pi^+$  and  $D^{*+} \rightarrow D^0\pi^+$ , are listed in tab. 4.1. In the following, whenever the PDG [10] invariant mass of a charged pion  $m_\pi$ , of a charged kaon  $m_K$  or the invariant masses of the  $D^0$  as well as of the  $D^{*+}$  are mentioned, the values can be looked up in tab. 4.1.

The mass difference of the  $D^{*+}$  and the  $D^0$  is  $m(D^{*+}) - m(D^0) = 145.421 \pm 0.010 \text{ MeV}/c^2$  [10], which is only  $5.85 \text{ MeV}/c^2$  larger than the rest mass of a pion  $m_\pi$ . Therefore the decay daughters of the  $D^{*+}$  in this particular channel acquire a very small amount of kinetic

#### 4. $D^{*+}$ reconstruction strategy

Particle	mass [MeV/ $c^2$ ]	$c\tau$ [ $\mu m$ ]	used dec. channel	branching ratio
$D^0$	$1864.86 \pm 0.13$	$122.9 \pm 0.3$	$D^0 \rightarrow K^- \pi^+$	$(3.88 \pm 0.05)\%$
$D^{*+}$	$2010.28 \pm 0.13$	$(2.1 \pm 0.5) \cdot 10^{-6}$	$D^{*+} \rightarrow D^0 \pi^+$	$(67.7 \pm 0.5)\%$
		$\leftrightarrow \Gamma = (96 \pm 22) \text{ keV}$		
$\pi^\pm$	$139.57018$ $\pm 0.00035$	$(7.805 \pm 0.001) \cdot 10^6$	-	-
$K^\pm$	$493.677$ $\pm 0.016$	$(3.712 \pm 0.006) \cdot 10^6$	-	-

**Table 4.1.:** The invariant masses, the mean proper decay lengths  $c\tau$  and the branching ratios of the involved particles of the decay channels  $D^0 \rightarrow K^- \pi^+$  and  $D^{*+} \rightarrow D^0 \pi^+$  used for the  $D^{*+}$  reconstruction. In case of the  $D^{*+}$  the decay width  $\Gamma$  of the decay  $D^{*+} \rightarrow D^0 \pi^+$  is given in addition to the mean proper decay length  $c\tau$ . The values have been taken from [10].

energy when the  $D^{*+}$  is at rest. Practically all of the kinetic energy of the  $D^0$  and the soft pion comes from the kinetic energy of the  $D^{*+}$ . Because of the low transverse momentum of the soft pion and  $D^0$  it is challenging to reconstruct the  $D^{*+}$  at low transverse momentum and the measurement of the  $D^{*+}$ - $v_2$  and  $v_3$  addressed in chap. 5 thus starts at  $p_T = 2 \text{ GeV}/c$ . In case of a  $D^0$  at low  $p_T$  the secondary vertex is very close to the primary vertex. This fact makes it impossible to separate the secondary decay vertex of the  $D^0$  from the primary vertex, whereas the displaced secondary vertex of charmed hadrons is the key ingredient for charmed hadron measurements performed by ALICE. The tracking and reconstruction efficiency in the ITS and TPC of low  $p_T$  pions with a  $p_T$  below  $p_T = 100 \text{ MeV}/c$  in case of the ITS and a  $p_T$  below  $p_T = 150 \text{ MeV}/c$  in case of the TPC in a Pb-Pb environment is practically zero and therefore these pions cannot be detected. The minimum  $p_T$ -reach for the TPC is given by the curvature of the charged pions in the magnetic field. The minimum  $p_T$ -reach for the ITS is given by the increasing energy loss with the consequent absorption in the material at low pion momentum as well as increasing multiple scattering with decreasing momentum, which restricts the ITS tracking to  $p_T > 100 \text{ MeV}/c$ . On the other hand, the advantage of the low Q-value of the decay channel  $D^{*+} \rightarrow D^0 \pi^+$  is that the phase-space is small. As we will see below, the identification of the  $D^{*+}$  is based on calculation of the variable  $M(K\pi\pi) - M(K\pi)$  using reconstructed tracks in one event. In order to calculate this variable, track triplets and associated track doublets are built by combining the tracks and then the invariant masses of a charged pion, respectively of a charged kaon are assigned to the tracks. Then the invariant masses of these triplets  $M(K\pi\pi)$  and associated doublets  $M(K\pi)$  are calculated. The amount of combinatorial background depends on the number of triplets and the associated doublets not stemming from  $D^{*+} \rightarrow D^0 \pi^+$  decays, for which the result of the calculated variable  $M(K\pi\pi) - M(K\pi)$  equals the  $m(D^{*+}) - m(D^0)$  value from the PDG [10] within the detector resolution  $\Delta(M(K\pi\pi) - M(K\pi))$ . The mentioned small phase-space of the decay channel  $D^{*+} \rightarrow D^0 \pi^+$  with the value for  $m(D^{*+}) - m(D^0)$  being close to the phase space boundary  $m_\pi$  keeps the combinatorial background on a reasonable level. Moreover, as we will see in sec. 4.3, the detector resolution  $\Delta(M(K\pi\pi) - M(K\pi))$  is mainly determined by the momentum resolution of the soft pion of the  $D^{*+} \rightarrow D^0 \pi^+$  decay. The momentum resolution contribution of the decay daughters of the  $D^0 \rightarrow K^- \pi^+$  decay to the total resolution  $\Delta(M(K\pi\pi) - M(K\pi))$  is small. The reason for this behavior

is the small mass difference of  $D^{*+}$  and  $D^0$  and the small momentum of the soft pion with respect to the momenta of the decay daughters of the  $D^0$ . In the following, the strategy to suppress the  $D^{*+}$ -background built up of randomly combined tracks using topological analysis cuts and  $D^{*+}$  decay daughter species identification using the TOF and TPC detectors is presented. The chapter closes with a section describing the  $D^{*+}$  yield extraction in real Pb-Pb-collision data using the  $\Delta M = M(K\pi\pi) - M(K\pi)$  mass difference method.

## 4.1. Analysis Cuts

In order to reconstruct the three decay daughters of the decay channel  $D^{*+} \rightarrow D^0\pi^+$  and the subsequent decay channel  $D^0 \rightarrow K^-\pi^+$ , a combined ITS-TPC tracking procedure based on the Kalman-filter [104] is performed event-by-event as described in chap. 3, sec. 3.2.6. The information whether the TPC and ITS backward refit failed or not is stored in the track parameter information. Another important track parameters stored at the distance of closest approach (DCA) in the xy-plane to the primary vertex are the momentum vector  $\vec{p} = (p_x, p_y, p_z)$ , number of clusters in the TPC and ITS, the pseudorapidity  $\eta$  and the impact parameters to the primary vertex  $d_{xy}$ , in the xy-plane and  $d_z$ , in the plane perpendicular to the xy-plane. For definition of the ALICE coordinate system see fig. 3.3 in chap. 3, sec. 3.2. The impact parameter  $d_{xy}$  is defined as:

$$d_{xy} = q \left[ R - \sqrt{(x_C - x_V)^2 + (y_C - y_V)^2} \right] \quad (4.1)$$

with  $R$  being the radius of the track curve, which is a circle,  $(x_C, y_C)$  the coordinates of the center of the circle in the xy-plane and  $(x_V, y_V)$  the coordinates of the primary vertex in the xy-plane. The quantity  $q$  is the charge of the track. With this representation the  $d_{xy}$  has a sign, which will be important later in this section when discussing the topological cut calculations based on the  $D^0$  secondary vertex determination. The impact parameter  $d_z$  is defined as:

$$d_z = z_{\text{track}} - z_V \quad (4.2)$$

with  $z_{\text{track}}$  being the z-coordinate of the track at the DCA in the xy-plane and  $z_V$  the z-coordinate of the primary vertex. The resolution  $\sigma(d_{xy,z})(p_T)$  of  $d_z$  as a function of the track transverse momentum  $p_T$  in PbPb-collisions at  $\sqrt{s_{\text{NN}}} = 2.76$  TeV of combined TPC-ITS tracks is shown in fig. 4.2 (left) and the one of  $d_{xy}$  in fig. 4.2 (right). The black data points represent the resolution obtained using real data and the red data points using Hijing Monte-Carlo simulations [99] with a full ALICE detector description. The resolution of  $d_{xy}$  is better than  $50 \mu\text{m}$  for tracks with  $p_T > 2$  GeV/ $c$  and the resolution of  $d_z$  is in general poorer. Therefore many cut variables, as we will see further below, are calculated in the xy-plane in order to obtain better resolution. The resolution of most of these cut variables depends on the spatial tracking resolution, which is better in the xy-plane as demonstrated in fig. 4.2. Before building  $D^0$  candidates out of the single tracks and then  $D^{*+}$  candidates out of  $D^0$  candidates and the soft pion candidates, the following single track cuts are applied to the tracks:

For the  $D^0$  daughters:

- required ITS refit success;

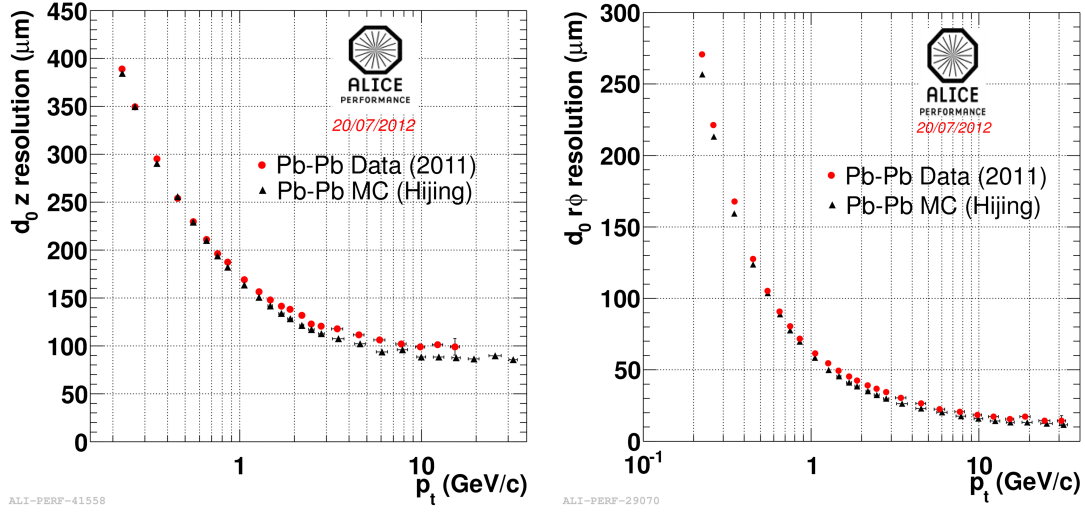


**Figure 4.2.:** Resolution  $\sigma_{d_{xy,z}}(p_T)$  of  $d_z$  (left) as a function of the track transverse momentum  $p_T$  in PbPb-collisions at  $\sqrt{s_{NN}} = 2.76$  TeV of combined TPC-ITS tracks and the one of  $d_{xy}$  (right). The black data points represent the resolutions using real data and the red data points using Hijing Monte-Carlo simulations [99] with a full ALICE detector description.

- at least 2 clusters in the ITS;
- at least 1 cluster in one of the two layers of the SPD;
- required TPC refit success.;
- at least 70 clusters in the TPC;
- an impact parameter range of  $0.0025 \text{ cm} < |d_{xy}| < 1.0 \text{ cm}$  for tracks with  $p_T < 2 \text{ GeV}/c$ ,  $|d_{xy}| < 1.0 \text{ cm}$  for tracks with  $p_T > 2 \text{ GeV}/c$  as well as  $d_z < 1.0 \text{ cm}$  for the full  $p_T$ -range;
- an  $\eta$ -range of  $|\eta| < 0.8$ ;
- a  $p_T$ -threshold of  $p_T > 0.5 \text{ GeV}/c$ .

The TPC and ITS cluster related cuts are applied to ensure acceptable momentum and pointing determination. The upper cuts on the impact parameters are applied to reduce background tracks stemming from strange meson decays, mainly  $K_S^0$  and  $\Lambda$  decays. The lower cut on  $|d_{xy}|$  and the  $p_T$ -threshold are applied to reduce the huge background at low  $p_T$  in the PbPb-environment from primary particles, mainly charged pions. Finally, the  $\eta$ -cut is applied to have a symmetric  $\eta$ -range for tracks. This cut removes only a tiny amount ( $< 1\%$ ) of tracks because the efficiency of the TPC decreases drastically for tracks with  $|\eta| > 0.8$  and is practically zero for tracks with  $|\eta| > 0.9$ .

For the soft pions combined with the  $D^0$  candidates the single track cuts are in general looser:

- at least 3 clusters in the ITS;

- required ITS refit;
- an impact parameter of  $|d_{xy}| < 1.0$  cm and  $d_z < 1.0$  cm for the full  $p_T$ -range;
- an  $\eta$ -range of  $|\eta| < 0.8$ ;
- a  $p_T$ -threshold of  $p_T > 0.1$  GeV/ $c$ .

In contrast to the cuts applied to the tracks used for the  $D^0$  reconstruction, neither a TPC refit success nor a minimum number of TPC clusters is required. The reason for this strategy is that the efficiency for tracks with  $p_T < 0.2$  GeV/ $c$  decreases drastically of ITS-TPC combined tracks. As we will see below in this section  $0.1 \text{ GeV}/c < p_T < 2.0 \text{ GeV}/c$  is the relevant  $p_T$ -range from the soft pion stemming from the decay channel  $D^{*+} \rightarrow D^0\pi^+$ . Using this strategy, the tracks do not have as high quality as the  $D^0$  daughter tracks, but the reconstruction efficiency for  $D^{*+}$  mesons especially at low transverse momentum is enhanced. At low  $p_T$ , for  $p_T < 200$  MeV/ $c$ , many tracks are reconstructed in the ITS-only and are not rejected since no TPC refit is required. The requirement on ITS refit rejects fakes, i.e. randomly connected ITS clusters stemming from different tracks. The cuts on  $\eta$  and the impact parameters are applied due to the same reasons as for the  $D^0$  daughter tracks. The  $\eta$ -cut is applied to have a symmetric  $\eta$ -range for tracks. This cut removes only a tiny amount ( $< 1\%$ ) of tracks because the efficiency of the TPC decreases drastically for tracks with  $|\eta| > 0.8$  and is practically zero for tracks with  $|\eta| > 0.9$ . The cuts on the impact parameters are applied to reduce background tracks stemming from strange meson decays, mainly  $K_S^0$  and  $\Lambda$  decays. A lower cut on the impact parameter in the xy-plane  $d_{xy}$  is not applied because in terms of the vertex resolution the  $D^{*+}$  decays at the primary vertex having a mean proper decay length of  $c\tau = 2.1 \cdot 10^{-6} \mu\text{m}$  [10]. This is about seven orders of magnitude lower than the primary vertex resolution of ALICE being of the order of  $\sigma_{\text{vertex}} \approx 25 \mu\text{m}$  in PbPb-collisions [91, 105]. Tabular 4.2 summarizes the cuts applied to the  $D^0$  candidate daughter tracks and to the soft pion candidate tracks.

### Building $D^{*+}$ candidates

Using the tracks described above, the  $D^{*+}$  candidates are reconstructed for each event as follows. First, a loop on all positively charged tracks is performed applying the single track cuts for the  $D^0$  candidate daughter tracks listed in tab. 4.2. Within this loop a second loop on negatively charged tracks is done applying again the single track cuts. For each track pair the secondary vertex is reconstructed applying an iterative  $\chi^2$ -minimization technique, which finds a vertex that has the smallest common distance from both tracks. The track errors from the covariance matrix are used as inverse weights to give more weight to the track that has parameters with smaller errors. For the reconstructed vertex itself a covariance matrix is determined. The track momentum vector of both tracks is determined at the DCA to the reconstructed secondary vertex position by propagating both tracks through the magnetic field. Using both vectors  $\vec{p}_1$ ,  $\vec{p}_2$  at the DCA, the invariant mass of the  $D^0$  candidates is determined assigning a charged kaon mass  $m_K$  to the negatively charged track ( $\vec{p}_1$ ) and a charged pion mass  $m_\pi$  to the positively charged track ( $\vec{p}_2$ ) as

#### 4. $D^{*+}$ reconstruction strategy

Cut	$ d_{xy} $	$ d_z $	ITS clusters	TPC clusters	TPC refit	ITS refit	$ \eta $	$p_T$
unit	cm	cm	-	-	-	-	-	GeV/c
type	upper/ lower	upper	lower	lower	bool	bool	upper	lower
<hr/>								
<i>p<sub>T</sub></i> -region [GeV/c <sup>2</sup> ]								
<b>D<sup>0</sup>-daugh- ters</b>								
0.5 – 2	> 0.0025 < 1.0	1.0	2	70	✓	✓	0.8	0.5
> 2	< 1.0	1.0	2	70	✓	✓	0.8	0.5
<b>soft <math>\pi</math></b>								
> 0.1	< 1.0	1.0	3	0	-	✓	0.8	0.1

**Table 4.2.:** List of applied single track cuts to the  $D^0$  candidate daughter tracks and to the soft pion candidate tracks. "type" specifies whether the cut is an upper cut (rejecting tracks with a value for the corresponding parameter, which is higher than the quoted value in table) or an lower cut.

well as vice versa for  $\overline{D^0}$ -candidates:

$$\begin{aligned}
 M(K^-\pi^+) &= \sqrt{\left(\sqrt{(m_K^2 + \vec{p}_1^2)} + \sqrt{(m_\pi^2 + \vec{p}_2^2)}\right)^2 - (\vec{p}_1 + \vec{p}_2)^2} \\
 M(K^+\pi^-) &= \sqrt{\left(\sqrt{(m_K^2 + \vec{p}_2^2)} + \sqrt{(m_\pi^2 + \vec{p}_1^2)}\right)^2 - (\vec{p}_1 + \vec{p}_2)^2}
 \end{aligned} \tag{4.3}$$

Thus each track pair yields two  $D^0$  candidates. At this point a third loop, this time on positively and negatively tracks, is opened. Positively charged tracks are combined with  $D^0$  candidates and negatively charged tracks with  $\overline{D^0}$ -candidates. Both track types have to fulfill the track criteria for the soft pion listed in tab. 4.2. Moreover, tracks are rejected, which have the track ID of one of the  $D^0$  candidate daughter tracks. The momentum vectors  $\vec{p}_3^+$  (positively charged track) and  $\vec{p}_3^-$  (negatively charged track) at the DCA to the primary vertex are determined. The  $D^0$  and  $\overline{D^0}$  candidates do not need to be propagated from the secondary vertex to the primary vertex because they have no charge and the momentum components do not change in the magnetic field. Therefore the invariant mass of the  $D^{*+}$  and the  $D^{*-}$  candidates is directly determined from the momentum vectors  $\vec{p}_1$ ,  $\vec{p}_2$  of the  $D^0$  candidate daughters at the  $D^0$  decay vertex and the momentum vector  $\vec{p}_3$  of the soft pion candidate. The rest mass of the charged pion  $m_\pi$  is

assigned to the soft pion candidate:

$$\begin{aligned}
M(K^-\pi^+\pi^+) &= \\
&\sqrt{\left(\sqrt{(m_K^2 + \vec{p}_1^2)} + \sqrt{(m_\pi^2 + \vec{p}_2^2)} + \sqrt{(m_\pi^2 + \vec{p}_3^2)}\right)^2 - (\vec{p}_1 + \vec{p}_2 + \vec{p}_3)^2} \\
M(K^+\pi^-\pi^-) &= \\
&\sqrt{\left(\sqrt{(m_K^2 + \vec{p}_2^2)} + \sqrt{(m_\pi^2 + \vec{p}_1^2)} + \sqrt{(m_\pi^2 + \vec{p}_3^2)}\right)^2 - (\vec{p}_1 + \vec{p}_2 + \vec{p}_3)^2}
\end{aligned} \tag{4.4}$$

The invariant mass difference  $\Delta M = M(K\pi\pi) - M(K\pi)$  for the  $D^{*+}$  candidates is obtained using eqs. 4.3, 4.4.

The task to suppress the large combinatorial background for the  $D^{*+}$  was achieved by applying further topological cuts exploiting the displaced decay vertex topology of the  $D^0$  in addition to the single track cuts listed in tab. 4.2. In order to study the cut variable distributions for signal-triplets, i.e. triplets of tracks stemming from the decay of the  $D^{*+}$  meson, and background-triplets, i.e. triplets not stemming from the  $D^{*+}$  decays, Hijing [99] minimum-bias PbPb Monte-Carlo simulations with on-top injected charm-signals using Pythia [100–102] were used. A full ALICE detector description was included into the simulations. The advantage of this technique is that one can obtain a good sample of reconstructed tagged  $D^{*+}$  mesons, i.e. identified with Monte-Carlo information, in a reasonable number of PbPb-events. However, the signal to background ratio  $S/B = \text{signal}/\text{background}$  and hence also the statistical significance studied as functions of the values used for the cut variables are not equal to the expected values for the significance, respectively the signal to background ratio in real PbPb-collisions. The statistical significance  $s$  is given by:

$$s = \frac{\text{signal}}{\sqrt{\text{signal} + \text{background}}} \tag{4.5}$$

It is the inverse of the relative statistical error of the signal ( $\Delta\text{signal}/\text{signal}$ ) and a measure of how strong the signal deviates from a possible statistical fluctuation, which is  $\approx \sqrt{\text{signal} + \text{background}}$ . The significance  $s$  and the signal to background ratio  $S/B$  obtained using the Hijing+Pythia Monte-Carlo simulations need to be corrected by a factor  $F$  to get the expected values in real PbPb-collisions the following way:

$$s_{\text{corrected}} = \frac{F \cdot \text{signal}}{\sqrt{F \cdot \text{signal} + \text{background}}}, \quad S/B_{\text{corrected}} = \frac{F \cdot \text{signal}}{\text{background}} \tag{4.6}$$

The most important input for the determination of the factor  $F$  is the production cross section of the  $D^{*+}$  in real PbPb-collisions, which was unknown at the time this study was done. However, in order to study the response of the statistical significance and the signal to background ratio to the applied values of topological cuts, the knowledge of absolute values of both quantities is not needed. Moreover, in case the signal is small compared to

#### 4. $D^{*+}$ reconstruction strategy

the background in the simulated data and in real data, the correction for the significance can be approximated by:

$$s_{\text{corrected}} \approx \frac{F \cdot \text{signal}}{\sqrt{\text{background}}} \quad (4.7)$$

Therefore both the significance and the signal to background ratio obtained with the Monte-Carlo simulations described above differ only by an arbitrary factor  $F$  to the expected values in real data.

Figures 4.3a, 4.3b show the measured  $p_T$ -distribution of the soft pion using PbPb Hi-

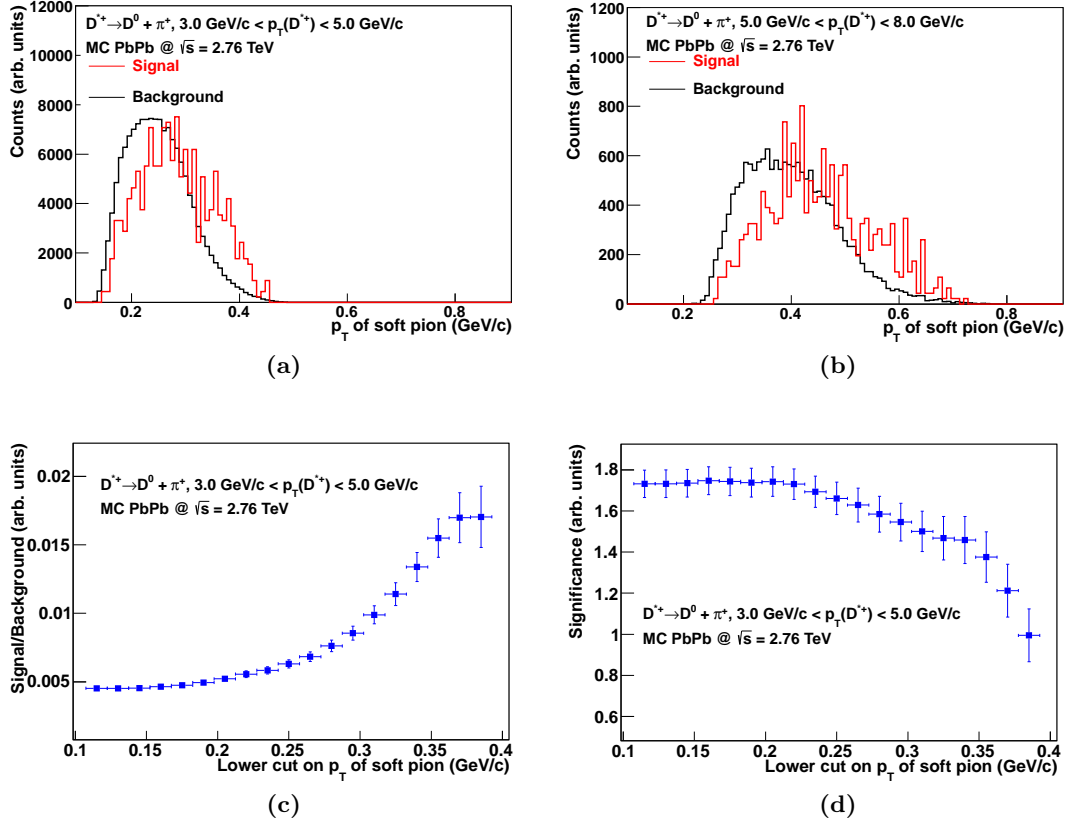


**Figure 4.3.:** (a) and (b): Measured  $p_T$ -distribution of the soft pions stemming from  $D^{*+} \rightarrow D^0\pi^+$  decays (red line) and from background (black line) using PbPb Hijing+Pythia Monte Carlo simulations [99–102] with a full ALICE detector description in two different  $p_T$ -regions of the  $D^{*+}$ :  $3 \text{ GeV}/c < p_T < 5 \text{ GeV}/c$  (a) and  $5 \text{ GeV}/c < p_T < 8 \text{ GeV}/c$  (b). Both signal-histograms are first normalized by their integrals and then scaled by the integral of the background-histogram for better comparison. (c) and (d): Response of the signal to background ratio (c) and of the significance (d) to a variable lower cut on the  $p_T$  of the soft pion for a  $D^{*+}$   $p_T$  of  $3 \text{ GeV}/c < p_T < 5 \text{ GeV}/c$ .

jing+Pythia Monte Carlo simulations with a full ALICE detector description, labeled as "soft  $\pi$ " on the abscissas of the figures, stemming from  $D^{*+} \rightarrow D^0\pi^+$  decays (red line) and not stemming from these decays but considered in the  $D^{*+}$  candidate building procedure described above (black line) in different  $p_T$ -regions of the  $D^{*+}$ :  $3 \text{ GeV}/c < p_T < 5 \text{ GeV}/c$  (a) and  $5 \text{ GeV}/c < p_T < 8 \text{ GeV}/c$  (b). Both signal-histograms are first normalized by

their integrals and then scaled by the integral of the background-histogram for better comparison. Figures 4.3c, 4.3d show the response of the signal to background ratio (c) and of the significance (d) to a minimum cut on the  $p_T$  of the soft pion for a  $D^{*+}$   $p_T$  of  $3 \text{ GeV}/c < p_T < 5 \text{ GeV}/c$ . Both quantities are given in "arb.units" due to the arbitrary factor  $F$  described above. As can be seen in fig. 4.3c the signal to background ratio improves by applying a lower cut on the  $p_T$  of the soft pion. However, the significance deteriorates, see fig. 4.3d. The goal of the single track and topological cut studies is to maximize the significance and not the signal to background ratio because this minimizes directly the statistical error of the  $D^{*+}$  signal. As a consequence this track cut is kept fixed at  $p_T > 0.1 \text{ GeV}/c$  for all  $p_T$ -regions of the  $D^{*+}$ .

Figures 4.4a, 4.4b show the measured impact parameter  $d_{xy}$ -distributions of pions (a) and kaons (b) stemming from the decay channel  $D^0 \rightarrow K^- \pi^+$  with the  $D^0$  originating from the  $D^{*+} \rightarrow D^0 \pi^+$  decay and from background (black line) using PbPb Hijing+Pythia Monte

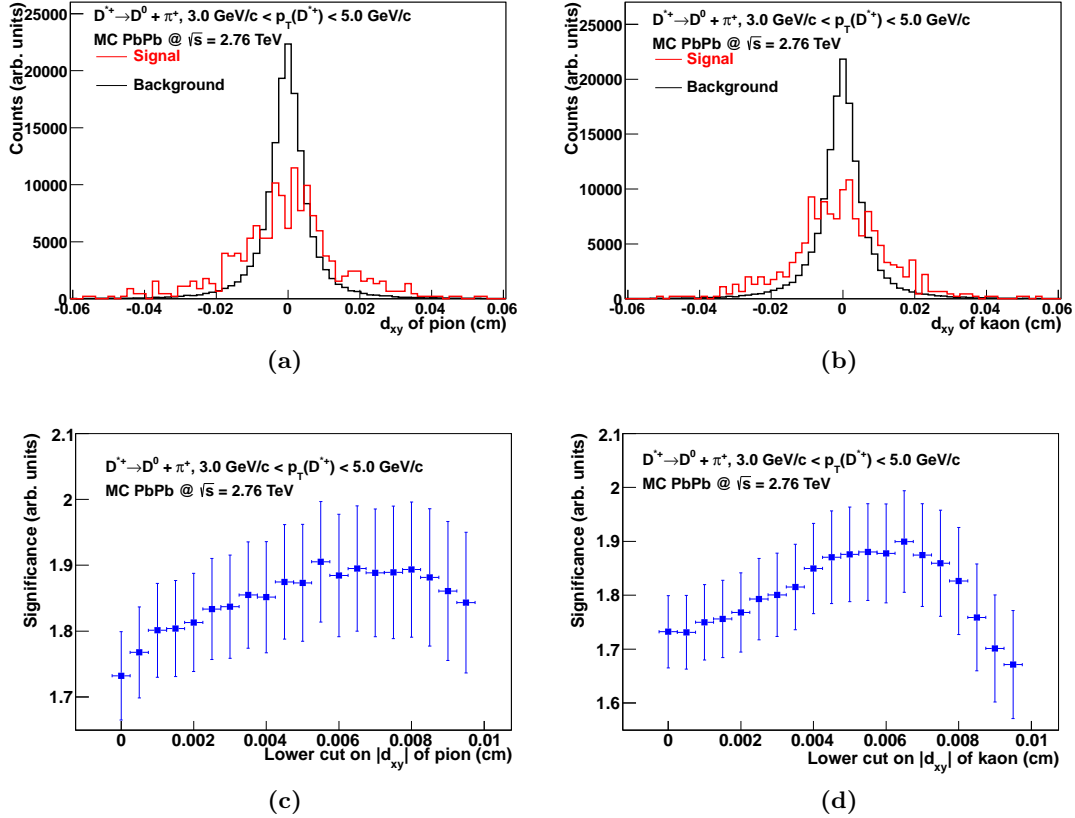


**Figure 4.4.:** (a) and (b): Measured impact parameter  $d_{xy}$ -distributions of pions (a) and kaons (b) stemming from the decay channel  $D^0 \rightarrow K^- \pi^+$  with the  $D^0$  originating from the  $D^{*+} \rightarrow D^0 \pi^+$  decay and from background (black line) using PbPb Hijing+Pythia Monte Carlo simulations [99–102] with a full ALICE detector description for a  $p_T$  of the  $D^{*+}$  of  $3 \text{ GeV}/c < p_T < 5 \text{ GeV}/c$ . Both signal-histograms are first normalized by their integrals and then scaled by the integral of the background-histogram for better comparison. (c) and (d): Response of the significance to a lower cut on the absolute value of the impact parameter  $d_{xy}$  of the pion (c) and the kaon (d).

Carlo simulations [99–102] with a full ALICE detector description for a  $p_T$  of the  $D^{*+}$  candidates of  $3 \text{ GeV}/c < p_T < 5 \text{ GeV}/c$ . The  $d_{xy}$ -distributions of the signal are broader than the background-distributions. This is expected due to the displaced vertices with respect to the primary vertex of the decaying  $D^0$  mesons. Figures 4.4c, 4.4d show the response of the significance to a lower cut on the absolute value of the impact parameter  $|d_{xy}|$  of the pion (c) and the kaon (d) for a  $D^{*+}$   $p_T$  of  $3 \text{ GeV}/c < p_T < 5 \text{ GeV}/c$ . The effect of these cuts on the significance is small and the cut was fixed at a value of  $|d_{xy}| > 0.0025 \text{ cm}$  (see tab. 4.2) for tracks with a  $p_T$  of  $p_T < 2 \text{ GeV}/c$  building the  $D^0$  candidates, see tab. 4.2. More powerful cut variables can be calculated when the information of both tracks and the position of the reconstructed  $D^0$  decay vertex are exploited simultaneously. These cuts are called topological cut because they are based on the topology of the  $D^{*+}$  or more precisely the  $D^0$  decay. They are introduced and discussed one by one in the following.

### Invariant mass of the $D^0$

The first topological cut variable presented here is the reconstructed invariant mass of the  $D^0$  introduced in eq. 4.3. Due to the finite momentum resolution of the ALICE de-

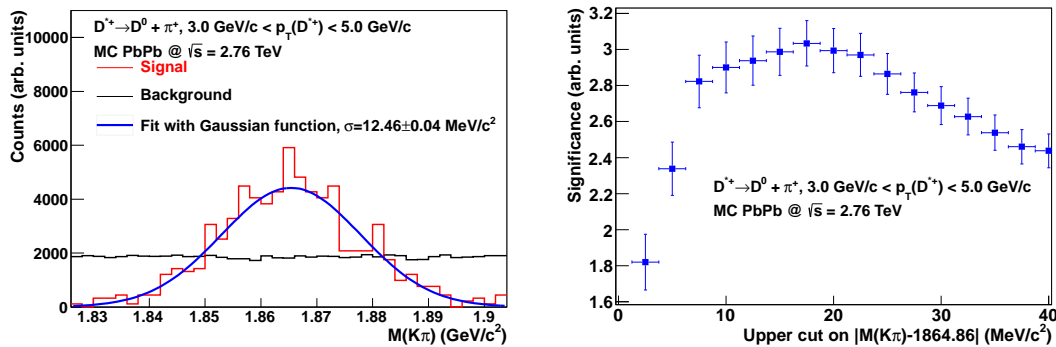


**Figure 4.5.:** (left) Measured invariant mass  $M(K\pi)$  distribution of the track doublet  $K\pi$  stemming from the decay channel  $D^0 \rightarrow K^- \pi^+$  with the  $D^0$  originating from the  $D^{*+} \rightarrow D^0 \pi^+$  decay and from background (black line) using PbPb Hijing+Pythia Monte Carlo simulations [99–102] with a full ALICE detector description for a  $p_T$  of the  $D^{*+}$  of  $3 \text{ GeV}/c > p_T > 5 \text{ GeV}/c$ . The signal-histogram is first normalized by its integral and then scaled by the integral of the background-histogram for better comparison. Moreover, the signal histogram is fitted with a Gaussian function. The value and the statistical error of the width  $\mu$  extracted from the fit are drawn in. (right) Response of the significance by applying an upper cut on the absolute value of the distance  $M(K\pi) - M(D^0)$  with  $M(D^0)$  being the PDG [10] value of the  $D^0$  invariant mass.

tector the distribution has a width of several  $10 \text{ MeV}/c^2$  depending on the  $p_T$  of the  $D^0$ . Figure 4.5 (left) shows the measured invariant mass distribution of the  $K\pi$  doublet for tracks originating from the decay channel  $D^0 \rightarrow K^- \pi^+$  with the  $D^0$  originating from the decay  $D^{*+} \rightarrow D^0 \pi^+$  (red line) and of uncorrelated tracks (black line) using the Hijing+Pythia Monte-Carlo simulations described above for  $D^{*+}$  candidates with a  $p_T$  of  $3 \text{ GeV}/c > p_T > 5 \text{ GeV}/c$ . The signal-histogram is first normalized by its integral and then scaled by the integral of the background histogram for better comparison. Figure 4.5 (right) shows the response of significance of the  $D^{*+}$  signal applying an upper cut on the absolute value of the difference between the measured  $K\pi$  doublet invariant

mass and the PDG value of  $m(D^0)$  in the range  $1 - 40 \text{ MeV}/c^2$ . The significance can be maximized when cutting on a value of about  $|M(K\pi) - m(D^0)| < 20 \text{ MeV}/c^2$  in that  $p_T$ -region, which corresponds to  $1.6\sigma$  in units of the resolution of  $M(K\pi)$ . The resolution is  $\sigma(M(K\pi)) = 12.5 \text{ MeV}/c^2$  in that  $p_T$ -region, and the Gaussian fit to the distribution of  $M(K\pi)$  is depicted in fig. 4.5 (left).

### Distance of closest approach of the pion and kaon

The distance of closest approach (DCA) of the kaon and pion stemming from the  $D^0 \rightarrow K^-\pi^+$  decay is another topological cut variable determined during the  $D^{*+}$  candidate building procedure. This distance is depicted in fig. 4.6a (blue line). It is the smallest distance in the  $xy$ -plane the two candidate track helices have from each other. In a perfect detector the DCA for signal tracks, i.e. stemming from the  $D^0 \rightarrow K^-\pi^+$  decay, would be zero. In a real detector the track helices are measured with a finite spatial resolution and thus the DCA distribution has a certain width. Figure 4.6b shows the measured DCA of pions and kaons stemming from the decay channel  $D^0 \rightarrow K^-\pi^+$  with the  $D^0$  originating from the  $D^{*+} \rightarrow D^0\pi^+$  decay (red line) and from background (black line) using the Hijing+Pythia Monte-Carlo simulations described above for  $D^{*+}$  mesons with high  $p_T$ , namely for  $8 \text{ GeV}/c > p_T > 12 \text{ GeV}/c$ . The signal-histogram is first normalized by its integral and then scaled by the integral of the background-histogram for better comparison. The signal-distribution resembles the positive side of a Gaussian function because it reflects the resolution of the measurement of the DCA. The width is of the order of  $\sigma \approx 0.05 \text{ cm}$  demonstrating the powerful sub-millimeter tracking precision of the ALICE detector. The background-distribution has a longer tail and it shows the measured DCA-distribution of randomly selected pairs of tracks. Figure 4.6c shows the response of the signal to background ratio applying an upper cut on the DCA-distribution. It can be improved at most by about a factor of 2 when cutting hard on the upper value of the DCA-distribution at that  $p_T$ .

### Cosine of pointing angle $\theta_{\text{pointing}}$

The cosine of the pointing angle  $\theta_{\text{pointing}}$  is another topological cut variable, which uses as ingredients the reconstructed positions of the primary vertex, the secondary decay vertex of the  $D^0$  and the reconstructed momentum vector  $\vec{p}$  of the  $D^0$ . The cosine of the pointing angle  $\theta_{\text{pointing}}$  is defined as:

$$\cos \theta_{\text{pointing}} = \frac{\vec{R} \cdot \vec{p}}{|\vec{R}| \cdot |\vec{p}|} \quad (4.8)$$

with  $\vec{R}$  being the vector connecting the primary and secondary vertex starting at the primary vertex, see fig. 4.6a. This cut variable can also be determined in the  $x$ - $y$  plane. In this case the projections into the  $xy$ -plane of  $\vec{R}$  and  $\vec{p}$  in eq. 4.8 have to be taken. Figure 4.7a shows the distribution of the measured cosine of the pointing angle  $\cos \theta_{\text{pointing,xyz}}$  of reconstructed  $D^0$  mesons using the simulations described above, stemming from the decay channel  $D^{*+} \rightarrow D^0\pi^+$  for a  $p_T$  of the  $D^{*+}$  of  $5 \text{ GeV}/c < p_T < 8 \text{ GeV}/c$ . The width of the peak at  $\cos(\theta_{\text{pointing,xyz}}) \approx 1.0$  is of the order of  $\Delta \cos(\theta_{\text{pointing,xyz}}) \approx 0.01$ , which yields a pointing angle resolution of  $\Delta \theta_{\text{pointing,xyz}} = \arccos(0.99) - \arccos(1.0) = 8^\circ$  at that  $p_T$ . Figure 4.7b shows the measured absolute value of the cosine of the pointing angle  $\cos \theta_{\text{pointing,xy}}$  in the  $xy$ -plane for the same configuration as for the three-dimensional pointing angle. The width

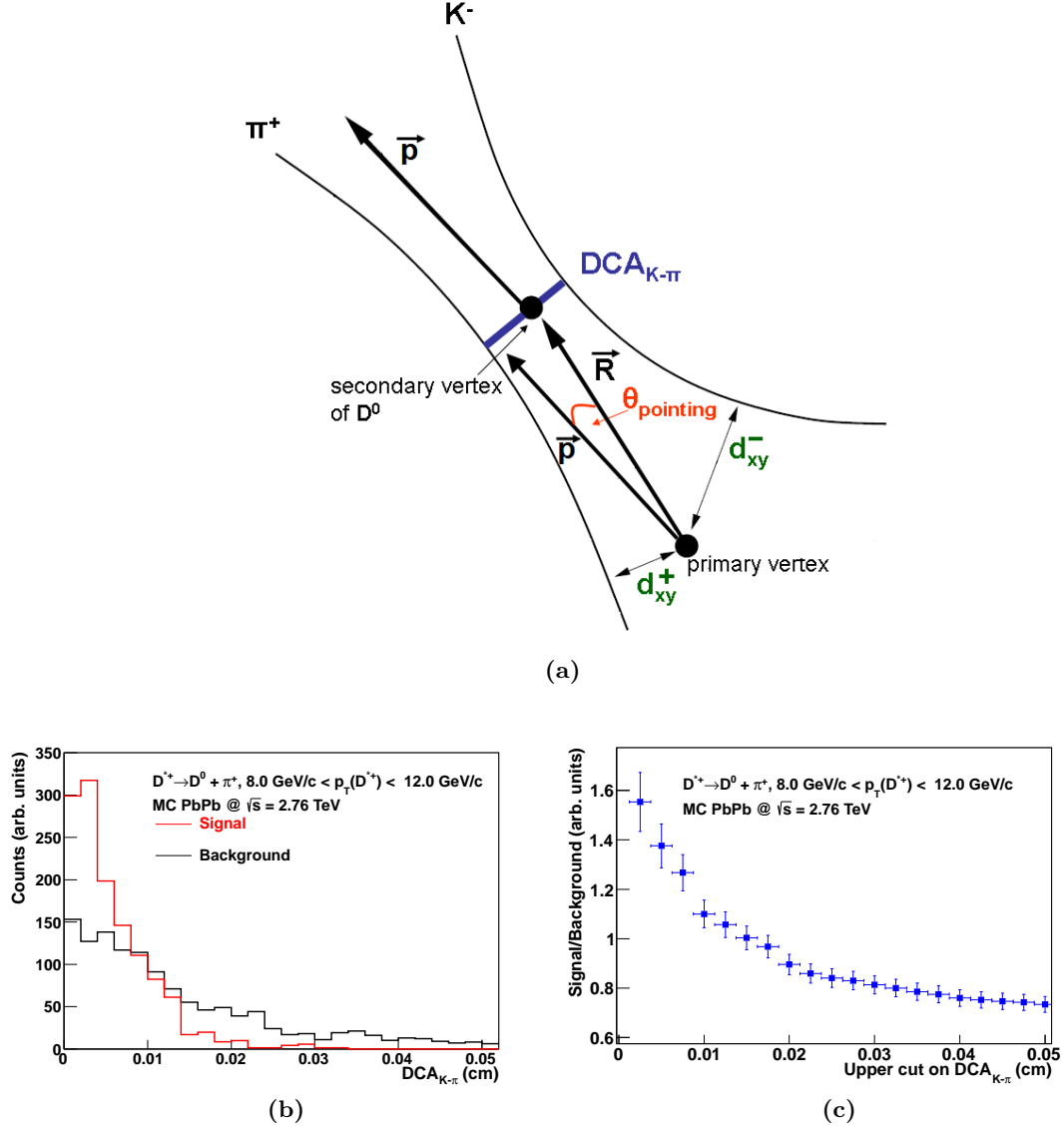


**Figure 4.6.:** (a) Sketch of the topological cut variables of the  $D^{*+}$  analysis exploiting the displaced vertex of the  $D^0$ .  $\vec{R}$  is the vector connecting the primary and secondary vertex,  $\vec{p}$  the reconstructed  $D^0$  momentum,  $\theta_{\text{pointing}}$  the angle between  $\vec{p}$  and  $\vec{R}$ ,  $DCA_{K-\pi}$  is the distance of closest approach of the two  $D^0$  daughter tracks and finally  $d_{xy}^{\pm}$  are the impact parameters to the primary vertex of the  $D^0$  daughter tracks defined in eq. 4.2. (b) Measured DCA distribution of pions and kaons stemming from the decay channel  $D^0 \rightarrow K^- \pi^+$  with the  $D^0$  originating from the  $D^{*+} \rightarrow D^0 \pi^+$  decay and from background (black line) using PbPb Hijing+Pythia Monte Carlo simulations [99–102] with a full ALICE detector description for a  $p_T$  of the  $D^{*+}$  of  $8 \text{ GeV}/c < p_T < 12 \text{ GeV}/c$ . The signal-histogram is first normalized by its integral and then scaled by the integral of the background-histogram for better comparison. (c) Response of the signal to background ratio by applying an upper cut on the value of the DCA.

of the peak in this case is of the order  $\Delta \cos(\theta_{\text{pointing,xy}}) = 0.001$ , which yields a pointing angle resolution in the  $xy$ -plane of  $\Delta \theta_{\text{pointing,xy}} = \arccos(0.999) - \arccos(1.0) = 2.6^\circ$  at that  $p_T$ . The reason why in case of the two-dimensional pointing angle the absolute value

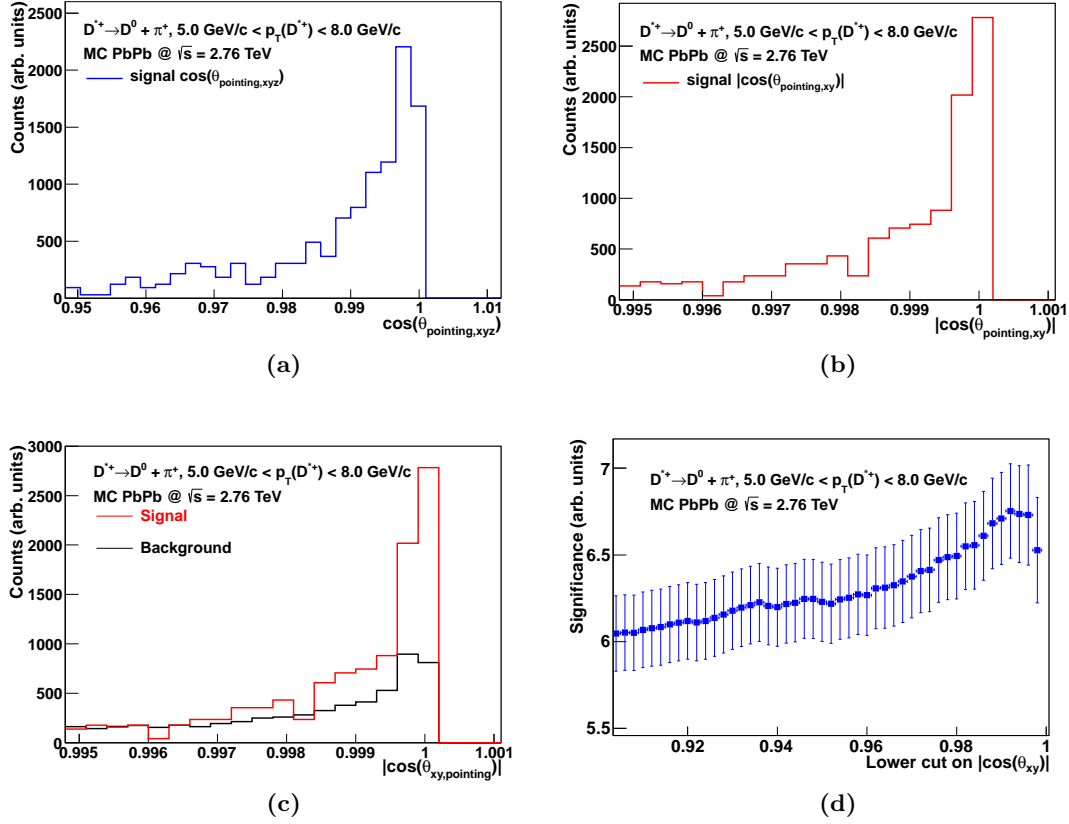


**Figure 4.7.:** (a), (b) and (c): Measured cosine of the pointing angle distribution in three coordinates (a) and in the xy-plane (b,c) of  $D^0$  mesons stemming from the decay channel  $D^{*+} \rightarrow D^0\pi^+$  (a, b, and c, red line) and of  $D^0$  candidates build with randomly selected tracks (c, black line) using PbPb Hijing+Pythia Monte Carlo simulations [99–102] with a full ALICE detector description for a  $p_T$  of the  $D^{*+}$  of  $5 \text{ GeV}/c < p_T < 8 \text{ GeV}/c$ . The signal-histograms in (a), (b) and (c) are first normalized by their integrals and then scaled by the integral of the background-histograms. In case of the cosine of the pointing angle in the xy-plane  $\cos(\theta_{\text{pointing,xy}})$  shown in (b) and (c) the absolute value is shown. (d) Response of the significance to a lower variable cut on the absolute value of pointing angle in the xy-plane  $|\cos(\theta_{\text{pointing,xy}})|$ .

of the cosine is taken is as follows. In the  $D^{*+}$  analysis only  $D^0$  candidates are selected that have a positive  $\cos(\theta_{\text{pointing,xyz}})$ , i.e. with a pointing angle of  $\theta_{\text{pointing,xyz}} < 90^\circ$ . Those having a negative one are removed from the sample. In some cases it can happen for reconstructed  $D^0$  mesons that the pointing angle is smaller than  $90^\circ$  but the pointing angle of the vectors projected on the xy-plane  $\theta_{\text{pointing,xy}}$  is negative, if their components in the xy-plane are small. Cutting on the signed value and not on the absolute value of the  $\cos\theta_{\text{pointing,xy}}$  would remove those candidates and thus remove signal. Cutting on the absolute value  $|\cos\theta_{\text{pointing,xy}}|$  prevents this effect. Figure 4.7c shows the measured absolute value of the cosine of the pointing angle  $\cos\theta_{\text{pointing,xy}}$  for  $D^0$  candidates stemming from the decay channel  $D^{*+} \rightarrow D^0\pi^+$  (red line) and for background (black line) using the simulations described above for a  $p_T$  of  $D^{*+}$  candidates of  $5 \text{ GeV}/c < p_T < 8 \text{ GeV}/c$ . The background-distribution is flatter than the signal-distribution and by applying a lower cut on the absolute value of the cosine of the pointing angle in the xy-plane  $\cos(\theta_{\text{pointing,xy}})$

the significance is improved. This is demonstrated in fig. 4.7d where the significance of the  $D^{*+}$  signal as a function of a lower cut on the quantity  $|\cos(\theta_{\text{pointing,xy}})|$  is shown.

#### Product of impact parameters $d_{xy}^K \times d_{xy}^\pi$

Another important cut variable is the product of the transverse impact parameters  $d_{xy}^K \times d_{xy}^\pi$ . As introduced in eq. 4.2, the impact parameters of the  $D^0$  daughters to the primary vertex  $d_{xy}^{K,\pi}$  are signed. Depending on how both helices of the daughters of the  $D^0$  candidates are oriented with respect to the primary vertex and on their charge sign, the product of the impact parameters in the xy-plane has a positive or negative sign. Figure 4.8a depicts the four possible orientations of the helices with respect to the primary vertex. The product of the impact parameters  $d_{xy}^K \times d_{xy}^\pi$  of the helices pairs corresponding to  $D^0$  decay daughters has a negative sign and of randomly selected combined tracks both signs, positive and negative. A negatively signed large product of the impact parameters  $d_{xy}^K \times d_{xy}^\pi$  is a feature of a displaced  $D^0$  vertex. Randomly selected tracks originating from the primary vertex have typically smaller impact parameters than those stemming from  $D^0$  decays as already shown in figs. 4.4a, 4.4b. Therefore the product of the impact parameters of those tracks is smaller than the product of impact parameters of tracks stemming from  $D^0$  decays as well. Figure 4.8b shows the measured distribution of the product of the transverse impact parameters  $d_{xy}^K \times d_{xy}^\pi$  of tracks stemming from the decay channel  $D^0 \rightarrow K^- \pi^+$  with the  $D^0$  originating from the  $D^{*+} \rightarrow D^0 \pi^+$  decay (red line) and of uncorrelated tracks (black line) using the Hijing+Pythia Monte-Carlo simulations described above for  $D^{*+}$  candidates with a  $p_T$  of  $3 \text{ GeV}/c > p_T > 5 \text{ GeV}/c$ . The signal-histogram is first normalized by its integral and then scaled by the integral of the background-histogram for better comparison. The signal distribution is highly asymmetric with few entries for a positive  $d_{xy}^K \times d_{xy}^\pi$ . These few entries originate from  $D^0$  decays, which are close to the primary vertex, and due to the finite precision of the impact parameter measurement presented in fig. 4.2, the product of impact parameters of the two decay daughters may have in rare cases a positive sign. The background distribution is symmetric and centered at 0. Thus the probability to measure a positively signed product of the impact parameters (fig. 4.8a, lower panel) or a negatively signed one (fig. 4.8a, upper panel) for randomly selected tracks is of the same order. By selecting  $D^0$  candidates with a  $d_{xy}^K \times d_{xy}^\pi$  smaller than zero the statistical significance of the  $D^{*+}$  yield in the  $p_T$ -range of  $3 \text{ GeV}/c > p_T > 5 \text{ GeV}/c$  can be improved by a factor of 2 as shown in fig. 4.8c. Here the significance as a function of an upper cut on the product of the transverse impact parameters  $d_{xy}^K \times d_{xy}^\pi$  is shown.

#### Decay length of the $D^0$ meson

The decay length  $L$  of the reconstructed  $D^0$  candidates is another quantity that allows to suppress the combinatorial background within the  $D^{*+}$  reconstruction procedure. The value  $L$  is simply the length of the vector  $\vec{R}$  depicted in fig. 4.6a which connects the primary vertex and secondary  $D^0$  decay vertex. As in case of the pointing angle  $\theta_{\text{pointing}}$  the resolution is higher when projecting the vector  $\vec{R}$  in the xy-plane. Moreover, in order to account for the finite resolution of the measurement, the decay length in the xy-plane  $L_{xy}$  is normalized by the error of its measurement  $\sigma L_{xy}$ . When applying a lower cut on the normalized decay length in the xy-plane  $L_{xy}$ , measurements with a large error are

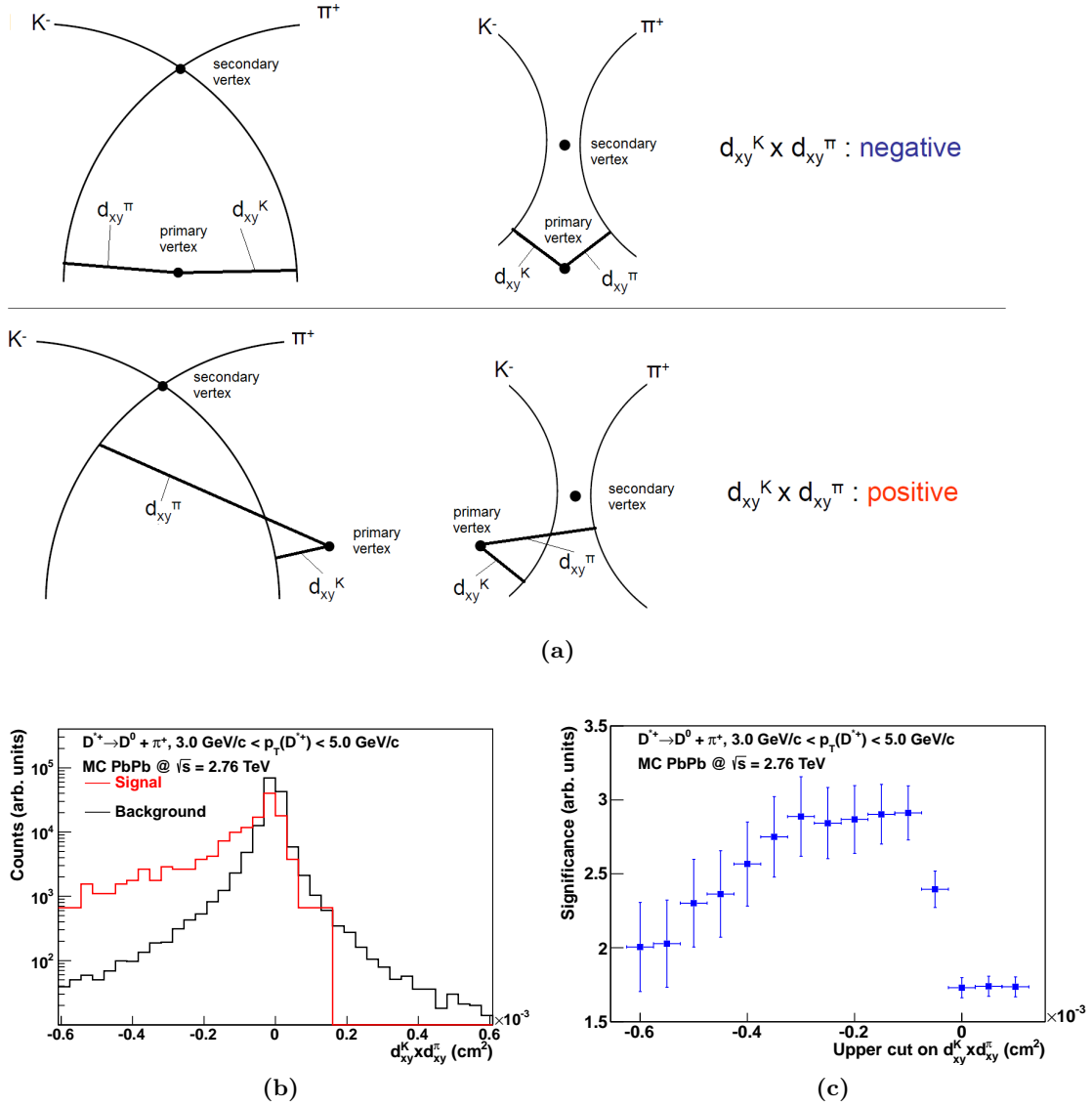


**Figure 4.8.:** (a) The four possible orientations of the helices of the  $D^0$  candidate decay daughters with respect to the primary vertex. The orientation in the upper panel yields a negative sign of the product of the transverse impact parameters  $d_{xy}^K \times d_{xy}^\pi$  and in the lower panel a positive sign. (b) Measured distribution of the product of the transverse impact parameters  $d_{xy}^K \times d_{xy}^\pi$  of tracks stemming from the decay channel  $D^0 \rightarrow K^- \pi^+$  with the  $D^0$  originating from the  $D^{*+} \rightarrow D^0 \pi^+$  decay (red line) and from background (black line) using PbPb Hijing+Pythia Monte Carlo simulations [99–102] with a full ALICE detector description for a  $p_T$  of the  $D^{*+}$  of  $3 \text{ GeV}/c < p_T < 5 \text{ GeV}/c$ . The signal-histogram is first normalized by its integral and then scaled by the integral of the background-histogram for better comparison. (c) Response of the significance of the  $D^{*+}$  signal to an upper cut on the value of the product of the transverse impact parameters  $d_{xy}^K \times d_{xy}^\pi$ .

suppressed because the error estimation is placed in the denominator of the normalized decay length. For the determination of the error, the covariance matrices of the determined primary and secondary vertices are used. This normalization yields then the significance

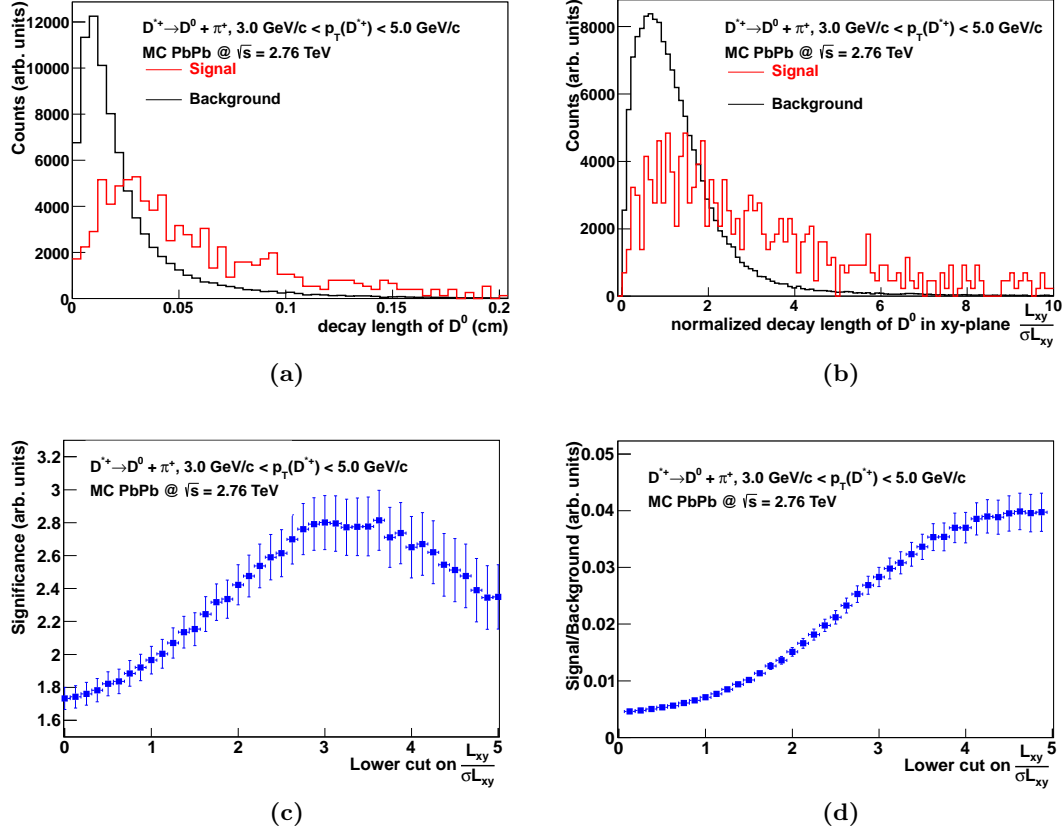


**Figure 4.9.:** (a) and (b): Measured distribution of the three-dimensional decay length in units of centimeters (a) and of the normalized decay length in the xy-plane (b) of  $D^0$  candidates stemming from the decay channel  $D^{*+} \rightarrow D^0 \pi^+$  (red line) and of  $D^0$  candidates built with randomly selected tracks (black line) using PbPb Hijing+Pythia Monte Carlo simulations [99–102] with a full ALICE detector description for a  $p_T$  of the  $D^{*+}$  of  $3 \text{ GeV}/c < p_T < 5 \text{ GeV}/c$ . Both signal-histograms are first normalized by their integrals and then scaled by the integral of the corresponding background-histogram for better comparison. (c) and (d): Response of the significance (c) respectively the signal to background ratio (d) of the  $D^{*+}$  signal to a lower cut on the normalized decay length in the xy-plane for a  $p_T$  of the  $D^{*+}$  of  $3 \text{ GeV}/c < p_T < 5 \text{ GeV}/c$ .

of the measured decay length in the xy-plane  $L_{xy}$ :

$$\text{Significance}(L_{xy}) = \frac{L_{xy}}{\sigma L_{xy}} \quad (4.9)$$

Figures 4.9a, 4.9b show the distributions of the measured three-dimensional decay length  $L$  of  $D^0$  candidates in units of centimeters (a) and the normalized decay length in the xy-plane  $L_{xy}/\sigma L_{xy}$  (b) stemming from the decay channel  $D^{*+} \rightarrow D^0 \pi^+$  (red lines) and from background (black lines) using the simulations described above for  $D^{*+}$  candidates with a  $p_T$  of  $3 \text{ GeV}/c < p_T < 5 \text{ GeV}/c$ . Both signal-histograms are first normalized by their integrals and then scaled by the integrals of the background-histograms for better comparison. In both cases the signal distributions are in general flatter, whereas the background distributions show a peak structure at low values close to zero. Figures 4.9c, 4.9d show the response of the signal to background ratio (c) and of the significance (d) to

a lower cut on the normalized decay length in the xy-plane for a  $D^{*+}$  candidate  $p_T$  of  $3 \text{ GeV}/c < p_T < 5 \text{ GeV}/c$ . The significance improves at most by about a factor of 1.5 and the signal to background ratio of the  $D^{*+}$  signal at most by about a factor of 10 by applying a hard lower cut of  $L_{xy}/\sigma L_{xy} > 5$  on the distribution of the normalized decay length in the xy-plane.

### Cosine of the angle $\theta^*$ , angle between the pion momentum in the $D^0$ rest frame and the $D^0$ flight line

The decay angle  $\theta^*$  is defined as the angle between the momentum vector of the pion stemming from the  $D^0 \rightarrow K^- \pi^+$  decay, which is Lorentz-boosted into the rest frame of the reconstructed  $D^0$  meson, and the momentum vector of the  $D^0$  meson itself. Figure 4.10a depicts this situation. In case the pion is not coming from a  $D^0$  decay, i.e. in case of a background  $D^0$  candidate, there is no correlation between the pion momentum vector and the momentum vector of the  $D^0$  candidates. The opening angle between the momentum vector of the pion and the momentum vector of the reconstructed  $D^0$  candidates is small because both momentum vectors are boosted in forward direction when dealing with  $D^0$  candidates originating from  $D^{*+}$  candidates with a  $p_T > 2 \text{ GeV}/c$ . The boost of the four momentum vector of the pion to the rest frame of the  $D^0$  candidate will not change much the flight direction of the pion but only the magnitude of its momentum. Therefore the orientation of the pion momentum boosted into the rest frame of the  $D^0$  candidate with respect to the momentum vector of the  $D^0$  candidate will preferably be parallel or anti-parallel. On the other hand, if the pion originates from a  $D^0 \rightarrow K^- \pi^+$  decay, the momentum vector of the pion boosted into the  $D^0$  rest frame will have an isotropic distribution with respect to the  $D^0$  flight line. The decay  $D^0 \rightarrow K^- \pi^+$  at rest is namely isotropic with no preferred flight direction of the decay daughters. The measured distribution of the cosine of the angle  $\theta^*$  using the simulations described above for pions stemming from the decay channel  $D^0 \rightarrow K^- \pi^+$  with the  $D^0$  originating from the decay  $D^{*+} \rightarrow D^0 \pi^+$  is shown in fig. 4.10b (red line) for a  $p_T$  of the  $D^{*+}$  candidates of  $5 \text{ GeV}/c < p_T < 8 \text{ GeV}/c$ . The according distribution for pions originating from background  $D^0$  candidates is also drawn in (black line). The signal-histogram is first normalized by its integral and then scaled by the integral of the background-histogram for better comparison. The background-distribution shows peaks at values of  $\cos(\theta^*) \approx \pm 0.8$ , i.e. for parallel, respectively anti-parallel orientation of the pion momentum with respect to the  $D^0$  momentum. The signal-distribution is flat without any peak structure. Figures 4.10c, 4.10d show the response of the signal to background ratio (c) and of the significance (d) to an upper cut on the absolute value of the cosine of the  $\theta^*$ , namely  $|\cos(\theta^*)|$ , for a  $D^{*+}$   $p_T$  of  $5 \text{ GeV}/c < p_T < 8 \text{ GeV}/c$ . The significance improvement is negligible within the statistical uncertainties but the signal to background ratio of the  $D^{*+}$  yield improves at most about by a factor of 2 applying a hard upper cut on the  $|\cos(\theta^*)|$  distribution.

### Multidimensional cut optimization

The significance of the  $D^{*+}$  signal depends on all the values of the applied topological cut variables presented above simultaneously. That means that the significance response behavior depicted e.g. in fig. 4.9c for the normalized decay length changes, if e.g. the cut on the cosine of the pointing angle  $\theta_{\text{pointing}}$  is varied. Moreover, as the spatial tracking

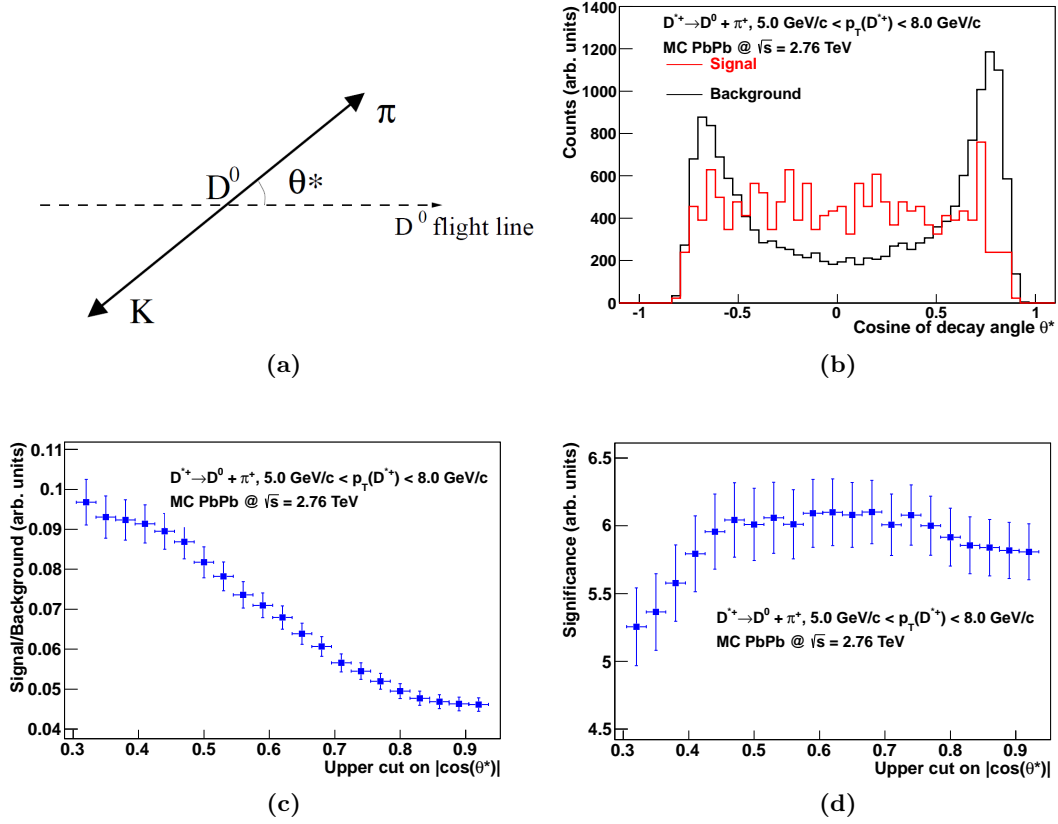


**Figure 4.10.:** (a) Sketch of the decay angle  $\theta^*$  of the pion with respect to the flight direction of the  $D^0$  in the rest frame of the  $D^0$ . (b) Measured distribution of the cosine of the decay angle  $\theta^*$  for pions stemming from  $D^0$  mesons originating from the  $D^{*+} \rightarrow D^0 \pi^+$  decay (red line) and from background (black line) using PbPb Hijing+Pythia Monte Carlo simulations [99–102] with a full ALICE detector description for a  $p_T$  of the  $D^{*+}$  candidates of  $5 \text{ GeV}/c < p_T < 8 \text{ GeV}/c$ . (c) and (d) Response of the signal to background ratio (c), respectively significance (d) to an upper variable cut on the absolute value of the cosine of the decay angle  $\theta^*$ .

resolution depends on the transverse momentum of the tracks, see fig. 4.2, all cut variables depend on the  $p_T$  of the  $D^{*+}$  meson, either, because this quantity is strongly correlated with the  $p_T$  of the decay daughters of the decay channel  $D^{*+} \rightarrow D^0 \pi^+$  and the subsequent channel  $D^0 \rightarrow K^- \pi^+$ . In order to find the best topological cut-set as function of the  $p_T$  of the  $D^{*+}$ , which yields the best significance, a multidimensional cut optimization on real PbPb-collision data was carried out. The  $D^{*+}$  signal significance determination on real data  $p_T$ -bin by  $p_T$ -bin was performed using the yield extraction method on real data presented in detail below in sec. 4.3. This procedure is required because in real data there is no possibility to distinguish between tracks, which originate from the decay channel  $D^{*+} \rightarrow D^0 \pi^+$ , and the ones, which originate from background. The study of the significance behavior as a function of the applied cuts using the Hijing+Pythia Monte Carlo simulations presented above was used to find starting values for the cut variables as well as for defining ranges within the multidimensional cut variation on real data. The single

track quality cuts, the  $p_T$ -thresholds and the cuts on  $\eta$  as well as on the impact parameters of the single tracks summarized in tab. 4.2 were fixed and not part of the multidimensional cut optimization procedure. The chosen centrality range was 30-50% because of the best achievable  $D^{*+}$  signal significance in that centrality range. In more central collisions, the combinatorial background becomes enormous and thus the significance of the  $D^{*+}$  signal deteriorates. In more peripheral collisions, the  $D^{*+}$  signal decreases drastically. Moreover, the expected  $v_2$ - and  $v_3$ -signals are largest and the event plane resolution for the event plane angles  $\Psi_2$  and  $\Psi_3$  is best at that centrality range as will be shown in chap. 5. The combination of these effects yields the smallest possible statistical error of the  $v_n$ -measurements.

The ranges and information which cut variable was varied and which fixed is given in tab. 4.3. In addition, the considered ranges for each topological cut variable are listed. The goal of this study was to find a maximum of the statistical significance in several

Cut variable	unit	fixed	range
$ M(K\pi) - m(D^0) $	MeV/ $c^2$	NO	20 – 60
$DCA_{\pi-K}$	cm	NO	0.01 – 0.06
$\cos(\theta_{\text{pointing,xyz}})$	-	YES	$0.9 \pm 0$
$\cos(\theta_{\text{pointing,xy}})$	-	NO	0.990 – 0.999
$ \cos(\theta^*) $	-	NO	0.5 – 0.9
$d_{xy}^K \times d_{xy}^\pi$	cm <sup>2</sup>	NO	$-0.5 \cdot 10^{-3} - 0.1 \cdot 10^{-3}$
$\frac{L_{xy}}{\sigma L_{xy}}$	-	NO	2 – 7

**Table 4.3.:** Ranges of the various topological cut variables used within the multidimensional cut optimization.

$p_T$ -bins of the  $D^{*+}$  candidates. The optimized values for the topological cut variables as a function of the  $p_T$  of the  $D^{*+}$  and the obtained significances in the various  $D^{*+}$   $p_T$ -bins will be given in sec. 4.3.

## 4.2. Particle Identification

In order to further improve the significance of the  $D^{*+}$  signal at low  $p_T$ , namely for  $2 \text{ GeV}/c < p_T < 5 \text{ GeV}/c$ , a  $D^0$  daughter particle identification (PID) procedure based on the signals of the TPC (see chap. 3, sec. 3.2.2) and the TOF (see chap. 3, sec. 3.2.3) detectors was performed.

A charged particle passing through the TPC gas loses energy by depositing charge. The energy loss depends on the momentum and the rest mass of the traversing particle. The amount of energy lost per unit length  $dE/dx$  is proportional to the deposited charge per unit length, which is then measured by the TPC in units of a dimensionless TPC signal. For a given particle species with a given rest mass the TPC signal as a function of the momentum of the particle is fitted with the ALEPH TPC Bethe-Bloch parameterization [106]:

$$f(\beta\gamma) = \frac{P_1}{\beta^{P_4}} \left( P_2 - \beta^{P_4} - \ln \left( P_3 + \frac{1}{(\beta\gamma)^{P_5}} \right) \right) \quad (4.10)$$

with  $\beta\gamma = p/m$  and  $\beta = p/\sqrt{p^2 + m^2}$  in natural units.  $P_i$  are five free parameters that are fitted to data. Figure 4.11 shows the TPC signal as a function of particle momentum for

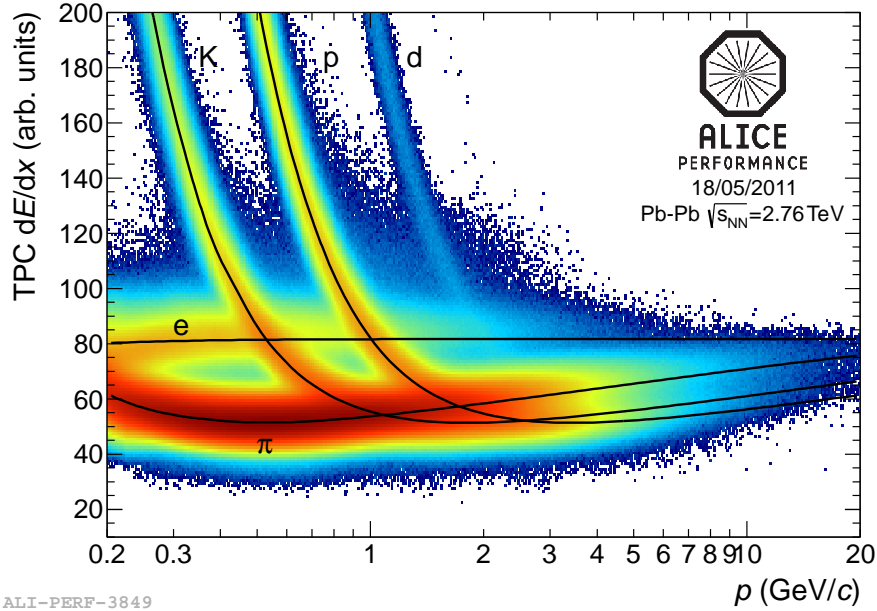


**Figure 4.11.:** The TPC signal as a function of the track momentum in minimum bias PbPb-collisions for tracks. The ALEPH TPC Bethe-Bloch parameterizations [106] (see eq. 4.10) fitted to the particle species bands are drawn in (black lines).

tracks reconstructed in PbPb-collisions. The proton, kaon, electron and pion bands are fitted with the formula presented in eq. 4.10. The relative  $dE/dx$ -resolution is about 6% in PbPb-collisions. When constructing the  $D^0$  candidates from track pairs as described in sec. 4.1, tracks that are assigned a kaon (pion) rest mass  $m_K$  ( $m_\pi$ ) are only selected if their measured TPC signal is within  $\pm 2\sigma$  of the kaon (pion) band shown in fig. 4.11.

The PID based on the signal of the TOF detector exploits the measured time  $t$  a particle needs to fly from the collision vertex to the TOF detector. With this information and using the track length  $l$ , the relativistic velocity  $\beta$  is given in natural units by  $\beta = t/l$ . On the other hand, the relation between  $\beta$  and the track momentum  $p$  in natural units is given by:

$$\beta = \frac{p}{E} = \frac{p}{\sqrt{m^2 + p^2}} \leftrightarrow p = \frac{\beta m}{\sqrt{1 - \beta^2}} \quad (4.11)$$

The measured relativistic velocity  $\beta$  as a function of the momentum  $p$  for tracks in minimum bias PbPb-collisions is shown in fig. 4.12. Clear bands for pions, kaons, protons and deuterons are visible. When constructing the  $D^0$  candidates from track pairs as described above, tracks that are assigned a kaon (pion) rest mass  $m_K$  ( $m_\pi$ ) are only selected if their measured relativistic velocity  $\beta$  is within  $\pm 3\sigma$  of the kaon (pion) band shown in fig. 4.12. The rejection of tracks outside the bands is only performed if the TOF signal is available. In case the particle does not reach the TOF detector because of absorption in the material between TPC and TOF or too low momentum, no TOF information is assigned to the

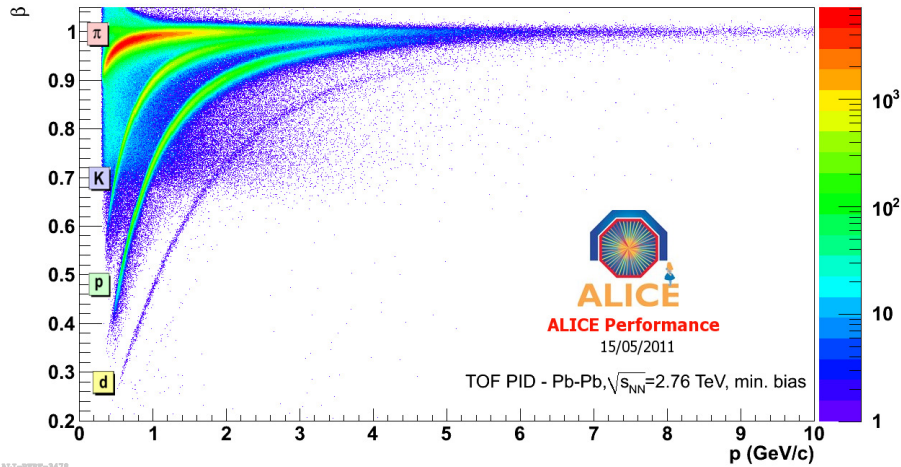


**Figure 4.12.:** The measured relativistic velocity  $\beta$  using the TOF time information and track length as a function of the track momentum in minimum bias PbPb-collisions for tracks.

track. The track is kept but only if it matches the TPC PID requirements and the single tracks cuts described above. If both TOF information and TPC information are available and their PID decisions disagree, e.g. the kaon candidate is identified as a kaon in the TPC and as a pion in TOF, the track is rejected.

### 4.3. Yield extraction

In order to extract the  $D^{*+}$  yield  $p_T$ -bin by  $p_T$ -bin in real PbPb-collision data, distributions of the  $\Delta M = M(K\pi\pi) - M(K\pi)$  variable introduced in eqs. 4.3, 4.4 of all  $D^{*+}$  candidates were created for 5  $p_T$ -bins. The  $D^{*+}$  candidates were selected by applying the single track cuts, the topological cuts and the particle identification procedure described above. Those distributions are fitted applying a log-likelihood maximization procedure using a sum of two functions, namely  $f_{SB} = f_S + f_B$ . The log-likelihood method is superior to the alternative  $\chi^2$ -minimization method in case the entries in the fitted bins are counts, which are Poisson-distributed. Especially in case of low statistics within the bins the  $\chi^2$ -minimization method gives wrong results assuming a Gaussian error of the bin entries, which is not correct. The two functions used for the fit are:

- a Gaussian function to describe the  $D^{*+}$   $\Delta M$ -peak:

$$f_S = \frac{I}{\sigma\sqrt{2\pi}} \exp - \frac{(\Delta M - \mu)^2}{2\sigma^2} \quad (4.12)$$

The parameter  $I$ , which is the integral of the Gaussian function as well as the mean  $\mu$  and the width  $\sigma$  are the free parameters of the fit. For the  $D^{*+}$   $\Delta M$ -peak description a Gaussian function is used because the momentum resolution of the reconstructed tracks is of Gaussian type. This Gaussian momentum resolution propagates to the resolution of the variable  $\Delta M(p_1, p_2, p_3) = M(K\pi\pi) - M(K\pi)$ , which depends on the 3 momenta  $p_1, p_2, p_3$  of the track triplet ( $K\pi\pi$ ).

- Two alternative background functions to describe the background shape:
  - a power-law function:  $f_B = a(\Delta M - m_\pi)^b$ , with  $a$  and  $b$  being the free parameters of the fit and  $m_\pi$  the rest mass of the charged pion;
  - a threshold function multiplied with an exponential function:  
 $f_B = a\sqrt{\Delta M - m_\pi} \cdot \exp(-b(\Delta M - m_\pi))$ , with  $a$  and  $b$  being the free parameters of the fit.

Both background functions are of empirical kind and have no strict physical justification. Both describe the background well as we will see below in the  $\Delta M$ -range  $m_\pi - 0.16 \text{ GeV}/c^2$ . The power-law function is used as default background-function, the threshold function as a consistency check and also for systematic uncertainty determination originating from the yield extraction in the  $D^{*+} v_n$ -analysis described in chap. 5, sec. 5.3.

Fits of the Gaussian function added to the power-law function  $f_{SB} = f_S + f_B$  in six different  $p_T$ -regions to the measured  $\Delta M$ -distribution for the  $D^{*+}$  and its charge conjugate  $D^{*-}$  are shown in fig. 4.13. The topological cut-set used for the background rejection are optimized on data with the procedure described at the end of sec. 4.1. The values for the topological cuts are given in tab. 4.4 labeled as cut-set 1. The values for the statistical significance, the extracted signal, the background, the mean of the Gaussian function  $\mu$  and the width of the Gaussian function  $\sigma$  together with their errors are calculated as follows:

- The mean  $\mu$  and the width  $\sigma$  are free fit parameters of the Gaussian function  $f_S(\Delta M)$ .
- The signal is given as the integral of the Gaussian function within  $\pm 3\sigma$  of the width divided by the bin width of the  $\Delta M$ -histogram:

$$S = \frac{1}{\text{bin width}} \int_{-3\sigma}^{3\sigma} f_S(\Delta M) d\Delta M. \quad (4.13)$$

The error of the signal is given as the relative error of the free parameter  $I$  of the Gaussian function, see eq. 4.12, multiplied by the signal:  $\Delta S = (\Delta I/I) \cdot S$ .

- The background is given as the integral of the background function within  $\pm 3\sigma$  of the width of the Gaussian function  $f_B(\Delta M)$  divided by the bin width of the  $\Delta M$ -histogram:

$$B = \frac{1}{\text{bin width}} \int_{-3\sigma}^{3\sigma} f_B(\Delta M) d\Delta M. \quad (4.14)$$

The error of the background is given as the relative error of the total background, which is given as  $\Delta B_{total}/B_{total} = 1/\sqrt{N_{total}}$ , multiplied by the background:  $\Delta B = (1/\sqrt{N_{total}}) \cdot B$ .  $N_{total}$  is the number of the total entries of the  $\Delta M$ -histogram outside the  $\pm 3\sigma$ -region left and right to the mean  $\mu$  of  $D^{*+}$   $\Delta M$ -peak.

- The significance is given by eq. 4.5 and the error is given by full error propagation of the signal and background assuming uncorrelated behavior of the two quantities.

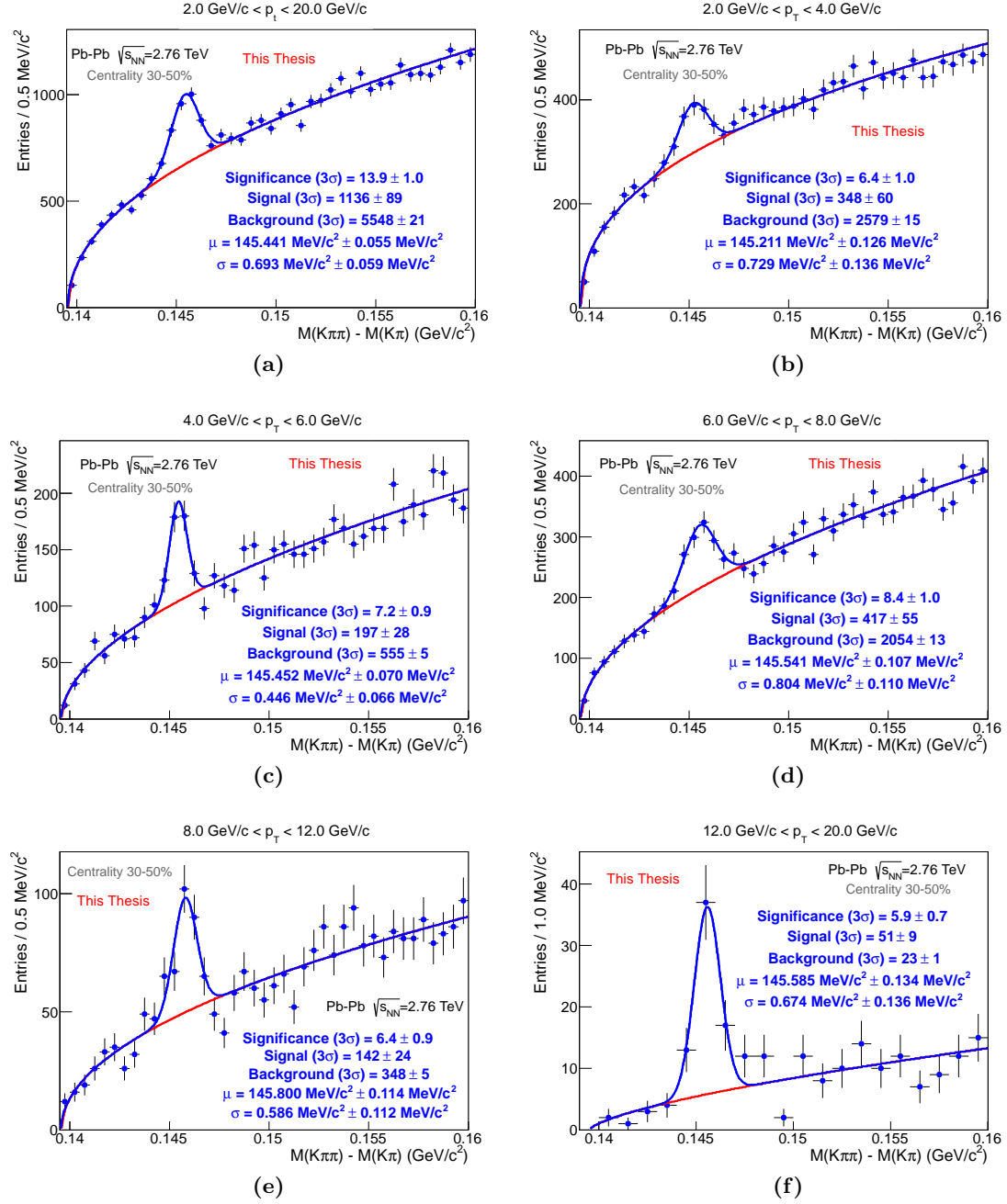


**Figure 4.13:**  $D^{*+}$  yield extraction by fits of a Gaussian function added to the power-law function  $f_{SB} = f_S + f_B$ , for details see text, to the measured  $\Delta M$ -distribution in six different  $p_T$ -regions of the  $D^{*+}$ :  $2 \text{ GeV}/c < p_T < 16 \text{ GeV}/c$  (a),  $2 \text{ GeV}/c < p_T < 4 \text{ GeV}/c$  (b),  $4 \text{ GeV}/c < p_T < 6 \text{ GeV}/c$  (c),  $6 \text{ GeV}/c < p_T < 8 \text{ GeV}/c$  (d),  $8 \text{ GeV}/c < p_T < 12 \text{ GeV}/c$  (e) and  $12 \text{ GeV}/c < p_T < 20 \text{ GeV}/c$  (f). The mean  $\mu$  and the width  $\sigma$  of the Gaussian function as well as the extracted numbers for the signal, background and statistical significance are drawn in. The centrality range is 30-50%, the number of events is  $9.5 \cdot 10^6$  and the used topological cut-set is cut-set 1 listed in tab. 4.4.

#### 4. $D^{*+}$ reconstruction strategy

According to fig. 4.13 the width of the Gaussian function is of the order of  $\sigma \approx 0.4 - 0.8 \text{ MeV}/c^2$  depending on the  $p_T$  of the  $D^{*+}$  and hence much smaller than e.g. the width of the distribution of the reconstructed  $D^0$  invariant mass shown in fig. 4.5 (left) labeled as signal. The reason for this behavior as explained at the beginning of chap. 4 is that detector resolution  $\Delta(M(K\pi\pi) - M(K\pi))$  is mainly determined by the momentum resolution of the soft pion from the  $D^{*+} \rightarrow D^0\pi^+$  decay. The momentum resolution contribution of the decay daughters of the subsequent decay channel  $D^0 \rightarrow K^-\pi^+$  to the total resolution  $\Delta(M(K\pi\pi) - M(K\pi))$  is small. This effect is due to the small mass difference of  $D^{*+}$  and  $D^0$  and the small momentum of the soft pion with respect to the momenta of the decay daughters of the  $D^0$  meson. This behavior was studied in the Hijing+Pythia Monte-Carlo simulations described in sec. 4.1. In particular the width of the  $D^{*+} \Delta M$ -peak of the  $D^{*+}$  for tagged  $D^{*+}$  mesons was studied. The  $D^{*+} \Delta M$ -peak including a fit with a Gaussian function using Hijing+Pythia Monte-Carlo simulations for  $D^{*+}$  mesons with a  $p_T$  of  $6 \text{ GeV}/c < p_T < 8 \text{ GeV}/c$  is shown in fig. 4.14a. Figure 4.14c shows the ratio of the width of the  $D^{*+} \Delta M$ -peak of the  $D^{*+}$  meson as a function of its  $p_T$  as measured

Cut var.	DCA $_{\pi K}$	$ M(K\pi) - m(D^0) $	$ \cos(\theta_{xy}^{\text{poi.}}) $	$ \cos(\theta^*) $	$d_{xy}^K \times d_{xy}^\pi$	$\frac{L_{xy}}{\sigma L_{xy}}$
unit	cm	MeV/ $c^2$	-	-	$10^{-3}\text{cm}^2$	-
type	upper	upper	lower	upper	upper	lower
$p_T$ -bin						
[GeV/ $c$ ]						
<b>Set 1</b>						
2 - 3	0.02	38	0.991	0.62	-0.332	6.75
3 - 4	0.03	26	0.992	0.74	-0.404	6.25
4 - 5	0.03	36	0.992	0.74	-0.116	5.50
5 - 6	0.04	26	0.997	0.66	-0.116	5.00
6 - 7	0.015	56	0.995	0.66	0.100	4.75
7 - 8	0.02	40	0.996	0.86	0.100	2.75
8 - 18	0.015	56	0.993	0.9	0.100	4.00
18 - 20	0.05	60	0.9905	0.9	0.100	2.50
<b>Set 2</b>						
2 - 3	0.02	28	0.992	0.54	-0.332	6.75
3 - 4	0.03	24	0.998	0.74	-0.404	6.25
4 - 5	0.03	30	0.999	0.74	-0.116	5.75
5 - 6	0.04	22	0.997	0.58	-0.188	6.00
6 - 7	0.025	50	0.998	0.86	-0.332	6.00
7 - 8	0.02	52	0.998	0.74	0.100	3.50
8 - 18	0.015	56	0.996	0.9	0.100	5.25
18 - 20	0.04	60	0.991	0.9	0.100	3.00

**Table 4.4.:** Two alternative lists of topological cuts used for the  $D^{*+}$  yield extraction in the centrality range 30-50% in PbPb-collision data. "type" specifies whether the applied cut is an upper cut or an lower cut on the value of the corresponding cut variable. Additional single track cuts are explained and listed in sec. 4.1, the particle identification cuts are described in sec. 4.2 and the lower cut on the cosine of the pointing angle in three dimensions  $\cos(\theta_{\text{pointing},xyz})$  is fixed at  $\cos(\theta_{\text{pointing},xyz}) > 0.9$  for all  $p_T$ -regions.

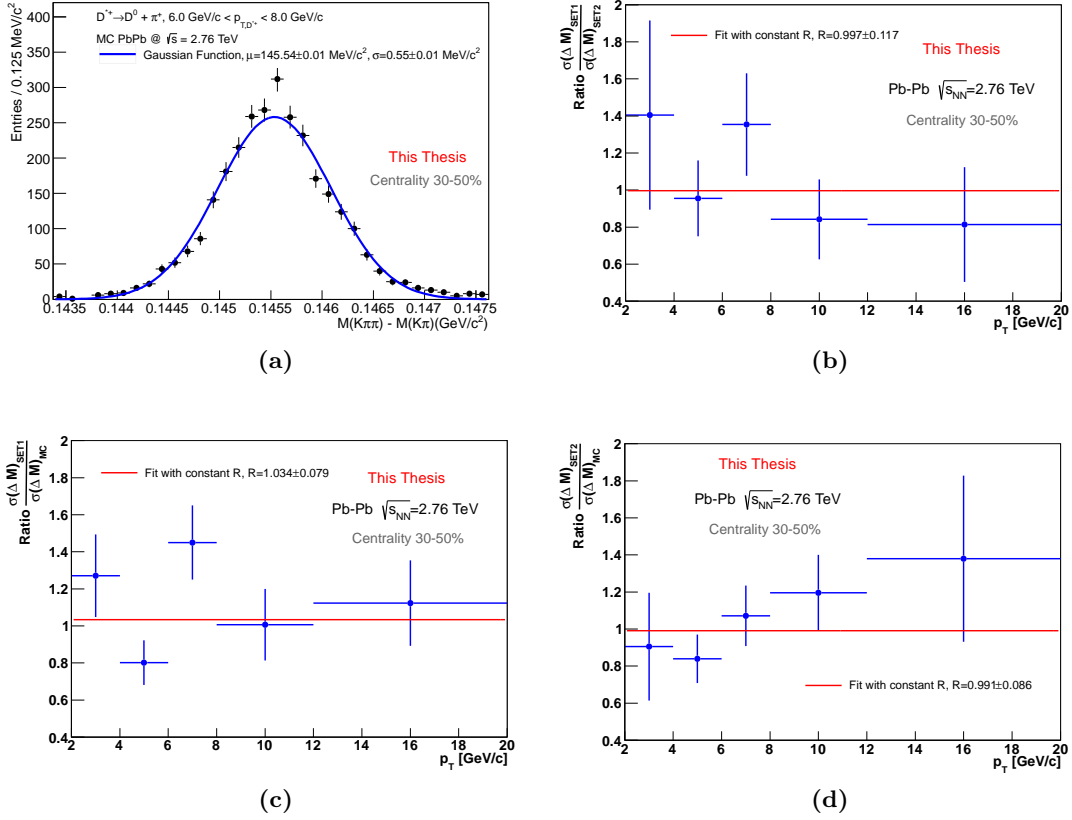


**Figure 4.14.:** (a)  $D^{*+}$   $\Delta M$ -peak including a fit with a Gaussian function using PbPb Hijing+Pythia Monte Carlo simulations [99–102] with a full ALICE detector description for  $D^{*+}$  mesons with a  $p_T$  of  $6 \text{ GeV}/c < p_T < 8 \text{ GeV}/c$ . (b), (c) and (d): Ratios of the resolution of the variable  $\Delta M = M(D^{*+}) - M(D^0)$  within the  $D^{*+}$  and  $D^0$  reconstruction procedure as a function of  $p_T$  of the  $D^{*+}$  in PbPb-collisions in the centrality range 30-50% for different combinations: (b) the resolution obtained with cut-set 1 with real PbPb-collision data divided by the resolution obtained with cut-set 2, (c) the resolution obtained with cut-set 1 with real PbPb-collision data divided by the resolution obtained with PbPb Hijing+Pythia Monte Carlo simulations [99–102] with a full ALICE detector description, (d) the resolution obtained with cut-set 2 with real PbPb-collision data divided by the resolution obtained with PbPb Hijing+Pythia Monte Carlo simulations [99–102] with a full ALICE detector description. For details about the two cut-sets see text and tab. 4.4.

in real PbPb-collision-data using cut-set 1 listed in tab. 4.4 and as measured in the Hijing+Pythia Monte-Carlo simulations in a centrality range of 30-50%. The ratio was fitted with a constant function and yields a mean ratio of  $R = 1.034 \pm 0.079$  being consistent with 1. In two out of five  $p_T$ -bins, namely in the  $p_T$ -ranges  $4 \text{ GeV}/c < p_T < 6 \text{ GeV}/c$  and  $6 \text{ GeV}/c < p_T < 8 \text{ GeV}/c$ , the ratio deviates more than  $1\sigma$  in units of the error of the ratio from being 1:  $1.7\sigma$  in the  $p_T$ -range  $4 \text{ GeV}/c < p_T < 6 \text{ GeV}/c$  and  $2.3\sigma$  in the  $p_T$ -range  $6 \text{ GeV}/c < p_T < 8 \text{ GeV}/c$ . No systematic error due to this discrepancy was assigned on the measured  $v_n$  when performing the  $v_n$ -extractions in chap. 5. In order to investigate the impact of changing the topological cuts on the extracted  $D^{*+}$   $v_n$ , an alternative cut-set, listed in tab. 4.4 and labeled as cut-set 2, was obtained and used

for the  $v_n$ -measurement as consistency check. In order to obtain this alternative cut-set the topological cut value were tuned so that the extracted signal is at least 20% lower in all  $p_T$ -bins with respect to the signal extracted using cut-set 1. The motivation for the second cut-set was to have a cut-set with alternative and at the same time tighter selections and with an improved signal to background ratio. At the same time the statistical significance was maximized. Figure 4.14d shows the ratio of the width of the  $\Delta M$ -peak of the  $D^{*+}$  as a function of its  $p_T$  as measured in real PbPb-collision-data using the cut-set 2 and as measured in Hijing+Pythia Monte-Carlo simulations in a centrality range of 30-50%. In this case the mean ratio obtained by fitting with a constant function is  $R = 0.991 \pm 0.086$  being consistent with 1. Here in only one  $p_T$ -bin, namely for a  $p_T$  of the  $D^{*+}$  of  $4 \text{ GeV}/c < p_T < 6 \text{ GeV}/c$ , the ratio deviates more than  $1\sigma$  in units of the error of the ratio from being 1. The deviation is  $1.2\sigma$ . Finally, fig. 4.14b shows the ratio of the width of the  $\Delta M$ -peak of the  $D^{*+}$  as a function of its  $p_T$  as measured in real PbPb-collision-data using the cut-set 1 and cut-set 2. The value for the mean ratio R is inserted.

Due to the overall higher statistical significance of the  $D^{*+}$  signal as depicted in fig. 4.15 and hence smaller statistical error of the  $v_n$ -measurements, the cut-set 1 was chosen as

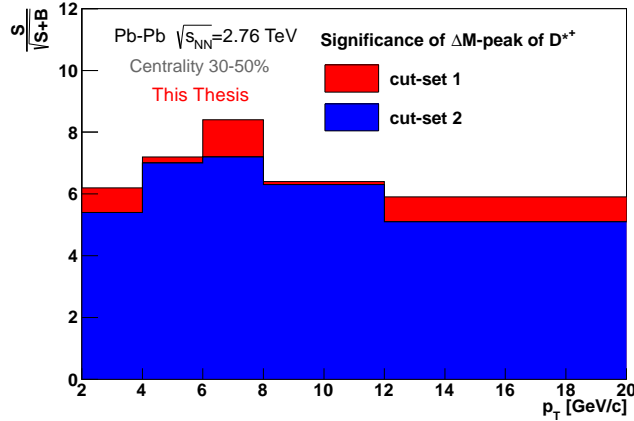


**Figure 4.15.:** Statistical significance of the  $D^{*+}$  signal in PbPb-collisions in the centrality range 30-50% obtained with the two alternative cut-sets, cut-set 1 and cut-set 2, see tab. 4.4 for details.

the default one.  $D^{*+}$   $v_n$  results obtained with cut-set 2 are used as a consistency check. Another consistency check, which also entered into the systematic error evaluation of the  $v_n$ -measurements, was to extract the  $D^{*+}$  yield with a bin-counting approach. In this case the values for the extracted signal and the background together with their errors are calculated as follows:

- The background is given by the integral of the background function within  $\pm 3.5 \text{ MeV}/c^2$  left and right to the PDG-value of the mass difference  $\Delta M = 145.421 \text{ MeV}/c^2$  [10]

divided by the bin width of the  $\Delta M$ -histogram:

$$B = \frac{1}{\text{bin width}} \int_{(145.421-3.5) \text{ MeV}/c^2}^{(145.421+3.5) \text{ MeV}/c^2} f_B(\Delta M) d\Delta M. \quad (4.15)$$

The error of the background is given by the relative error of the total background, which is given as  $\Delta B_{total}/B_{total} = 1/\sqrt{N_{total}}$ , multiplied by the background:

$\Delta(B) = (1/\sqrt{N_{total}}) \cdot B$ .  $N_{total}$  is the number of the total entries of the  $\Delta M$ -histogram outside the  $\pm 3\sigma$ -region left and right to the mean  $\mu$  of  $D^{*+}$   $\Delta M$ -peak.

- The signal is given by the difference between the total entries  $N_{\text{total}, \pm 3.5 \text{ MeV}/c^2}$  of the  $\Delta M$ -histogram  $\pm 3.5 \text{ MeV}/c^2$  left and right to the PDG-value of the mass difference  $\Delta M = 145.421 \text{ MeV}/c^2$  [10] and the value for the background  $B$ :  
 $S = N_{\text{total}, \pm 3.5 \text{ MeV}/c^2} - B$ . The error of the signal is given by the sum of the squared errors of both expressions:  $\Delta S = \sqrt{N_{\text{total}, \pm 3.5 \text{ MeV}/c^2}^2 + B^2}$ .

The yield extraction using this approach has the advantage that it does not depend on the width of the Gaussian function  $f_S$ . However, the integration window  $W$  around the PDG-value of the  $\Delta M$ -quantity was chosen large to be on the safe side that all of the  $D^{*+}$  signal is considered performing the integration. Choosing  $W = 7 \text{ MeV}/c^2$  ensures that even in the case when the sigma of the Gaussian function is at its maximum being  $\sigma = 0.8 \text{ MeV}/c^2$ , i.e. in the  $D^{*+}$   $p_T$ -range of  $6 \text{ GeV}/c < p_T < 8 \text{ GeV}/c$  using cut-set 1 (see fig. 4.13d), the integration window includes at least  $\pm 4\sigma$  of the signal region. The bin-counting method has the disadvantage that the statistical error of the signal is larger than in the method presented above where the integral of the Gaussian function  $f_S$  is used for the  $D^{*+}$  signal value. This will become evident in chap. 5, where values including the statistical error of the  $D^{*+}$   $v_n$  will be presented. A larger statistical error for the  $D^{*+}$  signal yields a larger statistical error for the measured  $D^{*+}$   $v_n$ . Therefore the default yield extraction method is the one using the integral of the Gaussian function and the method based on bin counting is used for determination of systematic errors from yield extraction within the  $v_n$ -measurements.

## 5. Road to the final results for the $D^{*+} v_2$ - and $D^{*+} v_3$ -anisotropy parameters

In this chapter the road to the azimuthal anisotropy parameters  $v_2$  and  $v_3$  of the  $D^{*+}$  meson is described. The symbol  $D^{*+}$  stands for both  $D^{*+}$  and  $D^{*-}$  and the decay channel  $D^{*+} \rightarrow D^0\pi^+$  for both  $D^{*+} \rightarrow D^0\pi^+$  and  $D^{*-} \rightarrow \overline{D^0}\pi^-$ . The chapter starts with a technical part about the symmetry planes  $\Psi_2$  and  $\Psi_3$  determination. As next step, the  $D^{*+} v_2$ - and  $D^{*+} v_3$ -extraction approaches are presented. Finally, the results using the various approaches are compared with each other and systematic errors are determined.

### 5.1. Event plane determination and flattening

The key ingredient to measure the  $D^{*+} v_2$  and  $D^{*+} v_3$  with the event plane method presented in chap. 2 is to determine the event plane angles  $\Psi_2$  and  $\Psi_3$  event-by-event. For this purpose the TPC and the VZERO sub-detectors described in chap. 3 are used.

#### TPC event planes $\Psi_2$ and $\Psi_3$

The event plane angles  $\Psi_2$  and  $\Psi_3$  are estimated using the Q-vector as explained in chap. 2 and eq. 2.19:

$$Q_n = \left( \frac{\sum_{i=0}^N w_i \cos(n\phi_i)}{\sum_{i=0}^N w_i \sin(n\phi_i)} \right) \quad \Psi_n = \frac{1}{n} \tan^{-1} \left( \frac{Q_{n,y}}{Q_{n,x}} \right). \quad (5.1)$$

The angle values  $\phi_i$  correspond to the reconstructed track angles from all tracks of one event using the TPC only to determine the track parameters. The tracks, which were used to reconstruct the  $D^{*+}$  mesons, are removed from the Q-vector determination candidate-by-candidate to remove auto-correlations. Thus every  $D^{*+}$  candidate has its own event plane angle and its own  $\Delta\phi = \phi_{D^{*+}} - \Psi_n$ . The ITS is not used to determine the track parameters entering into the Q-vector determination because it was not fully operational during the 2011 PbPb-run and has large efficiency holes. The goal is to have a  $\phi$ -distribution of tracks that is as few as possible affected by the detector imperfectness to avoid detector effects in the event plane determination. The following track quality cuts were applied to the TPC-only tracks:

- at least 50 clusters in the TPC and a  $\chi^2/\text{cluster}(\text{TPC}) < 4$  to ensure an acceptable  $p_T$ - and  $\phi$ -determination;
- a distance of closest approach to the primary vertex  $d_z < 3.2$  cm in  $z$  and  $|d_{xy}| < 2.4$  cm in the  $xy$ -plane to select primary tracks coming from the primary vertex;

- a  $p_T$  between 0.15 and 20 GeV/ $c$  and a pseudorapidity of  $|\eta| < 0.8$ ;
- rejection of "kinks", e.g. electrons that suffered Bremsstrahlung-emission or kaons and pions that decayed into muons and neutrinos in the active detector volume. The neutrinos carry away a fraction of energy and the track has a kink at the decay position, which is recognized by the tracking software.

The  $\phi$ -distribution of the tracks after the quality cuts described above is shown in fig. 5.1. An efficiency dip of about 6% at  $\phi \approx 3$  rad is visible. This efficiency dip is due to sectors

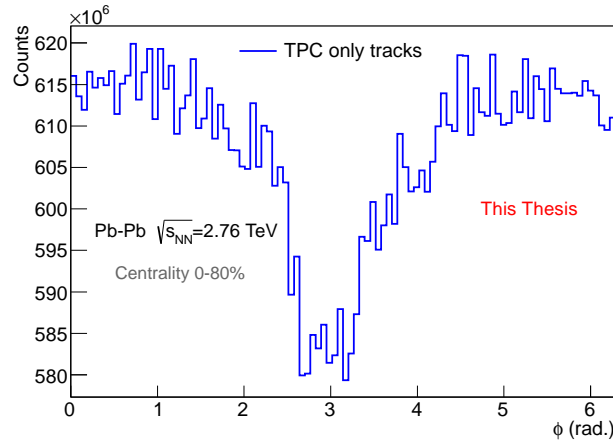


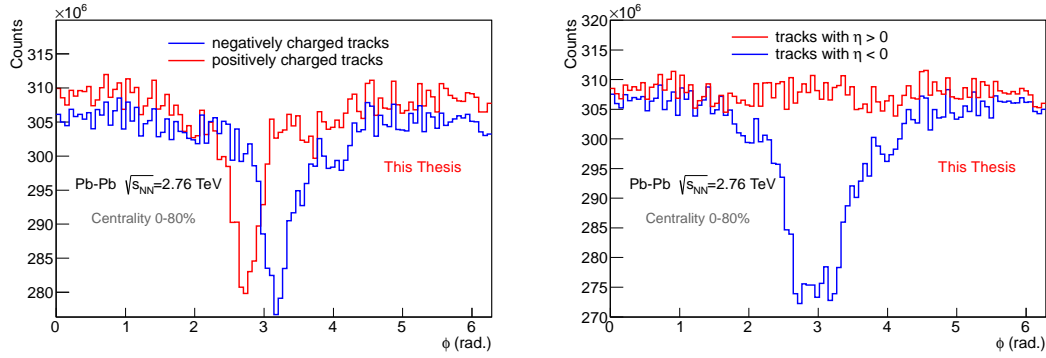
**Figure 5.1.:**  $\phi$ -distribution of TPC only tracks used for the TPC event plane determination after quality cuts (see text).

of the TPC that had to be operated with a lower gain or were even switched off during some runs because of the large luminosity during the 2011 PbPb-run. This caused noise and high voltage trips in some TPC sectors. This efficiency dip and also the efficiency fluctuations right and left to the dip were corrected by applying  $\phi$ -weights  $w_\phi(\phi)$ . Without  $\phi$ -weights the event plane angle distribution is biased by detector imperfectness effects. The event plane angle has to be determined by the anisotropy of the  $\phi$ -distribution of particle coming from the primary vertex on an even-by-event basis and a modulation of the  $\phi$ -distribution caused by detector inefficiencies disturbs this procedure. The  $\phi$ -weights,  $w_\phi(\phi)$ , are given by the inverse of the distribution shown in fig. 5.1. They are determined as a function of:

- Time, respectively data taking run number. The mentioned high voltage trips occurred only during a fraction of the runs during the data taking period.
- Pseudorapidity  $\eta$ . The problematic sectors were placed on the negative  $\eta$ -side of the TPC. Therefore tracks require different  $\phi$ -weights depending on their  $\eta$ .
- Track charge. The bending of tracks depends on their charge sign and therefore they cross the problematic TPC sectors in a different way.

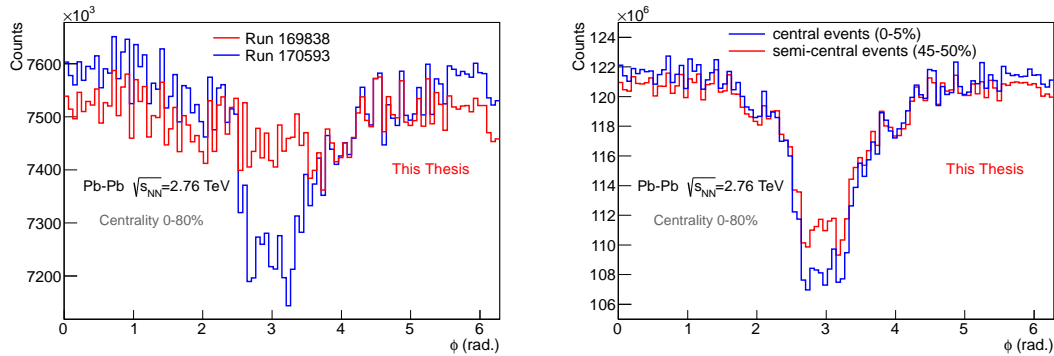
- Collision centrality. The efficiency weakly depends on the detector occupancy and hence on the collision centrality. The magnitude of the mentioned efficiency dip shown in fig. 5.1 depends accordingly on the collision centrality.

Figure 5.2 (left) shows the  $\phi$ -distribution for positively and negatively charged tracks. Both distributions differ significantly which requires different  $\phi$ -weights for each track type.



**Figure 5.2.:** (left)  $\phi$ -distribution of TPC only tracks used for the TPC event plane determination for positively and negatively charged tracks. (Right)  $\phi$ -distribution of TPC only tracks used for the TPC event plane determination for tracks from the positive, i.e. with  $0.0 < \eta < 0.8$ , and negative, i.e. with  $-0.8 < \eta < 0.0$ , TPC hemisphere.

Figure 5.2 (right) shows the  $\phi$ -distribution for tracks from the positive TPC hemisphere ( $\eta > 0$ ) and from the negative ( $\eta < 0$ ) TPC hemisphere. As the efficiency changes drastically as a function of  $\eta$ , the  $\phi$ -weights are calculated in bins with a width of  $\Delta\eta = 0.1$ . Figure 5.3 (left) shows the  $\phi$ -distribution for two different runs. During run 170593 some TPC read out chambers had problems. IROC A09 and IROC C13 were off and



**Figure 5.3.:** (left)  $\phi$ -distribution of TPC only tracks used for the TPC event plane determination for data taking runs 169838 and 170593. During run 169838 the TPC was fully operational, during run 170593 IROC A09 and IROC C13 were off and in OROC C08 the anode voltage was lowered by 50V. (Right)  $\phi$ -distribution of TPC only tracks used for the TPC event plane determination for tracks from central and semi-central events.

in OROC C08 the anode voltage was lowered by 50V. The OROCs and IROCs were

introduced in chap. 3, sec. 3.2.2. The labels "C" and "A" stand for C-side, respectively A-side of the ALICE detector, see chap. 3, and the numbers for an internal numbering scheme of the  $2 \times 2 \times 16 = 64$  read out chambers. During run 169838 the TPC was fully operational. As the efficiency changes as a function of run number, the  $\phi$ -weights are calculated for each run separately. Finally, fig. 5.3 (right) shows the  $\phi$ -distribution of TPC tracks for two different collision centralities, namely 0-5% and 45-50% for tracks from the negative TPC hemisphere. Here the efficiency dip depends weakly on the centrality and thus the  $\phi$ -weights are calculated in bins with a width of  $\Delta_{\text{cent}} = 5\%$ . In addition to the  $\phi$ -weights  $w_\phi(\phi)$  a track weight as a function of the track transverse momentum  $p_T$  is applied. The weight is proportional to the  $p_T$  of the track until  $p_T = 2$  GeV and then is kept constant. This is done because the  $v_2$  and  $v_3$  rise as a function of  $p_T$ , see fig. 2.14 in chap. 2. Applying a  $p_T$ -weighting gives more weight to tracks that show a higher  $v_n$  and this improves the event plane resolution [33]. The weights  $w_i$  in eq. 5.1 are thus given by  $w_i = p_{T,i} \cdot w_{\phi,i}(\phi)$ . Figure 5.4 shows the uncorrected (blue line) and the corrected  $\phi$ -distribution (red line) using the  $\phi$ -weights  $w_{\phi,i}(\phi)$ . As expected, the corrected

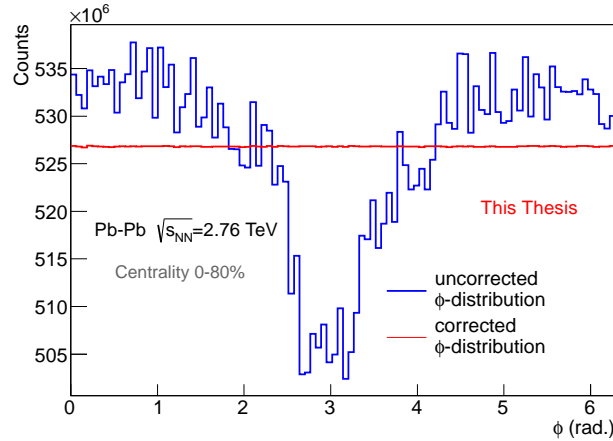


**Figure 5.4.:**  $\phi$ -distribution of TPC only tracks used for the TPC event plane determination corrected for efficiency holes and uncorrected.

$\phi$ -distribution does not show efficiency holes anymore. Moreover, the fluctuations on a smaller scale left and right to the efficiency dip are removed. Figure 5.5 shows the event plane angle  $\Psi_2$  (left) and  $\Psi_3$  (right) distributions for the full TPC hemisphere (red datapoints), i.e. using tracks with  $|\eta| < 0.8$ , and only the positive TPC hemisphere (blue datapoints), i.e. using tracks with  $0.0 < \eta < 0.8$ , calculated out of Q-vectors using  $p_T$ - and  $\phi$ -weights. The expected distributions must be homogeneous because both event plane angles are randomly distributed even-by-event. The large modulations of the full TPC distributions are due to remaining detector effects, which are not fully cured by the  $\phi$ -weights method. Therefore for the  $\Psi_3$  event plane angle determination another flattening technique was applied "on top" to remove the remaining detector imperfectness effects. As explained in [33] remaining detector effects, which impose a bias on the event plane angle determination, can be removed by the *recentering*-technique. Using this method one subtracts event-by-event from the Q-vector components  $Q_y$  and  $Q_x$  the means of the

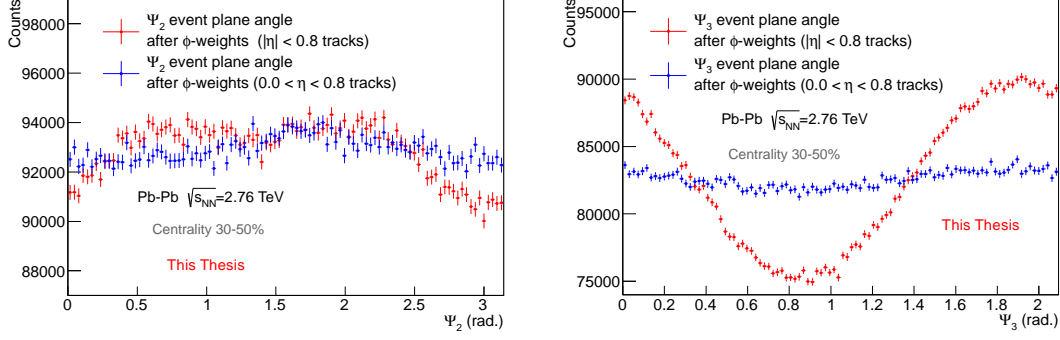


**Figure 5.5.:** Event plane angle  $\Psi_2$  (left) and  $\Psi_3$  (right) distributions for the full TPC hemisphere (red) and only the positive TPC hemisphere (blue) calculated out of Q-vectors using  $p_T$ - and  $\phi$ -weights.

components  $\langle Q_y \rangle$  and  $\langle Q_x \rangle$  averaged over many events:

$$Q_{x,y,corr} = \frac{Q_{x,y,uncorr} - \langle Q_{y,x} \rangle}{\text{RMS}(Q_{x,y})} \text{ (run - number, } \eta, \text{ centrality)} \quad (5.2)$$

This procedure is done as function of collision centrality, time (i.e run number), and  $\eta$  because the shifts  $\langle Q_{n,y} \rangle$  and  $\langle Q_{n,x} \rangle$  depend on these three quantities. Moreover, the final corrected event-by-event Q-components  $Q_{x,y,corr}$  are given in units of the RMS of the  $Q_{x,y}$ -distributions in order to have a consistent unit (i.e. the RMS) in all centrality percentiles. Figure 5.6 shows the performance of this technique applied to the determi-

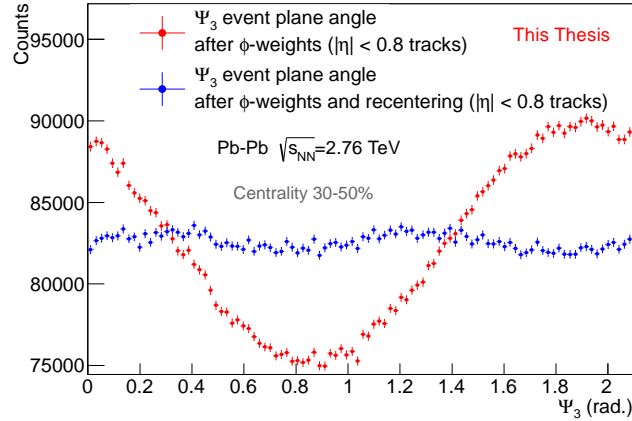


**Figure 5.6.:** Event plane angle  $\Psi_3$  distribution for the full TPC hemisphere after  $\phi$ -weights only (red datapoints) and after  $\phi$ -weights and recentering procedure (blue datapoints).

nation of the  $\Psi_3$  event plane angle. The blue datapoints show the event plane angle  $\Psi_3$  distribution for the full TPC hemisphere after  $\phi$ -weights and the recentering procedure. The modulation of the  $\Psi_3$  distribution is largely removed with respect to the  $\Psi_3$  angle distribution represented by the red datapoints, which correspond the  $\Psi_3$  distribution for

the full TPC hemisphere applying  $\phi$ -weights only.

### VZERO event plane

An alternative determination of the  $\Psi_3$  and  $\Psi_2$  event plane angles is to use the amplitudes of the signals in the 8 segments of the two VZERO (VZERO-A and VZERO-C) detectors at forward and backward rapidities, see chap. 3, sec. 3.2. In this case eq. 5.1 is used, either, for determination of the angles. However, the angles  $\phi_i$  are defined by the central azimuth of the  $i$ -th sector of the VZERO detector. The assumption is made that the amplitude of the signal in the  $i$ -th sector is proportional to the track multiplicity and therefore the quantities  $\cos(n\phi_i)$  and  $\sin(n\phi_i)$  in eq. 5.1 are multiplied on a event-by-event basis by the amplitude of the signal in the  $i$ -th sector to determine the event plane angles. It is possible to get the event plane angle of each individual VZERO sub-detector (VZERO-A and VZERO-C) or to sum the signals for each segment to get one event plane angle out of the two sub-detectors (full VZERO). Moreover,  $\phi$ -weights are used for each VZERO sub-detector separately to account for different efficiencies in the individual segments. These  $\phi$ -weights are the inverse of the distribution of the VZERO amplitudes as a function of  $\phi$  averaged over many events. In addition, a recentering procedure is carried out but only for the VZERO  $\Psi_2$  event plane angle. Figure 5.7 (left) shows the full VZERO  $\Psi_2$  event plane angle distribution after  $\phi$ -weighting and recentering and fig. 5.7 (right) the full

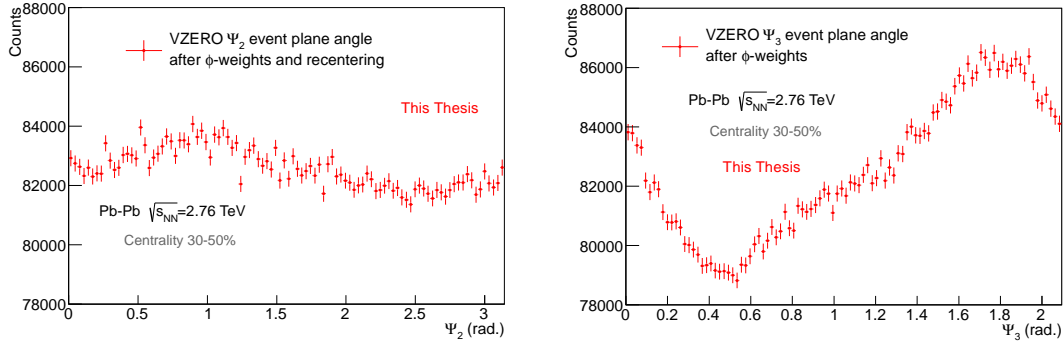


**Figure 5.7.:** Event plane angle  $\Psi_2$  (left) and  $\Psi_3$  (right) distributions using the full VZERO detector. For determination of the event plane angle  $\Psi_2$   $\phi$ -weights and a recentering procedure are performed, for determination of the event plane angle  $\Psi_3$   $\phi$ -weights only are used.

VZERO  $\Psi_3$  event plane angle distribution after  $\phi$ -weighting only. The event plane angle  $\Psi_3$  distributions shown in fig. 5.7 (right) shows a large modulation due to a currently missing recentering procedure. Therefore the event plane angle  $\Psi_3$  determined by the VZERO detector was not used in the systematic error study of the  $v_3$ -analysis addressed in detail in sec. 5.3. Possible non-flow effects of the measured  $D^{*+} v_3$  were quantified using a special  $\eta$ -gap analysis using the TPC only. This type of analysis will be presented further below. The advantage of the event plane determination using the VZERO detector with respect to the determination using the TPC in the full  $\eta$ -range is namely the  $\eta$ -separation of the tracks that are used to determine the event plane and the reconstructed  $D^{*+}$  mesons. This largely removes non-flow contributions to the measured  $v_n$ , see chap. 2, sec. 2.3. The

disadvantage is the poorer event plane resolution as will be show as next step and thus a larger statistical error of the  $v_n$ -measurement.

### Event plane resolution

As explained in chap. 2, sec. 2.3, the observed  $v_n^{\text{obs}}$  needs to be corrected by a factor  $C_n$  to account for the finite event plane resolution. This factor is given by:

$$C_n = \frac{1}{R_n} = \frac{1}{\langle \cos(n(\Psi_n - \Psi_{R,n})) \rangle} \quad (5.3)$$

with  $\Psi_n$  being the event plane angle of  $n$ -th order and  $\Psi_{r,n}$  the nominal event plane angle of  $n$ -th order. The nominal event plane angle is unknown but the correction  $C_n$  can be determined by the 2-sub-events method and the 3-sub-events method. For details about the different resolution determination techniques, see 2, sec. 2.3. Figure 5.8 (left) shows the  $\Psi_2$  event plane resolutions  $R_2$  with the following configurations:

- Resolution of the positive  $\eta$  TPC event plane angle  $\Psi_2$ , determined with the 2-sub-events method by splitting the positive  $\eta$  TPC events by a random selection of tracks.
- Resolution of the full  $\eta$  TPC event plane angle, determined with the 2-sub-events method by splitting the full  $\eta$  TPC events by a random selection of tracks.
- Resolution of the full VZERO event plane angle  $\Psi_2$ , determined with the 3-sub-events method. The three sub-events used to determine the resolution of the VZERO event plane angle  $\Psi_2$  are:
  1. the full VZERO sub-event, i.e charged particles detected with VZERO-A and VZERO-C;
  2. the positive  $\eta$  TPC sub-event using tracks with a pseudorapidity of  $0.0 < \eta < 0.8$ ;
  3. the negative  $\eta$  TPC sub-event using tracks with a pseudorapidity of  $-0.8 < \eta < 0.0$ ;

The better the event plane resolution, the smaller the correction factor that needs to be applied to correct the observed  $v_n^{\text{obs}}$ . The observed  $v_n^{\text{obs}}$  has a statistical error which increases with increasing correction factor, i.e. with decreasing event plane resolution. Therefore for the central  $D^{*+} v_2$  value, the TPC was used to determine the event plane angle. Figure 5.8 (left) shows that the TPC  $\Psi_2$  event plane angle resolution is by 10%-20% larger, depending on the centrality percentile, than the VZERO  $\Psi_2$  event plane angle resolution, even if only the positive  $\eta$  TPC side is used. According to fig. 5.5 (left) the flatness quality is best for the positive  $\eta$  TPC  $\Psi_2$  event plane angle distribution. Because of the acceptable resolution and best flatness quality the event plane determination configuration for the final  $D^{*+} v_2$ -measurement was TPC event plane using tracks from the positive hemisphere. The resolution  $R_2$  for the positive  $\eta$  TPC event plane angle, determined with the following three methods is shown in fig. 5.8 (left):

- 2-sub-events method by splitting the events by a random selection of tracks;

- 2-sub-events method by splitting the events by selecting positively and negatively charged tracks;
- 3-sub-events method; the three sub-events used to determine the resolution of the TPC event plane angle  $\Psi_2$  are:
  1. the positive  $\eta$  TPC sub-event;
  2. the VZERO-A sub-event, i.e charged particles detected with VZERO-A only;
  3. the VZERO-C sub-event, i.e charged particles detected with VZERO-C only;

According to these results the resolution estimation is not consistent within these three methods. The reason for this behavior was still not fully understood at the end of writing up this thesis and under investigation. The most probable reason for this discrepancy is a different non-flow correlation between the 2 (in the 2-sub-events method), respectively 3 (in the 3-sub-events method) sub-events. As pointed out in chap. 2, sec. 2.3 and in [33, 34] the requirement for the resolution estimation with the sub-events method is that the correlation of the sub-events is only due to flow. The question which one of the three methods ensures this requirement and even if this is known which resolution has to be taken to correct the observed  $v_2^{\text{obs}}$  is still under investigation. Therefore a systematic error was assigned on the final  $D^{*+} v_2$  because of this discrepancy. Details are given in sec. 5.3.

The  $v_2$  results using the VZERO event plane angle  $\Psi_2$  determination were used in order to quantify possible non-flow contributions to the obtained central  $v_2$  results with the positive  $\eta$  TPC event plane. As explained in chap. 2, sec. 2.3 non-flow contributions to the measured  $v_n$  are largely removed by  $\eta$ -gap analyses. Performing these analyses the

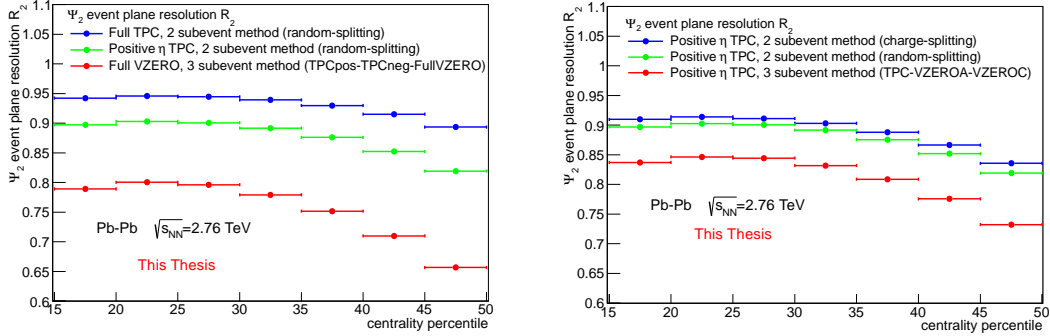


**Figure 5.8.:** (left) Event plane angle  $\Psi_2$  resolutions  $R_2$  for different configurations: (green datapoints) resolution of the positive  $\eta$  TPC event plane angle  $\Psi_2$ , determined with the 2-sub-events method by splitting the positive  $\eta$  TPC events by a random selection of tracks, (blue datapoints) resolution of the full  $\eta$  TPC event plane angle, determined with the 2-sub-events method by splitting the full  $\eta$  TPC events by a random selection of track, (red datapoints) resolution of the full VZERO event plane angle  $\Psi_2$ , determined with the 3-sub-events method. (right) Event plane angle  $\Psi_2$  resolution  $R_2$  using TPC tracks from the positive hemisphere ( $0.0 > \eta > 0.8$ ), determined with different methods: (green datapoints) 2-sub-events method by splitting the events by a random selection of tracks, (blue datapoints) 2-sub-events method by splitting the events by selecting positively and negatively charged tracks, (red datapoints) 3-sub-events method using the two VZERO sub-detectors VZERO-A and VZERO-C.

event plane angles are obtained from Q-vectors measured in different  $\eta$ -regions than the  $D^{*+}$  mesons, which are then correlated with the event plane angles. A sketch depicting this type of analysis is shown in fig. 5.9. Figure 5.9 (left) shows the principle of an  $\eta$ -gap analysis using the TPC only and fig. 5.9 (right) the principle of an  $\eta$ -gap analysis us-

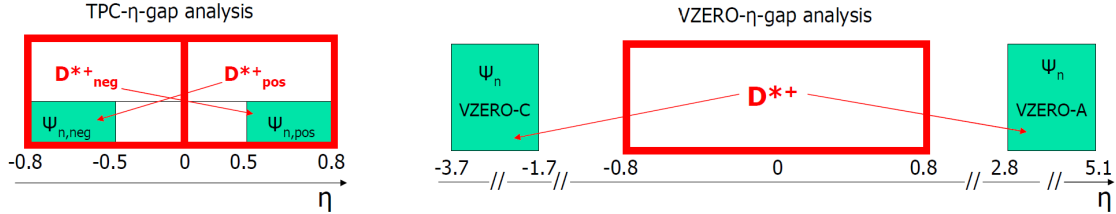


**Figure 5.9.:** (left) Principle of an  $\eta$ -gap analysis using the TPC only. Using this option the event plane angle is estimated from TPC tracks at forward (backward) rapidity and then the reconstructed  $D^{*+}$  mesons from the negative (positive)  $\eta$ -hemisphere are correlated with this event plane angle. (right) Principle of an  $\eta$ -gap analysis using the TPC and the VZERO. Using this option the VZERO-detectors at forward and backward rapidities are used to estimate the event plane angle  $\Psi_n$  and the reconstructed  $D^{*+}$  mesons at midrapidity are correlated with the estimated VZERO event plane angle.

ing the TPC and the VZERO. Using the second option the VZERO-detectors at forward and backward pseudorapidities are used to estimate the event plane angle  $\Psi_n$  and the reconstructed  $D^{*+}$  mesons at midrapidity are correlated with the estimated VZERO event plane angle. Using the first option the event plane angle is estimated from TPC tracks at forward (backward) rapidity and then the reconstructed  $D^{*+}$  mesons from the negative (positive)  $\eta$ -hemisphere are correlated with this event plane angle.

The  $D^{*+} v_3$ -analysis was performed using the TPC only. The reason is the non-acceptable flatness quality of the VZERO  $\Psi_3$  event plane presented in fig. 5.7 (right). Possible non-flow contribution were quantified using a TPC  $\eta$ -gap analysis depicted in fig. 5.9 (left). This non-flow quantification study will be presented in sec. 5.3. Figure 5.8 shows the resolution  $R_3$  for the TPC  $\Psi_3$  event plane as a function of the collision centrality using the following three resolution estimation methods:

- (blue datapoints) Resolution  $R_3$  of the event plane angle  $\Psi_3$  of the **full TPC events**, determined with the 2-sub-events method by splitting the events by selecting the tracks coming from the positive hemisphere of the TPC,  $0.0 < \eta < 0.8$ , and the negative hemisphere,  $-0.8 < \eta < 0.0$ . In this case the event plane angle  $\Psi_3$  resolution of the TPC sub-events is determined and then the  $\Psi_3$  resolution of the full TPC events is obtained by the extrapolation technique presented in eqs. 2.20, 2.21, 2.22, 2.23, 2.24 in chap. 2, sec. 2.3.
- (green datapoints) Resolution  $R_3$  of the event plane angle  $\Psi_3$  of the **TPC sub-events** with the 2-sub-events method and splitting the events by selecting the tracks coming from the positive hemisphere of the TPC,  $0.0 < \eta < 0.8$ , and the negative hemisphere,  $-0.8 < \eta < 0.0$ . In this case the event plane angle  $\Psi_3$  resolution of the TPC sub-events is determined and the extrapolation technique mentioned in the last item is not performed.

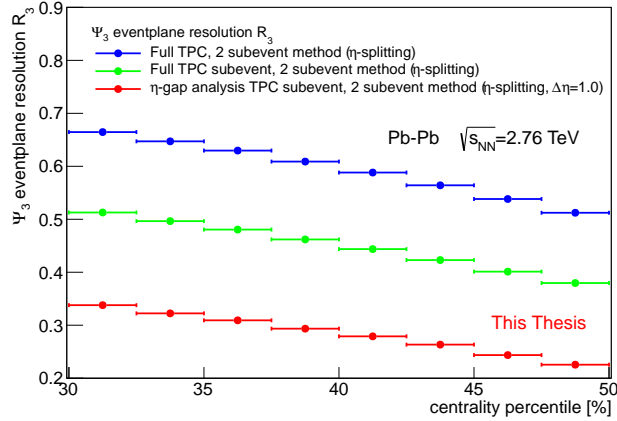


**Figure 5.10.:** Event plane angle  $\Psi_3$  resolutions  $R_3$  with the 2-sub-events method using the full TPC and splitting the events by selecting the tracks coming from the positive and negative hemisphere of the TPC: (blue datapoints) Full event resolution, (green datapoints) sub-event resolution, (red datapoints) sub-event resolution with an  $\eta$ -gap of  $\Delta\eta = 1.0$  between the sub-events.

- (red datapoints) Resolution  $R_3$  of the event plane angle  $\Psi_3$  of the **TPC sub-events** using the TPC with the 2-sub-events method with an  $\eta$ -gap of  $\Delta\eta = 1.0$  between the two sub-events. The two sub-event are built by using the racks coming from the positive hemisphere of the TPC,  $0.5 < \eta < 0.8$ , and the negative hemisphere,  $-0.8 < \eta < -0.5$ .

The ordering of the resolution  $R_3$  in fig. 5.10 is expected and due to the decreasing multiplicity used for determining the event plane angle  $\Psi_3$  with the three methods:  $\Psi_3$  angle resolution of full TPC event (blue datapoints, largest multiplicity  $\rightarrow$  best resolution),  $\Psi_3$  angle resolution of the half TPC event (green datapoints, medium multiplicity  $\rightarrow$  medium resolution),  $\Psi_3$  angle resolution of the half TPC event with restricted  $\eta$ -range (red datapoints, smallest multiplicity  $\rightarrow$  poorest resolution).

### $\Psi_2$ - $\Psi_3$ correlations

Another check in addition to the resolution determinations with different methods and the checks on the flatness was to investigate the correlation of the determined event plane angles  $\Psi_3$  and  $\Psi_2$  event-by-event. This was done to check whether their orientation originates from different effects and thus their orientation is uncorrelated as predicted by theory [107] and measured at RHIC by the PHENIX collaboration [108]. The  $\Psi_2$ - $\Psi_3$ -correlation has to be quantified by the expression  $\langle \cos[6(\Psi_3 - \Psi_2)] \rangle$ , according to [107, 108]. The factor 6 is the lowest common denominator of the fraction within the formula  $\Psi_n = 1/n \cdot \tan^{-1}(Q_{x,n}/Q_{y,n})$  for  $n = 2$  respectively  $n = 3$  used to determine the event plane angles  $\Psi_2$  and  $\Psi_3$ , see eq. 5.1. The factor 6 removes the ambiguities of the difference  $\Psi_2 - \Psi_3$ . Without applying this factor the difference  $\Psi_2 - \Psi_3$  is ambiguous because the two event plane angles are defined in different ranges and have different periodicities. If the determined event plane angles  $\Psi_3$  and  $\Psi_2$  are uncorrelated on an event-by-event basis, the average over a sample of results of the value  $\cos[6(\Psi_3 - \Psi_2)]$  obtained from

minimum-bias lead-lead events has to be  $\langle \cos [6 (\Psi_3 - \Psi_2)] \rangle \approx 0$  [107, 108]. Figure 5.11 shows the expression  $\langle \cos [6 (\Psi_3 - \Psi_2)] \rangle$  grouped in 5 bins of collision centrality. The

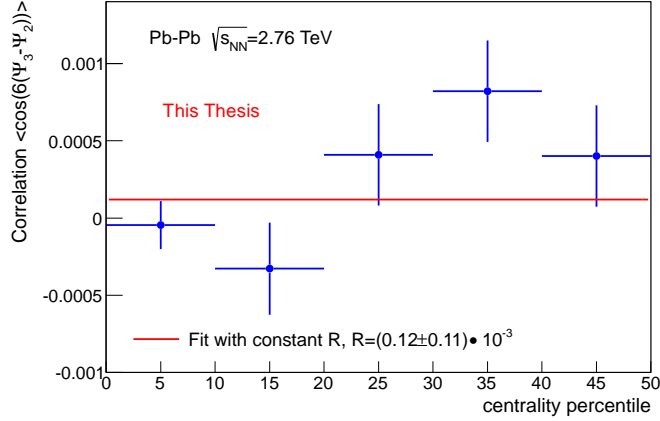


**Figure 5.11.:** The correlation strength  $\langle \cos [6 (\Psi_3 - \Psi_2)] \rangle$  as a function of collision centrality including a fit with a constant function to the datapoints. The centrality range is 0-50%, the number of analyzed events is  $40 \cdot 10^6$  and the event plane angles were estimated using tracks from the TPC.

shown centrality range is 0-50%, the number of analyzed events is  $40 \cdot 10^6$  and the event plane angles were estimated using tracks from the TPC. The error bars represent the statistical errors. The correlation is as expected by theory [107] and measured at RHIC [108] very small, below one per mille. A fit with a constant function to the datapoints yields  $\langle \cos [6 (\Psi_3 - \Psi_2)] \rangle = (0.12 \pm 0.11) \cdot 10^{-3}$ , which is consistent with zero.

## 5.2. $v_n$ -extraction with different approaches

In order to extract the  $D^{*+} v_n$ -parameter various approaches were applied. The principle of all of these approaches is that the  $D^{*+}$  mesons are correlated with the determined event plane angle. This method is known as the event plane method, see chap. 2, sec. 2.3 and [34]. In order to extract the  $v_n$  with the event plane method, one can exploit either eqs. 2.17, 2.18 or eq. 2.16 introduced in chap. 2, sec. 2.3. The first approach based on eqs. 2.17, 2.18 is called **m- $\Delta\phi$ -bins-method** because one extracts the  $D^{*+}$  yield in  $m \Delta\phi$ -bins, with  $\Delta\phi = \phi_{D^{*+}} - \Psi_n$ , and then the  $v_n$  is calculated out of the extracted  $D^{*+}$  signals in the  $m \Delta\phi$ -bins. Details of this procedure are given further below. The default method used for obtaining the central  $v_n$ -values is the  $m$ - $\Delta\phi$ -bins-method with  $m=2$ , which provides more robust  $D^{*+}$  yield extraction per  $p_T$ -bin in the 2  $\Delta\phi$ -bins with respect to the  $m$ - $\Delta\phi$ -bins-method with  $m > 2$ .

Using the second possibility based on eq. 2.16 one starts with a 2-dimensional histogram, where the  $\cos(n\Delta\phi)$  quantity is on the abscissa and the  $\Delta M$ -variable, the invariant mass difference between the  $D^{*+}$  candidates and the corresponding  $D^0$ -candidates, on the ordinate, see eqs. 4.3, 4.4 in chap. 4, sec. 4.1. There are two ways to extract the  $v_n$  exploiting eq. 2.16 making use of the 2-dimensional histogram. One is called the **fit- $v_n$ -to- $\Delta M$ -method** and the other simply the **sidebands-method**. The generic term of these two

approaches is **2D-methods** due to the 2-dimensional histogram used as a basic input. Both 2D-methods treat the task of background subtraction in a different manner than the  $m$ - $\Delta\phi$ -bins-method. This background subtraction procedure is described further below. The multitude of approaches is needed to estimate a systematic error on the  $v_n$  originating from  $D^{*+}$  yield extraction and background subtraction.

In the following, the principles of the 2D-methods and the  $m$ - $\Delta\phi$ -bins-method are described.

### $m$ - $\Delta\phi$ -bins-method

The key principle of the  $m$ - $\Delta\phi$ -bins-method is to extract the  $D^{*+}$  yield in  $m$  bins of  $\Delta\phi$ . Figure 5.12 shows the yield extraction for the  $D^{*+}$  and in case of 2  $\Delta\phi$ -bins, in-plane and out-of-plane, in the  $p_T$ -bin  $2 \text{ GeV}/c < p_T < 4 \text{ GeV}/c$  for the  $v_2$ -analysis ((a) and (b)) and

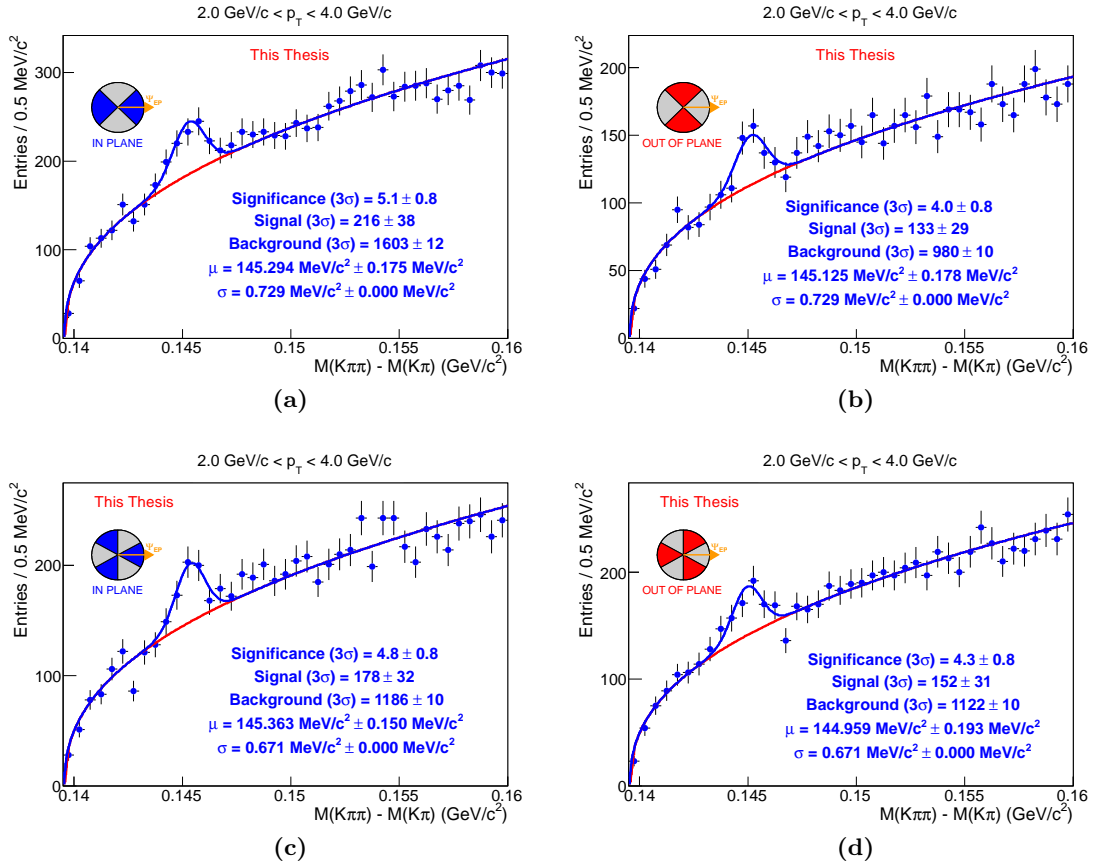


**Figure 5.12.:**  $D^{*+}$  yield extraction in-plane ((a) and (c)) and out-of-plane ((b) and (d)) in the  $p_T$ -bin  $2 \text{ GeV}/c < p_T < 4 \text{ GeV}/c$  for the  $v_2$ -analysis ((a) and (b)) and  $v_3$ -analysis ((c) and (d)). The centrality range is 30-50% and the topological cut set is cut-set 1 summarized in tab. 4.4 in chap. 4, sec. 4.1. The used event plane determination is TPC event plane using tracks only from the positive  $\eta$  side in the  $v_2$ -case ((a) and (b)) and using the full TPC but with an  $\eta$ -gap between the two TPC sub-events in the  $v_3$ -case ((c) and (d)), see sec. 5.1 and fig. 5.9 (left).

((b) and  $v_3$ -analysis ((c) and (d)). The centrality range is 30-50% and the topological cut set is cut-set 1 summarized in tab. 4.4 in chap. 4, sec. 4.1. The used event plane

determination is TPC event plane using tracks only from the positive  $\eta$ -side in the  $v_2$ -case (figs. 5.12a, 5.12b) and using the full TPC but with an  $\eta$ -gap (figs. 5.12c, 5.12d) between the two TPC sub-events, see sec. 5.1 and fig. 5.9 (left). The width of the  $D^{*+}$   $\Delta M$ -peak is first determined using the yield in the full  $\Delta\phi$ -range shown in fig. 4.13 in chap. 4, sec. 4.3 and then in the in-plane respectively out-of-plane  $D^{*+}$  yield extractions the width is kept fixed. Therefore the uncertainty of the width is given by  $\Delta\sigma = 0$  in the in-plane respectively out-of-plane yield extraction plots in fig. 5.12. The value for the extracted signal is obtained by yield extraction via integral of the Gaussian function  $f_S$  introduced in chap. 4, sec. 4.3. An alternative way to extract the yield via bin-counting, as explained in chap. 4, sec. 4.3, is also possible. Moreover, the yield in-plane and out-of-plane can be extracted without fixing the width of the  $D^{*+}$   $\Delta M$ -peak. The background function  $f_B$ , see chap. 4, sec. 4.3, can be changed from the default one being the power-law function to the one represented by a threshold function multiplied by an exponential function. Another access to a source of the systematic errors on the measured  $v_n$  originating from yield extraction is addressed by changing the binning of the  $\Delta M$ -histograms from a bin width of  $\Delta = 0.5 \text{ MeV}/c^2$ , which is used as default, to  $\Delta = 1.0 \text{ MeV}/c^2$ . Finally, the last variation is to extract the yield in 3 instead of 2  $\Delta\phi$ -bins, which is presented further below. These six ways to extract the uncorrected  $v_n$  are exploited to estimate the systematic error from yield extraction. Details are addressed in sec. 5.3. The default method providing the central  $v_n$ -values is to obtain the  $D^{*+}$  yield via integral of the Gaussian function  $f_S$ , fixing the width of the  $D^{*+}$   $\Delta M$ -peak in 2  $\Delta\phi$ -bins and using the power-law function as background parameterization. The yield extraction figures for both the  $v_2$ - and the  $v_3$ -case for the remaining  $p_T$ -bins in the  $p_T$ -region  $p_T > 4 \text{ GeV}/c$  are given in the appendix. The values for the extracted  $D^{*+}$  signals given in fig. 5.12 and in the appendix in the in-plane respectively out-of-plane regions are used to determine the central  $v_n$ -values. In order to determine the uncorrected  $v_n^{\text{obs}}$ -values as a first step, eq. 2.18 presented and derived in chap. 2, sec. 2.3 is used:

$$v_n^{\text{obs}} = \frac{\pi N_{\text{in-plane}} - N_{\text{out-of-plane}}}{4 N_{\text{in-plane}} + N_{\text{out-of-plane}}}$$

$$\text{with } N_{\text{in-plane}} = \frac{N_0}{2\pi} \cdot 2n \cdot \int_0^{\pi/2n} [1 + 2v_n \cos(n\Delta\phi)] d\Delta\phi \quad (\text{see figs. 5.12a, 5.12c}) \quad (5.4)$$

$$\text{and } N_{\text{out-of-plane}} = \frac{N_0}{2\pi} \cdot 2n \cdot \int_{\pi/2n}^{\pi/n} [1 + 2v_n \cos(n\Delta\phi)] d\Delta\phi \quad (\text{see figs. 5.12b, 5.12d})$$

Then the observed  $v_n^{\text{obs}}$ -values are corrected for the corresponding event plane resolution:  $v_n = C_n \cdot v_n^{\text{obs}}$ , with the correction factor  $C_n$  given in eq. 5.3.

The reason why the two integral ranges in eq. 5.4 are restricted to a fraction of  $2\pi$  depending on the harmonic  $n$  is that the function  $\cos(n\Delta\phi_{D^{*+}})$  has a periodicity of  $2\pi/n$ . The  $D^{*+}$  azimuthal angle  $\phi_{D^{*+}}$  is namely defined for  $0 < \phi_{D^{*+}} < 2\pi$ . The event plane angle  $\Psi_n$  range per definition is given by  $0 < \Psi_n < 2\pi/n$ . Therefore the range of the difference  $\Delta\phi = \phi_{D^{*+}} - \Psi_n$  is given by  $-2\pi/n < \Delta\phi_{D^{*+}} < 2\pi$ . Due to the periodicity of the function

$\cos(n\Delta\phi_{D^{*+}})$ , the range of the quantity  $\Delta\phi_{D^{*+}}$  is as a first step restricted to the range  $0 < \Delta\phi_{D^{*+}} < 2\pi/n$  by the following procedure:

- In case  $\Delta\phi_{D^{*+}} < 0$  a shift  $s_+ = 2\pi/n$  is added.
- In case  $\Delta\phi_{D^{*+}} > 2\pi/n$  shifts of  $s_- = -2\pi/n$  are added until  $\Delta\phi_{D^{*+}} < 2\pi/n$ .

As a second step the  $\Delta\phi_{D^{*+}}$  of all  $D^{*+}$  candidates with  $\Delta\phi_{D^{*+}} > 2\pi/2n$  is mirrored, i.e.  $\Delta\phi_{D^{*+}} \rightarrow 2\pi/n - \Delta\phi_{D^{*+}}$  because the function  $\cos(n\Delta\phi_{D^{*+}})$  is symmetric with respect to the value  $\Delta\phi_{D^{*+}} = 2\pi/2n$ . The final range of the  $\Delta\phi_{D^{*+}}$  is given by  $0 < \Delta\phi_{D^{*+}} < 2\pi/2n$ . This complicated procedure is performed to squeeze the extracted  $D^{*+}$  yield in a  $\Delta\phi$ -region, which corresponds to a half-period of the function  $\cos(n\Delta\phi_{D^{*+}})$ . This squeezing procedure provides the best performance in terms of  $v_n$ -extraction when dealing with only few  $\Delta\phi$ -bins and extracting the  $v_n$  with more than 2  $\Delta\phi$ -bins, which is addressed further below. In case of only two  $\Delta\phi$ -bins, the in-plane-yield  $N_{\text{in-plane}}$  is defined as the extracted signal in  $0 < \Delta\phi_{D^{*+}} < \pi/2n$ , see figs. 5.12a, 5.12c, and the out-of-plane yield  $N_{\text{out-of-plane}}$  as the extracted signal in  $\pi/2n < \Delta\phi_{D^{*+}} < \pi/n$ , see figs. 5.12b, 5.12d. The factor  $2n$  in eq. 5.4 cancels in the uncorrected  $v_n^{\text{obs}}$  determination.

In case of more than two  $\Delta\phi$ -bins the uncorrected  $v_n^{\text{obs}}$ -parameters are extracted by a fit of the following equation to the extracted  $D^{*+}$  yield as a function of  $\Delta\phi_{D^{*+}}$  (see eq. 2.17 in chap. 2, sec. 2.3):

$$\frac{dN}{d\Delta\phi_{D^{*+}}} = k [1 + 2v_n \cos(n\Delta\phi_{D^{*+}})] \quad (5.5)$$

The factor  $k$  is kept free, what matters is the amplitude of the cosine, which is twice the uncorrected  $v_n^{\text{obs}}$ . Figures 5.13a, 5.13b, 5.13c show the  $D^{*+}$  yield extraction in 3  $\Delta\phi$ -bins in the  $p_T$ -bin  $6 \text{ GeV}/c < p_T < 8 \text{ GeV}/c$ . The corresponding yield extractions in the  $p_T$ -bins  $2 \text{ GeV}/c < p_T < 4 \text{ GeV}/c$  and  $4 \text{ GeV}/c < p_T < 6 \text{ GeV}/c$  are given in the appendix. Only in these  $p_T$ -bins the significance is high enough to extract the  $D^{*+}$  in more than two  $\Delta\phi$ -bins. Figure 5.13d shows the fit of eq. 5.5 to the extracted yield as function of  $\Delta\phi$ . A  $\chi^2$ -minimization procedure is performed. The formula given in eq. 5.5 is not fitted to the datapoints, but integrals of the formula within the corresponding  $\Delta\phi$ -bins are fitted to the bin-entry multiplied with the bin-width. This is done because of the large widths of the  $\Delta\phi$ -bins. The error bars in the  $\Delta\phi$ -bins represent the statistical error of the yield extraction and the datapoints are placed in the center of the corresponding  $\Delta\phi$ -bin. The uncorrected  $v_2^{\text{obs}}$ -parameter in the  $p_T$ -bin  $6 \text{ GeV}/c < p_T < 8 \text{ GeV}/c$  using the 3- $\Delta\phi$ -bins approach is  $v_2^{\text{obs}} = 0.14 \pm 0.07$ . The error  $\pm 0.07$  is the statistical error of the fit procedure. In order to obtain the corrected  $v_n$ -value, the observed  $v_n^{\text{obs}}$ -values are corrected for the corresponding event plane resolution:  $v_n = C_n \cdot v_n^{\text{obs}}$ , with the correction factor  $C_n$  given in eq. 5.3. The results obtained with the 3- $\Delta\phi$ -bins approach are used in the systematic error estimation addressed in detail in sec. 5.3.

## 2D-methods

Both 2D-methods, the sidebands-method and the fit- $v_n$ -to- $\Delta M$ -method, require as a first input a 2-dimensional histogram with the  $\Delta M$ -variable on the ordinate and the  $\cos(n\Delta\phi)$  variable on the abscissa. Such a histogram is shown in fig. 5.14 (top left) for the  $v_2$ -case in the  $p_T$ -bin  $4 \text{ GeV}/c < p_T < 6 \text{ GeV}/c$ . The used event plane is TPC event plane using

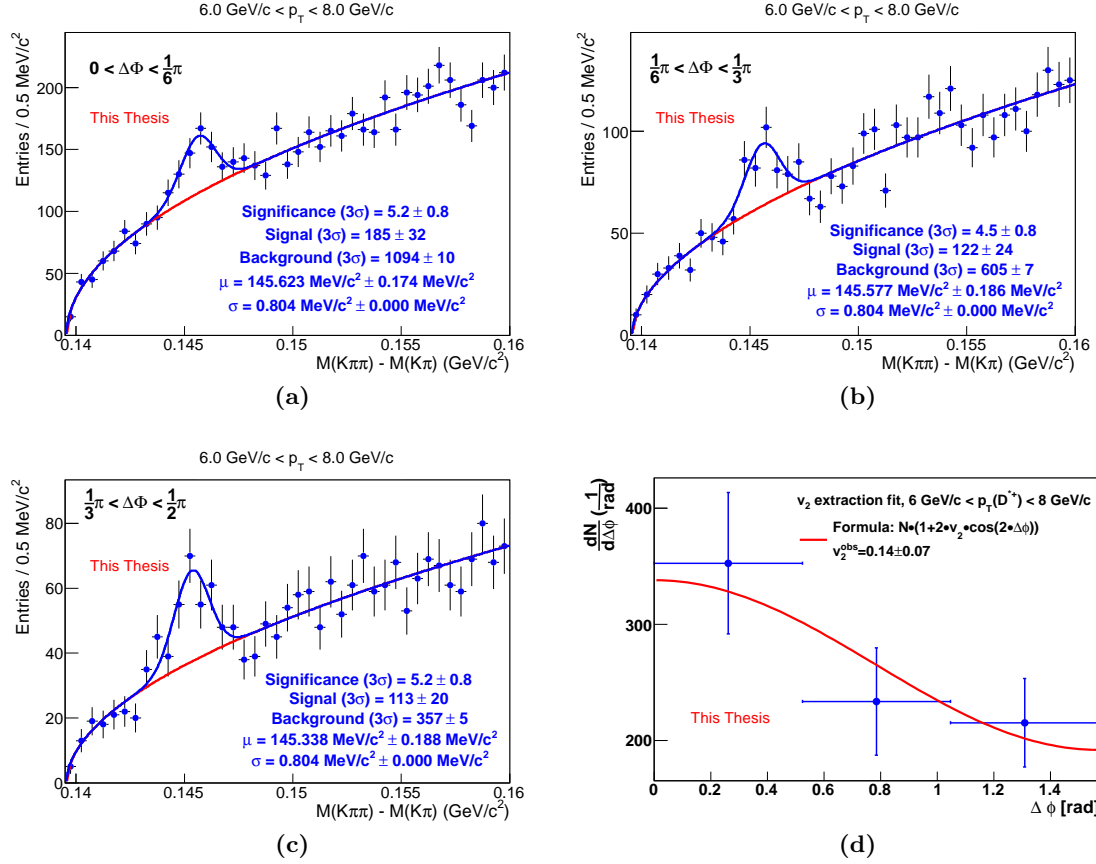


**Figure 5.13.:** (a), (b), (c):  $D^{*+}$  yield extraction in 3  $\Delta\phi$ -bins in the  $p_T$ -bin  $6 \text{ GeV}/c < p_T < 8 \text{ GeV}/c$ . The centrality range is 30-50% and the topological cut set is cut-set 1 summarized in tab. 4.4 in chap. 4, sec. 4.1. The used event plane determination is TPC event plane using tracks only from the positive  $\eta$ -side. (d): Fit of the formula given eq. 5.5 to the extracted  $D^{*+}$  yield as function of  $\Delta\phi$ . The error bars in the  $\Delta\phi$ -bins represent the statistical error of the yield extraction and the datapoints are placed in the center of the corresponding  $\Delta\phi$ -bin. For more details about the fit procedure see text.

tracks only from the positive  $\eta$ -side. Using the sidebands-method as a first step the usual  $\Delta M$   $D^{*+}$  yield extraction procedure is performed on the projection of the 2-dimensional histogram on the  $\Delta M$ -axis, recovering the full  $\Delta M$ -distribution. This fit procedure is shown in fig. 5.14 (top right). The power-law function for parametrizing the background and the usual Gaussian function to fit the  $D^{*+}$   $\Delta M$ -peak are used. Then the 2-dimensional histogram is projected on the  $\cos(n\Delta\phi)$ -axis for different regions of the  $\Delta M$ -axis. A signal region, see fig. 5.14 (top right, grey area), and two sideband regions, see fig. 5.14 (top right, blue and red areas), are defined. For the ranges of the signal and sidebands regions the parameters mean  $\mu$  and sigma  $\sigma$  of the  $D^{*+}$   $\Delta M$ -fit are used. The typical range for the signal region is  $\pm 3\sigma$  around the  $D^{*+}$   $\Delta M$ -peak and the sideband bounds in vicinity to the signal region are placed  $\pm 5\sigma$  away from to the mean  $\mu$  of the  $D^{*+}$   $\Delta M$ -peak. Next, the distribution of  $\cos(n\Delta\phi)$  is built for the signal region  $\cos(n\Delta\phi)_{SB}$  and the two side band regions, namely  $\cos(n\Delta\phi)_{B-left}$  and  $\cos(n\Delta\phi)_{B-right}$ , by projecting the 2-dimensional histogram on the  $\cos(n\Delta\phi)$ -axis for the 3 different ranges of the  $\Delta M$ -axis. The integrals of

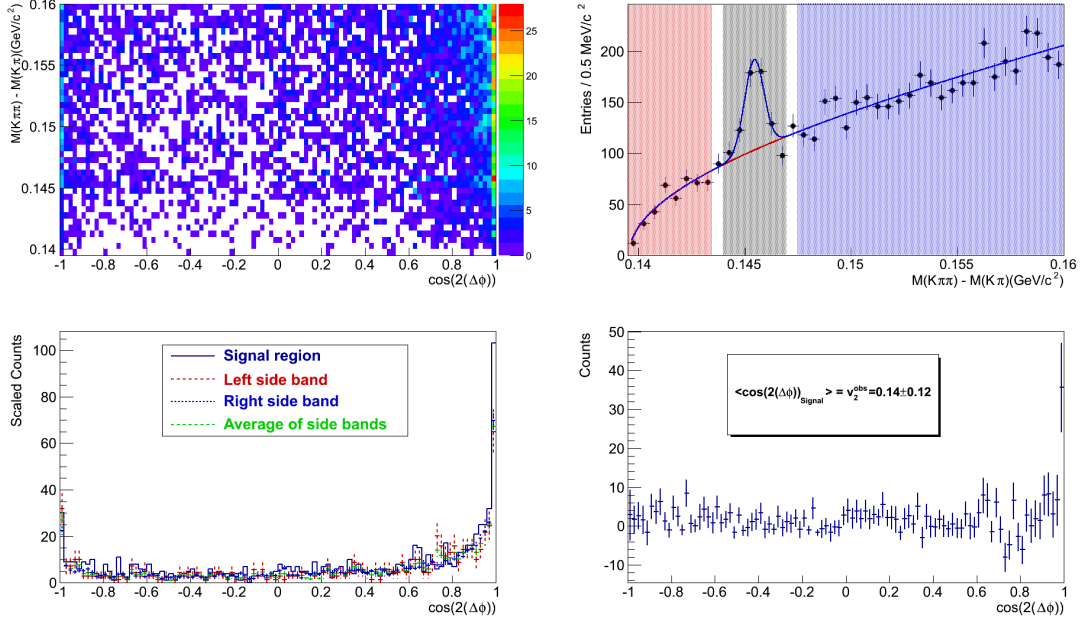


**Figure 5.14.:** Histograms used to extract the  $v_2$  with the sidebands-method for  $4 \text{ GeV}/c < p_T < 6 \text{ GeV}/c$ . The centrality range is 30-50%, the number of analyzed events is  $9.5 \cdot 10^6$ , the topological cut set is cut-set 1 introduced in chap. 4, sec. 4.1 and the used event plane is TPC event plane using tracks only from the positive  $\eta$ -side. For more details about the histograms see text.

the background fit function  $f_B(\Delta M)$  in the sidebands and signal regions, see fig. 5.14 (top right, grey, red and blue areas below the blue respectively red line), are used to extract scaling factors  $\alpha_1$  and  $\alpha_2$  for scaling the  $\cos(n\Delta\phi)$  histograms of the sideband regions, namely  $\cos(n\Delta\phi)_{B\text{-left}}$  and  $\cos(n\Delta\phi)_{B\text{-right}}$ . The formulas for obtaining these scaling factors are given further below. Figure 5.14 (bottom left) shows the scaled sidebands distributions  $\alpha_1 \cos(2\Delta\phi)_{B\text{-left}}$  (red dotted line),  $\alpha_2 \cos(2\Delta\phi)_{B\text{-right}}$  (blue dotted line), their average  $\frac{1}{2} \left( \alpha_1 \cos(2\Delta\phi)_{B\text{-left}} + \alpha_2 \cos(2\Delta\phi)_{B\text{-right}} \right)$  (green dotted line) as well as the signal region distribution  $\cos(2\Delta\phi)_{SB}$  (blue solid line). The difference between the  $\cos(n\Delta\phi)$  distribution of the signal region  $\cos(2\Delta\phi)_{SB}$  and the average of the two scaled ones from the sideband regions  $\frac{1}{2} \left( \alpha_1 \cos(2\Delta\phi)_{B\text{-left}} + \alpha_2 \cos(2\Delta\phi)_{B\text{-right}} \right)$  provides the distribution of  $\cos(2\Delta\phi)_{\text{signal}}$  for the signal shown in fig. 5.14 (bottom right). In formulas:

$$\cos(n\Delta\phi)_{\text{signal}} = \cos(n\Delta\phi)_{SB} - \frac{1}{2} \left( \alpha_1 \cos(n\Delta\phi)_{B\text{-right}} + \alpha_2 \cos(n\Delta\phi)_{B\text{-left}} \right)$$

$$\text{with } \alpha_1 = \frac{\int_{\Delta M_{SB1}}^{\Delta M_{SB2}} f_B(\Delta M) d\Delta M}{\int_{\Delta M_{B\text{-right}2}}^{\Delta M_{B\text{-right}1}} f_B(\Delta M) d\Delta M} \text{ and } \alpha_2 = \frac{\int_{\Delta M_{SB1}}^{\Delta M_{SB2}} f_B(\Delta M) d\Delta M}{\int_{\Delta M_{B\text{-left}2}}^{\Delta M_{B\text{-left}1}} f_B(\Delta M) d\Delta M} \quad (5.6)$$

The expressions  $\Delta M_{B-left1}$  and  $\Delta M_{B-left2}$  are the sidebands bounds of the left sideband,  $\Delta M_{B-right1}$  and  $\Delta M_{B-right2}$  of the right one and  $\Delta M_{SB1}$  and  $\Delta M_{SB2}$  of the signal region.  $\Delta M_{B-left1}$  is given by the background function threshold, which is the rest mass of a charged pion  $m_\pi$  and  $\Delta M_{B-left2}$  is placed  $5\sigma$  left to the mean  $\mu$  of the  $D^{*+}$   $\Delta M$ -peak.  $\Delta M_{B-right1}$  is placed  $5\sigma$  right to the mean  $\mu$  of the  $D^{*+}$   $\Delta M$ -peak and  $\Delta M_{B-right2} = 0.16 \text{ GeV}/c^2$ . The mean of the signal distribution  $\langle \cos(2\Delta\phi) \rangle_{signal}$  provides the uncorrected  $v_2^{obs}$ , which is  $v_2^{obs} = 0.14 \pm 0.12$  in the  $p_T$ -bin  $4 \text{ GeV}/c < p_T < 6 \text{ GeV}/c$ . The error  $\sigma = \pm 0.12$  is the statistical error. In order to obtain the corrected  $v_n$ -value, the observed  $v_n^{obs}$ -values are corrected  $p_T$ -bin by  $p_T$ -bin for the corresponding event plane resolution:  $v_n = C_n \cdot v_n^{obs}$ , with the correction factor  $C_n$  given in eq. 5.3. The results obtained with the sidebands-method are used in the systematic error estimation study from yield extraction and background subtraction addressed in detail in sec. 5.3.

The second 2D-method, the fit- $v_n$ -to- $\Delta M$ -method based on the 2-dimensional distribution of the  $\Delta M$ -distribution versus the  $\cos(n\Delta\phi)$ , see fig. 5.14 (top left), is performed by fitting the  $v_n$  of  $D^{*+}$  candidates versus the  $\Delta M$ -variable. As in case of the sidebands-method the usual  $D^{*+}$  yield extraction procedure is performed on the projection of the 2-dimensional histogram on the  $\Delta M$ -axis shown in fig. 5.14 (top right). The power-law function for parametrizing the background  $f_B$  and the usual Gaussian function  $f_S$  to fit the  $D^{*+}$   $\Delta M$ -peak are used. From this fit it is possible to build the distributions of the signal and background fractions  $\frac{f_S}{f_S+f_B}(\Delta M)$  and  $\frac{f_B}{f_S+f_B}(\Delta M)$  as a function of the  $\Delta M$ -variable. Both fraction distributions are shown in fig. 5.15 (left) for the  $p_T$ -bin  $4 \text{ GeV}/c < p_T < 6 \text{ GeV}/c$ . Then, for each  $\Delta M$ -bin, the  $v_n$  is computed from the  $\cos(n\Delta\phi)$

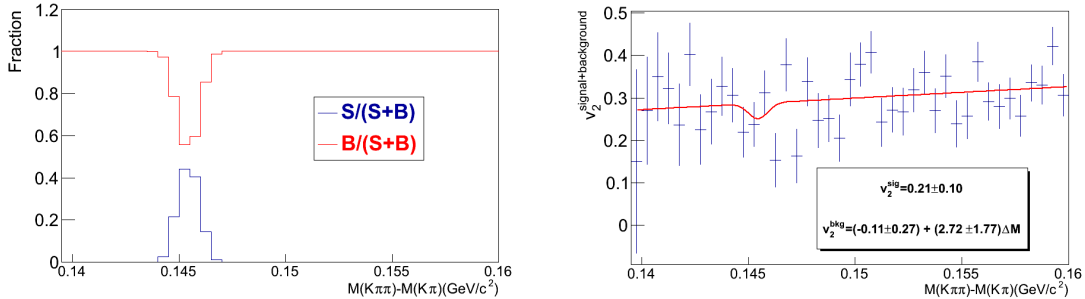


**Figure 5.15.:** Ingredients used to extract the  $v_2$  with the fit- $v_n$ -to- $\Delta M$  for  $4 \text{ GeV}/c < p_T < 6 \text{ GeV}/c$ . The centrality range is 30-50%, the number of analyzed events is  $9.5 \cdot 10^6$ , the topological cut set is Set1 introduced in chap. 4, sec. 4.1 and the used event plane is TPC event plane using tracks only from the positive  $\eta$  side. For more details about the histograms see text.

distribution obtained in that bin as  $v_n = \langle \cos(n\Delta\phi) \rangle$ . The  $v_2$  as a function of  $\Delta M$  for the  $p_T$ -bin  $4 \text{ GeV}/c < p_T < 6 \text{ GeV}/c$  is shown in fig. 5.15 (right, blue datapoints). The used event plane is the TPC event plane using tracks only from the positive  $\eta$  side. In order to disentangle the signal and background contributions, the  $v_n$  versus  $\Delta M$  distribution is fitted using the following function:

$$v_n^{\text{signal+background}}(\Delta M) = v_n^{\text{signal}} \frac{f_S}{f_S + f_B}(\Delta M) + v_n(\Delta M)^{\text{background}} \frac{f_B}{f_S + f_B}(\Delta M) \quad (5.7)$$

This fit for the  $v_2$ -case in the  $p_T$ -bin  $4 \text{ GeV}/c < p_T < 6 \text{ GeV}/c$  is shown in fig. 5.15 (right, red line). The  $v_n^{\text{signal}}$  is the signal contribution to the total  $v_n^{\text{signal+background}}$  and  $v_n^{\text{background}}$  is a function depending on  $\Delta M$ . A polynomial of first order, i.e.  $v_n(\Delta M)^{\text{background}} = a + b \cdot \Delta M$ , was assumed for the  $v_n$ -dependence on  $\Delta M$ . The extracted fit parameter  $v_2^{\text{signal}}$  of the shown fit in fig. 5.15 (right, red line) is the uncorrected  $v_2^{\text{obs}}$ , which is  $v_2^{\text{obs}} = 0.21 \pm 0.10$  in the  $p_T$ -bin  $4 \text{ GeV}/c < p_T < 6 \text{ GeV}/c$ . The error  $\sigma = \pm 0.10$  is the statistical error. In order to obtain the corrected  $v_n$ -value, the observed  $v_n^{\text{obs}}$ -values are corrected  $p_T$ -bin by  $p_T$ -bin for the corresponding event plane resolution:  $v_n = C_n \cdot v_n^{\text{obs}}$ , with the correction factor  $C_n$  given in eq. 5.3. The results obtained with the 2D-fit- $v_n$ -to- $\Delta M$  method are used in the systematic error estimation study from yield extraction and background subtraction addressed in detail in the next section.

### 5.3. Consistency checks and systematic

In this section the systematic error sources of the  $D^{*+} v_2$ - and  $D^{*+} v_3$ -measurements are addressed and quantified. The systematic error sources are classified into the following four categories:

1. yield extraction and background subtraction;
2. uncertainties of the event plane resolution  $R_n$  and hence of the correction factor  $C_n$ , see eq. 5.3;
3. non-flow contributions to the measured  $v_n$ .
4. B-feed-down: A certain fraction of the  $D^{*+}$  mesons used to determine the  $v_n$  originate from B meson decays. When considering the  $v_n$ -measurement of inclusive  $D^{*+}$  mesons, i.e. originating both from B meson decays and fragmentation of charm quarks, this systematic error is obsolete. However, if one wants to measure the  $v_n$  of prompt  $D^{*+}$  mesons, the contribution from the B-feed-down has to be estimated. As this estimation is currently based on theoretical predictions with theoretical uncertainties and several assumptions, a systematic error on the measured  $v_n$  has to be assigned if a prompt  $D^{*+} v_n$ -measurement is anticipated.

In the following the four systematic error categories are addressed and quantified one by one for the  $D^{*+} v_2$  and  $D^{*+} v_3$  measurements.

#### Systematic uncertainties from yield extraction and background subtraction

The systematic error on the  $D^{*+} v_n$ -measurement from yield extraction and background subtraction is determined by extracting the  $v_n$  with 8 different methods  $p_T$ -bin by  $p_T$ -bin, one method for determining the central  $v_n$ -value and 7 methods for determining the systematic uncertainty. For each of the 7 alternative methods specified below the absolute value  $\Delta v_n$  of the difference  $v_n^{\text{central}} - v_n^{\text{alternative}}$ , i.e.  $\Delta v_n = |v_n^{\text{central}} - v_n^{\text{alternative}}|$ , is determined. The maximum out of the 7 absolute values of the differences is taken as upper and lower systematic error. Thus the determined systematic error is always symmetric given by  $\Delta v_n = \pm |v_n^{\text{central}} - v_n^{\text{alternative}}|_{\text{max}}$ . The default method, which is used for the determination of the central  $v_n$ -value, is the  $2\text{-}\Delta\phi$ -bin-method, see sec. 5.2 and eq. 5.4.

The background function of choice is the power-law function  $f_B = a(\Delta M - m_\pi)^b$  and the  $D^{*+}$  yield in-plane respectively out-of-plane is extracted by taking the integral of the Gaussian function  $f_S$ . Figure 5.16 shows the extracted  $v_2$  as a function of the method of choice for the 5 considered  $p_T$ -bins. The error bars represent the statistical error of each method. The method labels from left to right on the abscissa have the following meanings:

- **2- $\Delta\phi$ -fit:** The method for determining the central  $v_n$ -value described above. The results of this method  $p_T$ -bin by  $p_T$ -bin are represented by red datapoints in fig. 5.16. The dotted red line serves as orientation and corresponds to the  $v_n$ -value obtained with the 2- $\Delta\phi$ -fit method on the ordinate.
- **2- $\Delta\phi$ -bctg:** The same approach as 2- $\Delta\phi$ -fit but the  $D^{*+}$  yield is extracted in-plane respectively out-of-plane via the bin-counting procedure, see chap. 4, sec. 4.3.
- **3- $\Delta\phi$ -fit:** The  $D^{*+}$  yield is extracted in 3  $\Delta\phi$ -bins by taking the integral of the Gaussian function  $f_S$  for each  $\Delta\phi$ -bin and then the  $\frac{dN}{d\Delta\phi}$ -distribution is fitted with the function given in eq. 5.5. This method is not available for  $p_T > 8$  GeV/ $c$  because the significance of the  $D^{*+}$   $\Delta M$ -peak drops below 3 in the individual  $\Delta\phi$ -bins and the yield extraction is hence not reliable. The corresponding datapoints in figs. 5.16d, 5.16e are missing.
- **2- $\Delta\phi$ -thresh.fit:** The same as 2- $\Delta\phi$ -fit but the threshold function  $f_B = a\sqrt{\Delta M - m_\pi} \cdot \exp(-b(\Delta M - m_\pi))$  is used instead of the power-law function to describe the background. This method is not available for the the first  $p_T$ -bin, i.e. for  $2$  GeV/ $c < p_T < 4$  GeV/ $c$  because the significance of the  $D^{*+}$   $\Delta M$ -peak drops below 3 in the out-of-plane  $\Delta\phi$ -bin and the yield extraction is hence not reliable. The corresponding datapoint in fig. 5.16a is missing.
- **2- $\Delta\phi$ -nonfixed:** The same as 2- $\Delta\phi$ -fit but the  $\sigma$  of the  $D^{*+}$   $\Delta M$ -peak is not fixed when extracting the  $D^{*+}$  in-plane and out-of-plane yield.
- **2- $\Delta\phi$ -binning:** The same as 2- $\Delta\phi$ -fit but the binning of the  $\Delta M$ -histograms is changed from counts per 500 MeV/ $c^2$ , see figs. 4.13(a)-(d) in sec. 4.3, to counts per 1000 MeV/ $c^2$  for  $2$  GeV/ $c < p_T < 12$  GeV/ $c$  and vice versa for  $12$  GeV/ $c < p_T < 16$  GeV/ $c$ . In this particular  $p_T$ -bin ( $12$  GeV/ $c < p_T < 16$  GeV/ $c$ ) the default binning is already counts per 1000 MeV/ $c^2$ , see fig. 4.13f in sec. 4.3. This variation of the bin-size cannot be performed for the  $p_T$ -bin  $4$  GeV/ $c < p_T < 6$  GeV/ $c$  because the  $D^{*+}$   $\Delta M$ -peak is described only by one datapoint when changing the binning from counts per 500 MeV/ $c^2$  to counts per 1000 MeV/ $c^2$ . The reason for this behavior is that in this particular  $p_T$ -range the width  $\sigma$  of the  $D^{*+}$   $\Delta M$ -peak, see fig. 4.13c in sec. 4.3, is smallest. Describing a Gaussian function with only one datapoint is not a reliable procedure. The corresponding datapoint in fig. 5.16b is missing.
- **2D-Fit- $v_n$ -To- $\Delta M$  and 2D-Sidebands:** these 2-dimensional methods are described in detail in sec. 5.2. They are not available for the  $p_T$ -bin  $12$  GeV/ $c < p_T < 16$  GeV/ $c$  because of too low statistics. These methods require a minimal number of entries in the sidebands of the  $\Delta M$ - $D^{*+}$  peak in the  $\Delta M$ -histograms to provide a reliable

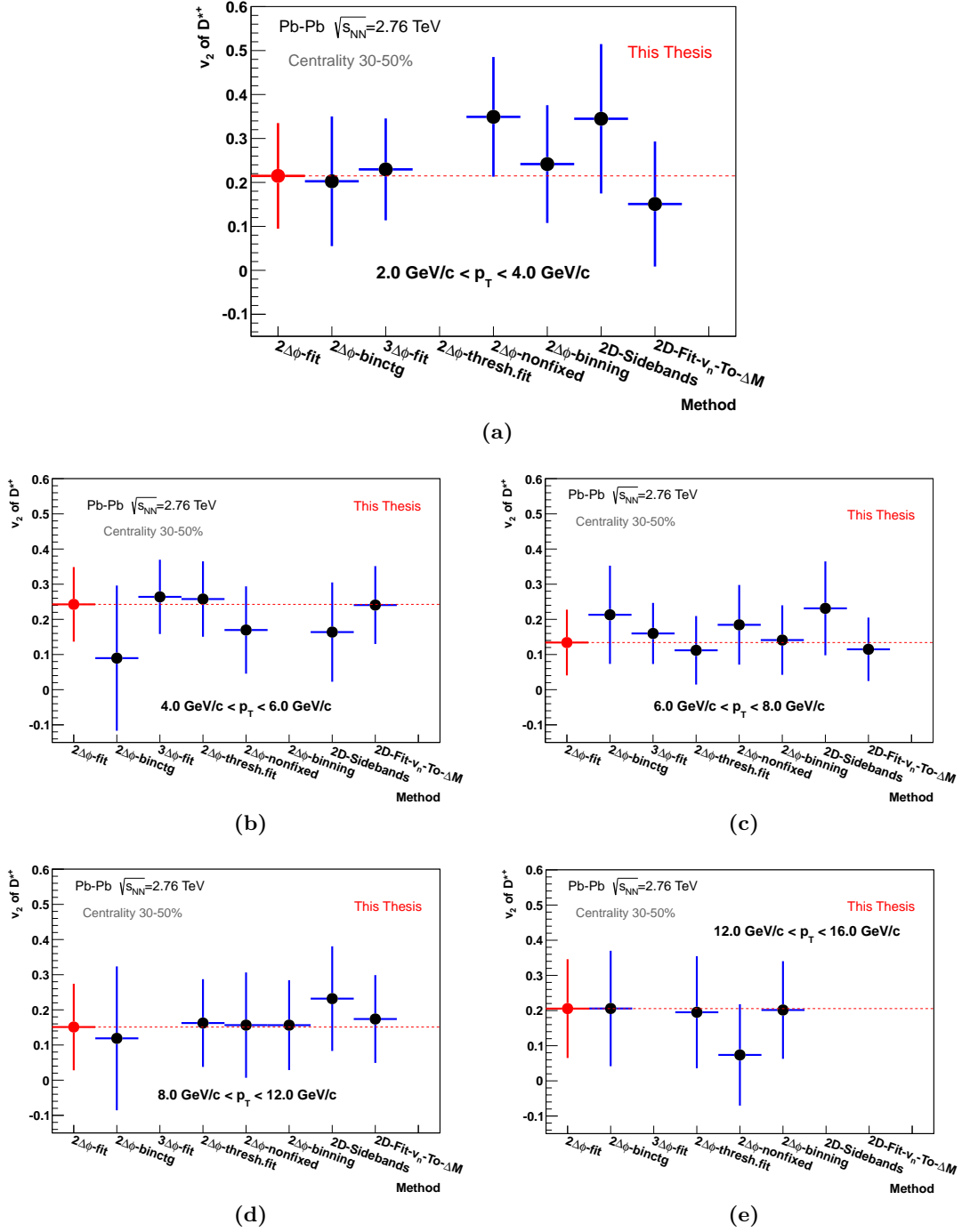


**Figure 5.16.:** Results of  $D^{*+}$   $v_2$ -extractions using the event plane method with different approaches for the background subtraction and  $D^{*+}$  yield extraction in 5  $p_T$ -bins:  $2 \text{ GeV}/c < p_T < 4 \text{ GeV}/c$  (a),  $4 \text{ GeV}/c < p_T < 6 \text{ GeV}/c$  (b),  $6 \text{ GeV}/c < p_T < 8 \text{ GeV}/c$  (c),  $8 \text{ GeV}/c < p_T < 12 \text{ GeV}/c$  (d),  $12 \text{ GeV}/c < p_T < 16 \text{ GeV}/c$  (e). The error bars represent the statistical error of each approach. The error bars in the horizontal direction are meaningless. For details about the different approaches see text.

background-subtraction for the final determination of the uncorrected  $v_n^{\text{obs}}$ -value of the  $D^{*+}$  signal. In the  $p_T$ -bin  $12 \text{ GeV}/c < p_T < 16 \text{ GeV}/c$  this requirement is not fulfilled.

Tabular 5.1 summarizes the statistical and systematic uncertainties estimated with the procedure described above exploiting the  $v_2$ -results obtained with the 8 different approaches. The relative statistical and systematic errors are both comparable and of the order of 50%

$p_T$ -bin [GeV/c]	Central $v_2$ value	statistical error	systematic error from yield extraction and background subtraction
2 – 4	0.21	$\pm 0.12$	$\pm 0.13$
4 – 6	0.24	$\pm 0.11$	$\pm 0.15$
6 – 8	0.13	$\pm 0.09$	$\pm 0.10$
8 – 12	0.15	$\pm 0.12$	$\pm 0.08$
12 – 16	0.21	$\pm 0.14$	$\pm 0.13$

**Table 5.1.:** List of central values for the  $v_2$  for various  $p_T$ -bins and the corresponding statistical errors as well as the systematic errors from yield extraction and background subtraction.

depending on the  $p_T$ -bin.

In order to obtain  $v_2$ -results with better precision, the analysis was repeated with increased  $p_T$ -ranges, namely in the following two  $p_T$ -bins:  $2 \text{ GeV}/c < p_T < 6 \text{ GeV}/c$  and  $6 \text{ GeV}/c < p_T < 16 \text{ GeV}/c$ . The respective  $v_2$ -results with the 8 methods in the wider  $p_T$ -bins are shown in fig. 5.17. The aim of this analysis was to obtain a value for the significance  $v_2/\sigma(v_2)$ , i.e. the distance of the obtained  $v_2$  from zero in units of the combination of the systematic and statistical error with decreased error bars with respect to the analysis with finer  $p_T$ -binning. The  $p_T$ -ranges were chosen with the purpose to have a low  $p_T$ -region ( $2 \text{ GeV}/c < p_T < 6 \text{ GeV}/c$ ), where the  $v_2$  is mainly generated by collective

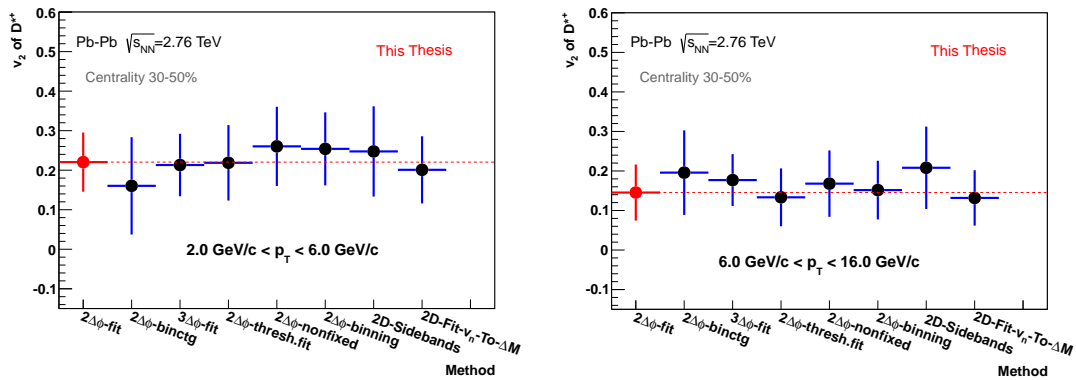


**Figure 5.17.:** Results of  $D^{*+}$   $v_2$ -extractions using the event plane method with different approaches for 2 wide  $p_T$ -bins:  $2 \text{ GeV}/c < p_T < 6 \text{ GeV}/c$  (left) and  $6 \text{ GeV}/c < p_T < 16 \text{ GeV}/c$  (right). The error bars represent the statistical error of each approach. The error bars in horizontal direction are meaningless. For details about the different approaches see text.

anisotropic flow, see chap. 2, sec. 2.3, and a high  $p_T$ -region ( $6 \text{ GeV}/c < p_T < 16 \text{ GeV}/c$ ), where the  $v_2$  is mainly generated by path length dependence of charm quark energy loss, see chap. 2, sec. 2.3 and sec. 2.4. For both analyses, in the following called "v<sub>2</sub>-wide" and "v<sub>2</sub>-fine", the event plane angle  $\Psi_2$  determination was carried out with the positive  $\eta$ -side of the TPC due to reasons discussed in sec. 5.1, namely best flatness quality and best resolution. The resolution was determined using the 2-sub-events method with random splitting of the positive  $\eta$ -event and the subsequent extrapolation of the sub-event resolution to the resolution of the full positive  $\eta$  sub-event, see fig. 5.8 (right, green datapoints), sec. 5.1. Tabular 5.2 summarizes the statistical and systematic uncertainties obtained for the v<sub>2</sub>-wide-analysis estimated with the procedure described above exploiting the v<sub>2</sub>-results obtained with the 8 different approaches. The relative statistical and systematic errors are both comparable and of the order 30% in the  $p_T$ -bin  $2 \text{ GeV}/c < p_T < 6 \text{ GeV}/c$

$p_T$ -bin [GeV/c]	Central $v_2$ value	statistical error	systematic error from yield extraction and background subtraction
2 – 6	0.22	$\pm 0.07$	$\pm 0.06$
6 – 16	0.15	$\pm 0.07$	$\pm 0.06$

**Table 5.2.:** List of central values for the v<sub>2</sub>-wide analysis for two  $p_T$ -bins and the corresponding statistical errors as well as the systematic errors from yield extraction and background subtraction.

and of the order of 45% in the  $p_T$ -bin  $6 \text{ GeV}/c < p_T < 16 \text{ GeV}/c$ .

In case of the v<sub>3</sub>-analysis, the event plane angle  $\Psi_3$  determination for the central v<sub>3</sub>-value was carried out with the full TPC but with an  $\eta$ -gap between the positive and negative  $\eta$  sub-event, see fig. 5.9 (left). The reason for this choice will become clear further below where possible systematic error sources from non-flow effects will be discussed. The resolution was determined using the 2-sub-events method, see fig. 5.10 (red datapoints), sec. 5.1. In this case the resolution of the sub-events was not extrapolated to the resolution of the full event, i.e. to the sum of the sub-events which have an  $\eta$ -gap between each other, because the D<sup>\*+</sup> mesons are correlated with either the positive  $\eta$  or the negative  $\eta$  sub-event. The selected sub-event depends on the pseudorapidity of the D<sup>\*+</sup>, see fig. 5.9 (left). Figure 5.16 shows the extracted v<sub>3</sub> as a function of the method of choice for 5  $p_T$ -bins:  $2 \text{ GeV}/c < p_T < 4 \text{ GeV}/c$  (a),  $4 \text{ GeV}/c < p_T < 6 \text{ GeV}/c$  (b),  $6 \text{ GeV}/c < p_T < 8 \text{ GeV}/c$  (c),  $8 \text{ GeV}/c < p_T < 12 \text{ GeV}/c$  (d) and  $12 \text{ GeV}/c < p_T < 20 \text{ GeV}/c$  (e). The upper limit of the highest  $p_T$ -bin is increased to  $p_T = 20 \text{ GeV}/c$  with respect to the upper limit within the v<sub>2</sub>-analysis. In general, the higher upper limit indeed increases to a small extent the significance of the D<sup>\*+</sup>  $\Delta M$ -peak in the highest  $p_T$ -bin and thus decreases the statistical error of the v<sub>n</sub>-measurement. However, the upper limits within the preliminary published and presumably final D<sup>0</sup>- and D<sup>+</sup>-v<sub>2</sub>-analyses carried out by the ALICE-collaboration, see [109–111], are set to  $p_T = 16 \text{ GeV}/c$ . In order to have a common  $p_T$ -binning of the 3 charmed mesons for the final publication [111], the  $p_T$ -range of the D<sup>\*+</sup> v<sub>2</sub>-analysis was restricted to  $p_T = 16 \text{ GeV}/c$ . The final combined v<sub>2</sub>-results of the 3 charmed mesons using the data from the 2011 PbPb-run will be presumably published in 2013 [111].

5. Road to the final results for the  $D^{*+}$   $v_2$ - and  $D^{*+}$   $v_3$ -anisotropy parameters

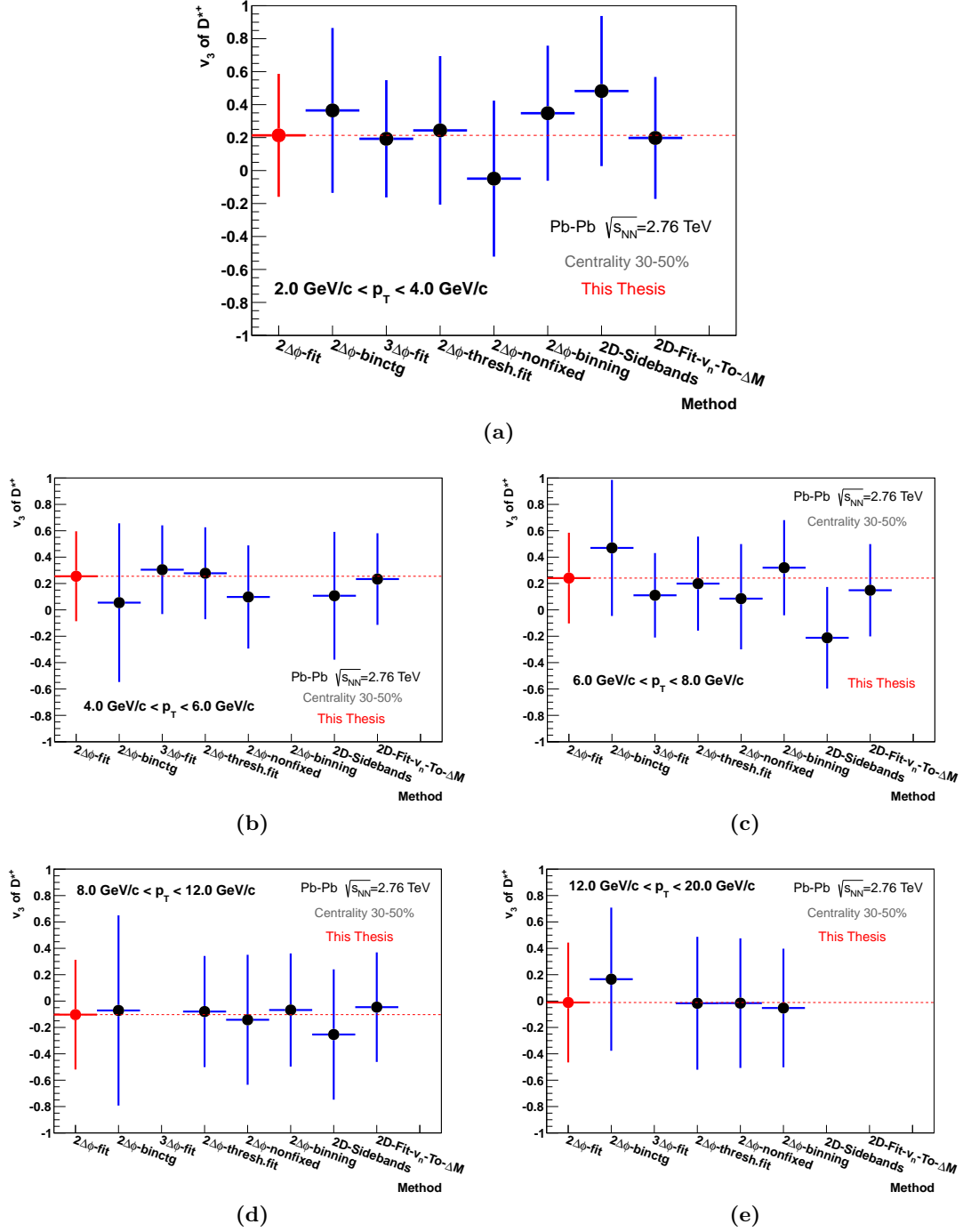


**Figure 5.18.:** Results of  $D^{*+}$   $v_3$ -extractions using the event plane method with different approaches for 5  $p_T$ -bins:  $2 \text{ GeV}/c < p_T < 4 \text{ GeV}/c$  (a),  $4 \text{ GeV}/c < p_T < 6 \text{ GeV}/c$  (b),  $6 \text{ GeV}/c < p_T < 8 \text{ GeV}/c$  (c),  $8 \text{ GeV}/c < p_T < 12 \text{ GeV}/c$  (d),  $12 \text{ GeV}/c < p_T < 20 \text{ GeV}/c$  (e). The error bars represent the statistical error of each approach. The error bars in horizontal direction are meaningless. For details about the different approaches see text.

The error bars in fig. 5.18 represent the statistical error of each method. The error bars in the horizontal direction are meaningless. The method labels from left to right on the abscissa have the same meaning as the ones for the  $v_2$ -analysis described above. The reasons for the absence of some datapoints in fig. 5.18 are the same as for the  $v_2$ -analysis with one exception in  $p_T$ -bin  $2 \text{ GeV}/c < p_T < 4 \text{ GeV}/c$ , see fig 5.18a. Here the datapoint for the method "2- $\Delta\phi$ -thresh.fit" is available in contrast to the  $v_2$ -analysis shown in fig. 5.16a because the significances of the  $\Delta M$ - $D^{*+}$  peaks in the in- and out-of-plane yield extraction procedures are large enough in the  $v_3$ -case. Tabular 5.3 summarizes the statistical and systematic uncertainties obtained for the  $v_3$ -analysis estimated with the procedure described

$p_T$ -bin [GeV/c]	Central $v_3$ value	statistical error	systematic error from yield extraction and background subtraction
2 – 4	0.21	$\pm 0.37$	$\pm 0.27$
4 – 6	0.25	$\pm 0.34$	$\pm 0.20$
6 – 8	0.24	$\pm 0.34$	$\pm 0.45$
8 – 12	-0.1	$\pm 0.41$	$\pm 0.15$
12 – 20	-0.01	$\pm 0.45$	$\pm 0.18$

**Table 5.3.:** List of central values for the  $v_3$  for various  $p_T$ -bins and the corresponding statistical errors as well as the systematic errors from yield extraction and background subtraction.

above exploiting the  $v_3$ -results obtained with the 8 different approaches. The relative statistical and systematic errors are both comparable and of the order of 100% – 200% in the  $p_T$ -range  $2 \text{ GeV}/c < p_T < 8 \text{ GeV}/c$ . For  $p_T > 8 \text{ GeV}/c$ -range the central  $v_3$  is of the order of  $\approx 0$  with currently large statistical uncertainties of the order of  $\pm 0.4$  and systematic uncertainties of the order of  $\pm 0.2$ . The main reason for the larger errors of the  $v_3$ -values with respect to the errors of the  $v_2$ -values is the poorer  $\Psi_3$  event plane resolution, see fig. 5.10 (red datapoints), with respect to the  $\Psi_2$  event plane resolution, see fig. 5.8 (right, green datapoints). The  $\Psi_3$  event plane resolution is poorer because of the smaller  $v_3$ -signal with respect to the  $v_2$ -signal provided by the charged particles, which is used to determine the  $\Psi_3$  event plane angle, see e.g. fig. 2.15 in sec. 2.3. Moreover, the used multiplicity to determine the  $\Psi_3$  event plane angle is smaller than in the  $v_2$  case because an  $\eta$ -gap between the two sub-events is used in the  $v_3$ -analysis, see fig. 5.9 (left). The  $D^{*+}$  mesons are correlated either with the event plane angle estimated from the positive  $\eta$  or negative  $\eta$  sub-event. The reason, why the  $\eta$ -gap configuration shown in fig. 5.9 (left) was chosen to determine the  $v_3$  will become clear further below while addressing possible non-flow contributions to the measured  $v_3$ .

### Systematic error from event plane resolution

The systematic error contribution to the measured  $v_n$  due to the uncertainties of the event plane resolution has two independent origins. The first origin is due the fact that the  $v_n$  is measured in a wide centrality percentile bin of  $\Delta = 20\%$  with an lower limit of 30% and upper limit of 50%. The event plane resolution varies significantly within this bin, see figs. 5.8 (right), 5.10. A possible correction for this effect would be to extract the  $D^{*+}$  yield in sufficient small centrality bins, e.g. in centrality percentile bins of  $\Delta = 5\%$ ,

and scale the resolution values centrality-bin by centrality-bin with the extracted  $D^{*+}$  yield in the corresponding centrality bin. However, this is not feasible because of the limited significance of the  $D^{*+} \Delta M$ -peaks in the  $p_T$ -bins, see fig. 4.13 in chap 2, sec. 4.3. As the resolution shows a monotonic decrease as a function of increasing centrality percentile, see figs. 5.8 (right), 5.10, the assigned relative systematic error  $\Delta(v_n)/v_n$  on the  $v_n$  was defined as:

$$\Delta(v_n)/v_n = 0.5 \cdot \frac{C_n(45 - 50\%) - C_n(30 - 35\%)}{C_n(30 - 50\%)} \quad (5.8)$$

with  $C_n$  defined in eq. 5.3 and  $C_n(XX - XX\%)$  being the correction factors obtained in the given centrality percentile ranges. The half spread of  $C_n(45 - 50\%) - C_n(30 - 35\%)$  and not the full spread was taken because  $C_n(30 - 50\%)$  is always in between  $C_n(45 - 50\%)$  and  $C_n(30 - 35\%)$ . This yields a relative systematic error contribution  $\Delta(v_n)/v_n$  of  $\pm 4\%$  in case of the  $v_2$  and  $\pm 20\%$  in case of the  $v_3$ . These systematic error contributions differ for the two cases because the variation of the correction factor  $C_n$  in the centrality range of 30-50% is stronger in the  $v_3$ - than in the  $v_2$ -case, see figs. 5.8 (right), 5.10. Note that  $C_n$  is given by the inverse value of the resolutions shown in these figures. These contributions are small in comparison to the statistical and systematic errors from yield extraction and background subtraction.

In addition, an asymmetric systematical error contribution in case of the  $v_2$ -measurement was assigned due to the 2-sub-events method versus 3-sub-events method discrepancy used for the event plane resolution determination shown in fig. 5.8 (right, red and green datapoints). The reason for this discrepancy was still not fully understood at the end of writing up this thesis and under investigation. The most probable reason for this difference is a different non-flow correlation between the 2 (in the 2-sub-events method), respectively 3 (in the 3-sub-events method) sub-events. However, as pointed out in chap. 2, sec. 2.3 and in [33, 34] the requirement for the resolution estimation with the sub-events method is that the correlation of the sub-events is only due to flow. The question which one of the three methods ensures this requirement and even if this is known which resolution has to be taken to correct the observed  $v_2^{\text{obs}}$  is still under investigation. The asymmetric relative systematic error due to this discrepancy  $\Delta(v_2)/v_2$  on the  $v_2$  was defined as:

$$\Delta(v_2)/v_2 = \frac{C_2^{\text{3-sub-events}}(30 - 50\%) - C_2^{\text{2-sub-events}}(30 - 50\%)}{C_2^{\text{2-sub-events}}(30 - 50\%)} = +9\% \quad (5.9)$$

#### **Systematic error contribution due to non-flow contributions to the measured $v_n$**

Possible non-flow contributions, see chap. 2, sec. 2.3, to the measured  $v_2$  were estimated by extracting the  $v_2$  using an  $\eta$ -gap-method by correlating the  $D^{*+}$  mesons with the second order event plane angle  $\Psi_2$  determined with the VZERO-detector, see fig. 5.9 (right). Figure 5.19 (left) shows the comparison of the extracted central  $D^{*+} v_2$ -value using the positive- $\eta$  TPC event plane angle (blue datapoints) and the  $D^{*+} v_2$ -value obtained using the event plane angle determined with the VZERO-detector (red datapoints). The error bars represent the statistical errors only. For both cases the same extraction method was used, namely the  $2-\Delta\phi$ -bin-method using the power-law background function and extracting the  $D^{*+}$  yield by taking the integral of the Gaussian function  $f_S$ . For  $p_T > 4$  GeV/ $c$  the  $v_2$ -values using the positive  $\eta$  TPC event plane angle are larger than the  $v_2$ -values

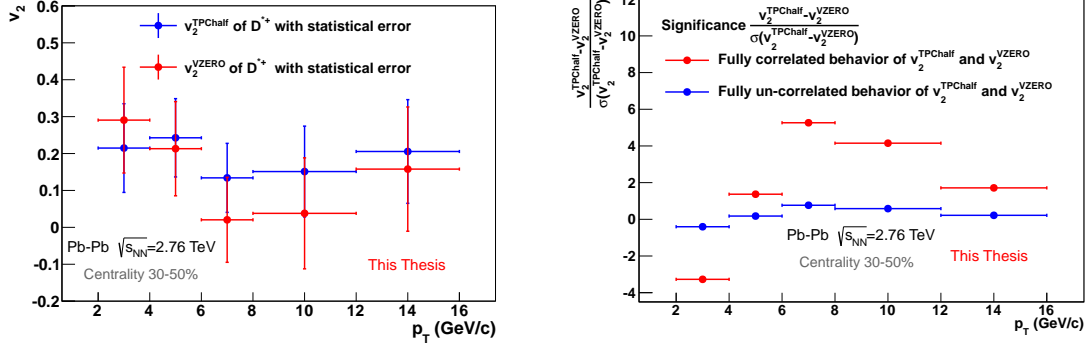


**Figure 5.19.:** (left) Comparison of the extracted central  $D^{*+}$   $v_2$ -value using the positive  $\eta$  TPC event plane angle (blue datapoints) and the  $D^{*+}$   $v_2$ -value obtained using the event plane angle determined with the VZERO-detector (red datapoints). The vertical error bars represent the statistical errors and the horizontal error bars the distances to the limits of the corresponding  $p_T$ -bin. The point coordinates on the abscissa are placed at the center of the corresponding  $p_T$ -bin. For both cases the same extraction method was used, namely the  $2\text{-}\Delta\phi$ -bind method using the power-law background function and extracting the yield by taking the integral of the Gaussian function  $f_S$ . (right) Significance  $(v_2^{\text{TPChalf}} - v_2^{\text{VZERO}}) / \sigma(v_2^{\text{TPChalf}} - v_2^{\text{VZERO}})$  as a function of  $p_T$  for two extreme scenarios of treating the error  $\sigma(v_2^{\text{TPChalf}} - v_2^{\text{VZERO}})$ . For details see text.

using the VZERO event plane, which might hint to possible non-flow contributions to the measured  $v_2$  using the TPC event plane. In order to answer the question whether the discrepancy is statistically significant, the measured quantity  $v_2^{\text{TPChalf}} - v_2^{\text{VZERO}}$ , i.e. the difference between the  $v_2$ -values obtained with the two alternative event plane  $\Psi_2$  determinations using the TPC respectively the VZERO, was normalized by the error of the quantity. For the error  $\sigma(v_2^{\text{TPChalf}} - v_2^{\text{VZERO}})$  two extreme scenarios were assumed:

1. The quantities  $v_2^{\text{TPChalf}}$  and  $v_2^{\text{VZERO}}$  are fully correlated, i.e. the correlation coefficient is 1. In this case the error of the difference  $v_2^{\text{TPChalf}} - v_2^{\text{VZERO}}$  is given by:

$$\sigma(v_2^{\text{TPChalf}} - v_2^{\text{VZERO}}) = \sqrt{\sigma(v_2^{\text{TPChalf}})^2 + \sigma(v_2^{\text{VZERO}})^2 - 2\sigma(v_2^{\text{TPChalf}})\sigma(v_2^{\text{VZERO}})} \quad (5.10)$$

The minus sign in the root of eq. 5.10 is due to the product of the two partial derivatives  $\frac{\partial(v_2^{\text{TPChalf}} - v_2^{\text{VZERO}})}{\partial v_2^{\text{VZERO}}} = -1$  and  $\frac{\partial(v_2^{\text{TPChalf}} - v_2^{\text{VZERO}})}{\partial v_2^{\text{TPChalf}}} = 1$ .

2. The quantities  $v_2^{\text{TPChalf}}$  and  $v_2^{\text{VZERO}}$  are uncorrelated, i.e. the correlation coefficient is 0. In that case the error of the difference  $v_2^{\text{TPChalf}} - v_2^{\text{VZERO}}$  is given by:

$$\sigma(v_2^{\text{TPChalf}} - v_2^{\text{VZERO}}) = \sqrt{\sigma(v_2^{\text{TPChalf}})^2 + \sigma(v_2^{\text{VZERO}})^2} \quad (5.11)$$

The true correlation and thus the error  $\sigma(v_2^{\text{TPChalf}} - v_2^{\text{VZERO}})$  are somewhere between the two extreme cases. Systematic errors are not considered here and they might contribute to the error  $\sigma(v_2^{\text{TPChalf}} - v_2^{\text{VZERO}})$ . Figure 5.19 (right) shows the significance

$(v_2^{\text{TPChalf}} - v_2^{\text{VZERO}}) / \sigma(v_2^{\text{TPChalf}} - v_2^{\text{VZERO}})$  as a function of  $p_T$ . In two cases, for the  $p_T$ -bins  $6 \text{ GeV}/c < p_T < 8 \text{ GeV}/c$  and  $8 \text{ GeV}/c < p_T < 12 \text{ GeV}/c$ , the significance is larger than 3 for the scenario, where the quantities  $v_2^{\text{TPChalf}}$  and  $v_2^{\text{VZERO}}$  are fully correlated. However, in the  $p_T$ -bin  $2 \text{ GeV}/c < p_T < 4 \text{ GeV}/c$  the significance is larger than 3, either, but in the wrong direction in the sense that  $v_2^{\text{TPChalf}}$  is apparently significantly smaller than  $v_2^{\text{VZERO}}$ . Non-flow contributions, however, always increase the measured  $v_2$  [33]. This shows that the error  $\sigma(v_2^{\text{TPChalf}} - v_2^{\text{VZERO}})$  is clearly underestimated assuming a correlation coefficient of 1 between  $v_2^{\text{TPChalf}}$  and  $v_2^{\text{VZERO}}$ , which yields too large values for the significance  $(v_2^{\text{TPChalf}} - v_2^{\text{VZERO}}) / \sigma(v_2^{\text{TPChalf}} - v_2^{\text{VZERO}})$ . As a consequence no systematic error due to non-flow contributions was assigned to the central  $D^{*+}$   $v_2$ -results, given also the fact that the significance estimated with an underestimated error  $\sigma(v_2^{\text{TPChalf}} - v_2^{\text{VZERO}})$  reaches the value of  $\approx 5$  in only one  $p_T$ -bin, namely for  $6 \text{ GeV}/c < p_T < 8 \text{ GeV}/c$ .

The non-flow contribution quantification in case of the  $v_3$ -measurement was treated by comparing the  $v_3$ -results using the event plane angle  $\Psi_3$  determination with the TPC only, applying two options. The  $\Psi_3$  estimation using the VZERO was not used due to a currently missing recentering procedure and hence not acceptable flatness quality of the distribution of  $\Psi_3^{\text{VZERO}}$ , see fig. 5.7 (right). The two options using the TPC only were an  $\eta$ -gap-analysis, see fig. 5.9 (left), and the analysis without an  $\eta$ -gap. Figure 5.20 (left) shows the comparison of the measured  $v_3$  using these two options. The analysis results including the statistical error using an  $\eta$ -gap are represented by the blue datapoints and the ones without an  $\eta$ -gap by the red datapoints. The analysis without an  $\eta$ -gap yields extreme  $v_3$ -values up to  $v_3 = 0.5$  for  $p_T > 6 \text{ GeV}/c$ . Both analyses were

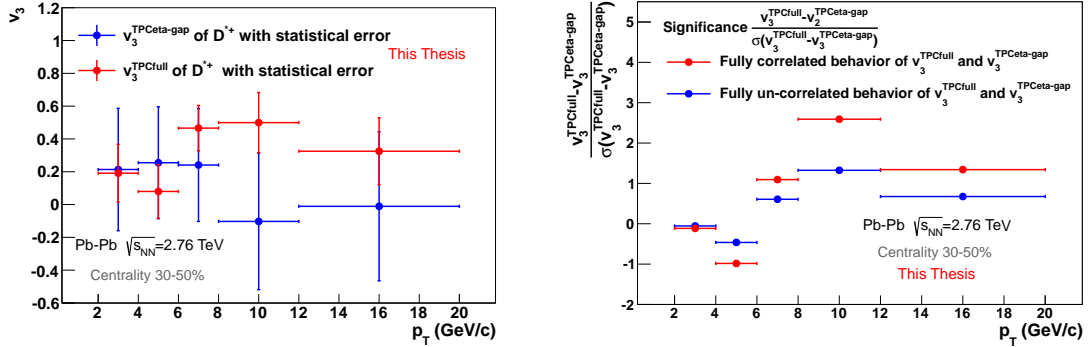


**Figure 5.20.:** (left) Comparison of the extracted central  $D^{*+}$   $v_2$ -value using the positive  $\eta$  TPC event plane angle (blue datapoints) and the  $D^{*+}$   $v_2$ -value obtained using the event plane angle determined with the VZERO-detector (red datapoints). The vertical error bars represent the statistical errors and the horizontal error bars the distances to the limits of the corresponding  $p_T$ -bin. The point coordinates on the abscissa are placed at the center of the corresponding  $p_T$ -bin. For both cases the same extraction method was used, namely the  $2\text{-}\Delta\phi$ -bind method using the power-law background function and extracting the yield by taking the integral of the Gaussian function  $f_S$ . (right) Significance  $(v_2^{\text{TPChalf}} - v_2^{\text{VZERO}}) / \sigma(v_2^{\text{TPChalf}} - v_2^{\text{VZERO}})$  as a function of  $p_T$  for two extreme scenarios of treating the error  $\sigma(v_2^{\text{TPChalf}} - v_2^{\text{VZERO}})$ . For details see text.

compared with each other using the same procedure as for the  $v_2$ -case above. The significance  $\left(v_3^{\text{TPCfull}} - v_3^{\text{TPC-}\eta\text{-gap}}\right) / \sigma\left(v_3^{\text{TPCfull}} - v_3^{\text{TPC-}\eta\text{-gap}}\right)$  is shown in fig. 5.20 (right) for the two extreme scenarios for determination of the error  $\sigma\left(v_3^{\text{TPCfull}} - v_3^{\text{TPC-}\eta\text{-gap}}\right)$  as described above for the  $v_2$ -case. The significance is smaller than 3 for all  $p_T$ -bins assuming both extreme scenarios. However, the difference to the  $v_2$ -case shown in figs 5.19 is that here the error  $\sigma\left(v_3^{\text{TPCfull}} - v_3^{\text{TPC-}\eta\text{-gap}}\right)$  in both extreme correlation scenarios for determining the error  $\sigma\left(v_3^{\text{TPCfull}} - v_3^{\text{TPC-}\eta\text{-gap}}\right)$  is dominated by the large statistical error of the TPC  $\eta$ -gap measurement. The error  $\sigma\left(v_3^{\text{TPC-}\eta\text{-gap}}\right)$  is about a factor 2 larger than the statistical error of the TPC  $v_3$ -measurement without an  $\eta$ -gap  $\sigma\left(v_3^{\text{TPCfull}}\right)$ , see fig. 5.20 (left). In the  $v_2$ -case the difference of the errors  $\sigma\left(v_2^{\text{TPChalf}}\right)$  and  $\sigma\left(v_2^{\text{ZERO}}\right)$  was much smaller as shown in fig. 5.19 (left). The conclusion is that the non-flow contributions to the  $v_3$  TPC analysis results without an  $\eta$ -gap cannot be quantified by using the  $v_3$ -results from the TPC analysis with an  $\eta$ -gap. The reason is the insufficient precision of the  $v_3$  TPC analysis with an  $\eta$ -gap. As a consequence, the results of the  $v_3$  TPC analysis without an  $\eta$ -gap were discarded because an unknown, with the current statistics not quantifiable amount  $v_3$ , which is generated by non-flow effects. The results using the  $v_3$  TPC analysis with an  $\eta$ -gap with larger statistical errors but with suppressed non flow-contributions were used for determining the central  $v_3$ -values.

The systematic error study considering systematic error contributions from event plane resolution as well as from yield extraction and background subtraction, see fig. 5.18, were accordingly carried out on the results using the TPC analysis with an  $\eta$ -gap.

### Systematic error from B-feed-down

A certain fraction of  $D^{*+}$  mesons in the following called " $f_c$ " produced in high-energy nuclear collisions at the LHC originate from decays of produced B mesons. These are mesons with one b-quark and one up-, down-, strange- or charm-quark. In case one is interested in measuring a  $v_n$  of an inclusive sample of  $D^{*+}$  mesons, i.e. from fragmentation or coalescence of c-quarks with other quarks including feed-down decays of B mesons, this systematic error contribution to the measured  $v_n$  is obsolete. However, if a  $v_n$ -measurement of prompt  $D^{*+}$  mesons, i.e.  $D^{*+}$  mesons originating only from fragmentation or coalescence of c-quarks with other quarks, is anticipated, the contribution to the measured  $v_n$  of the  $D^{*+}$  mesons stemming from B meson decays has to be subtracted. The  $v_2$ -predictions provided by theoretical models shown in fig 2.27 in chap. 2, sec. 2.4 are in any case provided for prompt  $D^{*+}$  mesons. The  $v_n$  is an additive quantity, which can be easily shown using the formula for the observed  $v_n^{\text{obs}}$  in eq. 5.4 and splitting the yield in 2 fractions, namely:

1.  $N_{\text{in-plane+out-of-plane}}^{\text{feed-down}} = (1 - f_c) \cdot N_{\text{in-plane+out-of-plane}}^{\text{total}}$

2.  $N_{\text{in-plane+out-of-plane}}^{\text{prompt}} = f_c \cdot N_{\text{in-plane+out-of-plane}}^{\text{total}}$

Then, the two ways (a) and (b) to get the total uncorrected  $v_n^{\text{total,obs}}$  in the following equation equals:

$$\begin{aligned}
 v_n^{\text{total,obs}} &= f_c \cdot v_n^{\text{prompt,obs}} + (1 - f_c) \cdot v_n^{\text{feed-down,obs}} & \text{(a)} \\
 &= \frac{\pi}{4} \frac{\left( N_{\text{in-plane}}^{\text{feed-down}} + N_{\text{in-plane}}^{\text{prompt}} \right) - \left( N_{\text{out-of-plane}}^{\text{feed-down}} + N_{\text{out-of-plane}}^{\text{prompt}} \right)}{N_{\text{in-plane}}^{\text{prompt}} + N_{\text{in-plane}}^{\text{feed-down}} + N_{\text{out-of-plane}}^{\text{prompt}} + N_{\text{out-of-plane}}^{\text{feed-down}}} & \text{(b)} \quad (5.12)
 \end{aligned}$$

with  $v_n^{\text{prompt,obs}}$  being the observed  $v_n$  of prompt  $D^{*+}$  mesons and  $v_n^{\text{feed-down,obs}}$  the observed  $v_n$  of secondary  $D^{*+}$  mesons stemming from B meson decays. As the event plane resolution used for correcting  $v_n^{\text{prompt,obs}}$  and  $v_n^{\text{feed-down,obs}}$  is equal, eq. 5.12 (a) holds for both the corrected values  $v_n^{\text{prompt}}$  and  $v_n^{\text{feed-down}}$  and the uncorrected values  $v_n^{\text{prompt}}$  and  $v_n^{\text{feed-down}}$ .

The  $v_n$  of B mesons is unknown and therefore the  $v_n$  of  $D^{*+}$  mesons stemming from B meson decays is unknown, either. Two extreme cases were assumed to determine the contribution of the secondary  $D^{*+}$  meson  $v_n$ :

1. Heavy b-quarks do not take part in the collective flow of the expanding medium and at higher  $p_T$ , where the measured  $v_n$  originates from path length dependence of quark energy loss, the b-quarks do not interact with the medium and as a consequence do not lose any energy. In this case the expected  $v_n^{\text{feed-down}}$  is zero. According to eq. 5.12, the measured  $v_n$  of the prompt  $D^{*+}$  mesons is thus given by:  $v_n^{\text{prompt}} = (1/f_c) \cdot v_n^{\text{total}}$ , with  $v_n^{\text{total}}$  being the  $v_n$ -result obtained from the inclusive  $D^{*+}$   $v_n$ -analysis. This yields an asymmetric relative systematic error on the prompt  $D^{*+}$   $v_n$  of  $\frac{\Delta v_n^{\text{prompt}}}{v_n^{\text{prompt}}} = \frac{1}{f_c} - 1$ . As  $f_c$  is always smaller than 1, this systematic error contribution is always positive.
2. Heavy b-quarks take part in the collective flow of the expanding medium to the same extent as c-quarks and at higher  $p_T$  the energy loss of b-quarks is equal to the energy loss of c-quarks. In this case the expected  $v_n^{\text{feed-down}}$  is of the order of  $v_n^{\text{prompt}}$ ,  $v_n^{\text{feed-down}} \approx v_n^{\text{prompt}}$ . According to eq. 5.12 the measured  $v_n$  of the prompt  $D^{*+}$  mesons is thus given by:  $v_n^{\text{prompt}} = v_n^{\text{total}}$ , with  $v_n^{\text{total}}$  being the  $v_n$ -result obtained with the inclusive  $D^{*+}$   $v_n$ -analysis. This yields a relative systematic error on the prompt  $D^{*+}$   $v_n$  of 0%.

In order to estimate the factor  $f_c$ , which is the fraction of the reconstructed  $D^{*+}$  mesons stemming from c-quarks, the following ingredients were used:

- The first category of ingredients are production cross sections at midrapidity of B mesons  $\frac{d\sigma(\text{B})}{dp_T}$  and prompt  $D^{*+}$  mesons  $\frac{d\sigma(\text{D}^{*+})^{\text{prompt}}}{dp_T}$  provided by theoretical FONLL [68] pQCD calculations in proton-proton collisions. These cross sections describe well the measured corrected prompt  $D^{*+}$  yields at the LHC with ALICE, see [112], and the B meson production cross section at the LHC measured with LHCb, see [113] and CMS, see [114]. The uncertainty bands of the cross sections  $\frac{d\sigma}{dp_T}$  using these pQCD calculations are given by varying the factorization and renormalization scales  $\mu_F$  and  $\mu_R$  as well as by varying the charm and beauty quark masses. In pQCD calculations the renormalization scale  $\mu_R$  is needed to absorb

short range (ultraviolet) singularities. On the other hand, the quantity  $\mu_F$  is the factorization scale and is needed to avoid long-range (infrared) singularities.

- The second module is the EvtGen-package, see [115], which simulates the B meson decays to  $D^{*+}$  mesons and samples the  $p_T$  of the  $D^{*+}$  mesons. This procedure together with the B meson production cross section given by FONLL  $\frac{d\sigma(B)}{dp_T}$  provides the expected production cross section of secondary  $D^{*+}$  mesons  $\frac{d\sigma(D^{*+})^{\text{feed-down}}}{dp_T}$  in proton-proton collisions. The most contributing decay channels of B mesons with an  $D^{*+}$  in the final state are the following ones:

- $B^0 \rightarrow D^{*-} + e(\mu)^+ + \nu_{e(\mu)}$  respectively  $\bar{B}^0 \rightarrow D^{*+} + e(\mu)^- + \bar{\nu}_{e(\mu)}$  with a branching ratio of  $(4.95 \pm 0.11)\%$  [10].
- $B^0 \rightarrow D^{*-} + \tau^+ + \nu_\tau$  respectively  $\bar{B}^0 \rightarrow D^{*+} + \tau^- + \bar{\nu}_\tau$  with a branching ratio of  $(1.5 \pm 0.5)\%$  [10].
- $B^+ \rightarrow D^{*-} + e(\mu)^+ + \nu_{e(\mu)} + \pi^+$  respectively  $B^- \rightarrow D^{*+} + e(\mu)^- + \bar{\nu}_{e(\mu)} + \pi^-$  with a branching ratio of  $(0.6 \pm 0.06)\%$  [10].

- The third input for estimating the factor  $f_c$  are efficiencies at midrapidity calculated using PbPb Hijing+Pythia Monte Carlo simulations, see chap. 3, sec. 3.2.6 and [99–102] with a full ALICE detector description of the prompt  $D^{*+}$  mesons  $(\epsilon)^{\text{prompt}}$  as well as of the secondary  $D^{*+}$  mesons  $(\epsilon)^{\text{feed-down}}$ .
- The last ingredient is a currently unknown ratio of the nuclear modification factors of  $D^{*+}$  mesons stemming from B meson decays and prompt  $D^{*+}$  mesons:  $\frac{R_{AA}(D^{*+})^{\text{feed-down}}}{R_{AA}(D^{*+})^{\text{prompt}}}$ . The  $R_{AA}$  of prompt  $D^{*+}$  meson in high energy-nuclear collisions at  $\sqrt{s_{NN}} = 2.76$  TeV has been indeed measured by ALICE, see [116]. However, the  $R_{AA}$ -measurement of B mesons at LHC by the CMS-collaboration [114] is restricted to  $p_T > 6$  GeV and is measured in very large  $p_T$ - and centrality-bins. Moreover, the measurement is not performed via full reconstruction of B mesons but using displaced  $J/\Psi$  mesons stemming from B meson decays. Due to these restrictions the CMS-measurement is currently not used to impose upper nor lower limits on the B meson  $R_{AA}$ .

Using these four classes of ingredients listed above, the factor  $f_c$  is thus given by the following formula:

$$\begin{aligned}
 f_c &= \frac{\left(\frac{d\sigma(D^{*+})}{dp_T} \cdot R_{AA}(D^{*+}) \cdot (\epsilon)\right)^{\text{prompt}}}{\left(\frac{d\sigma(D^{*+})}{dp_T} \cdot R_{AA}(D^{*+}) \cdot (\epsilon)\right)^{\text{prompt}} + \left(\frac{d\sigma(D^{*+})}{dp_T} \cdot R_{AA}(D^{*+}) \cdot (\epsilon)\right)^{\text{feed-down}}} \\
 &= \left(1 + \frac{\left(\frac{d\sigma(D^{*+})}{dp_T} \cdot R_{AA}(D^{*+}) \cdot (\epsilon)\right)^{\text{feed-down}}}{\left(\frac{d\sigma(D^{*+})}{dp_T} \cdot R_{AA}(D^{*+}) \cdot (\epsilon)\right)^{\text{prompt}}}\right)^{-1}
 \end{aligned} \tag{5.13}$$

The factor  $f_c$  and all ingredients used in eq. 5.13 depend on the  $p_T$  of the  $D^{*+}$  and have been omitted for brevity. The values for the integrated luminosity  $\mathcal{L}_{\text{int}}$  and for the number of binary nucleus-nucleus collisions occurring in a lead-lead collision  $\langle N_{\text{coll}} \rangle$  are not needed in eq. 5.13 because they cancel in the ratio of the estimated prompt and feed-down  $D^{*+}$  yields. The uncertainty band of the  $f_c$  is given by the envelope, which is obtained varying the ratio  $\frac{R_{AA}(D^{*+})^{\text{feed-down}}}{R_{AA}(D^{*+})^{\text{prompt}}}$  in the range  $0.3 < \frac{R_{AA}(D^{*+})^{\text{feed-down}}}{R_{AA}(D^{*+})^{\text{prompt}}} < 3$  as well as the cross sections  $\frac{d\sigma(B)}{dp_T}$  and  $\frac{d\sigma(D^{*+})^{\text{prompt}}}{dp_T}$  within their theoretical uncertainties. According to [116] the  $R_{AA}$  of prompt  $D^{*+}$  mesons is about 0.5 in the centrality range 30-50%. Thus the variation of the ratio  $\frac{R_{AA}(D^{*+})^{\text{feed-down}}}{R_{AA}(D^{*+})^{\text{prompt}}}$  in the given range covers a  $R_{AA}$ -range of secondary  $D^{*+}$  mesons of 1.5 – 0.15.

Figure 5.21 shows the upper and the lower limit of  $f_c$  as a function of  $p_T$ . The limits

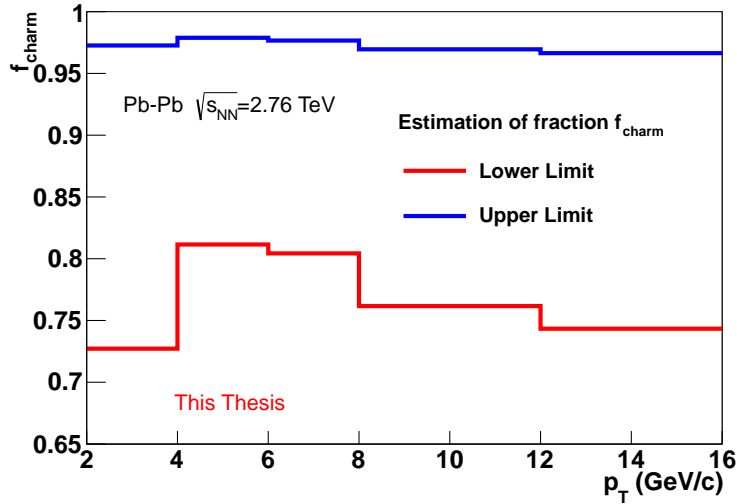


**Figure 5.21.:** Upper and lower limit of the estimated charm fraction factor  $f_c$  using inputs from theoretical FONLL [68] predictions and Monte-Carlo simulations. For more details see text.

originate from the variations described above. The relative asymmetric systematic error contribution to the measured  $v_n$  is given by  $\frac{\Delta v_n^{\text{prompt}}}{v_n^{\text{prompt}}} = \frac{1}{f_c} - 1$ . For determination of the relative asymmetric systematic error contribution the lower limit of  $f_c$  is taken, which yields an upper limit for the systematic error due to B-feed-down on the measured  $v_n^{\text{prompt}}$ , following a conservative approach. This systematic error contribution is largest for  $2 \text{ GeV}/c < p_T < 4 \text{ GeV}/c$  and yields  $\Delta v_n^{\text{prompt}}/v_n^{\text{prompt}} = +37\%$  in this  $p_T$ -bin.

### Consistency checks

In order to investigate the effect of varying the topological cuts used for extracting the  $D^{*+}$  yields in the  $p_T$ - and  $\Delta\phi$ -bins on the  $v_2$ -results, the  $v_2$ -analysis was carried out with an alternative cut-set, namely with cut-set 2 listed in tab. 4.4 in chap. 4, sec. 4.1. Moreover, the results obtained with the positive  $\eta$  TPC event plane angle  $\Psi_2$  used as

central  $v_2$ -values were compared to  $v_2$ -values obtained with the full  $\eta$  TPC event plane angle  $\Psi_2$ . Figure 5.22 (left) shows the comparison of the  $v_2$ -results using the two alternative

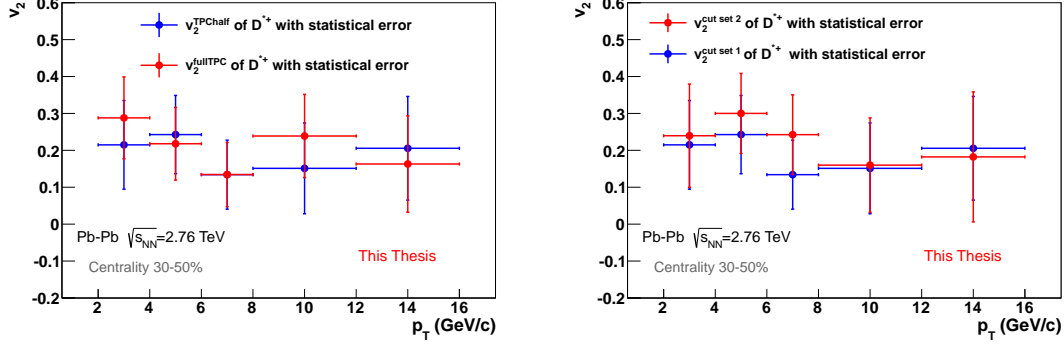


**Figure 5.22.:** (left) Comparison of the extracted central  $D^{*+}$   $v_2$ -value using the positive  $\eta$  TPC event plane angle  $\Psi_2$  (blue datapoints) and the  $D^{*+}$   $v_2$ -value obtained using the event plane angle determined with the full  $\eta$  TPC event plane angle  $\Psi_2$  (red datapoints). The error bars represent the statistical errors. (right) Comparison of the extracted central  $D^{*+}$   $v_2$ -value using the positive  $\eta$  TPC event plane angle  $\Psi_2$  and the topological cut-set 1 (blue datapoints) and the  $D^{*+}$   $v_2$ -value obtained using the same event plane angle determination method but the topological cut-set 2 (red datapoints). Both cut-sets are listed in tab. 4.4 in chap. 4, sec. 4.1. The vertical error bars represent the statistical errors and the horizontal error bars the distances to the limits of the corresponding  $p_T$ -bin. The point coordinates on the abscissa are placed at the center of the corresponding  $p_T$ -bin.

methods for determining the event plane angle  $\Psi_2$  (blue datapoints: positive- $\eta$  TPC, red datapoints: full- $\eta$  TPC) and fig. 5.22 (right) the comparison of the  $v_2$ -results using two different sets of topological cuts both listed in tab. 4.4, chap. 4, sec. 4.1 (blue datapoints: cut-set 1, red datapoints: cut-set 2). The error bars in both figures represent the statistical errors. In both cases the datapoints of the alternative analyses (red datapoints) move by  $\pm 1\sigma$  up and down on the ordinate in units of the statistical errors of the datapoints of the analyses used for the central  $v_2$ -values (blue datapoints). These fluctuations mostly originate from the fluctuations in the yield extraction procedure. The systematic errors (not drawn in) of the central  $v_2$ -values represented by the blue datapoints in fig. 5.22 originating from yield extraction are of the same order as the statistical errors, see tab. 5.1. Thus the magnitude of the fluctuations of the red datapoints representing the alternative analyses is included in the detailed systematic study presented above, where the systematic uncertainty originating from yield extraction was addressed. By assigning an additional independent systematic error due to the discrepancies shown in fig. 5.22 the systematic error contribution from yield extraction would be double- or even triple-counted. Therefore neither an additional systematic error due to topological cut selection nor due to TPC event plane selection was assigned.

### Summary

The statistical errors and the individual systematic error contributions to the measured  $v_n$  are listed in tab. 5.4. Three analysis-types are considered:  $v_2$ -fine,  $v_2$ -wide and  $v_3$ -fine. The first two ones are the analyses based on the positive  $\eta$  TPC event plane angle with coarse and fine  $p_T$ -binning. The last one is the  $v_3$ -analysis based on the TPC full  $\eta$

5. Road to the final results for the  $D^{*+}$   $v_2$ - and  $D^{*+}$   $v_3$ -anisotropy parameters

	Central value	stat.	syst. (Yield)	syst. (EP-reso-1)	syst. (EP-reso-2)	syst. (total)	syst. (B-feed)
$p_T$ -bin [GeV/ $c$ ]							
<b><math>v_2</math>-fine</b>							
2 – 4	0.21	$\pm 0.12$	$\pm 0.13$	$\pm 0.01$	+0.02	$^{+0.14}_{-0.13}$	+0.08
4 – 6	0.24	$\pm 0.11$	$\pm 0.15$	$\pm 0.01$	+0.02	$\pm 0.15$	+0.06
6 – 8	0.13	$\pm 0.09$	$\pm 0.10$	$\pm 0.01$	+0.01	$\pm 0.10$	+0.03
8 – 12	0.15	$\pm 0.12$	$\pm 0.08$	$\pm 0.01$	+0.01	$\pm 0.08$	+0.08
12 – 16	0.21	$\pm 0.14$	$\pm 0.13$	$\pm 0.01$	+0.02	$\pm 0.13$	+0.07
<b><math>v_2</math>-wide</b>							
2 – 6	0.22	$\pm 0.07$	$\pm 0.06$	$\pm 0.01$	+0.02	$\pm 0.06$	+0.04
6 – 16	0.15	$\pm 0.07$	$\pm 0.06$	$\pm 0.01$	+0.01	$\pm 0.06$	+0.04
<b><math>v_3</math>-fine</b>							
2 – 4	0.21	$\pm 0.37$	$\pm 0.27$	$\pm 0.04$	-	$\pm 0.27$	+0.08
4 – 6	0.25	$\pm 0.34$	$\pm 0.20$	$\pm 0.05$	-	$\pm 0.21$	+0.06
6 – 8	0.24	$\pm 0.34$	$\pm 0.45$	$\pm 0.05$	-	$\pm 0.46$	+0.06
8 – 12	-0.1	$\pm 0.41$	$\pm 0.15$	$\pm 0.02$	-	$\pm 0.15$	-0.03
12 – 20	-0.01	$\pm 0.45$	$\pm 0.18$	$\pm 0.002$	-	$\pm 0.18$	-0.004

**Table 5.4.:** List of central values for the  $v_2$  and  $v_3$ , the corresponding statistical errors, systematic error contributions, the total systematic errors excluding the B-feed-down contribution and the error contribution from B-feed-down for various  $p_T$ -bins and three analysis types:  $v_2$ -fine,  $v_2$ -wide and  $v_3$ -fine. For details see text.

event plane angle with an  $\eta$ -gap of  $\Delta\eta = 1.0$  between the two sub-events. Four types of individual systematic error sources and the total systematic error excluding the B-feed-down systematic error contribution are listed:

- syst. (Yield): The symmetric systematic error contribution from yield extraction and background subtraction. This uncertainty is the dominating systematic error source in the  $v_2$  and  $v_3$ -analysis. It is of the same order as the statistical error and the relative magnitude  $\Delta(v_n)/v_n$  is in the range 27%-73% for the  $v_2$ -case. For the  $v_3$ -case this relative systematic error contribution is in the range of 79%-190% for a  $p_T$  of the  $D^{*+}$  of  $2 \text{ GeV}/c < p_T < 8 \text{ GeV}/c$ . For  $p_T > 8 \text{ GeV}/c$  the absolute systematic uncertainty contribution from yield extraction and background subtraction to the total  $D^{*+}$   $v_3$  systematic error is of the order of  $\pm 0.3$ .
- syst. (EP-reso-1): The symmetric systematic error contribution from event plane resolution uncertainty due to the wide centrality-bin of 20% with an lower limit of 30% and upper limit of 50%. The relative magnitude  $\Delta(v_n)/v_n$  is 4% in the  $v_2$ -case and 20% in the  $v_3$ -case. This systematic error contribution differs for the two cases because the variation of the correction factor  $C_n$  in the centrality range of 30-50% is stronger in the  $v_3$ - than in the  $v_2$ -case, see figs. 5.8 (right), 5.10. Note that  $C_n$  is given by the inverse value of the resolutions shown in these figures.
- syst. (EP-reso-2): The asymmetric systematic error contribution from event plane

resolution uncertainty due to the discrepancy of using different methods for the resolution determination shown in fig. 5.8 (right). The relative magnitude  $\Delta(v_n)/v_n$  is +9% in the  $v_2$ -case and 0% in the  $v_3$ -case. In the latter case only one method to determine the event plane resolution was performed due to the expected negligible impact on the total error, which is currently very large.

- syst. (B-feed): The asymmetric systematic error contribution from B-feed-down. The relative magnitude  $\Delta(v_n)/v_n$  is in the range + (25% – 37%) in the  $v_2$ -case and in the  $v_3$ -case.
- syst. (total): The individual positive and negative systematic error contributions are assumed uncorrelated and summed in quadrature and then the square-root is calculated. The B-feed-down systematic error contribution is excluded from this procedure. The total systematic uncertainty is of the same order as the statistical error and the relative magnitude  $\Delta(v_n)/v_n$  is in the range 29%-73% for the  $v_2$ -case. For the  $v_3$ -case the relative total systematic error is in the range of 81%-190% for a  $p_T$  of the  $D^{*+}$  of  $2 \text{ GeV}/c < p_T < 8 \text{ GeV}/c$ . For  $p_T > 8 \text{ GeV}/c$  the total absolute systematic uncertainty of the  $D^{*+} v_3$  is of the order of  $\pm 0.3$ .

## 6. Final $D^{*+}$ $v_n$ -results

In this chapter the final anisotropy parameters  $v_2$  and  $v_3$  of the charmed meson  $D^{*+}$  are compared to the  $v_n$ -results of charged particles containing only light flavored up-, down- and strange-quarks measured by the ALICE collaboration [39], to the  $v_2$ -predictions provided by theoretical models described in chap. 2 and to the  $v_2$ -results for the charmed mesons  $D^0$  and  $D^+$  measured by the ALICE collaboration [109, 110]. The anisotropy parameters  $v_2$  and  $v_3$  have been determined with the event plane method [34] determining the event plane angles  $\Psi_2$  and  $\Psi_3$  with the Time Projection Chamber. In this chapter first the  $D^{*+}$   $v_2$ - and  $D^{*+}$   $v_3$ -results are presented. As next step, the  $D^{*+}$   $v_2$  results are compared to the  $v_2$ -results of the charmed mesons  $D^0$  and  $D^+$  and to the measured  $v_2$  of charged particles. Then, the  $D^{*+}$   $v_2$  results are compared together with an existing charmed meson nuclear modification factor ( $R_{AA}$ ) measurement to model predictions for the  $R_{AA}$  and  $v_2$ . Finally, the extracted  $D^{*+}$   $v_3$  is compared to the  $v_3$ -measurement of charged particles.

### 6.1. $D^{*+}$ $v_2$ - and $D^{*+}$ $v_3$ -results

In this section the final  $D^{*+}$   $v_2$ - and  $D^{*+}$   $v_3$ -results are presented. Figure 6.1 shows the measured  $D^{*+}$   $v_2$  (left), respectively the  $D^{*+}$   $v_3$  (right) as a function of the transverse momentum  $p_T$  of the  $D^{*+}$ . The vertical error bars represent the statistical errors and

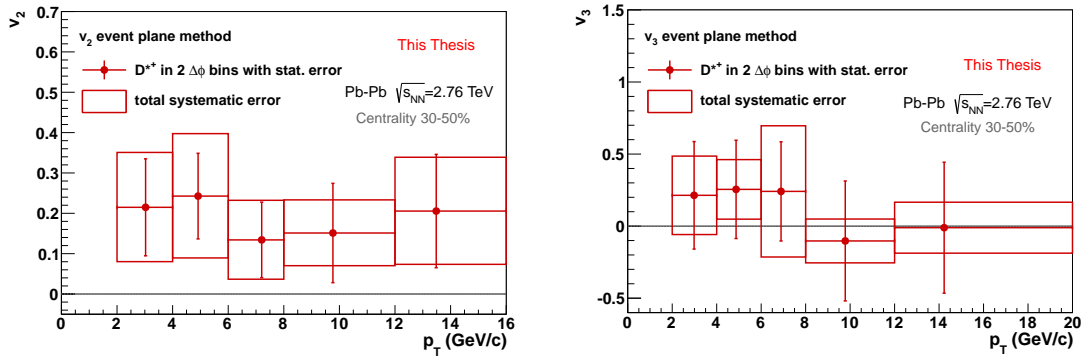


**Figure 6.1.:** Final central results of the  $D^{*+}$   $v_2$  (left) and the  $D^{*+}$   $v_3$  (right) with statistical errors (red error bars in vertical direction) and the total systematic errors without the B-feed-down contribution (red boxes spreads in vertical direction). The upper respectively lower limits represented by the red error bars and by the red boxes in horizontal direction are the bounds of the corresponding  $p_T$ -bin. The point coordinate on the abscissa of the corresponding  $p_T$ -bin is the mean  $p_T$ .

the spread of the boxes in vertical direction the total systematic errors without the B-feed-down contribution listed in tab. 5.4 in chap. 5, sec. 5.3. The relative statistical

uncertainty of the  $D^{*+}$   $v_2$ -measurement is in the range of 44% – 81%. In case of the  $D^{*+}$   $v_3$  the relative statistical uncertainty is in the range of 130% – 175% for the  $p_T$ -range of the  $D^{*+}$  of  $2 \text{ GeV}/c < p_T < 8 \text{ GeV}/c$ . For  $p_T > 8 \text{ GeV}/c$  the central  $v_3$ -value is of the order of  $\approx 0$  with currently large statistical uncertainties of the order of  $\pm 0.4$ . A measurement with increased sizes of the  $p_T$ -bins in the  $v_2$ -case has been carried out with decreased statistical and systematic error and will be shown further below compared to the  $v_2$ -measurement of charged particles and to  $v_2$ -predictions from models. The total systematic uncertainties without the B-feed-down contribution are of the same order as the statistical uncertainties and the relative magnitude  $\Delta(v_n)/v_n$  is in the range of 54%-73% for the  $v_2$ -case depending on the  $p_T$ -bin and in the range 81%-190% for the  $v_3$ -case for a  $p_T$  of the  $D^{*+}$  of  $2 \text{ GeV}/c < p_T < 8 \text{ GeV}/c$ . For  $p_T > 8 \text{ GeV}/c$  the current absolute total systematic uncertainty without the B-feed-down contribution of the  $D^{*+}$   $v_3$  is of the order of  $\pm 0.2$ .

The limits given by the horizontal error bars and the spread of the systematic error boxes in horizontal direction represent the bounds of the corresponding  $p_T$ -bin. The point coordinate on the abscissa of the corresponding  $p_T$ -bin is the mean  $p_T$ . The mean  $p_T$  for each  $p_T$ -bin  $\langle p_T \rangle$  is determined with the same background subtraction procedure as used for the determination of the quantity  $\langle \cos(n\Delta\phi) \rangle$  applying the 2D-sidebands method described in sec. 5.2. Here the only difference is that the main input to the method is a histogram with the  $p_T$  instead of the variable  $\cos(n\Delta\phi)$  on the abscissa and the  $\Delta M$ -variable on the ordinate, see fig. 5.14 in sec. 5.2.

## 6.2. $D^{*+}$ $v_2$ comparison to other $v_2$ -measurements

In this section the final  $D^{*+}$   $v_2$ -measurement is compared to  $v_2$ -measurements of the charmed hadrons  $D^0$  and  $D^+$  carried out by the ALICE collaboration, see [109, 110]. This comparison is performed to demonstrate the robustness of the three  $v_2$ -analyses of the charmed mesons  $D^{*+}$ ,  $D^0$  and  $D^+$ . The  $v_2$ -results of the three charmed mesons have to be consistent within the uncertainties because the  $v_2$  is mainly generated by interaction of charm quarks with the anisotropically expanding QGP, which fragment to D mesons. For more details see chap. 2, secs. 2.3. 2.4. Moreover, the final  $D^{*+}$   $v_2$ -measurement is compared to the measured  $v_2$  of charged particles carried out by the ALICE-collaboration [39] in this section. This comparison is performed to investigate whether charm quarks take part in the collective expansion of the QGP to the same extent as light flavored up-, down- and strange-quarks. This question can be addressed by comparing the magnitude of the measured  $v_2$  of  $D^{*+}$  mesons for a  $p_T$  of up to  $p_T \approx 6 \text{ GeV}/c$  with the magnitude of the measured  $v_2$  of charged particles, which are mainly pions, kaons, and protons. For a  $p_T$  of  $p_T \gtrsim 6 \text{ GeV}/c$  this comparison addresses the question to which extent charm quarks also experience the effect of path length dependent energy loss, see chap. 2, secs. 2.3. 2.4.

Figures 6.2a, 6.2b show the comparison of the  $D^{*+}$   $v_2$ -result to the results obtained for charmed mesons  $D^+$  and  $D^0$  [109, 110]. In order to determine the  $v_2$  of the three charmed mesons the same dataset and event plane determination method were used. The meaning of the error bars and boxes for the  $D^{*+}$  is equal to the situation in fig. 6.1 described above. The meaning of the error bars and the sizes of the systematic error boxes in vertical direc-

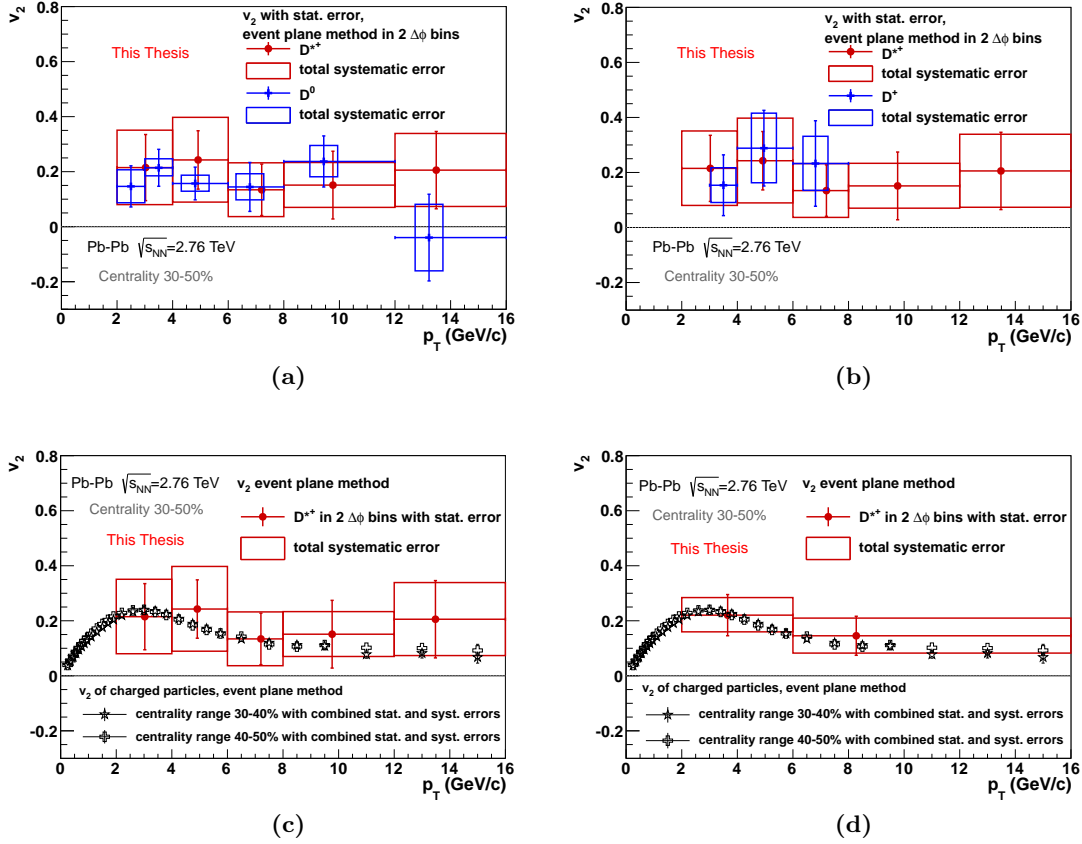


**Figure 6.2.:** Comparison of the  $D^{*+}$   $v_2$ -fine-result to the results obtained for the charmed mesons  $D^0$  (a) [109, 110] and  $D^+$  (b) [109, 110] and to the  $v_2$  of charged particles (c) extracted with the event plane method using the VZERO event plane [39] in two centrality classes (30-40% and 40-50%). (d) Comparison of the  $D^{*+}$   $v_2$ -wide-result to the  $v_2$  of charged particles [39].

The error bars of the charged particles  $v_2$ -measurements represent the combined systematic and statistical errors, which were summed in quadrature and then the square root of the sum was calculated. The vertical error bars of the charmed meson  $v_2$ -measurements represent the statistical errors and the spread of the boxes in vertical direction the total systematic errors without the B-feed-down contribution. The error bars in horizontal direction represent the distances from the point coordinate on the abscissa to the upper and lower limit of the corresponding  $p_T$ -bin. The point coordinate on the abscissa of the corresponding  $p_T$ -bin is the mean  $p_T$  in case of the charmed mesons and the edges of the systematic error boxes in horizontal direction represent the upper and the lower limit of the corresponding  $p_T$ -bin in case of the  $D^{*+}$ . In case of the  $D^0$  and  $D^+$  the spread of the boxes in horizontal direction is set to an arbitrary value of 0.8 GeV/c. The center in horizontal direction of these boxes is placed at the center of the corresponding  $p_T$ -bin in case of the  $D^{*+}$ , respectively at the mean  $p_T$  in case of the  $D^0$  and  $D^+$ .

tion for the  $D^0$  and  $D^+$  is similar to the  $D^{*+}$  case. However, in case of the  $D^0$  and  $D^+$  the spread of the boxes in horizontal direction is set to an arbitrary value of 0.8 GeV/c for better visibility. The center in horizontal direction of these boxes is placed at the mean  $p_T$  of the corresponding  $p_T$ -bin of the  $D^0$ , respectively  $D^+$ . Both the  $D^0$ - and the  $D^+$ - $v_2$ -results are consistent with the  $D^{*+}$   $v_2$ -results within the statistical and systematic uncertainties. A Physical Review Letter [111] is being prepared, which will contain the  $v_2$ -results of the

three charmed meson species. An averaged  $v_2$  as a function of  $p_T$  will be given as well as a statement how large the significance  $v_2/\sigma(v_2)$  in the  $p_T$ -range  $2 \text{ GeV}/c < p_T < 6 \text{ GeV}/c$  becomes by using the combined result of the three meson species.

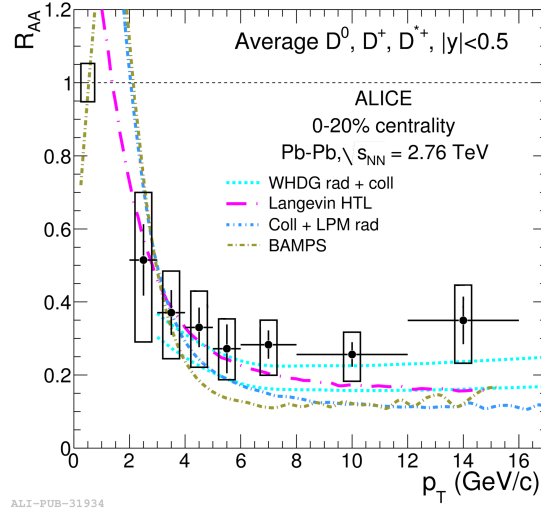
Figures 6.2c, 6.2d show the comparison of the  $D^{*+}$   $v_2$ -result in the two  $p_T$ -binning configurations "fine" (c) and "wide" (d) to the  $v_2$ -results obtained for unidentified charged particles with the ALICE detector. The  $v_2$  was determined with the event plane method, where the event plane angle  $\Psi_2$  was obtained using the VZERO-detector. The results for two centrality-bins are shown for 30-40% and 40-50%. For more analysis details see [39]. The  $D^{*+}$   $v_2$ -measurement is consistent with both charged particles  $v_2$ -measurements within its statistical and systematic uncertainties, which is a hint that charm-quarks take part in the collective expansion of the QGP to the same extent as light quarks. The  $D^{*+}$   $v_2$ -wide measurement in fig. 6.2d follows the same trend as a function of  $p_T$  as the  $v_2$  of charged particles but due to the large uncertainties this trend might originate from a statistical fluctuation. In case of the  $D^{*+}$   $v_2$ -measurement with the wider  $p_T$ -binning, the significance  $v_2/\sigma(v_2)$  for a non-zero  $v_2$  in the  $p_T$ -range  $2 \text{ GeV}/c < p_T < 6 \text{ GeV}/c$  is:

- $v_2/\sigma(v_2) = \mathbf{3.0}$  if considering only the statistical error.
- $v_2/\sigma(v_2) = \mathbf{2.2}$  if considering the statistical and the systematic error. Both errors are summed in quadrature and then the square root is calculated.

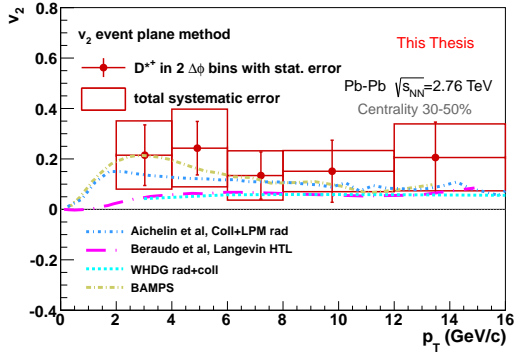
### 6.3. $D^{*+}$ $v_2$ comparison to $v_2$ -predictions from models

In this section the final  $D^{*+}$   $v_2$  results are compared to existing prompt D meson  $v_2$ -predictions from theoretical models. These state-of-the-art models are described in detail in chap. 2, sec. 2.4. These models provide a simultaneous prediction of the prompt D meson nuclear modification factor  $R_{AA}$  and the  $v_2$ . Therefore these predictions are compared both to the measured  $D^{*+}$   $v_2$  and to the prompt D meson  $R_{AA}$  carried out by the ALICE-collaboration [116].

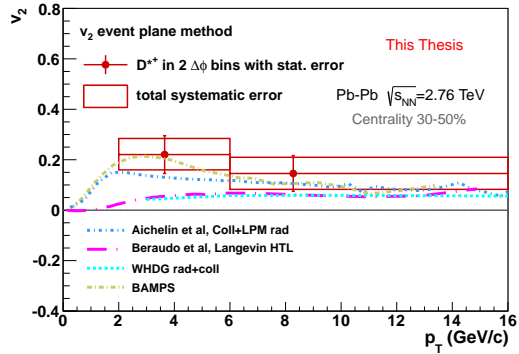
Figure 6.3a shows the comparison of the averaged prompt D meson  $R_{AA}$ -measurement [116] in a centrality range of 0-20% to the prompt D meson  $R_{AA}$ -predictions provided by theoretical models described in chap. 2, sec. 2.4. The average  $R_{AA}$  has been computed from the individual  $R_{AA}$ -measurements of the  $D^0$ ,  $D^+$  and  $D^{*+}$  mesons. The contributions of the individual  $R_{AA}$ -measurements were weighted by their statistical uncertainties. The vertical error bars represent the statistical errors and the spread of the boxes in vertical direction the systematic errors. The error bars in horizontal direction represent the distances from the point coordinate placed at the center of the corresponding  $p_T$ -bin to the upper and lower limit of the bin. The edges of the systematic error boxes in horizontal direction are set to an arbitrary value. For more details about the  $R_{AA}$ -analysis including the systematic error evaluation and B-feed-down treatment see [116]. Figures 6.3b, 6.3c show the comparison of the  $D^{*+}$   $v_2$ -result in the two  $p_T$ -binning configurations "fine" (b) and "wide" (c) to the various  $v_2$ -predictions provided by the same theoretical calculations, which were used to determine the  $R_{AA}$ -predictions. The definition of the sizes of the error bars and error boxes is identical to the datapoints shown in fig. 6.1. None of the models can be currently discarded on a  $3\sigma$ -level neither by the D meson  $R_{AA}$ -measurements nor by the  $D^{*+}$   $v_2$  measurement:



(a)



(b)



(c)

**Figure 6.3.:** Comparison of the averaged D meson  $R_{AA}$ -measurement [116] in a centrality range of 0-20% (a) and of the  $D^{*+}$   $v_2$ -result in the  $p_T$ -binning configurations "fine" (b) and "wide" (c) to  $v_2$ - and  $R_{AA}$ -predictions provided by theoretical models described in chap. 2, sec. 2.4. The vertical error bars of the averaged D meson  $R_{AA}$ -measurement and of the  $D^{*+}$   $v_2$ -measurements represent the statistical errors and the spread of the boxes in vertical direction the total systematic errors. For details about the  $R_{AA}$ -analysis including the systematic error evaluation and B-feed-down treatment see [116]. The error bars in horizontal direction represent the distances from the point coordinate on the abscissa to the upper and lower limit of the corresponding  $p_T$ -bin. The point coordinate on the abscissa of the corresponding  $p_T$ -bin is the mean  $p_T$  in case of the  $D^{*+}$   $v_2$ -measurements and the center of the  $p_T$ -bin in case of the averaged D meson  $R_{AA}$ -measurement. The edges of the systematic error boxes in horizontal direction represent the upper and the lower limit of the corresponding  $p_T$ -bin in case of the  $D^{*+}$   $v_2$ -measurement and are set to an arbitrary value in case of the averaged D meson  $R_{AA}$ -measurement. The center in horizontal direction of these boxes is placed at the center of the corresponding  $p_T$ -bin.

- The model provided by "Aichelin *et al.*" labeled as "Coll + LPM rad" in the  $R_{AA}$ -figure 6.3a (blue dotted line) and the BAMPs-model (golden dotted line) predict a large  $v_2$  for  $p_T < 6$  GeV/c of up to  $\approx 0.22$ , which levels of at  $v_2 \approx 0.1$  for higher

$p_T$ . The  $D^{*+} v_2$ -wide measurement in fig. 6.3c follows the same trend but due to the large uncertainties this trend might originate from a statistical fluctuation. The  $R_{AA}$ -measurement is reproduced well by these two models up to a  $p_T$  of about  $p_T \approx 4$  GeV/c and for  $p_T > 4$  GeV/c the  $R_{AA}$  is underestimated, i.e. the charm quark energy loss is overestimated.

- The WHDG-model (cyan dotted line) and the Langevin dynamics model [84] (magenta dotted line) predict a moderate D meson  $v_2$  of  $\approx 0.05$ , which shows a monotonic increase from zero at  $p_T \approx 2$  GeV/c and then levels off at  $v_2 \approx 0.05$  at  $p_T \approx 4$  GeV/c. The predicted  $v_2$  underestimates the measured  $D^{*+} v_2$  over the full  $p_T$ -range but the discrepancy is below a  $3\sigma$ -level in all  $p_T$ -bins, even using the  $D^{*+} v_2$ -wide measurement. Both models describe the measured D meson  $R_{AA}$  well in the full  $p_T$ -range, whereas the values for the  $R_{AA}$ -predictions are at the lower edge of the error bands of the measured  $R_{AA}$  for  $p_T > 7$  GeV/c.

## 6.4. $D^{*+} v_3$ comparison to other $v_3$ -measurements

In this section the measured  $D^{*+} v_3$  results are compared to the measured  $v_3$  of charged particles carried out by the ALICE-collaboration [39]. This comparison is performed to

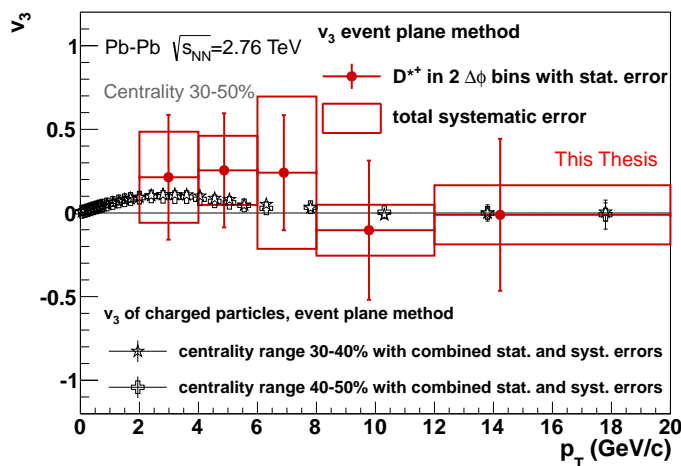


**Figure 6.4.:** Comparison of the  $D^{*+} v_3$  result to the  $v_3$  of charged particles [39] extracted with the event plane method using the VZERO event plane [39] in two centrality classes (30-40% and 40-50%). The error bars of the charged particles  $v_3$ -measurements represent the combined systematic and statistical errors, which were summed in quadrature and then the square root of the sum was calculated. The vertical error bars of the  $D^{*+} v_3$ -measurement represent the statistical errors and the spread of the boxes in vertical direction the total systematic errors without the B-feed-down contribution. The error bars in horizontal direction represent the distances from the point coordinate on the abscissa to the upper and lower limit of the corresponding  $p_T$ -bin. The point coordinate on the abscissa of the corresponding  $D^{*+} p_T$ -bin is the mean  $p_T$  and the edges of the systematic error boxes in horizontal direction represent the upper and the lower limit of the corresponding  $D^{*+} p_T$ -bin. The center in horizontal direction of these boxes is placed at the center of the corresponding  $D^{*+} p_T$ -bin.

investigate whether charm quarks thermalize in the expanding QGP and show the same magnitude of triangular flow as gluons and the light flavored quarks up, down and strange, which then fragment into the charged particles and contribute together to the charged particles  $v_3$ . The measurement of the anisotropy parameter  $v_3$  is particularly interesting because its magnitude puts constraints on initial conditions selection and the value used for the shear viscosity to entropy density ratio  $\eta/s$  within hydrodynamic models describing the expansion of a QGP. The  $v_3$  is namely driven by fluctuations in the individual nucleon-nucleon collision points from collision to collision. Figure 6.4 shows a comparison of the  $D^{*+}$   $v_3$ -result to the  $v_3$ -results obtained for unidentified charged particles with the ALICE detector, see [39]. The meaning of the error bars and boxes for the  $D^{*+}$   $v_3$  measurement is equal to the situation in fig. 6.1 described above. The  $v_3$  of the charged particles was determined with the event plane method and the event plane angle  $\Psi_3$  was obtained using the VZERO-detector. The results for two centrality-bins are shown for 30-40% and 40-50%. Due to its large statistical and systematic error bars the  $D^{*+}$   $v_3$ -measurement is currently consistent with zero in all  $p_T$ -bins and with both  $v_3$ -measurements of the charged particles. The  $D^{*+}$   $v_3$  measurement follows the same trend as a function of  $p_T$  as the  $v_3$  of charged particles but due to the large uncertainties this trend might originate from statistical fluctuations.

## 7. Summary and Outlook

Within this thesis the anisotropy parameters  $v_2$  and  $v_3$  of the fully reconstructed charmed  $D^{*+}$  meson and its charge conjugate  $D^{*-}$  in the fully reconstructed decay channels  $D^{*+} \rightarrow D^0\pi^+$ , respectively  $D^{*-} \rightarrow \bar{D}^0\pi^-$  were extracted. These measurements were carried out at a center-of-mass energy of  $\sqrt{s_{NN}} = 2.76$  TeV per nucleon. The  $v_2$ - and  $v_3$ -parameters were determined as a function of the transverse momentum  $p_T$  of the  $D^{*+}$  in a range of  $2 \text{ GeV}/c < p_T < 20 \text{ GeV}/c$ . For this study lead-lead collision data from the LHC heavy-ion run end of 2011 was exploited. In total  $9.5 \cdot 10^6$  lead-lead events in a collision centrality percentile range of 30-50% were analyzed. For extracting the anisotropy parameters  $v_2$  and  $v_3$  the event plane method was carefully implemented into the analysis framework for the charmed meson  $D^{*+}$  using the fully reconstructed decay channel  $D^{*+} \rightarrow D^0\pi^+$ . The central  $v_n$  results were obtained by usage of the event plane angles  $\Psi_2$  and  $\Psi_3$  determined with reconstructed tracks in the Time Projection Chamber event-by-event. In order to remove detector acceptance effects, which bias the determination procedure of these angles, an event plane angle flattening procedure based on particle weights as a function of  $\phi$  and on a recentering procedure of the Q-vectors was implemented. These Q-vectors are used to determine the event plane angles  $\Psi_2$  and  $\Psi_3$ . The detailed systematic error study for the  $D^{*+} v_2$ - and  $D^{*+} v_3$ -parameters was carried out by determining these parameters with various extraction methods.

The final central  $D^{*+} v_n$  results were compared to existing  $v_2$ -measurements of the open charmed mesons  $D^0$  and  $D^+$  [109, 110]. For the  $v_2$  measurement of the  $D^0$  and  $D^+$  mesons the event plane method using the Time Projection Chamber as for the  $D^{*+}$  meson described above was used. Moreover, the final central  $D^{*+} v_n$  results were compared to  $v_n$ -measurements of light flavored unidentified particles [39] within this thesis. In both cases the  $D^{*+} v_n$  measurements were consistent with the  $v_n$  measurements of the other particles provided by the ALICE collaboration within the statistical and systematic uncertainties. The relative statistical uncertainty of the  $D^{*+} v_2$  is in the range of 34% – 81% depending on the  $p_T$ -range. In case of the  $D^{*+} v_3$  the relative statistical uncertainty is in the range of 130% – 175% for the  $p_T$ -range of the  $D^{*+}$  of  $2 \text{ GeV}/c < p_T < 8 \text{ GeV}/c$ . For  $p_T > 8 \text{ GeV}/c$  the central  $v_3$ -value is of the order of  $\approx 0$  with currently large statistical uncertainties of the order of  $\pm 0.4$ . The total systematic uncertainties without the B-feed-down contribution are of the same order as the statistical uncertainties and the relative magnitude  $\Delta(v_n)/v_n$  is in the range of 29%-73% for the  $v_2$ -case in the full  $p_T$ -range and in the range 81%-190% for the  $v_3$ -case for a  $p_T$  of the  $D^{*+}$  of  $2 \text{ GeV}/c < p_T < 8 \text{ GeV}/c$ . For  $p_T > 8 \text{ GeV}/c$  the current absolute total systematic uncertainty of the  $D^{*+} v_3$  is of the order of  $\pm 0.3$ . The significance for a non-zero  $D^{*+} v_2$  in the  $p_T$  range of  $2 \text{ GeV}/c < p_T < 6 \text{ GeV}/c$  is 3.0 if considering the statistical error only, respectively 2.2 if considering both the total systematic uncertainty and the systematic uncertainty of the  $D^{*+} v_2$  measurement in that  $p_T$ -range.

The  $v_2$  results obtained within this thesis are the first measurement of the elliptic flow of the fully reconstructed charmed  $D^{*+}$  meson and its charge conjugate  $D^{*-}$  in the fully reconstructed decay channels  $D^{*+} \rightarrow D^0\pi^+$ , respectively  $D^{*-} \rightarrow \bar{D}^0\pi^-$ . These results together with the already published nuclear modification factor  $R_{AA}$  for charmed mesons [116] pose the most stringent constraints on modern state-of-the-art charmed hadron production models. Within this thesis, the extracted  $D^{*+} v_2$  was compared to  $v_2$  predictions provided by various models, whose  $R_{AA}$  predictions were already compared to a charmed meson  $R_{AA}$  measurement by the ALICE collaboration, see [116].

None of the models presented in this thesis provides a proper simultaneous description of the charmed meson  $R_{AA}$  and  $v_2$ . However, the current limited precision of the  $D^{*+} v_2$  measurement does not allow to exclude predictions provided by these models on a  $3\sigma$ -level. This precision will significantly improve using the data, that will be taken in the years 2015-2017 after the current long shutdown of the LHC. The expected integrated luminosity for the lead-lead data taking until reaching the next long shutdown presumably end of 2017 is of the order of  $\mathcal{L}_{\text{int}} = 1 \text{ nb}^{-1}$  for ALICE. This corresponds to about  $1.6 \cdot 10^9$  events in the centrality percentile range of 30-50%. This yields a factor  $f = 160$  with respect to the number of events, which were used for this thesis. The expected relative uncertainty of the  $D^{*+} v_2$  will be in the range of 3% – 6% depending on the  $p_T$  and in the range of 10% – 14% in case of the  $D^{*+} v_3$  using the data taken in the future. Figure 7.1 shows the final central results of the  $D^{*+} v_2$  (left) and the  $D^{*+} v_3$  (right) with the expected

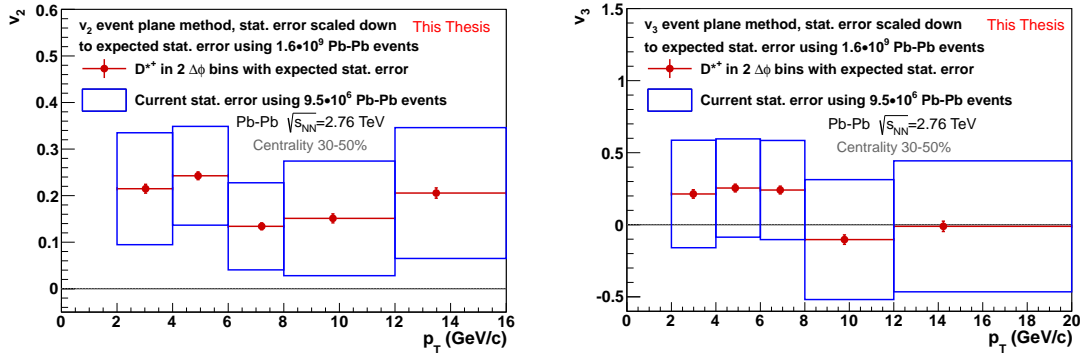


**Figure 7.1.:** Final central results of the  $D^{*+} v_2$  (left) and the  $D^{*+} v_3$  (right) with the statistical errors (red error bars) decreased by a factor, which accounts for the increased expected number of lead-lead events collected with the ALICE experiment until reaching the next long shutdown of the LHC in the year 2018. The current statistical errors of the  $D^{*+} v_n$ -measurements (blue boxes) are drawn in, either.

statistical errors using the data presumably taken in the years 2015-2017 (red error bars) as well as with the current statistical errors of the  $D^{*+} v_n$ -measurement (blue boxes). The new datapoints will naturally move within the blue boxes or even outside the blue boxes in some  $p_T$ -bins depending on the statistical fluctuations, when extracting the  $D^{*+} v_n$  results with the data taken in the future.

The enhanced statistics will also allow to extract the  $D^{*+} v_n$  at lower transverse momenta than to the current limit of  $p_T > 2 \text{ GeV}/c$ . At that low  $p_T$ , an efficient  $D^{*+}$  yield

---

extraction requires an advanced particle identification procedure on the decay daughters of the decay channel  $D^0 \rightarrow K^- \pi^+$  originating from the decay channel  $D^{*+} \rightarrow D^0 \pi^+$ . A particle identification method of the  $D^0$  daughters based on a reliable application of a Bayesian particle identification approach is currently under development [117]. This new method will improve the performance of the  $D^{*+}$  yield extraction at low  $p_T$ . Moreover, the upgrade of the Inner Tracking System of ALICE and the expected integrated luminosity of  $\mathcal{L}_{\text{int}} \approx 10 \text{ nb}^{-1}$  after 2018 will presumably enable ALICE to perform an  $R_{AA}$  and  $v_n$  measurement of fully reconstructed B mesons. A performance study on the full reconstruction of B mesons using the upgraded Inner Tracking System of ALICE is currently carried out [118]. A B meson  $v_2$  measurement will help to decrease the systematic error on the  $D^{*+} v_n$  measurement originating from the B-feed-down.

Using this thesis as a door-opener, it will be possible to achieve a high precision  $D^{*+} v_n$  measurement and to discard or favor model predictions. A precise  $D^{*+} v_3$  measurement will put constraints on initial conditions selection and on the viscosity to entropy ratio  $\eta/s$  within these models. The  $v_3$  is namely driven by fluctuations in the individual nucleon-nucleon collision points from collision to collision and is more sensitive to the viscosity to entropy ratio  $\eta/s$  than the  $v_2$ . These QGP density fluctuations can be probed by the heavy charm quarks which fragment to  $D^{*+}$  mesons.

# A. Appendix

## A.1. $D^{*+}$ yield extraction figures for the $3\text{-}\Delta\phi$ -bin case

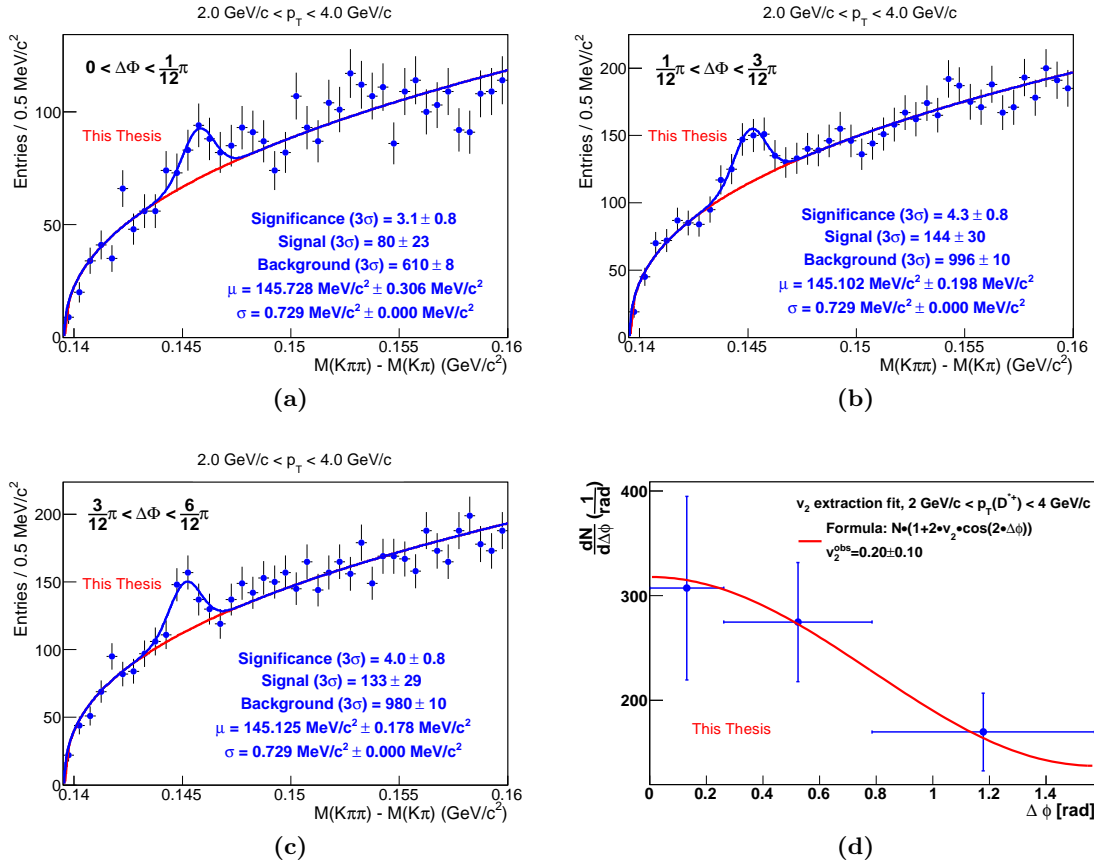


**Figure A.1.:** (a), (b), (c):  $D^{*+}$  yield extraction in 3  $\Delta\phi$ -bins in the  $p_T$ -bin  $2 \text{ GeV/c} < p_T < 4 \text{ GeV/c}$ . The centrality range is 30-50% and the topological cut set is cut-set 1 summarized in tab. 4.4 in chap. 4, sec. 4.1. The used event plane determination is TPC event plane using tracks only from the positive  $\eta$ -side. (d): Fit of the formula given eq. 5.5 to the extracted  $D^{*+}$ -yield as function of  $\Delta\phi$ . The error bars in the  $\Delta\phi$ -bins represent the statistical error of the yield extraction and the datapoints are placed in the center of the corresponding  $\Delta\phi$ -bin.

## A.1. $D^{*+}$ yield extraction figures for the 3- $\Delta\phi$ -bin case

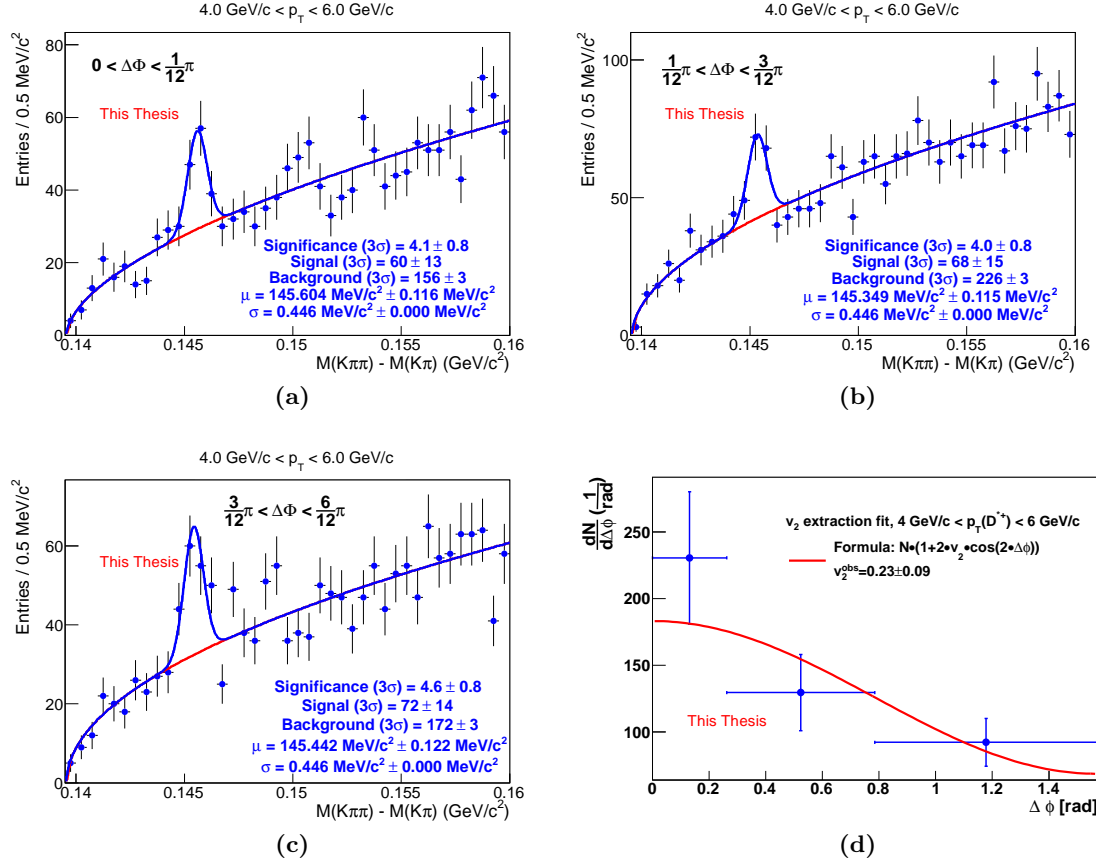


**Figure A.2.:** (a), (b), (c):  $D^{*+}$  yield extraction in 3  $\Delta\phi$ -bins in the  $p_T$ -bin  $4 \text{ GeV}/c < p_T < 6 \text{ GeV}/c$ . The centrality range is 30-50% and the topological cut set is cut-set 1 summarized in tab. 4.4 in chap. 4, sec. 4.1. The used event plane determination is TPC event plane using tracks only from the positive  $\eta$ -side. (d): Fit of the formula given eq. 5.5 to the extracted  $D^{*+}$ -yield as function of  $\Delta\phi$ . The error bars in the  $\Delta\phi$ -bins represent the statistical error of the yield extraction and the datapoints are placed in the center of the corresponding  $\Delta\phi$ -bin.

## A.2. $D^{*+}$ yield extraction figures for the $2-\Delta\phi$ -bin case

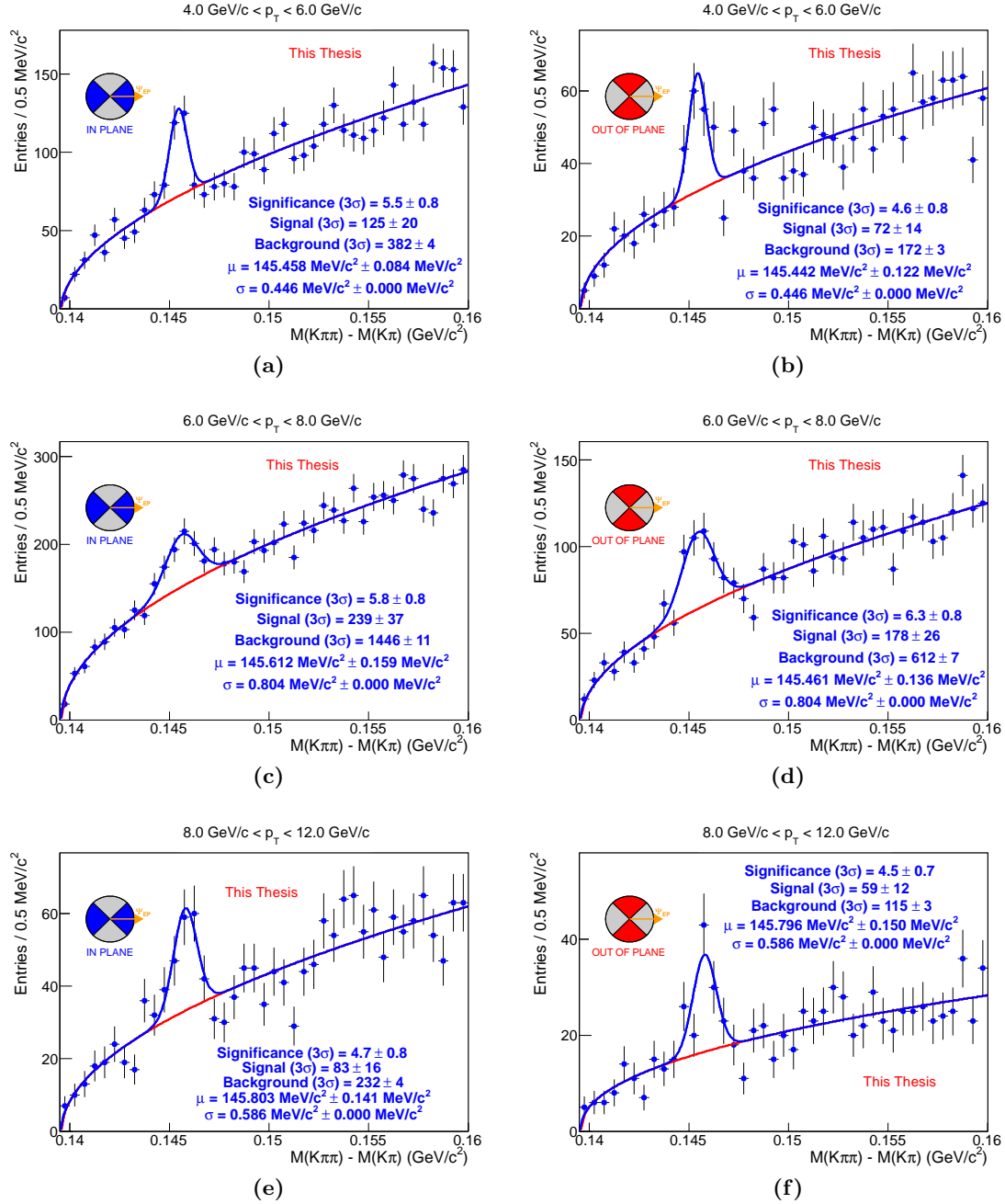


**Figure A.3.:**  $D^{*+}$  yield extraction in-plane and out-of-plane 3 different intermediate  $p_T$ -bins for the  $v_2$ -analysis:  $4 \text{ GeV}/c < p_T < 6 \text{ GeV}/c$  ((a), (b)),  $6 \text{ GeV}/c < p_T < 8 \text{ GeV}/c$  ((c), (d)) and  $8 \text{ GeV}/c < p_T < 12 \text{ GeV}/c$  ((e), (f)). The centrality range is 30-50% and the topological cut set is cut-set 1 summarized in tab. 4.4 in chap. 4, sec. 4.1. The used event plane determination is TPC event plane using tracks only from the positive  $\eta$ -side.

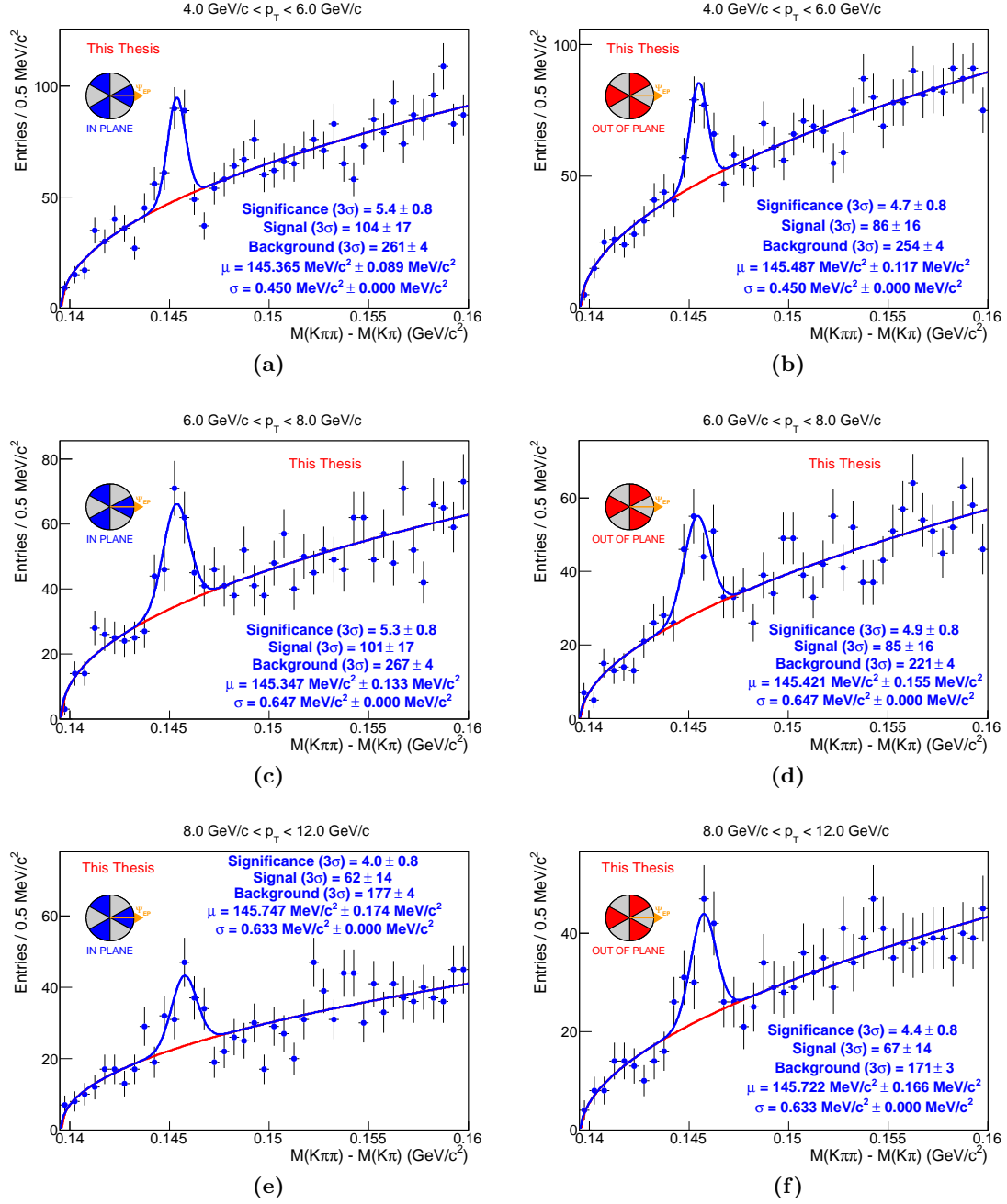


**Figure A.4.:**  $D^{*+}$  yield extraction in-plane and out-of-plane 3 different intermediate  $p_T$ -bins for the  $v_3$ -analysis:  $4 \text{ GeV}/c < p_T < 6 \text{ GeV}/c$  ((a), (b)),  $6 \text{ GeV}/c < p_T < 8 \text{ GeV}/c$  ((c), (d)) and  $8 \text{ GeV}/c < p_T < 12 \text{ GeV}/c$  ((e), (f)). The centrality range is 30-50% and the topological cut set is cut-set 1 summarized in tab. 4.4 in chap. 4, sec. 4.1. The used event plane is the TPC event plane with  $\eta$ -gap as depicted in fig. 5.9.

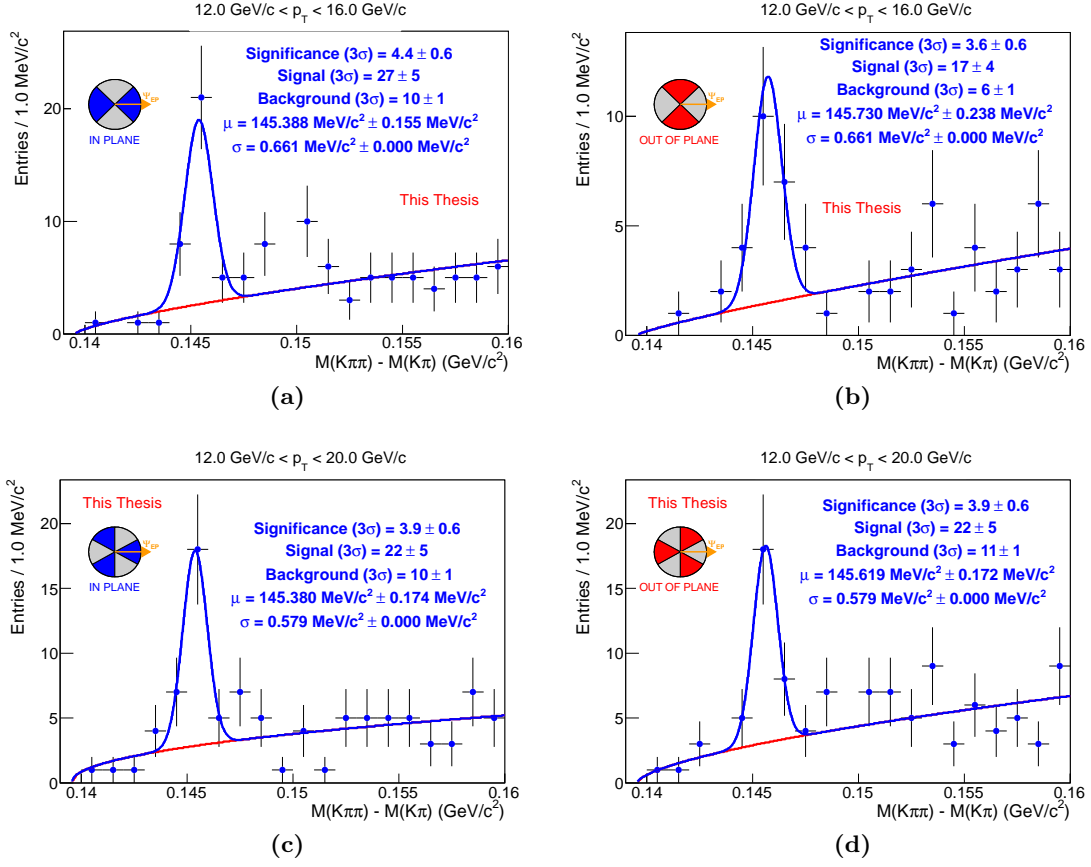


**Figure A.5.:**  $D^{*+}$  yield extraction in-plane and out-of-plane in the highest  $p_T$ -bin,  $12 \text{ GeV}/c < p_T < 16 \text{ GeV}/c$  for the  $v_2$ -analysis ((a), (b)) and  $12 \text{ GeV}/c < p_T < 20 \text{ GeV}/c$  for the  $v_3$ -analysis ((c), (d)). The centrality range is 30-50% and the topological cut set is cut-set 1 summarized in tab. 4.4 in chap. 4, sec. 4.1. The used event plane is the TPC event plane with  $\eta$ -gap as depicted in fig. 5.9 in the  $v_3$ -case and TPC event plane using tracks only from the positive  $\eta$ -side in the  $v_2$ -case.

# Bibliography

- [1] Cabibbo N and Parisi G 1975 *Phys. Lett. B* **B59** 67–69
- [2] Collins J C and Perry M J 1975 *Phys. Rev. Lett.* **34**(21) 1353–1356 URL <http://link.aps.org/doi/10.1103/PhysRevLett.34.1353>
- [3] Zhu X, Bleicher M, Huang S, Schweda K, Stoecker H, Xu N and Zhuang P 2007 *Phys. Lett. B* **647** 366
- [4] Miller M L, Reygers K, Sanders S J and Steinberg P 2007 *Ann. Rev. Nucl. Part. Sci.* **57** 205–243 URL <http://arxiv.org/abs/nucl-ex/0701025>
- [5] Website URL [http://www.interactions.org/sgtw/2006/1025/star\\_grid\\_more.html](http://www.interactions.org/sgtw/2006/1025/star_grid_more.html)
- [6] Luzum M 2011 *J. Phys. G* **38** 124026 URL <http://arxiv.org/abs/1107.0592>
- [7] Alver B and Roland G 2010 *Phys. Rev. C* **81**(5) 054905
- [8] Aamodt K *et al.* (ALICE Collaboration) 2011 *Phys. Rev. Lett.* **107** 032301 URL <http://arxiv.org/abs/1105.3865>
- [9] Schenke B, Jeon S and Gale C 2011 *Phys. Lett. B* **702** 59–63 URL <http://arxiv.org/abs/1102.0575>
- [10] Beringer J *et al.* (Particle Data Group) 2012 *Phys. Rev. D* **86** 010001
- [11] Borka Jovanovic V, Ignjatovic S, Borka D and Jovanovic P 2010 *Phys. Rev. D* **82** 117501 URL <http://arxiv.org/abs/1011.1749>
- [12] Gross D J and Wilczek F 1973 *Phys. Rev. Lett.* **30**(26) 1343–1346 URL <http://link.aps.org/doi/10.1103/PhysRevLett.30.1343>
- [13] Politzer H D 1973 *Phys. Rev. Lett.* **30**(26) 1346–1349 URL <http://link.aps.org/doi/10.1103/PhysRevLett.30.1346>
- [14] Satz H 1984 *Nucl. Phys. A* **418** 447C–465C
- [15] Yagi K, Hatsuda T and Miake Y 2005 *Quark-Gluon Plasma* (Cambridge: Cambridge University Press)
- [16] Bergische Universität Wuppertal website URL <http://astro.uni-wuppertal.de/html/Projekte/CBM.htm>
- [17] Abelev B *et al.* (ALICE Collaboration) 2012 *Phys. Rev. Lett.* **109**(25) 252301 URL <http://link.aps.org/doi/10.1103/PhysRevLett.109.252301>

- [18] Hagedorn R 1968 *Il Nuovo Cimento A* **56**(4) 1027–1057
- [19] Karsch F 2007 *PoS LAT2007* 015 URL <http://arxiv.org/abs/0711.0661>
- [20] Karsch F 2002 *Nucl. Phys. A* **698** 199–208 URL <http://arxiv.org/abs/hep-ph/0103314>
- [21] Kramer F 2006 *Studie zur Messung von Quarkonia mit dem ALICE-TRD und Aufbau eines Teststandes fuer seine Ausleseammern*, Diploma-thesis, Goethe University Frankfurt
- [22] Sarkar S, Satz H and Bikash S 2010 *Lect. Notes Phys.* **785** 1–369
- [23] Bjorken J D 1983 *Phys. Rev. D* **27**(1) 140–151
- [24] Website of Prof. Dr. In-Kwon Yoo URL [http://him.phys.pusan.ac.kr/~yoo/welcome\\_e.html](http://him.phys.pusan.ac.kr/~yoo/welcome_e.html)
- [25] Reygers K and Stachel J 2011 *Quark-Gluon Plasma Physics: from fixed target to LHC*, lecture notes, University of Heidelberg URL [http://www.physi.uni-heidelberg.de/~reygers/lectures/2011/qgp/qgp\\_lecture\\_ss2011.html](http://www.physi.uni-heidelberg.de/~reygers/lectures/2011/qgp/qgp_lecture_ss2011.html)
- [26] Hirano T, Heinz U W, Kharzeev D, Lacey R and Nara Y 2006 *Phys. Lett. B* **636** 299–304 URL <http://arxiv.org/abs/nuc1-th/0511046>
- [27] Hirano T and Tsuda K 2002 *Phys. Rev. C* **66** 054905 URL <http://arxiv.org/abs/nuc1-th/0205043>
- [28] Back B *et al.* (PHOBOS Collaboration) 2002 *Phys. Rev. C* **65** 061901 URL <http://arxiv.org/abs/nuc1-ex/0201005>
- [29] Iancu E and Venugopalan R 2003 *The Color glass condensate and high-energy scattering in QCD*, review for QGP3, Eds. Hwa R and Wang X N URL <http://arxiv.org/abs/hep-ph/0303204>
- [30] Adams J *et al.* (STAR Collaboration) 2005 *Nucl. Phys. A* **757** 102–183 URL <http://arxiv.org/abs/nuc1-ex/0501009>
- [31] Adams J *et al.* (STAR Collaboration) 2004 *Phys. Rev. C* **70**(4) 041901 URL <http://link.aps.org/doi/10.1103/PhysRevC.70.041901>
- [32] Qiu Z and Heinz U W 2011 *Phys. Rev. C* **84** 024911 URL <http://arxiv.org/abs/1104.0650>
- [33] Voloshin S A, Poskanzer A M and Snellings R 2008 *Collective phenomena in non-central nuclear collisions*, review paper, as accepted for publication URL <http://arxiv.org/abs/0809.2949>
- [34] Poskanzer A M and Voloshin S 1998 *Phys. Rev. C* **58** 1671–1678 URL <http://arxiv.org/abs/nuc1-ex/9805001>

- 
- [35] Aad G *et al.* (ATLAS Collaboration) 2012 *Phys. Rev. C* **86** 014907 URL <http://arxiv.org/abs/1203.3087>
- [36] Chatrchyan S *et al.* (CMS Collaboration) 2013 *Phys. Rev. C* **87** 014902 URL <http://arxiv.org/abs/1204.1409>
- [37] Chatrchyan S *et al.* (CMS Collaboration) 2012 *Phys. Rev. Lett.* **109** 022301 URL <http://arxiv.org/abs/1204.1850>
- [38] Snellings R *Anisotropic flow from ALICE*, talk given at the Quark Matter Conference 2011 in Annecy, France URL <http://qm2011.in2p3.fr>
- [39] Abelev B *et al.* (ALICE Collaboration) 2012 *Phys. Lett. B* **719** 18–28 URL <http://arxiv.org/abs/1205.5761>
- [40] Aamodt K *et al.* (ALICE Collaboration) 2010 *Phys. Rev. Lett.* **105** 252302 URL <http://arxiv.org/abs/1011.3914>
- [41] Glashow S, Iliopoulos J and Maiani L 1970 *Phys. Rev. D* **2** 1285–1292
- [42] Berger C 2006 *Elementarteilchenphysik* (Heidelberg: Springer)
- [43] Gaillard M and Lee B W 1974 *Phys. Rev. D* **10** 897
- [44] Goldhaber G, Pierre F, Abrams G, Alam M, Boyarski A *et al.* 1976 *Phys. Rev. Lett.* **37** 255–259
- [45] Peruzzi I, Piccolo M, Feldman G, Nguyen H, Wiss J *et al.* 1976 *Phys. Rev. Lett.* **37** 569–571
- [46] Feldman G, Peruzzi I, Piccolo M, Abrams G, Alam M *et al.* 1977 *Phys. Rev. Lett.* **38** 1313
- [47] Pumplin J, Stump D, Huston J, Lai H, Nadolsky P M *et al.* 2002 *JHEP* **0207** 012 URL <http://arxiv.org/abs/hep-ph/0201195>
- [48] Aaron F *et al.* (H1 and ZEUS Collaboration) 2010 *JHEP* **1001** 109 URL <http://arxiv.org/abs/0911.0884>
- [49] Dainese A 2003 *Charm production and in-medium QCD energy loss in nucleus nucleus collisions with ALICE: A Performance study*, Doctoral-thesis, Padova University URL <http://arxiv.org/abs/nucl-ex/0311004>
- [50] Peterson C, Schlatter D, Schmitt I and Zerwas P M 1983 *Phys. Rev. D* **27** 105
- [51] Wilkinson J 2011 *Analysis and Extrapolation of D Meson Cross Sections at the LHC*, Bachelor-thesis, University of Heidelberg URL <http://www.phys.uni-heidelberg.de/Publications/bachelor-jeremy-wilkinson.pdf>
- [52] Schael S *et al.* (ALEPH Collaboration, DELPHI Collaboration, L3 Collaboration, OPAL Collaboration, SLD Collaboration, LEP Electroweak Working Group, SLD Electroweak Group, SLD Heavy Flavour Group) 2006 *Phys. Rept.* **427** 257–454 URL <http://arxiv.org/abs/hep-ex/0509008>

- [53] Kartvelishvili V, Likhoded A and Petrov V 1978 *Phys. Lett. B* **78** 615
- [54] Bowler M 1981 *Z. Phys. C* **11** 169
- [55] Collins P and Spiller T 1985 *J. Phys. G* **11** 1289
- [56] Vogt R (Hard Probe Collaboration) 2003 *Int. J. Mod. Phys. E* **12** 211–270 URL <http://arxiv.org/abs/hep-ph/0111271>
- [57] Shuryak E V and Xiong L 1993 *Phys. Rev. Lett.* **70** 2241–2244 URL <http://arxiv.org/abs/hep-ph/9301218>
- [58] Uphoff J, Fochler O, Xu Z and Greiner C 2010 *Phys. Rev. C* **82** 044906 URL <http://arxiv.org/abs/1003.4200>
- [59] Migdal A B 1956 *Phys. Rev.* **103**(6) 1811–1820
- [60] Peitzmann T and Thoma M H 2002 *Phys. Rept.* **364** 175–246 URL <http://arxiv.org/abs/hep-ph/0111114>
- [61] Peigne S and Peshier A 2008 *Phys. Rev. D* **77** 114017 URL <http://arxiv.org/abs/0802.4364>
- [62] Mustafa M G, Pal D, Srivastava D K and Thoma M 1998 *Phys. Lett. B* **428** 234–240 URL <http://arxiv.org/abs/nuc1-th/9711059>
- [63] Braaten E and Thoma M H 1991 *Phys. Rev. D* **44**(9) R2625–R2630
- [64] Dokshitzer Y L and Kharzeev D 2001 *Phys. Lett. B* **519** 199–206 URL <http://arxiv.org/abs/hep-ph/0106202>
- [65] Gossiaux P, Bierkandt R and Aichelin J 2009 *Phys. Rev. C* **79** 044906 URL <http://arxiv.org/abs/0901.0946>
- [66] Gossiaux P and Aichelin J 2008 *Phys. Rev. C* **78** 014904 URL <http://arxiv.org/abs/0802.25256>
- [67] Aichelin J, Gossiaux P and Gousset T 2012 *Acta Phys. Polon. B* **43** 655–662 URL <http://arxiv.org/abs/1201.4192>
- [68] Cacciari M, Greco M and Nason P 1998 *JHEP* **9805** 007 URL <http://arxiv.org/abs/hep-ph/9803400>
- [69] Kolb P F and Heinz U W 2003 URL <http://arxiv.org/abs/nuc1-th/0305084>
- [70] Molnar D 2005 *J. Phys. G* **31** S421–S428 URL <http://arxiv.org/abs/nuc1-th/0410041>
- [71] Dover C B, Heinz U, Schnedermann E and Zimányi J 1991 *Phys. Rev. C* **44**(4) 1636–1654
- [72] Uphoff J, Fochler O, Xu Z and Greiner C 2012 *Phys. Lett. B* **717** 430–435 URL <http://arxiv.org/abs/1205.4945>

- 
- [73] Uphoff J, Fochler O, Xu Z and Greiner C 2011 *Phys. Rev. C* **84** 024908 URL <http://arxiv.org/abs/1104.2295>
- [74] Xu Z and Greiner C 2005 *Phys. Rev. C* **71** 064901 URL <http://arxiv.org/abs/hep-ph/0406278>
- [75] Xu Z and Greiner C 2007 *Phys. Rev. C* **76** 024911 URL <http://arxiv.org/abs/hep-ph/0703233>
- [76] Uphoff J private communication
- [77] Adare A *et al.* (PHENIX Collaboration) 2011 *Phys. Rev. C* **84** 044905 URL <http://arxiv.org/abs/1005.1627>
- [78] Wicks S, Horowitz W, Djordjevic M and Gyulassy M 2007 *Nucl. Phys. A* **784** 426–442 URL <http://arxiv.org/abs/nucl-th/0512076>
- [79] Horowitz W and Gyulassy M 2011 *J. Phys. G* **38** 124114 URL <http://arxiv.org/abs/1107.2136>
- [80] Thoma M H and Gyulassy M 1991 *Nucl. Phys. B* **351** 491–506
- [81] Braaten E and Thoma M H 1991 *Phys. Rev. D* **44** 1298–1310
- [82] Djordjevic M and Gyulassy M 2004 *Nucl. Phys. A* **733** 265–298 URL <http://arxiv.org/abs/nucl-th/0310076>
- [83] Vitev I 2006 *J. Phys. Conf. Ser.* **50** 119–126 URL <http://arxiv.org/abs/hep-ph/0503221>
- [84] Alberico W, Beraudo A, De Pace A, Molinari A, Monteno M *et al.* 2011 *Eur. Phys. J. C* **71** 1666 URL <http://arxiv.org/abs/1101.6008>
- [85] CERN press release website URL <http://press.web.cern.ch/press/PressReleases/Releases2008/PR09.08E.html>
- [86] LHC Programme Coordination web pages URL <http://lpc.web.cern.ch/lpc/>
- [87] Aad G *et al.* (ATLAS Collaboration) 2008 *JINST* **3** S08003
- [88] Alves A Augusto J *et al.* (LHCb Collaboration) 2008 *JINST* **3** S08005
- [89] Chatrchyan S *et al.* (CMS Collaboration) 2008 *JINST* **3** S08004
- [90] CERN website URL [http://espace.cern.ch/liu-project/LIU\\_images/Forms/DispForm.aspx?ID=1](http://espace.cern.ch/liu-project/LIU_images/Forms/DispForm.aspx?ID=1)
- [91] Carminati F E *et al.* (ALICE Collaboration) 2004 *J. Phys. G* **30** 1517–1763
- [92] Aamodt K *et al.* (ALICE Collaboration) 2010 *JINST* **5** P03003 URL <http://arxiv.org/abs/1001.0502>

- [93] Aamodt K *et al.* (ALICE Collaboration) 2010 *JINST* **5** P03003 URL <http://arxiv.org/abs/1001.0502>
- [94] Ortona G 2012 *D<sup>+</sup> meson analysis at the LHC with ALICE*, Doctoral-thesis, University of Turin URL <http://personalpages.to.infn.it/~ortona/PhD.html>
- [95] Kalweit A 2008 *Energy Loss Calibration of the ALICE Time Projection Chamber*, Master-thesis, TU Darmstadt
- [96] Aamodt K *et al.* (ALICE Collaboration) *JINST* **3** S08002
- [97] 2000 *ALICE Time-Of-Flight system (TOF): Technical Design Report* Technical Design Report ALICE (Geneva: CERN)
- [98] Abelev B *et al.* (ALICE Collaboration) 2013 *Centrality determination of Pb-Pb collisions at  $\sqrt{s_{NN}} = 2.76$  TeV with ALICE*, article in preparation URL <http://arxiv.org/abs/1301.4361>
- [99] Wang X N and Gyulassy M 1991 *Phys. Rev. D* **44**(11) 3501–3516 URL <http://link.aps.org/doi/10.1103/PhysRevD.44.3501>
- [100] Sjostrand T 1994 *Comput. Phys. Commun.* **82** 74
- [101] Sjostrand T and Skands P 2006 *JHEP* **0605** 026
- [102] Skands P 2010 *Phys. Rev. D* **82** 074018
- [103] ALICE Collaboration, *The ALICE Offline Bible*, URL <http://aliweb.cern.ch/secure/Offline/sites/aliweb.cern.ch.Offline/files/uploads/OfflineBible.pdf>
- [104] Fruhwirth R 1987 *Nucl. Instrum. Meth. A* **262** 444–450
- [105] Alessandro G E *et al.* (ALICE Collaboration) 2006 *J. Phys. G* **32** 1295–2040
- [106] Blum W and Rolandi L 1998 *Particle Detection with Drift Chambers* (Berlin: Springer)
- [107] Qiu Z and Heinz U 2012 *Phys. Lett. B* **717** 261–265 URL <http://arxiv.org/abs/1208.1200>
- [108] Adare A *et al.* (PHENIX Collaboration) 2011 *Phys. Rev. Lett.* **107** 252301 URL <http://arxiv.org/abs/1105.3928>
- [109] Grajcarek R (ALICE Collaboration) 2012 *Measurement of heavy-flavor production in Pb-Pb collisions at the LHC with ALICE*, conference proceedings of a talk given at the 11th International Conference on Nucleus-Nucleus Collisions (NN2012), San Antonio, Texas, USA, to appear in the NN2012 Proceedings in Journal of Physics: Conference Series (JPCS) URL <http://arxiv.org/abs/1209.1925>

- [110] Caffarri D (ALICE Collaboration) 2012 *Measurement of the D meson elliptic flow in Pb-Pb collisions at  $\sqrt{s_{\text{NN}}} = 2.76$  TeV with ALICE*, conference proceedings of the Quark Matter 2012 conference in Washington, DC, USA URL <http://arxiv.org/abs/1212.0786>
- [111] Abelev B *et al.* (ALICE Collaboration) *D meson elliptic flow in non-central Pb-Pb collisions at  $\sqrt{s_{\text{NN}}} = 2.76$  TeV*, letter in preparation, to be published in 2013
- [112] Abelev B *et al.* (ALICE Collaboration) 2012 *JHEP* **1207** 191 URL <http://arxiv.org/abs/1205.4007>
- [113] Aaij R *et al.* (LHCb Collaboration) 2010 *Phys. Lett. B* **694** 209–216 URL <http://arxiv.org/abs/1009.2731>
- [114] Khachatryan V *et al.* (CMS Collaboration) 2011 *Eur. Phys. J. C* **71** 1575 URL <http://arxiv.org/abs/1011.4193>
- [115] Lange D 2001 *Nucl. Instrum. Meth. A* **462** 152–155
- [116] Abelev B *et al.* (ALICE Collaboration) 2012 *JHEP* **1209** 112 URL <http://arxiv.org/abs/1203.2160>
- [117] Wilkinson J Doctoral-thesis, University of Heidelberg, in preparation
- [118] Stiller J Doctoral-thesis, University of Heidelberg, in preparation



# Acknowledgements

At this point I would like to express my gratitude to the people who made this thesis possible and supported me:

I'm deeply grateful to my supervisor Dr. Kai Schweda who gave me the unique opportunity to work in such an interesting field such as high energy physics with the ALICE detector. Due to his knowledge and experience I profited from many fruitful discussions about physics with him during my years as PhD student. He always listened patiently to my questions and problems and was always interested in the current status of my work. Moreover, the large number of XXL-giant-hamburgers he invited me to in Heidelberg's Hemmingway's helped me through hard times.

Prof. Dr. Johanna Stachel I'd like to thank for giving me the unique possibility to be part of the Heidelberg ALICE TRD working group. Being part of it, enabled me to concentrate on my PhD due to an appropriate environment within the working group, to travel to important conferences and to CERN presenting my research results and to profit from the scientific expertise in her working group. Moreover, I profited a lot from her experience by providing me useful hints during my talks about my work in our group meetings.

I'm thankful to Prof. Dr. Ulrich Uwer, who agreed to be the second referee of this thesis. Dr. C. Yvonne Pachmayer, Dr. Antonin Maire, Dr. Martin Holthausen and Dr. Jan Uphoff I'd like to thank for reading my thesis to reduce mistakes and their suggestions which improved this thesis.

Dipl. Phys. Daniel Lohner I thank for fruitful discussions about anisotropic flow analysis and how to treat systematic and statistical uncertainties.

Concerning solving any kind of computer and software problems special thanks go to Dr. Minjung Kweon and to Martin Gabel.

Last but not least, I want to thank Miriam and my parents for their encouragement and support, which made this thesis possible.

This work has been supported by the Helmholtz Association under contract number VH-NG-147 and the Federal Ministry of Education and Research under promotional reference 06HD197D.